



## PhD Thesis:

# The Impact of Hydrogen Addition on Gas Turbine Power Generation Resilience

CDT: RESILIENT DECARBONISED FUEL ENERGY  
SYSTEMS

**James Bain B.Eng M.Sc**

SUBMISSION DATE: 30TH OF DECEMBER, 2023.

# Quotes

*“It’s up to us collectively and individually saying “how do we make a better versus a worse Anthropocene?” We can think about how we can work to connect the earth system, rather than accidentally cause all these consequences. We can purposefully look after the living world in a way the the living world helps people. Human ingenuity is the hope we have for having a positive future.”*

Prof. Garry Peterson

*“Beyond a wholesome discipline, be gentle with yourself.”*

Max Ehrmann



# Acknowledgements

I would like to express my deepest gratitude to my supervisors Prof Richard Marsh and Prof Phil Bowen for your continued support during my research. Your encouragement and insightful questions illuminated the path of this project. I am also grateful for your inspiring teaching during my undergraduate and master's studies, which sparked my passion for our shared field of study. I extend my sincerest gratitude to RWE Generation UK for the sponsorship of this doctoral project, and to all at RWE who have supported this work.

Special thank you goes to the remarkable team at the GTRC. Steve Morris, Dr Burak Goktepe, Dr Tony Giles and Jack Thomas. I have thoroughly enjoyed being an addition to the great research culture you have all created at the GTRC and value your contributions to this project greatly. And of course, I must thank you for the mind-expanding conversations at lunch!

A sincere thank you goes to my parents, Ian and Lynne Bain. Your patience, kindness and generosity will never be lost on me. Billie, my brother, I thank you for being you, you are the magnetic north in my moral compass.

To my friends, while there are too many to name individually, notable thank-you's go to Elis Williams, Alexander Davies, Callum MacHattie and George Hunt-Pain. Times we have shared have been a constant source of joy, laughter, and even a little smattering of profundity.

And finally, to Emma Kolano. I express my most heartfelt gratitude to you for your unwavering support, unconditional love and deepest belief in me, I simply would not have been able to do it without you. Here's to the next chapter.

# Contents

<b>1</b>	<b>Introduction</b>	<b>1</b>
1.1	Motivation: Climate Change & Security of Supply . . . . .	1
1.1.1	Energy Trilemma . . . . .	3
1.2	Combustion . . . . .	5
1.2.1	Societal Challenges of Combustion . . . . .	6
1.2.2	Sustainable Challenges of Combustion . . . . .	8
1.3	Institutional Policies, Treaties and Strategies . . . . .	9
1.3.1	International Treaties . . . . .	10
1.3.2	European Policies . . . . .	10
1.3.3	UK Acts and Policies . . . . .	11
1.4	Power Sector: Global and UK Trends . . . . .	13
1.5	Gas Turbine Development . . . . .	15
1.6	Alternative Fuels . . . . .	17
1.6.1	Hydrogen & Ammonia Fuel . . . . .	18
1.6.2	Additional Technologies - Power Decarbonisation . . . . .	21
1.7	Research Sponsor - RWE Generation UK . . . . .	22
1.7.1	Project Aims for RWE . . . . .	24
1.7.2	Project Aims . . . . .	24
<b>2</b>	<b>Literature Review</b>	<b>26</b>
2.1	Fundamentals of Hydrogen . . . . .	26
2.1.1	Calorific Content . . . . .	27

2.1.2	Adiabatic Flame Temperature . . . . .	28
2.1.3	Autoignition . . . . .	29
2.1.4	Flame speed & Flashback . . . . .	30
2.2	Fundamentals of Hydrogen and Methane Fuel Blends . . . . .	31
2.2.1	Flame Speed of Methane/Hydrogen Blends . . . . .	32
2.2.2	Ignition Delay Time of Methane/Hydrogen Blends . . . . .	33
2.2.3	Adiabatic Flame Temperature of Methane/Hydrogen Blends . . . . .	35
2.2.4	Flame Stability . . . . .	36
2.2.5	Fundamentals Conclusion . . . . .	37
2.3	GT fuel Flexibility . . . . .	38
2.3.1	Wobbe Index . . . . .	38
2.4	Current State of the Art of GT Hydrogen Capability . . . . .	40
2.4.1	Diffusion Based Combustors . . . . .	40
2.4.2	Premixed Based Combustors . . . . .	41
2.5	GT26 Research . . . . .	43
2.5.1	GT26 Operating Principles . . . . .	44
2.5.2	EV Burner . . . . .	46
2.5.3	SEV Burner . . . . .	46
2.5.4	Hydrogen Capabilities of the GT26 . . . . .	49
2.5.5	High Efficiency Upgrade Relevance for Hydrogen Capabilities . . . . .	57
2.6	Hypothesis . . . . .	59
2.7	Turbulent Autoignition Literature . . . . .	60
2.7.1	GT36 - Industrially Relevant Turbulent Autoignition . . . . .	66
2.8	Literature Review Conclusion . . . . .	68
2.8.1	Project Objectives . . . . .	69
<b>3</b>	<b>Design and Commissioning of Novel High Temperature Inhomogeneous Mixture Autoignition Facility.</b>	<b>70</b>
3.1	Essential Criteria of Design . . . . .	71
3.1.1	Flow through Rig . . . . .	71

3.1.2	Optical Access . . . . .	73
3.1.3	Change in Turbulence . . . . .	73
3.2	Design Decisions . . . . .	73
3.2.1	Air Heater vs GSB . . . . .	74
3.2.2	Electric Air Heater Detail . . . . .	76
3.2.3	Fuel Delivery . . . . .	76
3.2.4	Turbulence Devices . . . . .	77
3.3	Ancillary Components . . . . .	80
3.3.1	Fuel Delivery . . . . .	80
3.3.2	Steam Injection . . . . .	82
3.3.3	Transition Piece . . . . .	83
3.3.4	Quartz tube . . . . .	84
3.3.5	Insulation . . . . .	87
3.4	Instrumentation . . . . .	87
3.4.1	Oxidant Flow Temperature Measurement . . . . .	87
3.4.2	Fuel Flow Measurement . . . . .	89
3.4.3	Design Conclusions . . . . .	90
3.5	Health & Safety . . . . .	91
3.6	Commissioning . . . . .	92
3.6.1	First Flame . . . . .	92
3.6.2	Methane Testing . . . . .	94
3.6.3	Methane/Hydrogen Fuel Blend Testing . . . . .	95
3.6.4	Pure Natural Gas Case . . . . .	101
3.6.5	Pure Hydrogen Case . . . . .	102
3.6.6	Axial Temperature Profile . . . . .	104
3.6.7	Commissioning Major Findings . . . . .	104
3.7	TIMAR Development Conclusions . . . . .	106

**4 Experimental Methodologies Pertaining to Novel Turbulent Inhomogeneous Mixture Autoignition Facility Testing. 107**

4.1	Development of Experimental Philosophy . . . . .	108
4.1.1	Decision Triangle . . . . .	108
4.1.2	Maintaining Flow Field Conditions . . . . .	110
4.1.3	Maintaining Thermal Power . . . . .	111
4.2	Test Matrix Development . . . . .	112
4.2.1	Fundamental Study of Each Constituent in the Oxidant. . . . .	112
4.2.2	Applied Conditions Relevant to the Fuel Blend Under Evaluation. . . . .	113
4.2.3	Air as Oxidant . . . . .	114
4.3	Testing Methodology . . . . .	117
4.4	Flow Field Particle Image Velocimetry . . . . .	118
4.4.1	PIV Operating Principles . . . . .	118
4.4.2	PIV Setup . . . . .	119
4.4.3	Dynamically Similar Conditions . . . . .	121
4.4.4	PIV Methodology . . . . .	122
4.4.5	Particle Image Velocimetry Settings Optimisation for Data Acquisition . . . . .	124
4.4.6	Optimisation of Image Pre-Processing and Analysis Settings. . . . .	130
4.4.7	Methods of PIV Analysis of Varying Turbulence Devices . . . . .	137
4.4.8	PIV Methodology Conclusions . . . . .	140
4.5	Data Acquisition Techniques . . . . .	140
4.5.1	Measured Lifted Flame Height . . . . .	141
4.5.2	Measured Flame Establishment Time . . . . .	144
4.5.3	FET: Measuring Equipment and Set-up . . . . .	145
4.5.4	Calculated Ignition Delay Time . . . . .	146
4.5.5	Calculated Damköhler Number . . . . .	147
4.6	Uncertainty Analysis . . . . .	148
4.6.1	Direct Measurements . . . . .	148
4.6.2	Calculated Variables . . . . .	149

4.6.3	Uncertainty Analysis Conclusion . . . . .	150
4.7	Experimental Methodologies Conclusions . . . . .	150

**5 Turbulence and Temperature Effects on Autoignition of Hydrogen**

<b>Enriched Fuels</b>		<b>153</b>
5.1	Particle Image Velocimetry - Results . . . . .	154
5.1.1	Turbulence Intensity and Lengthscales . . . . .	154
5.1.2	Centreline Velocity . . . . .	155
5.1.3	Centreline Turbulence Intensity . . . . .	155
5.1.4	Turbulence Intensity Contours . . . . .	158
5.2	Particle Image Velocimetry Discussion . . . . .	160
5.2.1	Fuel Jet Seeding . . . . .	160
5.2.2	Air Flow Seeding . . . . .	161
5.2.3	Variation in Velocity Between Air and Fuel Flows . . . . .	161
5.2.4	PIV Analysis Outcomes . . . . .	162
5.3	Temperature Effects - Results . . . . .	163
5.3.1	Temperature Effects: Lifted Flame Height vs Hydrogen Content	163
5.3.2	Temperature Effects: Flame Establishment Time vs Hydrogen Content . . . . .	164
5.3.3	Temperature Effects: Ignition Delay Time vs Hydrogen Content	165
5.3.4	Temperature Effects: Damkhöler vs Hydrogen Content . . . . .	166
5.4	Temperature Effects Discussion . . . . .	167
5.4.1	Temperature Effects: Lifted Flame Height vs Hydrogen Content	168
5.4.2	Temperature Effects: Flame Establishment Time vs Hydrogen Content . . . . .	168
5.4.3	Temperature Effects: Ignition Delay Time vs Hydrogen Content	169
5.4.4	Temperature Effects: Damkhöler Number vs Hydrogen Content	170
5.4.5	Temperature Effects Conclusion . . . . .	170
5.5	Turbulence Effects Results . . . . .	172
5.5.1	Turbulence Effects: Lifted Flame Height vs Hydrogen Content	172

5.5.2	Turbulence Effects: Flame Establishment Time vs Hydrogen Content . . . . .	173
5.5.3	Turbulence Effects: Ignition Delay Time vs Hydrogen Content	174
5.5.4	Turbulence Effects: Damkhöler vs Hydrogen Content . . . . .	176
5.6	Turbulence Effects Discussion . . . . .	177
5.6.1	Turbulence Effects: Lifted Flame Height vs Hydrogen Content	177
5.6.2	Turbulence Effects: Flame Establishment Time vs Hydrogen Content . . . . .	178
5.6.3	Turbulence Effects: Ignition Delay Time vs Hydrogen Content	179
5.6.4	Turbulence Effects: Damkhöler Number vs Hydrogen Content	180
5.7	Results Conclusions . . . . .	181
<b>6</b>	<b>Computational Fluid Dynamic Simulations of Inhomogeneous Mixture Autoignition</b>	<b>184</b>
6.1	CFD Theory . . . . .	185
6.2	CFD Geometry . . . . .	187
6.3	Mesh Independence Study . . . . .	188
6.4	Determining the Turbulence Model . . . . .	191
6.5	Combustion Model Inputs . . . . .	193
6.5.1	Species Transport PDF Table . . . . .	193
6.5.2	Materials . . . . .	194
6.5.3	Inlet Conditions . . . . .	194
6.5.4	Radiation Modelling . . . . .	195
6.5.5	Convergence Criterion . . . . .	197
6.5.6	Solution Controls . . . . .	198
6.5.7	Inclusion of Compressibility Effects . . . . .	198
6.6	Combustion CFD Results . . . . .	199
6.7	Combustion CFD Discussion . . . . .	203
<b>7</b>	<b>Conclusions and Future Work.</b>	<b>208</b>

7.1	Conclusions . . . . .	209
7.1.1	Development of Experimental Test Campaign . . . . .	209
7.1.2	The TIMAR Development . . . . .	209
7.1.3	Methodologies . . . . .	210
7.1.4	Impact of Turbulence . . . . .	211
7.1.5	Industrial Relevance . . . . .	211
7.2	Future Work . . . . .	212
7.2.1	Synthesised Reheat Oxidant Compositions . . . . .	212
7.2.2	Fuel Lance Design . . . . .	212
7.2.3	Emission Analysis . . . . .	213
7.2.4	Turbulence Devices . . . . .	213
7.2.5	Elevated Pressure . . . . .	214
7.2.6	CFD . . . . .	214
<b>A</b>	<b>APPENDIX A: Technical Drawings</b>	<b>215</b>
<b>B</b>	<b>APPENDIX B: MATLAB Scripts</b>	<b>222</b>
B.1	Oxidant Thermocouple Correction. . . . .	222
B.1.1	Oxidant Thermocouple Correction Description. . . . .	222
B.1.2	Oxidant Thermocouple Correction Script. . . . .	222
B.2	Fuel Lance Thermocouple Correction. . . . .	226
B.2.1	Fuel Lance Thermocouple Correction Description. . . . .	226
B.2.2	Fuel Lance Thermocouple Correction Script. . . . .	229
B.3	Chemiluminescence Image Processing. . . . .	234
B.3.1	Chemiluminescence Image Processing Description. . . . .	234
B.3.2	Chemiluminescence Image Processing Script. . . . .	236
B.4	Turbulence Intensity and Radial Velocity Profile . . . . .	242
B.4.1	Turbulence Intensity and Radial Velocity Profile Description . . . . .	242
B.4.2	Turbulence Intensity and Radial Velocity Profile Script . . . . .	243
B.5	Turbulent Lengthscale Calculator. . . . .	250



B.5.1	Turbulent Lengthscale Calculator Description. . . . .	250
B.5.2	Turbulent Lengthscale Calculator Script. . . . .	250
<b>C</b>	<b>APPENDIX C: CFD Contours</b>	<b>254</b>
<b>D</b>	<b>APPENDIX D: Health and Safety Documentation</b>	<b>264</b>
D.1	Risk Assessment . . . . .	264
D.2	DSEAR Assessment . . . . .	273
D.2.1	DSEAR Specific Case Document . . . . .	273
D.2.2	DSEAR Supporting Standard Document . . . . .	279
D.2.3	Supporting Calculations . . . . .	279
D.3	COSSH Assessment . . . . .	281
D.4	Safe Operating Procedure . . . . .	288
D.5	SEV Oxidant Inlet Composition Investigation . . . . .	298
D.5.1	Introduction . . . . .	298
D.5.2	Test Matrix Development . . . . .	298
D.5.3	Fundamental Study of Each Constituent in the Oxidant. . . . .	298
D.5.4	Applied Conditions Relevant to the Fuel Blend Under Evalu- ation. . . . .	299
D.5.5	Adiabatic Flame Temperature . . . . .	300
D.5.6	O <sub>2</sub> Level into the HPT. . . . .	301
D.5.7	O <sub>2</sub> Level Entering the SEV Combustor . . . . .	302
D.5.8	Determining ER for CH <sub>4</sub> combustion in GT26. . . . .	304
D.5.9	Confidential 0D Model. . . . .	305
D.5.10	Flue Compositions From EV . . . . .	305
D.5.11	Conclusion . . . . .	307

# Abstract

As industries turn to hydrogen as a key strategy for mitigating CO<sub>2</sub> emissions, this doctoral thesis investigates the impact of hydrogen on the resilience of Gas Turbines (GT) employed in Power Generation. Given the wide use of carbonaceous fuels in operational GTs, and the difference in reactivity between hydrogen and carbonaceous fuels, investigations into the feasibility of conversion are required. This research identifies the GT26 GT is limited by the autoignition of highly reactive fuels within the GT26 under its current configuration.

This thesis investigates the impact of turbulence on the ignition of hydrogen-enriched fuels in inhomogeneous mixtures of fuel and oxidant at elevated temperatures. To test this hypothesis, a novel combustion facility is designed and commissioned at Cardiff University's Gas Turbine Research Centre. Quantification of turbulence characteristics is achieved by Particle Image Velocimetry analysis of the flow field resulting from three different turbulence devices. The turbulence impact revealed that smaller turbulent lengthscales exert an inhibitory effect on the ignition of fuel blends with higher hydrogen proportions. A highly valuable finding in this study is the interplay between the rate of reactants mixing and the rate of the chemistry reaction, as characterised by the non-dimensional Damköhler Number. This highlights the ability to control the ignition of hydrogen-enriched fuels in the GT26 by introducing carefully designed geometric features to create the desired turbulence characteristics to ensure the reaction rate is dominated by the reactant mixing rate.

# Nomenclature

## List of Acronyms

**AFR** Air Fuel Ratio

**AFT** Adiabatic Flame Temperature

**CfD** Contracts for Difference

**CLAHE** Contrast Limited Adaptive Histogram Equalisation

**CPSC** Constant Pressure Sequential Combustor

**DLN** Dry Low NO<sub>x</sub>

**DLR** Deutsches Zentrum für Luft- und Raumfahrt

**ER** Equivalence Ratio

**EU** European Union

**EV** Environmental Burner

**FET** Flame Establishment Time

**FSF** Fuel-Steam Flange

**GE** General Electric

**GHG** Greenhouse Gas

**GSB** Generic Swirl Burner

**GT** Gas Turbine

**GTRC** Gas Turbine Research Centre

**IDT** Ignition Delay Time

**JICF** Jet-in-cross-flow

**LFH** Lifted Flame Height

**LPM** Lean Premixed

**MHI** Mitsubishi Heavy Industries

**MD** Mixing Duct

**MMX** Micromix

**NDC** Nationally Determine Contributions

**NG** Natural Gas

**OEM** Original Equipment Manufacturer

**PIV** Particle Image Velocimetry

**RCHI** Reduced Catalytic Hydrogen Injector

**RES** Renewable energy Source

**ROI** Region of Interest

**SEV** Sequential Environmental Burner

**TDV** Turbulence Device

**TIMAR** Turbulent Inhomogeneous Mixture Autoignition Rig

**TRN** Transition Piece

**UNFCCC** United Nation Framework Convention on Climate Change

**VG** Vortex Generators

**VIGV** Variable Inlet Guide Vanes

**WI** Wobbe Index

**WLE** Wet Low Emissions

### List of Symbols

- $\alpha$  Absorption Coefficient [ $m^2/mol$ ]
- $\beta$  Oxygen Mole Fraction in Mixture
- $\gamma$  Adiabatic Index
- $\delta_T$  Boundary Layer Thickness [ $m$ ]
- $\epsilon$  Emissivity Coefficient [ $W/m^2$ ]
- $\eta$  Kolmogorov Lengthscale [ $mm$ ]
- $\mu$  Dynamic Viscosity [ $Ns/m^2$ ]
- $\mu_0$  Reference Dynamic Viscosity [ $Ns/m^2$ ]
- $\rho$  Density [ $kg/m^3$ ]
- $\sigma$  Stefan-Boltzmann Constant [ $W/m^2K^4$ ]
- $\sigma_i$  Uncertainty
- $\sigma_{RSS}$  Root Squared Sum
- $\tau_{IGN}$  Ignition Delay Time [ $s$ ]
- BFL Back Focal Length [ $mm$ ]
- C Sutherland Constant [ $^{\circ}R$ ]
- c Speed of Sound [ $m/s$ ]

$C_{p,oxi}$	Oxidant Heat Capacity [ $J/K$ ]
CT	Central Thickness [ $mm$ ]
D	Diameter [ $mm$ ]
Da	Damköhler Number
EFL	Effective Focal Length [ $mm$ ]
ET	Edge Thickness [ $mm$ ]
f	Frequency [ $Hz$ ]
G	Relative Density [ $kg/m^3$ ]
$f_{fuel}$	Fuel Heat Transfer Coefficient [ $W/m^2K$ ]
HHV	Higher Heating Value [ $MJ/kg$ ]
$k_{peak}$	Peak Wavenumber
Ka	Karlovitz Number
L	Integral Lengthscale [ $mm$ ]
$L_{IGN}$	Ignition Length [ $mm$ ]
LHV	Lower Heating Value [ $kg/m^3$ ]
k	Turbulence Dissipation Rate [ $m^3/s^2$ ]
$M_i$	Molecular Mass [ $g/mol$ ]
$\dot{m}_{fuel}$	Fuel Mass Flow Rate [ $g/s$ ]
$\dot{m}_{max}$	Maximum Mass Flow Rate [ $g/s$ ]
$\dot{m}_{min}$	Minimum Mass Flow Rate [ $g/s$ ]
$\dot{m}_{oxi}$	Oxidant Mass Flow Rate [ $g/s$ ]

Mach	Mach Number
Nu	Nusselt Number
$P_{therm}$	Thermal Power [ $kW$ ]
<b>Pr</b>	Prandtl
<b>Q</b>	Volumetric Flow Rate [ $m^3/s$ ]
$R_1$	Radius of Curvature [ $mm$ ]
<b>Re</b>	Reynolds Number
<b>t</b>	Time [ $s$ ]
<b>T</b>	Temperature [ $^{\circ}C$ ]
<b>T<sub>0</sub></b>	Reference Temperature [ $^{\circ}C$ ]
<b>T<sub>flc</sub></b>	Fuel Lance Temperature [ $^{\circ}C$ ]
<b>T<sub>oxi</sub></b>	Oxidant Temperature [ $^{\circ}C$ ]
<b>T<sub>i</sub></b>	Iteration Temperature [ $^{\circ}C$ ]
TI	Turbulence Intensity [%]
U	Fuel/Oxidant Velocity Ratio [ $m/s$ ]
$U_{bulk}$	Bulk Velocity [ $m/s$ ]
$U_{max}$	Maximum Velocity [ $m/s$ ]
$u_{FFT}$	Fast Fourier Transform Velocity [ $m/s$ ]
$u_{fuel}$	Fuel Velocity [ $m/s$ ]
$u_{MD}$	Mixing Duct Velocity [ $m/s$ ]
$U_{MW}$	Mass Weighted Velocity Velocity [ $m/s$ ]

$u_{oxi}$  Oxidant Velocity [ $m/s$ ]  
 $u_{RMS}$  Root Mean Squared Velocity [ $m/s$ ]  
 $u'$  Velocity Fluctuation [ $m/s$ ]  
 $u(t)$  Velocity at Time Interval  $t$  [ $m/s$ ]  
 $y_i$  Mass Fraction  
 $Z$  Specific Compression Ratio



# Chapter 1

## Introduction

This thesis is positioned to improve the environmental performance of heavy-duty Gas Turbines (GTs) and hence, support civilisation's realisation of a decarbonised economy. This chapter provides a brief introduction to climate science, offering context for the supporting policies required to achieve a decarbonised society. Additionally, this chapter introduces the potential role of hydrogen, specifically hydrogen-fuelled GTs, in power generation. The primary focus of this thesis is directed toward assessing the hydrogen capability of the GT26 Gas Turbine, a subject of particular interest to the author's industrial sponsors: RWE Generation UK, referred to as RWE herein. The relevance of the objectives of this thesis for RWE is explored within this chapter. The hypothesis and technical details regarding the GT26 will be introduced in the subsequent chapter.

### **1.1 Motivation: Climate Change & Security of Supply**

Climate change represents a pervasive concern within social consciousness and governmental strategies. It is an issue that is induced by human activities characterised by the excessive exploitation of natural resources, resulting in alteration to the global ecosystem and in turn increased concentration of greenhouse gases (GHG) in the

atmosphere. The GHG effect has caused alteration in our climate due to its warming effects of trapping radiation into our atmosphere [1].

This phenomenon is further exacerbated by widespread mono-culture farming practices, extensive utilisation of fertilisers, and the ongoing process of deforestation, leading to desertification in numerous regions worldwide. Consequently, the task of upholding a balanced and resilient biosphere capable of sustaining life grows progressively more arduous. Many believe that a precipice of irreversible and runaway changes to the climate is imminent [2]. It has been posited by many climate and geographical scientists that we are currently in a new geological epoch termed the Anthropocene, which is characterised by humanity's profound influence on the planet's climate [3].

It has been reported by NASA [4] that since the industrial revolution (circa 1880) global temperature of Earth has increased by approximately 1°C, as shown by Figure 1.1.1, with more than half of that increase occurring since 1975. Hence, there have been strong signals by The International Energy Agency (IEA) and non-Governmental Organisations (NGO) as to the direction industries must take in a bid to maintain global temperature's below agreed limits (resulting from Paris Agreement [5]). It is said that the achievement of Net Zero GHG emissions would enable the realisation of the Paris Agreements aims, which will be discussed in further detail in Section 1.3. The IEA have stated that for humanity to reach Net Zero emissions by 2050, that all fossil fuel exploration must immediately stop at the time of publishing their Global Energy Sector Roadmap (May, 2021) and no new coal plants to be built (as of 2022) [6] [7].

However, due to the Russian invasion of Ukraine in 2022, the global oil and gas industry took a tumultuous dive as a result of sanctions upon Russian natural resources. This in turn induced a cost of energy crisis and saw many countries increase their domestic coal use and fossil fuel exploration as the security of supply had been challenged as a result of geopolitical pressures [8].

With the ever increasing energy demand seen globally and as developing countries

become industrialised [9] the need for the developing clean energy systems that are cost effective, provide a secure supply, environmentally sustainable and reliable is becoming increasingly important. This may be considered as a socio-economic driver for countries with little natural fuel resource to consider a domestic production industry of an alternative fuel, such as hydrogen, that has the *potential* to manage the energy trilemma.

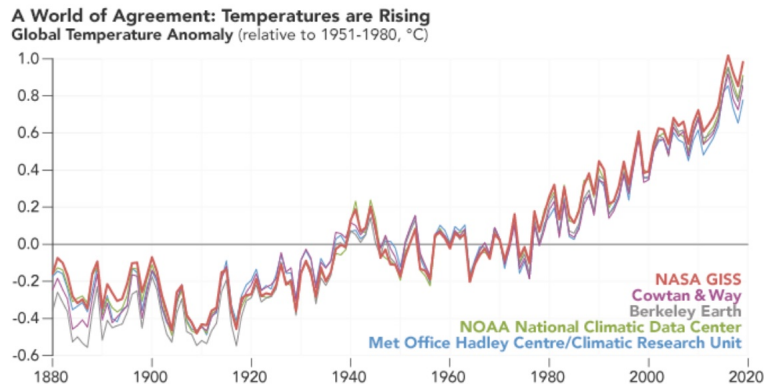


*Figure 1.1.1: Agreement on Global temperature rise, reproduced from [4]*

### 1.1.1 Energy Trilemma

The energy trilemma is a concept that connects the challenges that are faced by policymakers and energy industry stakeholders in managing energy systems. The challenges considered are (i) energy security, (ii) energy sustainability and (iii) energy equity or affordability. Thus describing the need for energy of a reliable and uninterrupted supply, with minimal negative impact on the environment from production and consumption of energy, at a cost that is accessible to all members of society to minimise social inequalities. The interplay between these three facets is depicted by Figure 1.1.2 below.

The energy trilemma signifies the need and challenge in balancing these three factors, as by pursuing one factor often comes at the expense of the others. For example, increasing energy security through the development of domestic fossil fuel resources may lead to higher GHG emissions and negatively impact environmental sustainability. Conversely, prioritising environmental sustainability by rapidly tran-

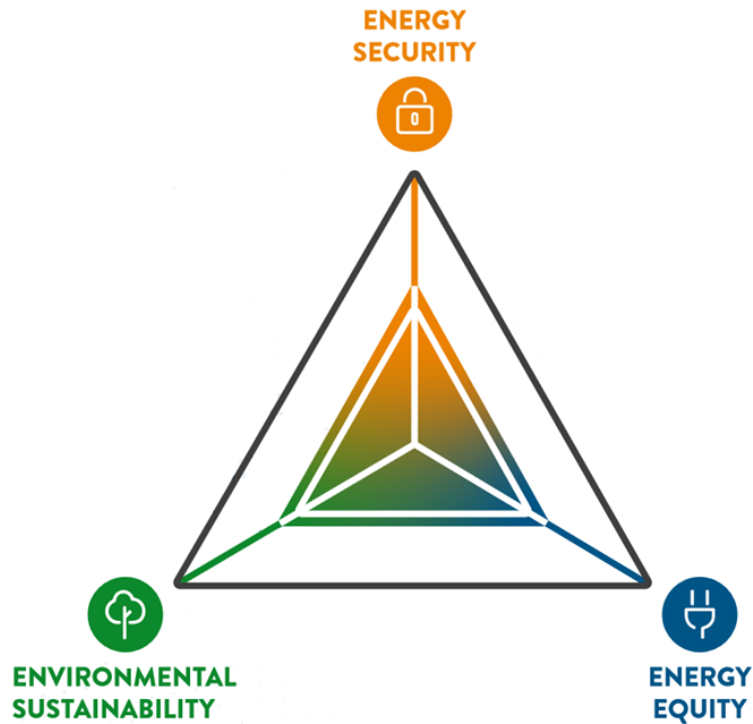


*Figure 1.1.2: Energy Trilemma Infographic, relating the three aspects of the energy trilemma, reproduced from [10]*

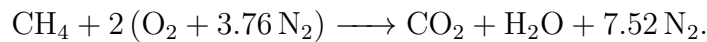
sitioning to Renewable Energy Sources (RES) may initially result in higher energy costs and potentially affect energy equity.

The crux of the challenge confronting the industry emerges from a confluence of factors. These include the pronounced geopolitical tensions associated with the Russo-Ukraine war, the far-reaching economic consequences stemming from the war itself, alongside the ongoing challenges related to the recovery from COVID-19. An additional threat to energy costs may arise due to the conflict between Hamas and Israel. However, at the time of writing, it is regarded as a possible threat rather than an actuality [11] [12].

Furthermore, elevated energy prices and their substantial impact on inflation exacerbate the industry's dilemma. In tandem with these challenges, the increasing influence of GHG emissions and the continued destruction of the natural environment compound the complexity of the situation. Recognising the multifaceted and demanding nature of these challenges, it becomes imperative to adopt a proactive approach that places a strong emphasis on innovation.

## 1.2 Combustion

Combustion is defined as the rapid-oxidation of a fuel that liberates the stored energy in the fuels chemical bonds and converts the stored energy into heat and light. Subsequently, new products are made resulting from the reaction, as detailed in the chemical equation for the complete combustion of methane below.



Combustion has been central for the development of human life throughout our history as a species. The control and daily use of fire is considered to date back as far as 300,000 years [13]. It was used for warmth, light, defence against predators and perhaps more importantly, used to cook. The advent of cooking also coincides with the growth of human brain size, leading to the development of human intelligence and thus our advancement as a species [13]. Now, the technology is vilified by the predominant use of unabated combustion with carbonaceous fuels, yet it is still essential to all human life, prosperous or not.

In recent years, combustion accounts for an overwhelming majority of 90% of today's global energy use [14], as depicted by Figure 1.2.1. The use of combustion is extensive and ingrained in the lives of developed societies from the use of heat for space heating of buildings; generation of heat for industrial processes such steel and cement production; use of fuels such as petrol, diesel and kerosene in the transport and aviation industries to provide thrust to drive their respective systems; the incineration of waste and of particular interest to this thesis, the generation of electricity. Combustion was accountable for circa 63% of global electricity production in 2019 [14], as shown in Figure 1.2.2.

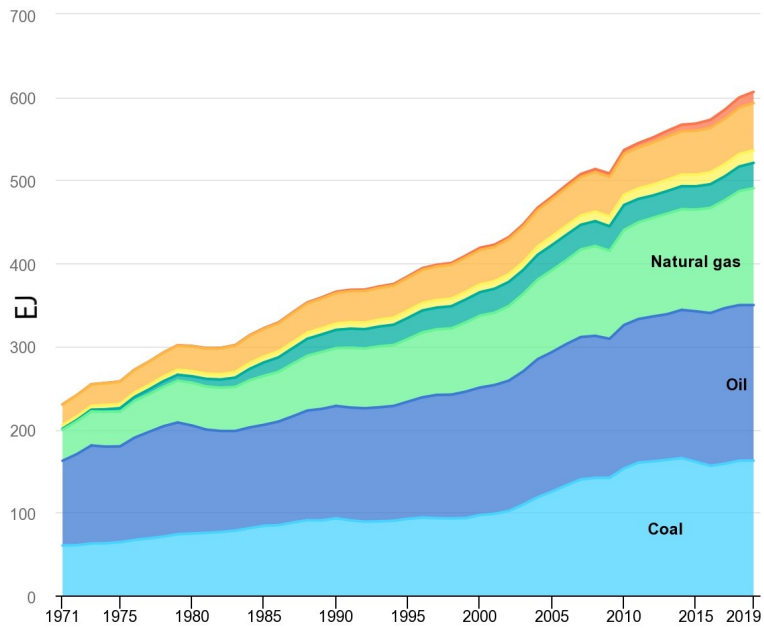


**Figure 1.2.1:** Global Energy supply by fuel, fuel types not labelled in ascending order from Natural Gas are; Nuclear, Hydro, Biofuels & Waste, and Other, reproduced from [14].

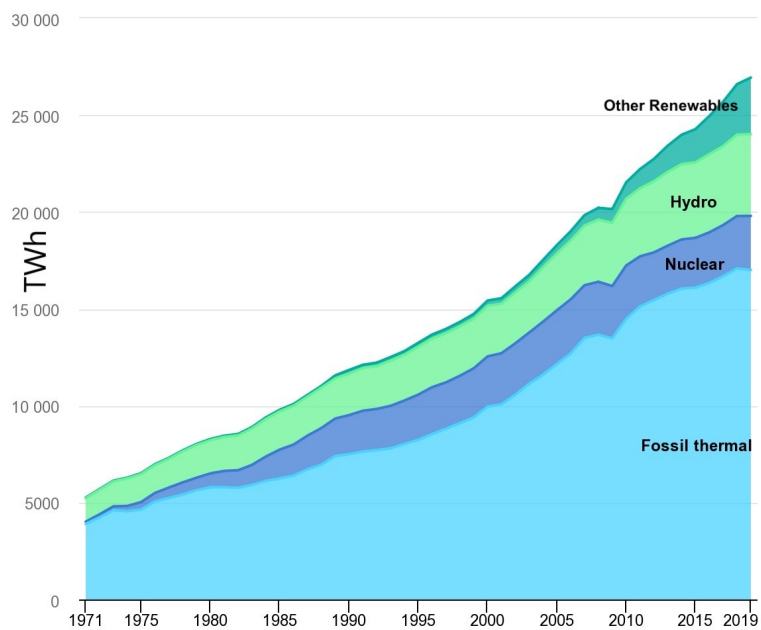


**Figure 1.2.2:** Global Electricity Production by source, reproduced from [14]

### 1.2.1 Societal Challenges of Combustion

Traditionally, carbonaceous fossil fuels have been the fuel of choice in combustion systems, yet there are a number of challenges to consider that have become more prominent in recent years. Since fossil fuels are a finite source, there are concerns

regarding cost and security of supply. Despite the accelerated use of fossil fuels, the timescales of exhaustion of said supply continues to grow with improvements in recovery technologies and resource economics [15]. However, this will ultimately result in fossil fuels becoming prohibitively expensive as is natural with a finite resource increasing in scarcity.

Due to the geographical concentration of fossil resources, there are additional concerns regarding security of supply since not every country has an indigenous supply of a fossil fuels, thus, requiring countries to import their resources. This can leave many susceptible to the volatility of geopolitics and resource prices on the energy market.

No example is clearer than Europe, or more specifically Germany's, over-reliance on Russian natural gas, where 40% and 55% of the gas consumed in Europe and Germany was supplied by Russia [16]. This resulted in Europe having a lessened ability to take strong geopolitical stances against Russia in the ongoing Russo-Ukraine war, until a divestment from Russian supply was made. This naturally caused market fluctuations, and severe gas price increases as European demand was hoped to be satisfied by the remaining market.

The energy landscape is complex, and geopolitical events can have profound effects on energy markets and global economies. Addressing these challenges often requires a multifaceted approach that includes diversifying energy sources, improving energy efficiency, and adopting sustainable energy practices to mitigate risks associated with supply disruptions and price fluctuations. Energy security is as consequential as ever when considering the Energy Trilemma [17].

#### **1.2.1.1 Demand & Population Growth**

The global population is projected to grow as presented in Figure 1.2.3. Couple that with the expected growth in the global economy, and the accelerated growth in non-OECD countries, particularly in Asia, an increase in global energy demand is expected. Whilst the technology is already present to address these energy needs,

it is likely to come at the the detriment of at least one facet of the energy trilemma.

Considering the power sector, the rise of Electric Vehicles (EV), heat pumps and many processes being decarbonised through electrification, the demand for electrical power has been projected to increase by nearly threefold by 2050, compared to 2010 levels, according to the IEA World Energy Outlook [18].

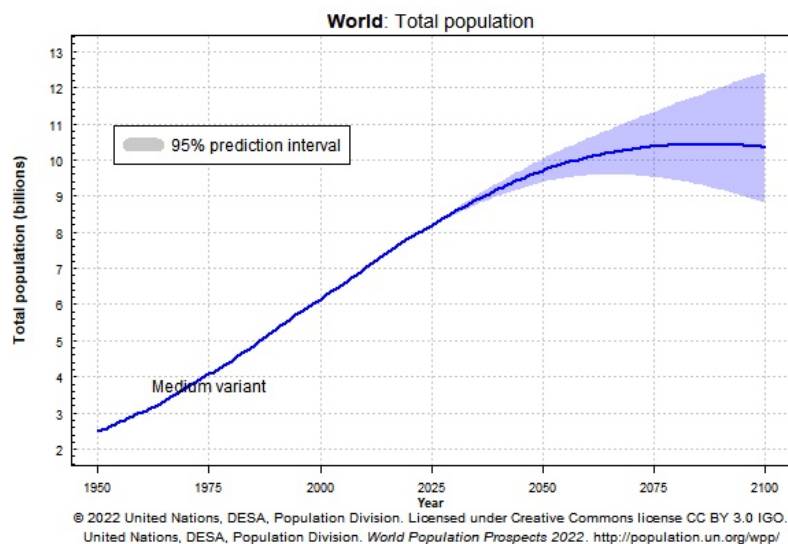


*Figure 1.2.3: World Population Projections reported by United Nations, reproduced from [19].*

## 1.2.2 Sustainable Challenges of Combustion

The challenge of the greatest existential concern and the defining issue of the 21st century, is the impact of emissions from the combustion of fossil fuels. The formation of compounds such as  $\text{CO}_2$ ,  $\text{N}_2\text{O}$ ,  $\text{NO}_x$ ,  $\text{SO}_x$  and  $\text{CO}$ , along with the release of particulate matter (PM) have been adversely impacting the climate. Hence, if the ultimate aim is for humanity to become a sustainable species, there is a need for a reduction in the use and, ultimately, the replacement of unabated combustion of fossil fuels for its energy.

It is important to make the distinction that combustion itself is not a negative phenomenon. Whether combustion is favourable or not is reliant on the fuel used in the combustion reaction. Alternative carbon-independent fuels such as hydrogen and ammonia are widely considered across various sectors as the “fuels of the future” to achieve their respective industries emission targets. At present, the pro-



duction of these fuels have an environmental penalty due to their unabated nature. However, developments are underway to establish greener solutions by utilising renewable power to produce them. Section ?? details the current methods of hydrogen production and the developing “green” hydrogen production method, which green ammonia production would use as a feedstock to the Haber-Bosch process. The use of alternative fuels will be considered in more depth in Section 1.6, yet it would be remiss not to introduce them ahead of the introduction of current policies.

Carbon Capture and Storage (CCS) technologies have gained recent traction due to their capacity for retrofitting to existing assets. CCS captures carbon either before or after combustion through various methods, depending on the technology, effectively mitigating atmospheric emissions. Past drawbacks, such as increased operational costs and energy penalties, are now accepted in the pursuit of Net Zero targets. Although this thesis does not delve into CCS, its significant role is projected in the next two decades, especially with the concurrent expansion of the green fuel production industry. For a more in-depth exploration of the role of CCS across industries and value chains, please refer to the review paper [20].

### **1.3 Institutional Policies, Treaties and Strategies**

Attaining Net Zero emissions by 2050 demands a holistic strategy, incorporating policy, legislation, and financial frameworks. Governments must establish ambitious emission reduction targets and foster a conducive regulatory environment to incentivise the shift towards low-carbon alternatives. Financial frameworks, utilising incentives such as carbon pricing and green bonds, can drive investments in green technologies and climate-resilient infrastructure. The combination of these elements creates a virtuous cycle, promoting sustainable practices and expediting the transition to cleaner energy sources for a Net Zero future by 2050.

This section will elucidate the manner in which global policies permeate through various geographical tiers, from global, to continental to national levels.

### 1.3.1 International Treaties

Internationally, the Paris Agreement, a pivotal climate accord succeeding the 1997 Kyoto Protocol, stands out as a major milestone. Introduced in December 2015 at the 21st UNFCCC conference (COP21), the agreement aims to drive global cooperation and incentivise a green and equitable energy transition. Notably, it commits to capping the rise in average global surface temperature at 2°C above pre-industrial levels, with efforts to limit it to 1.5°C—an acknowledgement of the severe consequences warned by scientific consensus [5].

Each participating country (197 currently) is obligated to declare and strive to achieve Nationally Determined Contributions (NDC), subject to revision every five years [5]. Developed nations are expected to lead with greater contributions and reach peak emissions earlier due to their economic advantage, contrasting with developing nations anticipated to reach their emissions peak later.

Concerning developing countries, it has been proposed to annually mobilise \$100 billion USD for sustainable development, steering away from cheaper carbonaceous sources, however, this has yet to materialise. The deadline for this funding has been extended to 2025.

### 1.3.2 European Policies

As aforementioned, such policies then cascade to the next geographical level. The European Union (EU), as a collective, submitted an enhanced NDC's of reducing their emissions by at least 55% by 2030 from 1990 levels in December 2020 (initial target 40%) [21]. The EU has revised and legally enforced the Renewable Energy Directive since its inception in 2009 to achieve its NDCs. The new target is to derive 45% of the EU's energy consumption from RES. Originally, the directive aimed for a share of 20% renewable energy, but the revised version reflects the EU's heightened commitment to transition towards cleaner and sustainable energy sources [22].

The EU have also taken a leadership role in the adoption of hydrogen, or more

specifically, green hydrogen as a major fuel source through their Hydrogen Strategy [23]. It suggested policy action in 5 areas, that being: investment support; supporting production and demand; the creation of hydrogen market; research and international cooperation. The EU aims to produce and import 10 million tonnes of hydrogen, respectively, by the year 2030 [23]. This is to be achieved through the EU’s ‘hydrogen accelerator’ concept to scale up the domestic deployment of green hydrogen, that is to be supported by the European Hydrogen Bank that aims to create investment security and business opportunities [24].

### 1.3.3 UK Acts and Policies

Progressing through geographic layers, the UK marked a historic milestone with the enactment of the Climate Change Act in 2008, pioneering the legal commitment to combat long-term climate change. Initially targeting an 80% reduction in GHG emissions below 1990 levels by 2050, this goal was later revised in 2019 to achieve Net Zero emissions by 2050. The legislation introduced carbon budgets, setting binding emissions limits for five-year periods, overseen by the independent Climate Change Committee.

The Energy Act of 2013, in addition to the Climate Change Act 2008, significantly influenced UK energy policies. It introduced Contracts for Difference (CfDs), a successful financial framework incentivising low-carbon energy technology adoption. CfDs offer a fixed “strike price” [£/MWh] to low-carbon power generators, shielding them from energy market price volatility. This framework, depicted in Figure 1.3.1, is hailed for its success in promoting Renewable Energy Source (RES) adoption and associated cost reductions in the UK.

Several strategies proposed by the UK government, including the Clean Growth Strategy (2017), Road to Net Zero (2018), and “The Ten Point Plan for a Green Industrial Revolution,” outline decarbonisation efforts while sustaining economic growth [26].

Positive developments include increased Electric Vehicle (EV) adoption [27];

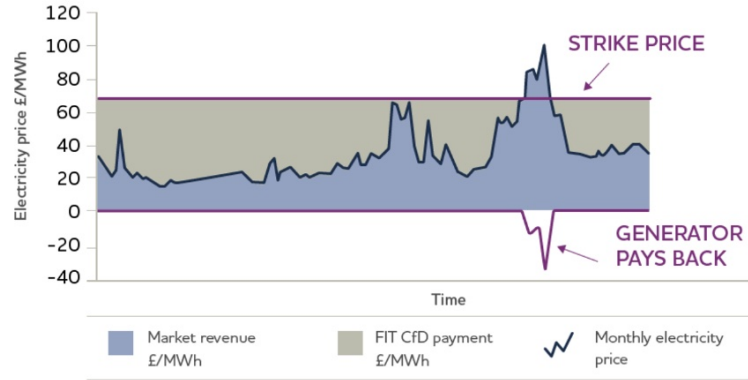


**Figure 1.3.1:** Contract for Difference mechanism depicted, reproduced from [25]

progress in Small Modular Reactor nuclear technology and the development of Hinckley Point C [28]; and the development of the world’s largest offshore wind farm off the East coast of England, operational by 2026 [29].

In 2021, the UK Government also set the ambition for all power generators to decarbonise their assets by 2035, as per their “Decarbonisation of the Power Sector” report [30]. Whilst at present approximately 60% of the UK’s power comes from low-carbon sources such as RES and nuclear, the remaining is accounted for by gas fired power stations [30]. This report states that gas fired assets must be converted to include CCS or operate using hydrogen as a fuel source to achieve their aim.

In light of this the UK Government introduced the Dispatchable Power Agreement (DPA) (2022) [31], which is a private law contract between the UK Government and carbon emitting power generators that offers a business model for compensating the power generators for the associated costs of capturing and storing the emitted carbon through CCS technologies [31]. A hydrogen for power business model is currently under development at the time of writing to support generators in their transition to hydrogen fired solutions.

Despite early leadership, the UK’s transition to Net Zero has regressed with over 100 new licenses for oil and gas exploration in the North Sea [8]. Continued use of terms like ‘low-carbon hydrogen’ (targeting 10GW production capacity by 2030 [32]) suggests a persistence of fossil fuels, especially with the adoption of blue hydrogen production [32]. While blue hydrogen outperforms grey hydrogen in terms of emis-

sions, prioritising green hydrogen production via renewable power and electrolysis appears deficient.

Ensuring energy security and decarbonising challenging sectors, necessitates a balanced approach. Hence, an equal approach towards production of green substitute fuels is proposed. If green fuels realise the financial success akin to Wind and Solar via responsible CfD allocation or similar, suggests potential financial viability surpassing that of CCS. As fossil fuel reserves deplete, CCS costs are expected to rise, driven by competition for CO<sub>2</sub> storage space and resource economics. The substantial production of green fuels, like hydrogen, is essential for displacing fossil fuels. Therefore, a balanced approach and a committed effort to decisively achieve emission targets are imperative.

## 1.4 Power Sector: Global and UK Trends

The power sector has arguably been the most progressive heavy industry in decarbonising, and has been in an energy transition since the turn of the century. Prior to 1990, coal was considered king in the energy industry, accounting for the majority of energy consumed at the time and the main fuel source in the production of power. Coal was near exclusively used in the inception of the industrial revolution due to the technological capabilities of extracting the resource. In more recent years, following the backdrop of both nuclear and oil politics of the 1960's to the 1980's, coal secured itself as a firm favourite in the power sector as the main means of baseloading. However, a drive to cleaner fuels has been required since coal produces the greatest proportion of CO<sub>2</sub> emissions than any other fuel type [33].

In the late '80s and early '90s, industrial countries, including the UK, US, Netherlands, and Canada, underwent a “dash to gas” as highly efficient Combined Cycle Gas Turbine (CCGT) technology emerged [34]. CCGTs integrate a Gas Turbine engine with a steam generator, enhancing efficiency by recovering exhausted heat. This technological leap, achieved efficiency improvements from circa. 30%-40% to exceeding 60% today. Due to the drastic increase in efficiency, operators were quick

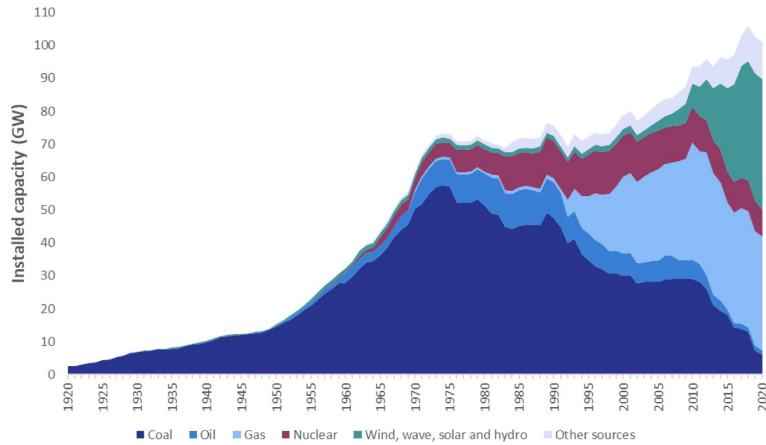


**Figure 1.4.1:** *Historical Trend of Installed Capacity by source in the UK, reproduced from [35]. Other sources are defined as; coke oven gas, waste from chemical processes, pumped storage generation, bioenergy and energy from municipal waste.*

to adopt this technology due to its commercial attractiveness. Figure 1.4.1 illustrates the evolving power generation trend in the UK from 1920 to 2020, which depicts the wide adoption of gas power. Also shown in Figure 1.4.1 above, there has been an increasing proportion of energy produced by RES. RES are considered any form of energy that is inexhaustible, non-finite resource. RES include the harnessing of the wind, tide, gravitational potential of water (hydro) and solar energy most commonly. Other technologies can cautiously be considered renewable such as biomass, as many disagree with this classification due to the carbon emissions and sustainability issues that associated with biomass combustion [36] [37].

In the context of this introduction, when discussing RES herein, the focus is specifically on wind and solar technologies. This emphasis stems from their predominant share in generating capacity and their significant potential for scaling up. RES' share has been steadily increasing due to their successful reduction in cost and as a result of various policies described in Section 1.3.3. Their adoption continues to increase as a result of them being commercially competitive with traditional thermal power stations. The UK Government published predictions of the 'Levelised Cost of Energy' (LCOE) of Solar and Onshore Wind, and expect by 2025 that their cost will be half the cost of operating a gas powered plant.

The growth rate of power generated by RES in the UK between the years 2011-

2021 has been on average 14.7% increase per annum [38], which has naturally benefited the sectors carbon emissions.

However, the challenge lies in the fluctuating nature of the highest installed capacity RES. Since these technologies rely on the temporal weather conditions, they in turn produce a fluctuating power generation source. Hence, RES have the disadvantage of potentially inducing grid instabilities such as; voltage instabilities, frequency variations, grid imbalances and grid overload, potentially resulting in blackouts. Fortunately there are mitigation methods that are continuously practiced by grid operators such as; demand side management, interconnection, forecasting, energy storage, and the utilisation of flexible and grid balancing generating assets.

The latter proves to be one of the most effective means of stabilising the energy grid for grid operators, as they typically embody the following characteristics; a fast ramp rate; ability to perform as a peaking plant; offer blackstart capability and to provide frequency response to grid to maintain a stable frequency. Technology types used are: Gas Turbines (both open and closed cycle), Internal Combustion Engines and Diesel generators.

In turn, the more we turn to renewable energy for our power needs the more we rely on flexible generating assets, such as GTs.

## 1.5 Gas Turbine Development

Gas Turbine (GT) technologies have evolved since their late 19th-century inception, making a commercial debut in 1939 and continuing to progress. They play a vital role in the power industry, providing flexible generation that aids in stabilising and responding to grid fluctuations induced by RES [39, 40, 41]. With the increasing reliance on RES for energy generation and the imperative to achieve Net Zero targets [42], omitting emissions from GT power generation has become essential.

The evolution of Gas Turbines (GTs) has progressed from early design and combustion knowledge to the current emphasis on compliance with stringent regulations. As illustrated by Figure 1.5.1, the development of high temperature materials, cool-

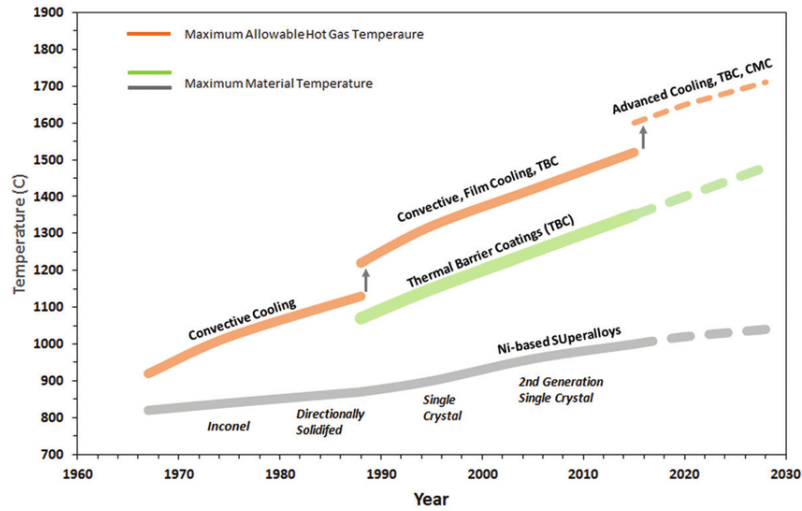


**Figure 1.5.1:** Historical trend of hot gas temperature's achievable aligned with material developments, reproduced from [45].

ing strategies and deploying them in combination have facilitated a significant increase in allowable gas temperatures. Initially limited to approximately  $820^{\circ}\text{C}$  (without convective cooling) and  $900^{\circ}\text{C}$  (including convective cooling) near the commercial deployment of GT technologies. Today, GTs operate with hot gas temperatures in excess of  $1600^{\circ}\text{C}$ , as showcased by Mitsubishi Heavy Industries (MHI) [43] and GE [44], for example. This progress was made possible by the development and utilisation of advanced cooled, thermal barrier coated and ceramic matrix composite hot gas path components. In addition to the developments in temperatures achievable in GTs, their pressure ratios have also increased. At their inception, pressure ratios of approximately 4:1 in the combustor [46]. Present day GTs have developed vastly with H-class turbines now exceeding pressure ratios of 20:1 []. The development in pressure ratios utilised in such GTs has enabled GTs to achieve greater efficiencies, higher power outputs and therefore an overall improvement in their performance.

These advancements align with tightening  $\text{CO}_2$  restrictions, positioning natural gas as a bridging fuel to facilitate a transition from coal and oil, resulting in lower carbon emissions and improved air quality by reducing  $\text{NO}_x$  [34]. However, escalating  $\text{CO}_2$  restrictions, exemplified by international treaties like the Paris Climate Change Agreement [5], intensify the pressure on Original Equipment Manufacturers (OEMs) and researchers to advance GT technologies to adhere to increasing



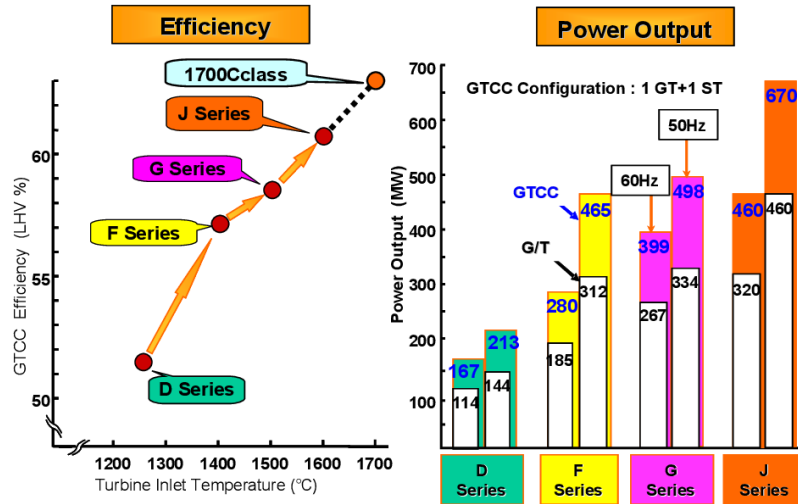


**Figure 1.5.2:** Development of firing temperatures, efficiency and power output of CCGTs, reproduced from [48].

emission constraints.

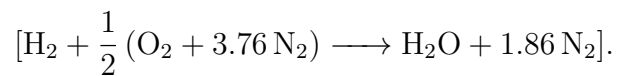
This has subsequently translated to developments to attain higher firing temperatures to realise increases in the efficiency and power output of CCGTs, as illustrated by 1.5.2, where OEMs are targeting higher firing temperatures in excess of 1700°C and ever increasing pressure ratios in the combustor [47] in a bid to improve GT performance further.

## 1.6 Alternative Fuels

Hence, contemporary research and developments in the field of combustion has experienced a paradigm shift in where the use of alternative fuels is being considered earnestly and the use of such fuels is becoming prevalent within future planning policy-making, research and industrial development [49]. Alternative fuels in this instance are considered to be a fuel with a reduced carbon footprint when compared to conventional fossil fuels such as natural gas. Most notable examples would be hydrogen, ammonia and biofuels, as will be described in the subsequent sections. Whilst not an alternative fuel for combustion, nuclear is considered for its potential role in future energy mixes.

### 1.6.1 Hydrogen & Ammonia Fuel

?? The attractiveness of hydrogen is due to its carbon independence, resulting in direct emission free of CO<sub>2</sub>, CO and unburnt hydrocarbons; nil particulate matter formation and no SO<sub>x</sub>, when compared to carbonaceous fuels. When combusted in air its main emissions are NO<sub>x</sub> and H<sub>2</sub>O vapour - as shown by the complete combustion equation of hydrogen in air displayed below.



Specifically for use within gas turbines (GTs), there are proposals to introduce hydrogen either through fuel blending with natural gas or by using pure hydrogen to minimise and eventually mitigate carbon emissions from these critical energy assets. Figure 1.6.1 demonstrates that as the hydrogen content in the fuel increases, the reduction in carbon dioxide (CO<sub>2</sub>) emissions becomes more significant. It is important to note that this relationship is not linear due to differences in the volumetric densities of the fuels constituents. For example, achieving a roughly 50% reduction in CO<sub>2</sub> emissions would require a natural gas/hydrogen fuel blend with approximately 20% natural gas and 80% hydrogen by volume.

Waste gases from industries such as refineries and chemical production, as well as syngas from solid fuel gasification, often contain hydrogen. Using these gases in GTs offer an additional and efficient use of the fuel to produce either electrical energy or work [50], whilst maintaining low carbon emissions.

The utilisation of hydrogen offers a dual advantage, serving as both an energy storage medium and a clean fuel source. As the number of large-scale Renewable Energy Systems (RES) projects continues to rise, a natural consequence is the occasional disparity between power demand and the availability of renewable energy for generation. This presents a prime opportunity to harness surplus renewable energy for storage. One effective approach is to employ this excess renewable energy for the production of green hydrogen [51]. Green hydrogen production involves electrolysis

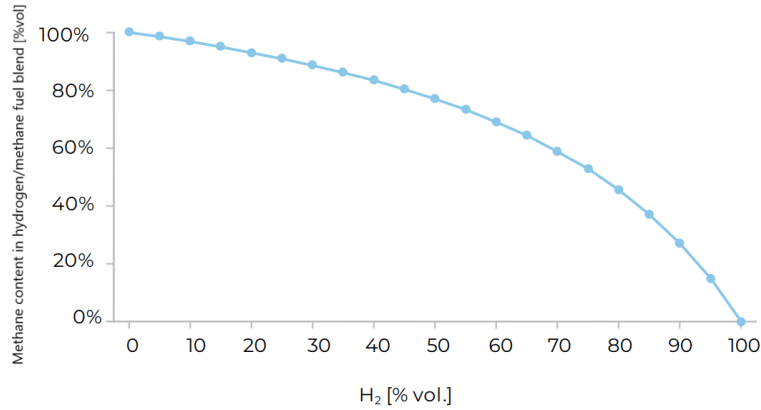


**Figure 1.6.1:** Carbon Intensity of emission from  $CH_4/H_2$  combustion emissions, reproduced from [39]

powered by renewable electricity sources like solar and wind [52]. The advancement of such production technologies marks a shift away from the predominant reliance on fossil fuels, which currently constitute 96% of global hydrogen production [53].

Hydrogen production from fossil fuels has relied on processes such as pyrolysis of solid fuels like coal or biomass, or the reformation of natural gas. The pyrolysis method involves heating the solid fuel to temperatures ranging from 500°C to 1000°C in an oxygen-free environment, causing the fuel to decompose into syngas, with hydrogen being one of its constituents. To obtain a pure stream of hydrogen, the syngas undergoes additional processing, including the Water Gas Shift reaction, to separate hydrogen from the syngas. The resultant hydrogen product is commonly referred to as brown hydrogen [52].

As stipulated above, hydrogen can be derived from natural gas through Steam Methane Reforming (SMR), a process where natural gas reacts with steam at temperatures around 700-1000°C to produce a syngas containing hydrogen and carbon monoxide. The syngas undergoes further purification to separate the hydrogen product, constituting what is termed grey hydrogen production, as the associated carbon emissions are released into the atmosphere [52]. In efforts to enhance the environmental sustainability of grey hydrogen production, recent advancements have introduced carbon capture processes to capture a significant portion (85-95%) of the emitted carbon, resulting in what is known as blue hydrogen [52].

While utilising hydrogen-powered GTs may lead to improved stack emissions, it's essential to cautiously evaluate the environmental impact of the hydrogen's source.

Whilst this subsection may have focused on hydrogen, it is necessary to consider other alternative carbon-independent fuels such as ammonia, which is considered to be a solution for future fuel use by the IEA [54]. Both hydrogen and ammonia fuels offer polarity in their combustion characteristics, with natural gas fuels being the median of their characteristics. Ammonia fuel is characterised by slow combustion dynamics due to its high ignition temperature and slow flame speed, yet has advantages in terms of, higher volumetric energy density and; ease of storage and transport [55]. However, ammonia does carry safety concerns regarding its handling due to its toxicity. Ammonia is expected to have its largest penetration in the maritime shipping industry, and used elsewhere in GTs that have a geographically convenient source of ammonia.

Research in this field is highly active and innovative, with a focus given to the minimisation of NO<sub>x</sub> emissions. Extensive work has been undertaken at Cardiff University in the field of Ammonia [56] [57], including the utilisation of plasma assisted combustion. NO<sub>x</sub> emissions are considered the main challenge of ammonia utilisation.

Hydrogen, on the other hand, is intensely reactive with low ignition energies, wide flammability limits and poses a significant explosive risk. Hydrogen's storage and transport also proves to be challenging due to its diffusivity. That being said, hydrogen appears to be enjoying its current position as the "fuel of the future" with many, if not all carbon emitting industries and governments considering its use for its potential to decarbonise hard-to-decarbonise sectors. Hydrogen is therefore considered favourable over ammonia in society at large. Yet, ammonia's utility should not be at all discounted.

## 1.6.2 Additional Technologies - Power Decarbonisation

Whilst outside of the scope of this thesis, biofuels are certainly a valuable fuel type to consider. Biofuels is a catch-all term for a wide variety of fuels and is defined by Gupta, K.K. et al. as; “*alternative fuels, made from renewable sources and having an environmental benefit*” [58]. Whilst the use of renewable in the definition may be considered contentious, it is undeniable that the environmental impact is certainly lesser than conventional fossil fuels.

Producing fuels like biomethane offers an opportunity for environmental improvement while using a fuel nearly identical to its fossil counterpart. Positioned as a bridging fuel, biomethane serves as an excellent option during the ongoing development of the decarbonised fuel industry. Unlike hydrogen, which demands extensive infrastructure, safety measures, workforce upskilling, and substantial production scale, biomethane can achieve a reduced environmental impact while operating in existing assets and infrastructure without immediate retrofits.

While diverging from the thesis’s primary focus, it is considered necessary to include nuclear power in the discussion on the decarbonisation of the power sector. Nuclear power’s steady-state operation makes it a baseload generation method, offering significant volumes of carbon-free energy, a distinctive feature among low-carbon methods.

Despite its potential, nuclear power receives minimal attention in public and political discourse for meeting energy demands in a low-carbon manner. Historical anti-nuclear sentiments, intertwined with nuclear weapon rhetoric, hindered global development. Environmental victories over nuclear power have, paradoxically, led to increased environmental costs, as proposed nuclear stations were replaced with coal plants [59].

Concerns regarding radioactive waste, safe operation, and fuel scarcity linked to Uranium, the current nuclear fuel, can be addressed by considering Thorium [60] [61]. Thorium not only mitigates weapon proliferation concerns [62] but also offers a fuel source of greater abundance [63], reduced risk of meltdowns, improved safety

features [64] and reduced waste management [65].

## 1.7 Research Sponsor - RWE Generation UK

This research project is sponsored by RWE Generation UK, a part of the multinational RWE AG group based in Germany. RWE AG encompasses various aspects, including thermal power generation, renewable generation, and a supply and trading arm. Its global reach extends across Europe, the United States, and the Asia-Pacific region.

With a history spanning over 125 years as a power generator, RWE, formerly associated with numerous coal plants, has transformed in response to the evolving global energy landscape. Now a leader in renewable energy, RWE focuses on wind farms, solar power, and battery storage facilities. From 2012 to 2021, RWE successfully reduced their UK carbon intensity by 43% [66]. Demonstrating their commitment, RWE pledged to achieve Carbon Neutrality of the entire companies operation by 2040 in 2019 [67], accompanied by the intermediary goals stated below [68]. This transformation has been adapted for the UK market to align with the UK government's aim to decarbonise the power sector by 2035 [30] [69].

- Scope 1 and 2 emissions to be reduced by 50% by 2030 (relative to 2019 levels of 591 CO<sub>2</sub>e/kWh).
- Scope 3 emissions reduced by 30% of the same 2019 levels.

RWE have also expressed great interest in the potential for hydrogen as a technology that will enable the decarbonisation of power generation with involvement in numerous projects across Europe, that cover the entire hydrogen supply chain [70]. Pembroke Net Zero Centre (PNZC) is a project focused on the integration of innovative decarbonisation technologies including the hydrogen production via electrolysis (initial pathfinding project of 300MW whilst investigating GW potential), CCS and floating offshore wind, as depicted by Figure 1.7.1. The PNZC is optimally positioned in Milford Haven which is a significant player in the UK's energy sector

due to its extensive industrial activities that include one of the UK’s largest LNG terminals [66].

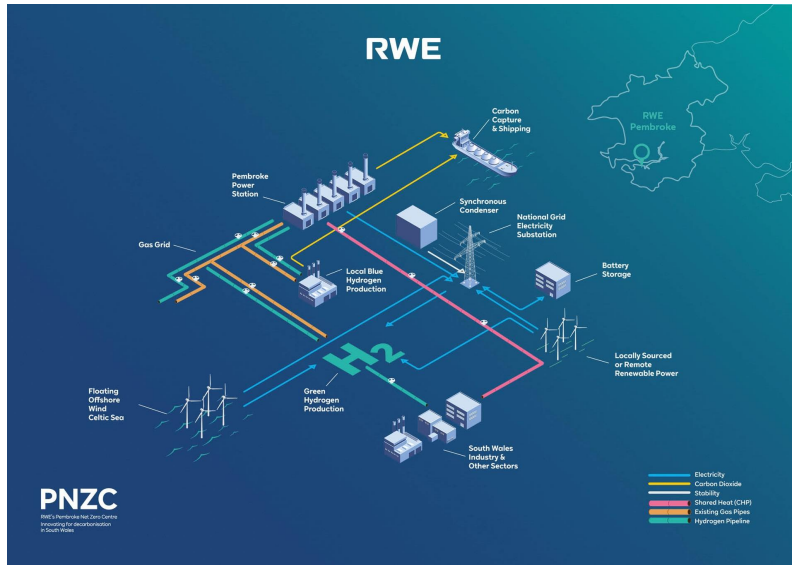


*Figure 1.7.1: Infographic of PNZC reproduced from [66]*

On the European continent, RWE collaborates in the GET H<sub>2</sub> Nukleus consortium with partners like Nowega, BP, and BASF, aiming to construct 135 kilometres of hydrogen infrastructure in Germany [71]. A 100MW electrolyser will produce green hydrogen using renewable electricity, setting a pathfinding industry standard and demonstrating the scalability of electrolysis technologies [71]. Additionally, in Switzerland, RWE leverages their hydro power asset in Alpbbruck for green hydrogen production via electrolysis. The advanced hydro power station generates 660 GWh of green electricity annually, a portion of which will be dedicated to hydrogen production to meet varying electricity demands [72].

The examples provided are by no means exhaustive, since RWE have 30 green hydrogen projects in progress. The examples aim to provide a flavour of the work that RWE are undertaking across the hydrogen value chain.

It is acknowledged that Power Generation companies are well-positioned to expand their presence in future global energy markets. Historically, oil and gas companies dominated the energy sector, amassing significant assets valued at USD 2.236 Trillion among the top 10 companies. Their inclination to divest from these assets

is not purely altruistic, given the substantial investments made over the past 150 years. Recognising that green fuel production relies on electricity, power generation companies, exemplified by RWE, are strategically poised to play a pivotal role in shaping and dominating the evolving energy landscape. RWE stands as a leading example of a large, energy-intensive corporation adapting to environmental pressures and becoming an agent of positive change in a high-emission industry and beyond.

### **1.7.1 Project Aims for RWE**

Whilst RWE have been driving innovation in the production side of the hydrogen value chain, considerations for the impact of hydrogen in their assets has also been on-going. Hence, the sponsoring of this doctoral project that is focused on the investigation of the effect of hydrogen in the GT26 GT. The stark differences in combustion behaviours that is exhibited between hydrogen and Natural Gas, that will be discussed in Section 2.1, requires extensive research to ensure that such assets do not become stranded with the changing energy landscape.

RWE owns and operates 9 GT26 gas turbines in the UK, located at Staythorpe and Pembroke Power Stations, contributing 4.03 GW of electrical capacity. Recognising the future role of hydrogen in the power sector, RWE seeks understanding of the impact of hydrogen on their generating assets. The challenge lies in adapting assets designed for carbonaceous fuels to accommodate higher volumes of hydrogen, thus preventing the risk of stranded assets. It is the remit of this project to investigate the hydrogen capability of the GT26 at present, through literature search, and identify possible routes for enabling and derisking high hydrogen capability in the GT26.

### **1.7.2 Project Aims**

The primary aim of this doctoral project is to identify limiting factors related to the GT26's hydrogen capability and explore potential enhancements. The sequential



burner, unique to the GT26, is identified as a constraint on hydrogen operation. An experimental test campaign is devised to investigate whether modifying the flow field can favourably alter the combustion reactions propagation, addressing the increased reactivity of hydrogen. A new combustion facility at Cardiff University's Gas Turbine Research Centre (GTRC) is developed for this purpose.

Within this test campaign, various methane and hydrogen fuel blends are examined to identify transitional regions where hydrogen's presence induces changes in combustion chemistry, affecting the reaction rate. Experimental work is complemented by a Computational Fluid Dynamics (CFD) model to provide additional insights into combustion mechanisms during testing.

# Chapter 2

## Literature Review

This literature review serves as a description of the challenges associated with the conversion of assets originally designed to operate on carbonaceous fuels to run on hydrogen enriched fuels. It begins by comparing the fundamental properties of these fuels, followed by an introduction to the current challenges and state of the art technologies to address hydrogen usage in GTs. The GT26 and its operating principles are subsequently introduced. Moreover, this review delves into dedicated research conducted specifically on elements of the GT26 gas turbine.

An investigative approach is employed to explore the challenges confronting the GT26 concerning its hydrogen capability, contributing to the central hypothesis of this thesis. The literature review culminates with an overview of pertinent literature related to the phenomena under investigation in the experimental aspect of this doctoral research project.

### 2.1 Fundamentals of Hydrogen

The introduction of hydrogen as a fuel will induce complexities in GT operation as the characteristics of carbonaceous fuels, such as natural gas, differ vastly from hydrogen, as will be described within this section. Note, that natural gas shall be approximated to its main constituent methane ( $\text{CH}_4$ ) for the purpose of comparing the fuels. The true composition of natural gas will include varying contents of

other hydrocarbons (depending on their geographical point of extraction) such as ethane and propane that will effect the combustion characteristics [73] [74]. For example, adiabatic flame temperatures (under stoichiometric conditions with air, a temperature of 20°C and atmospheric pressure) of methane, ethane and propane increase from 1950°C, to 1955°C to 1967°C, respectively [75]. Laminar flame speeds (LFS) for the three fuels also increase with methane having a LFS of  $\tilde{3}4.5\text{cm/s}$ , to ethane with a LFS of  $\tilde{3}6.4\text{cm/s}$  to propane exhibiting a LFS of  $37.3\text{cm/s}$ , at an initial temperature of 298K and at atmospheric pressure [76]. Table 2.1 lists a number of fuel properties for hydrogen and methane.

**Table 2.1:** *Fuel Properties of Hydrogen and Methane*

<b>Fuel</b>	<b>Hydrogen</b>	<b>Methane</b>	<b>Reference</b>
LHV (MJ/Nm <sup>3</sup> )	10.8	35.8	[77], [77]
LHV (MJ/kg)	120	50	[77], [77]
Flammability Limits in air (% vol)	4-74%	5.3-15%	[78], [78]
Ignition Energy* (mJ)	0.02	0.29	[79], [80]
Adiabatic Flame Temperature* in air (°C)	2045	1875	[81], [81]
Laminar Flame Speed* (cm/s)	207.5	34.5	[76] [76]

*\*Properties are evaluated at initial conditions of 20°C, 1 atmosphere and stoichiometric. Initial conditions and method of evaluation can impact the measured value.*

### 2.1.1 Calorific Content

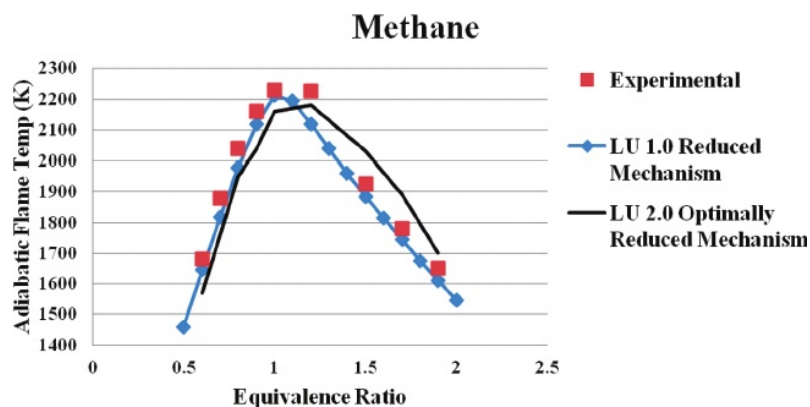
As denoted by Table 2.1, there is a distinct difference in the calorific content of hydrogen and methane, on a mass basis, hydrogen is more energy dense. Conversely, on a volumetric basis, methane is more energy dense. When considering fuel flowrates for GT operation, fuel flowrates are considered on a volumetric basis which in turn implies that if a given GT were to maintain its fuel flowrate then a reduction in its specific work will occur [82], thus potentially de-rating the machine. This is expected to be resolved by increasing the flow capability of ancillary equipment related

to fuel delivery.

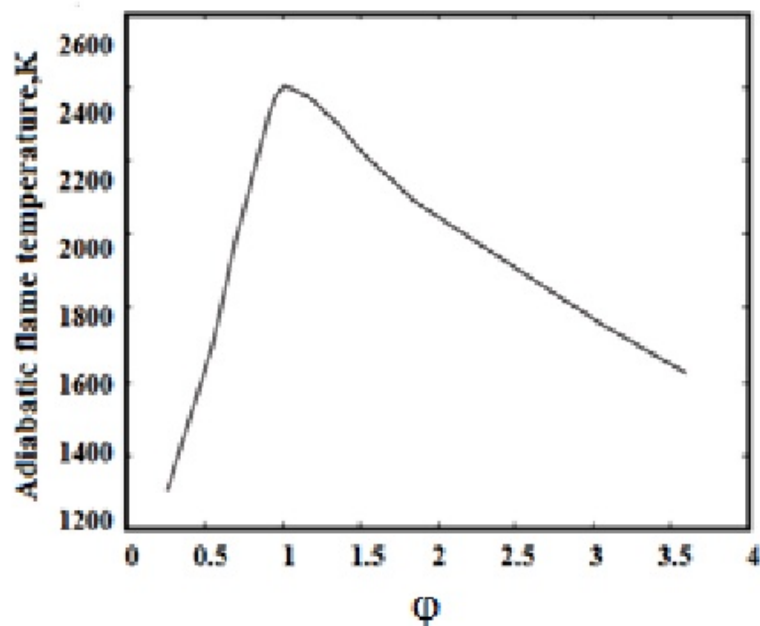
## 2.1.2 Adiabatic Flame Temperature

In Table 2.1, the flame temperature of hydrogen is shown to be greater than that of methane. Idealised flame temperatures are defined as the ‘‘Adiabatic Flame Temperature’’ (AFT), which denotes the maximum isothermal temperature achieved by the given fuel-oxidant blend at the given equivalence ratio.

Below in Figure’s 2.1.1a and 2.1.1b, the trend for the AFT versus Equivalence Ratio (ER) for methane and hydrogen is respectively displayed.



(a) Graphical representation of  $CH_4$  AFT versus ER for both experimental and numerical consideration, reproduced from [83]



(b) Graphical representation of  $H_2$  AFT versus ER, reproduced from [84].

Figure 2.1.1: AFT relationship to ER for  $CH_4$  and  $H_2$ , respectively.

The higher AFT of hydrogen in turn induces the preferential pathway of the Zeldovich NO<sub>x</sub> production mechanism [85]. Lean combustion regimes are typically deployed in GT engines to reduce the overall flame temperature and thwart the production of NO<sub>x</sub> production via the Zeldovich mechanism [86] [85].

The higher hydrogen AFT will also result in increased thermal loading on GT combustor components which already require highly sophisticated cooling air systems to minimise thermal loading on hot path components [87]. Secondly, as the moisture content in the flue gas of a hydrogen containing fuel is greater than that of a carbonaceous fuel, there is an increase in heat transfer to hot path components and the occurrence of hot corrosion [39].

### 2.1.3 Autoignition

Autoignition is the spontaneous ignition of fuel, due to elevated temperature conditions, without a direct ignition source. While autoignition temperatures are commonly cited, it is crucial to acknowledge the absence of a singular autoignition temperature due to various conditional variables that can influence it, such as Temperature, Pressure and Equivalence Ratio [88] [89].

Therefore, attempts were made to establish Ignition Delay Times (IDT) that could be correlated with specific initial conditions, including temperature, pressure, and mass fractions of reactants [88]. The IDT is conventionally described as the duration for a homogeneous mixture of fuel and oxidant to undergo initial slow low-temperature chemistry, succeeded by the commencement of high-temperature chemistry characterised by an exponential increase in the rate of reactant consumption.

The risk of an autoignition event when using hydrogen is more pronounced due to flammability range being wider and its ignition energy is less than that of methane. This is a challenge that will require appropriate management in combustors that utilise premixed combustion regimes and, fuel and air preheat systems for improved efficiency [39]. Ignition research activities typically take two forms, the determi-

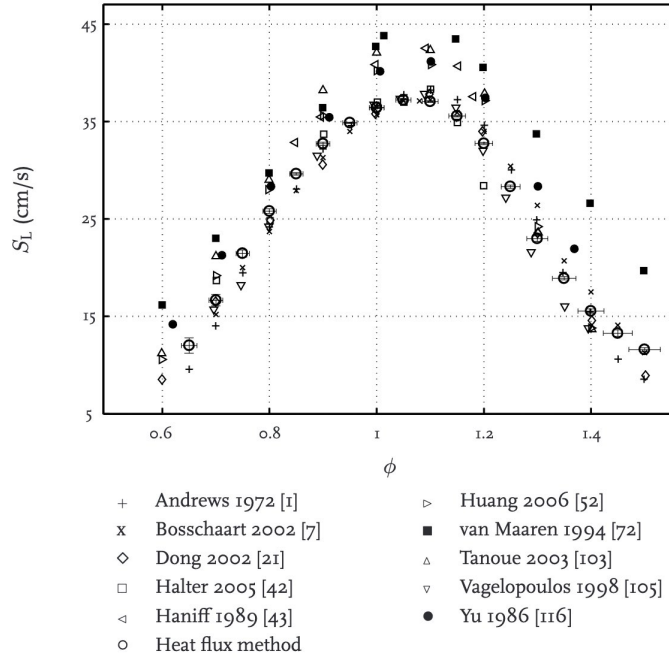
nation of such properties from homogeneous mixtures, as described, and that in inhomogeneous mixtures. Historically, the perception was that inhomogeneous ignition was considered to be analogous to that of homogeneous mixtures due to the high importance given to the chemistry and the under appreciation of the effect of turbulence and mixing [88] [90] [91].

Whilst it is pertinent to develop an understanding of the characteristics of homogeneous fuel-oxidant mixtures, not only for the purpose of developing understanding regarding chemical kinetics but to provide partial insight into the more complex inhomogeneous ignition of fuel-oxidant mixtures. However, as stated by Markides [88]: *“It is generally dangerous to extrapolate results and conclusions outside the bounds of the physical process for which they were reached and it does not always follow that knowledge from the simplified cases can be applied blindly to more complex ones.”* Hence, it is important to undertake study to address the current gap in the literature. Research in this field will be introduced in Section 2.7.

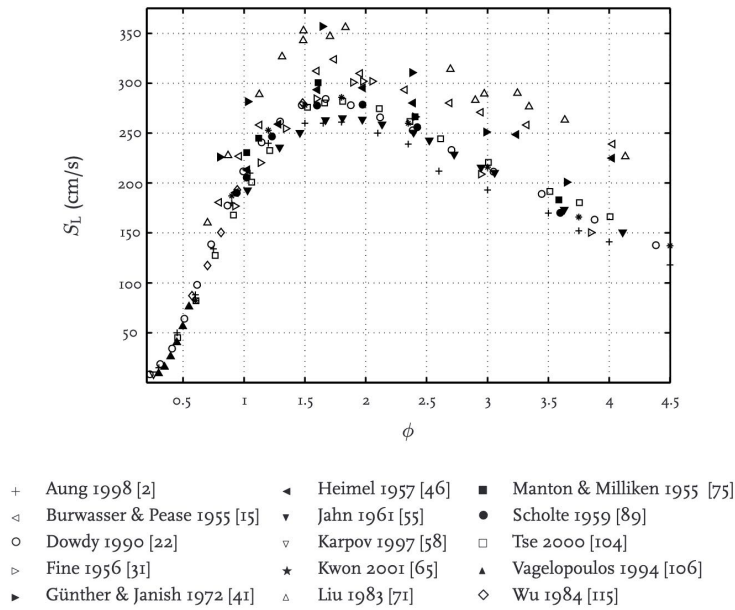
#### **2.1.4 Flame speed & Flashback**

A fuel’s Flame Speed represents the rate at which the flame travels through a mixture of unburnt gas, which is a function of factors like initial temperatures and pressures. Inadequate fuel injection velocity relative to Flame Speed can lead to flashback, where the flame tracks back through the combustor and fuel delivery system, posing safety risks and potentially causing damage. Hydrogen, with its higher laminar Flame Speed and reduced IDT compared to methane (as shown in Table 2.1), demonstrates a greater proclivity for flashback.

As shown by the following two Figures 2.1.2a and 2.1.2b, the laminar Flame Speed of hydrogen is an order of magnitude quicker than that of methane across the range of equivalence ratio tested and is unanimously agreed by the experimental work described in [92].



(a) Experimental  $\text{CH}_4$  laminar flame speeds from various sources\* reproduced from [92].



(b) Experimental  $\text{H}_2$  laminar flame speeds from various sources\* reproduced from [92].

**Figure 2.1.2:** Experimentally derived laminar flame speeds of hydrogen and methane. **N.B.** The sources\* denoted in Figure 2.1.2 refer to the references displayed in Figures 2.1.2a and 2.1.2b, and can be found in [92]

## 2.2 Fundamentals of Hydrogen and Methane Fuel Blends

Due to the heating values of hydrogen and methane described in Table 2.1, when fuel blending at low percentages on a volumetric basis, the impact of  $\text{CO}_2$  reduction

is insignificant as is shown in Figure 1.6.1. Hence, it is desirable to implement high hydrogen proportions in fuels to realise significant CO<sub>2</sub> emission reductions. However, hydrogen-methane fuel blends exhibit different behaviours depending on their ratio to one another.

### 2.2.1 Flame Speed of Methane/Hydrogen Blends

Fundamental flame characteristics have been evaluated through means of numerical and experimental analysis to determine the effect of introducing hydrogen into a methane fuel blend. Numerical studies by Gauducheau [93] and Chen et al [94] showed that the introduction of 20% of hydrogen in a methane fuel blend increased the laminar flame speed. Fairweather et al. [95] extended their study to 50% hydrogen content in the fuel blend with methane and found that the flame speed of the fuel with a higher percentage of hydrogen content had faster flame speeds under all experimental conditions included in this study (10%, 20% and 50%). This was also shown by Ilbas et al. [96], where the study extended to numerical modelling and to experimental validation of blends from 0% to 100% hydrogen. From the reproduced Figure 2.2.1 it is clearly shown how the inclusion of hydrogen drastically increases the laminar flame speed. Another study was undertaken by Siemens [97] in determining the hydrogen capability of their assets (ranging from their SGT-A05 [4MW] to SGT5-9000HL [592MW]). This included a chemical kinetics study that was undertaken at engine relevant conditions (i.e. 20bar and 450°C air temperature). Since this study was considered in the context of industrial engines it was necessary to consider the importance of the combustor exit or turbine inlet temperature as a design criterion. Hence, this study was performed at varying levels of constant adiabatic flame temperature. The trend is illustrated in Figure 2.2.2. This study shows the increase in reactivity on account of both the increase in adiabatic flame temperature and the increase in hydrogen content in the fuel blend. The increasing hydrogen content has a more pronounced effect at the higher adiabatic flame temperature [97].



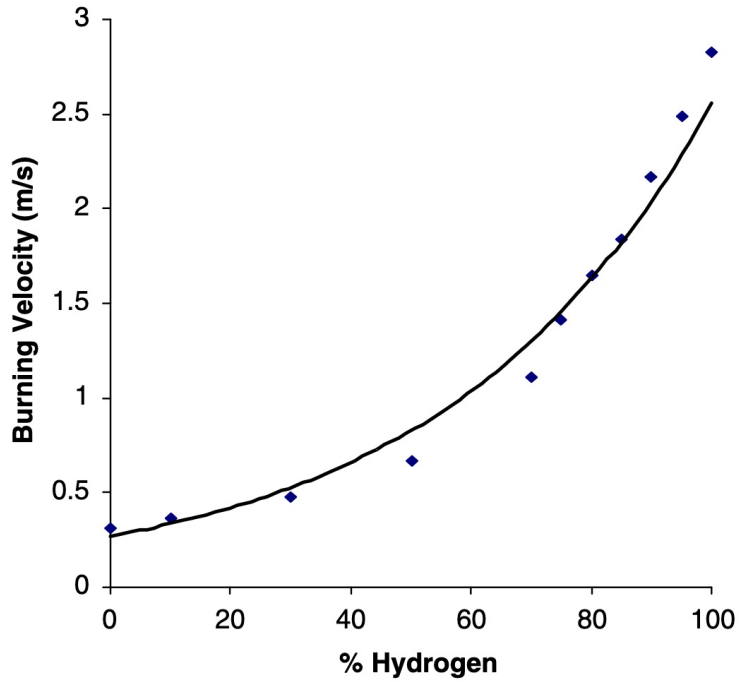


**Figure 2.2.1:** Laminar burning velocity (akin to laminar flame speed) for different percentages of hydrogen in hydrogen-methane fuel blend at an Equivalence Ratio of unity. Data points indicate measured values and the trend line is a line of best fit, reproduced from [96]

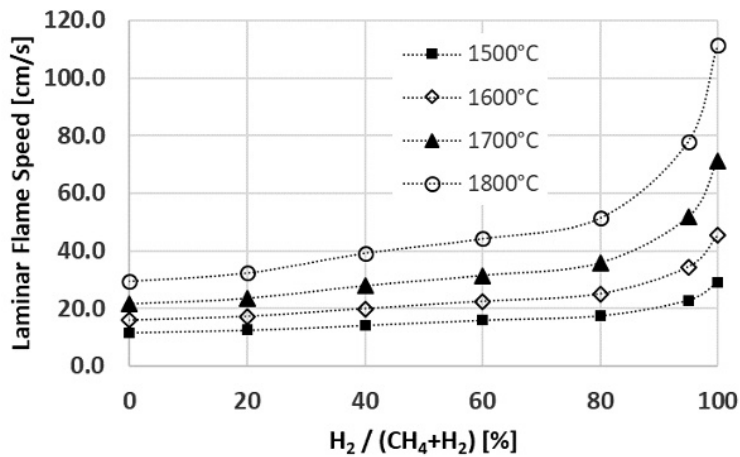


**Figure 2.2.2:** Laminar Flame Speed from chemical kinetics study at gas turbine relevant conditions and constant adiabatic flame temperature, reproduced from [97].

## 2.2.2 Ignition Delay Time of Methane/Hydrogen Blends

The fundamental studies of Gersen et al. [98] demonstrated reduced IDTs with increasing hydrogen content, with the effect being more pronounced at higher temperatures and diminishing with pressure increases. Similar effects were observed by Liu et al. [99] under elevated pressure (20bar) and increased temperature conditions.

A study led by Zhang [100] showed that there were three ignition regimes pertaining to the ignition of methane/hydrogen blends.

1. Methane chemistry dominated ignition ( $X_{\text{H}_2} < 40\%$ )
2. Combined chemistry of methane and hydrogen dominating ignition ( $X_{\text{H}_2} = 60\%$ )
3. Hydrogen chemistry dominated combustion ( $X_{\text{H}_2} > 80\%$ )

It was found that the ignition delay time would decrease with increasing hydrogen content of the fuel [100]. Another study performed by Zhang et al. [101] described the effect of increasing pressure on the ignition delay of methane/hydrogen blends. It was shown that typical reductions in ignition delay time described by pure methane chemistry remained true for blends of 40% hydrogen or less. At 60% hydrogen, neither hydrocarbon or hydrogen ignition behaviour was present. However, at hydrogen fractions of 80% and above, hydrogen ignition behaviour was clear and even exhibited a complex non-monotonic pressure dependency [101]. This non-monotonic trend is captured in the preliminary stages of the study by Poyyapakkam et al. [102] that is related to the GT26 GT - this trend is illustrated below in Figure 2.2.3. This work will prove to be highly valuable in the determining potential operating ranges that the secondary burner in the GT26 can operate as a result of the pressure drop incurred in the engine following the High Pressure Turbine and potential role that the “Wide Logic C<sub>2</sub><sup>+</sup>” control system has in managing highly reactive fuels. The operating principles of the GT26 and the “Wide Logic C<sub>2</sub><sup>+</sup>” control system will be introduced in Section’s 2.5.1 and 2.5.3, respectively.

Siemens’ study [97] into their hydrogen capabilities was extended to consider the ignition delay time of hydrogen blends. Similar in methodology as described above, a range of constant adiabatic flame temperature were held, and the autoignition of hydrogen blended fuels was evaluated with the same engine relevant initial conditions of 20bar and 750°C. A steep reduction in ignition delay time was shown for the initial 20% of hydrogen. With further reductions observed with increasing proportions of

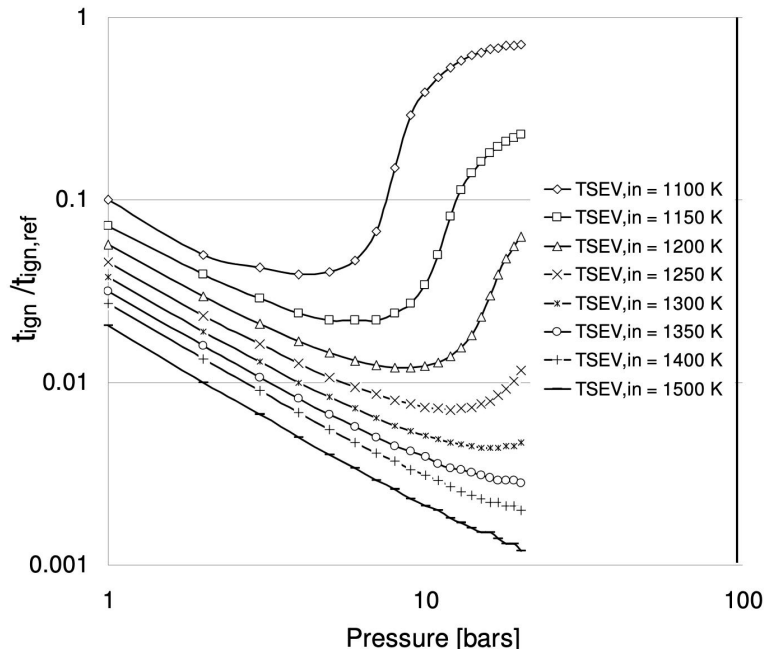


*Figure 2.2.3: Non-monotonic trend of hydrogen ignition delay time relative to the operating pressures, reproduced from [102].*

hydrogen in the fuel blend, as is depicted by Figure 2.2.4 below [97].

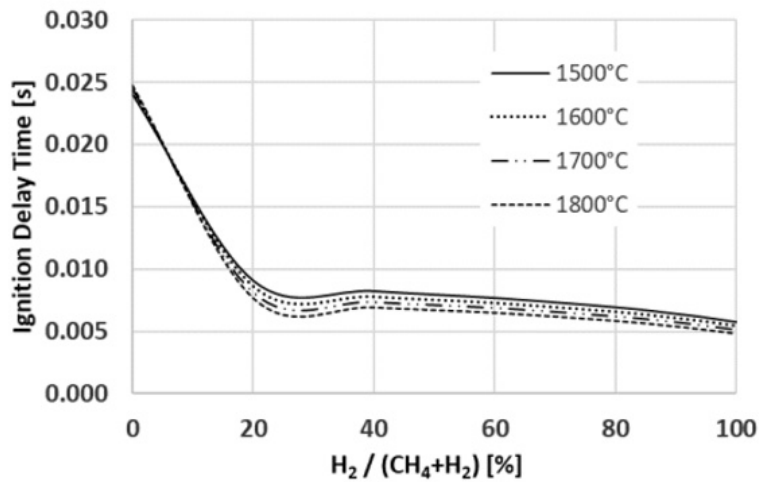


*Figure 2.2.4: Chemical Kinetic results of the ignition delay time for methane-hydrogen fuel blends at various adiabatic flame temperatures under engine relevant conditions, reproduced from [97].*

### 2.2.3 Adiabatic Flame Temperature of Methane/Hydrogen Blends

It has previous been described that hydrogen has a higher adiabatic flame temperature than that of many other hydrocarbon fuels, including methane. This is due

to hydrogen having a higher energy content per unit mass and releases more heat during combustion. Therefore, if hydrogen is mixed with methane in various proportions, the resulting AFT would be influenced by the hydrogen content within the mixture.

In studies performed by Zhang et al. [103], Yunusi et al. [104] and Hasche et al. [105], researchers have investigated the AFT of different methane/hydrogen fuel blends with varying proportions of hydrogen. These studies have consistently shown that as the hydrogen content in the mixture increases, the AFT of the blend increases proportionally. This relationship between hydrogen content and AFT is significant because it impacts the combustion characteristics and performance of engines or turbines using these fuel blends.

AFT serves as a valuable aid in understanding the practical implications of operating a GT on different fuel blends. In the context of hydrogen blending with hydrocarbon fuels, the increased AFT associated with the increase of hydrogen in the fuel blend would incur additional thermal impact to hot gas path components. Hence, it is likely that a GT operator/OEM would reduce the fuel flow rate to maintain the designed flame temperature within the combustor.

#### **2.2.4 Flame Stability**

In all combustion systems, flame stability is vital for safe and well performing operation. This has led to studies performed by Ren et al. [106] and Hu et al. [107] to evaluate the impact of strain rates on the combustion of methane/hydrogen fuel blends under premixed conditions. Strain relates to the deformation of small volumes of fluid that are induced by forces or velocity gradients within the flow. The strain rate is a measure of how the strain changes over time. Both studies conclude that the hydrocarbon dominant fuels are more susceptible being extinguished at lower strain rates than that observed by fuels with higher proportions of hydrogen in the fuel blend, thus, enabling hydrogen enriched fuel blends to operate at higher strain rates and lower equivalence ratios [106] [107].

This is further assessed through Lewis number analysis. Where Lewis number is defined mathematically by the following equation:

$$Le = \frac{\alpha}{D}$$

where,  $\alpha$  is the thermal diffusive property of the fluid and  $D$  relates to the mass diffusivity of the fluid, under the conditions analysed. A Lewis number of greater than unity suggests that the flow is dominated by thermal diffusivity and that Lewis numbers less than unity are dominated by mass diffusivity. When considering the mass diffusivity of both hydrogen and methane, hydrogen has a higher mass diffusivity than methane as a result of its lower molecular weight, meaning that hydrogen molecules can diffuse more rapidly in a mixture when compared to methane.

A study undertaken by Okafor E. et al. [108] where the influence of hydrogen concentration in a hydrogen/methane fuel blend was evaluated for laminar premixed flames showed an increase in the unstretched laminar burning velocity as the hydrogen concentration increased. The study performed by Bouvet, N. et al [109], through numerical and experimental studies, showed that the increased Lewis number of hydrogen containing blends of hydrogen and hydrocarbons increased the flames stability and ability to operate at leaner combustion conditions, where lower NO<sub>x</sub> emissions are achievable. These findings are also congruent with the observations made by Frenillot, J. P. et al [110] and Bell, S.R & Gupta M. [111] who tested the impact of hydrogen concentration in hydrocarbon fuel blends under engine relevant configurations.

## 2.2.5 Fundamentals Conclusion

This literature review examined the differences between the fundamental properties of methane, hydrogen, and methane/hydrogen blends, a consistent trend emerges: the addition of hydrogen significantly increases the reactivity of the fuel across all properties considered. While these heightened reactivity characteristics will intro-

duce challenges to hydrogen’s use in GTs, it is important to acknowledge that these challenges are not insurmountable and can be addressed through thoughtful design and robust research and development efforts. Furthermore, it will be *necessary* for these challenges to be overcome if the utilisation of hydrogen in GTs is going to contribute to global emission targets.

## 2.3 GT fuel Flexibility

The fuel flexibility of GTs has been an area of prominent research over recent years. Within power generation the state of the art combustor technology in GTs has been Lean Premixed (LPM) swirl stabilised combustion and the fuel most typically used is natural gas. Despite GTs in general having an ability to operate with a wide range of heating values, individual machines have limited variation in the fuel they can accommodate [112] as a result of Original Equipment Manufactures (OEM) are tuning installed GTs to perform optimally for the given natural gas composition delivered to a given site.

### 2.3.1 Wobbe Index

Runyon, J. [113] noted that the variability of fuels delivered to GTs is managed first by allowing a permissible fuel quality onto the national gas grid specified by the GS(M)R regulations [114], which are given in Table 2.2. Furthermore, OEMs will often specify a given Wobbe Index (WI) that the operator must adhere to. The WI is a measure of the given “*energy injected to the combustor at a fixed pressure ratio*” [112] within a combustion system, and the mathematical definition for a real gas is given below. Its intention is to provide a definition for the interchangeability of fuels within a combustion system.

$$WI_{real,gross}(t1; t2, p2) = \frac{HHVG(t1; t2, p2)}{\sqrt{G(t2, p2)}} \quad (2.1)$$

where ‘ $G$ ’ is the relative density of the real gas determined from the specific compression ratio as noted by Runyon [113] and specified in British Standard document BS EN ISO 6976:2016 [115].

**Table 2.2:** Gas quality specification for fuel permissible on UK national gas grid currently, reproduced from [113]

Parameter	
Wobbe Index ( $MJ/Nm^3$ )	47.20 - 51.41
Total Sulfur content ( $mg/m^3$ )	50 (max)
Hydrogen Sulfide ( $H_2S$ ) + Carbonyl Sulfide ( $COS$ ) ( $mg/m^3$ )	5 (max)
Oxygen ( $O_2$ ) (%vol)	0.2 (max)
Hydrogen ( $H_2$ ) (%vol)	0.1 (max)
Incomplete Combustion Factor	0.48 (max)
Soot Index	0.60 (max)

The Incomplete Combustion Factor is an empirical measure correlating to the gas’s inclination to undergo incomplete combustion within a gas appliance, a tendency influenced by its composition. The Soot Index is a measure of the amount of soot or particulate matter that is produced during combustion [114].

Despite the WI being able to indicate the heat content of the fuel that is supplied to the GT combustor it does have significant shortcomings in determining combustion characteristics that are exhibited by the fuel and hence limit understanding of phenomena such as flashback and acoustic instabilities [113].

### 2.3.1.1 Fuel Interchangeability Indices

The introduction of hydrogen into a fuel blend with natural gas would reduce the WI of the fuel, proportional to its blend. With increasing hydrogen content the flame’s reactivity will increase which is unaccounted for by the WI. Since major economies such as European Union are devising means of converting their GT industry to utilise hydrogen through a transitional period of fuel blending [39] and WI is heavily relied upon for fuel interchangeability criteria in Europe. Therefore adoption of other

means of determining a fuels interchangeability is recommended. It was stated by the American Gas Association (AGA) that:

*“the matter of satisfactory interchangeability is obviously of extreme importance since no value can be attached [sic] to any supplemental gas which, if mixed with the base natural gas in any substantial proportion will not permit customers to continue to utilize their appliances in a normal manner”* [116].

This statement is deeply applicable for the consideration of hydrogen fuel blending in GT combustion. AGA have acknowledged through the prospect of increasing LNG importation that their gas supply composition is likely to change, despite maintaining relatively similar calorific contents. AGA advise not only the use of WI but also the AGA index and the Weaver index. The latter two indices account for the combustion behaviours of fuels in atmospheric burners which are not addressed by the WI and are fundamentally empirical in their application [117].

The Weaver index takes into consideration the following fuel characteristics: Flashback Index, Yellowtipping Index, Incomplete Combustion Index, Lifting Index, Primary Air Ratio, Heat Rate Ratio [117].

Due to the heightened reactivity of fuels with high hydrogen content compared to natural gas and their anticipated widespread adoption, the author strongly recommends evaluating fuels using both the Weaver index and the Wobbe index to ascertain their suitability for interchange within specific combustion systems.

## **2.4 Current State of the Art of GT Hydrogen Capability**

In this section, the current state of the art in terms of H<sub>2</sub> fuelled GTs is introduced.

### **2.4.1 Diffusion Based Combustors**

At present, 100% hydrogen GTs are available - consider the likes of GE's 6B.03 (without Dry Low NO<sub>x</sub> upgrade) for example [118], which operates a diffusion flame in its



combustor. This leads to less effective mixing compared to premixed combustion, causing local regions of high ER and, consequently, high NO<sub>x</sub> production within the flame. However, diffusion flames are known for their robustness and have a wider operating range compared to premixed flames.

Whilst the 6B.03 engine has demonstrated success with hydrogen, it exhibits high NO<sub>x</sub> emissions. Integration of Wet Low Emission (WLE) technologies, such as steam injection into the combustion process, can mitigate this. Siemens' aero-derivative SGT-A65 utilises this system, allowing 100% hydrogen operation with lower NO<sub>x</sub> emissions compared to untreated hydrogen diffusion combustion [119] [120]. WLE technologies do carry inherent disadvantages such as consumption of significant volumes of treated water, introducing potential for corrosion and reductions in GT efficiency.

## 2.4.2 Premixed Based Combustors

Current ambitions in terms of technological developments in the GT industry come in the form of: i) the application of lean premixed combustion technologies with high, if not pure hydrogen containing fuels and ii) the development of fuel flexible lean premixed combustion GTs that are capable of operating on 100% natural gas through to 100% hydrogen without the requirement of any component changes.

Challenges in flame stability arise with natural gas and LPM combustion technologies, and these challenges are likely to persist when applied to hydrogen due to its increased reactivity and the inherent sensitivity of lean premixed combustors. While hydrogen may offer advantages in lean premixed combustion due to its extremely lean blow-off limit, it has been reported that operating hydrogen under such conditions can lead to a significant emission of N<sub>2</sub>O, as reported by Colorado et al. [121]. This emission of N<sub>2</sub>O can negate the emission performance improvements achieved by not emitting CO<sub>2</sub>, given that N<sub>2</sub>O has a Global Warming Potential (GWP) 294 times that of CO<sub>2</sub> and is susceptible to photolysis, which, in turn, destroys the ozone [121].

Despite such challenges, there are offerings available by most GT OEMs, that operate a partially hydrogen-fuelled combustor under premixed conditions. General Electric (GE) report two Dry Low NO<sub>x</sub> (DLN) burners that they can offer their E and F-class GTs. The first being DLN1, which has a typical lean premixed combustor design, offers the capability of combusting up to 33% by volume of hydrogen for their 6B, 7E and 9E frames. This has been improved by the introduction of their DLN2.6e combustor, that utilises multiple smaller scale premixed flames, that can enable 50% of hydrogen by volume [122].

Mitsubishi Heavy Industries (MHI) currently report a 30% hydrogen capability with their present DLN combustors, across their range. MHI have stipulated that a multi-cluster (DLN) burner is under development which will be offered across their range that are targeting 100% hydrogen capability [39], that deploy a similar method to that described for GE's DLN2.6e.

Solar Turbines also offer a DLN based combustor, named SoLoNO<sub>x</sub>. It has been reported that this combustor has been successfully field tested in a Titan 130 GT using a fuel gas blend of up to 20% hydrogen [123]. Moreover, in collaboration with Precision Combustion Inc., Solar Turbines developed a full-scale rich catalytic hydrogen injector (RHCI) that achieved single-digit NO<sub>x</sub> emissions with a fuel mixture containing 42% hydrogen, and the remaining proportion being nitrogen [123]. Whilst this is not the idealised fuel for consideration, it is a positive development in the reduction in NO<sub>x</sub> emissions from such engines.

Ansaldo Energia's GT36 engine, which belongs to the same family as the GT26 (detailed in Section 2.5.4), accommodates fuel blends with up to 50% hydrogen through its Constant Pressure Sequential Combustor (CPSC) in its current configuration [39]. It has also been demonstrated through full-scale high-pressure testing that up to 70% hydrogen by volume was feasible with minimal impact, or need for dilution of selective catalyst reduction [39]. Ansaldo also provides a "Flamesheet combustor" upgrade, compatible with GE, Siemens, and MHI E- and F-class engines. This upgrade has proven effective in handling hydrogen volumes of up to 40%

in commercial machines, with rig tests demonstrating up to 80% [39].

Siemens also offer engines capable of 30% to 60% hydrogen, dependent on the burner utilised. through their control and hardware upgrade package “H<sub>2</sub>DeCarb” hydrogen capability of up to 60% is possible in their E- and F-class engines. Siemens have also announced their goal to progress to offer 100% hydrogen capability across their entire fleet of GTs by 2030 [124].

The existing literature indicates that traditional DLN combustors are limited to around 50%, but recent advancements are introducing multi-flame burners to achieve higher hydrogen capabilities. A notable example is the Micro-Mix (MMX) combustors, developed over 30 years, as discussed by Funkee et al. [125]. MMX combustion employs miniature jet-in-cross-flow fuel injection into combustion air, resulting in short flame height and residence time, preventing NO<sub>x</sub> formation and flashback risks [125].

A compelling demonstration of potential is evident in the field testing conducted by Kawasaki, AcUAS, and B&B-AGEMA GmbH [126] [127]. They deployed a co-generation system with an MMX combustor in an M1A-17 GT in Kobe City, Japan. The trials achieved notable successes, including compliance with Japanese environmental regulations (below 84ppmv NO<sub>x</sub> at 15% O<sub>2</sub>), a 2MW electrical output, absence of combustion instabilities, and improved efficiency compared to traditional premixed technologies using water injection for NO<sub>x</sub> reduction. Single can testing validated MMX’s fuel flexibility, operating seamlessly with H<sub>2</sub>/CH<sub>4</sub> fuel blends from 100/0 to 57/43 [% vol] without physical component changes, demonstrating exceptional combustion efficiency and remarkably low NO<sub>x</sub> emissions, peaking at 4ppm (@15% O<sub>2</sub>) [128].

## 2.5 GT26 Research

In this section, the research dedicated to the GT26 will be introduced, beginning with an exploration of its operational principles and then delving into the efforts made to incorporate hydrogen into its fuel source.

## 2.5.1 GT26 Operating Principles

GTs utilise the Brayton Power cycle and will often see inclusions of cycle modifications to improve the cycle performance. The GT26 is unique in the respect that it utilises the addition of reheat in its power cycle, as is shown by Figure 2.5.1. Schematic of the engine cross-section is given in Figure 2.5.2 to enable reference to the engine components and their role in the reheat Brayton cycle.

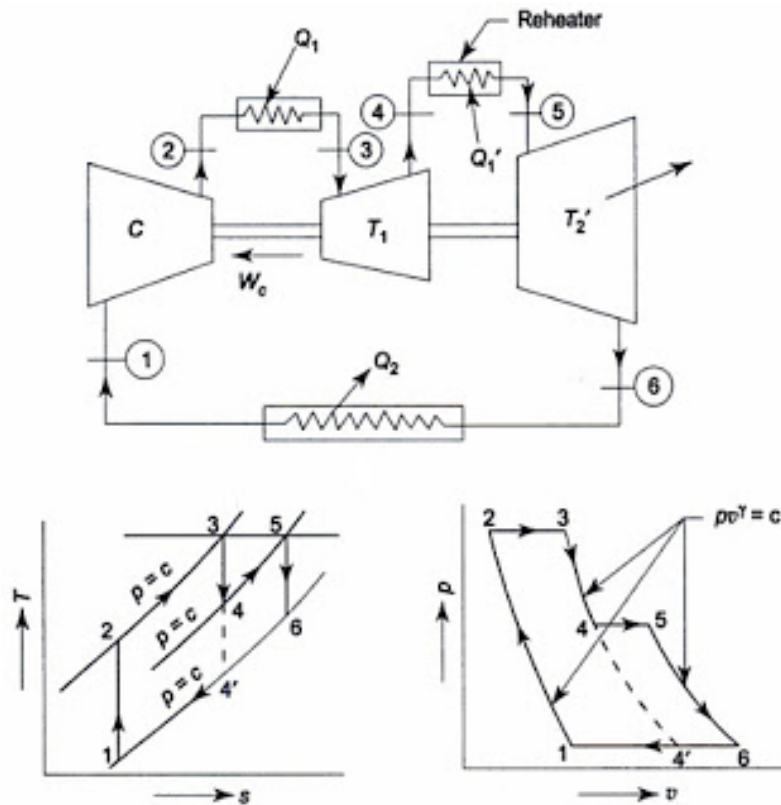


**Figure 2.5.1:** Operating Principle of Reheat Brayton cycle in the context of the GT26 compared to conventional Brayton cycle, reproduced from [129].

In the initial stage, air undergoes compression (1-2) using the GT26's 22-stage compressor, reaching 30bar at full load. Variable Inlet Guide Vanes (VIGVs) on early compressor stages enhance flow and adjust load based on grid demands [130]. Heat addition follows fuel ignition (ca. 50% at base load, reported by [129]) in the first-stage EV burner within the EV combustor (2-3). Partial expansion through a single-stage high-pressure turbine extracts work, reducing pressure by a factor of 2 (3-4). Further reheat occurs in the secondary combustor, known as the SEV burner, (4-5), with fuel autoigniting due to high temperatures. The working fluid

then undergoes expansion through a low-pressure turbine (5-6), extracting work for electricity production as described by Güthe et al. [129], concluding with gas exhaustion.

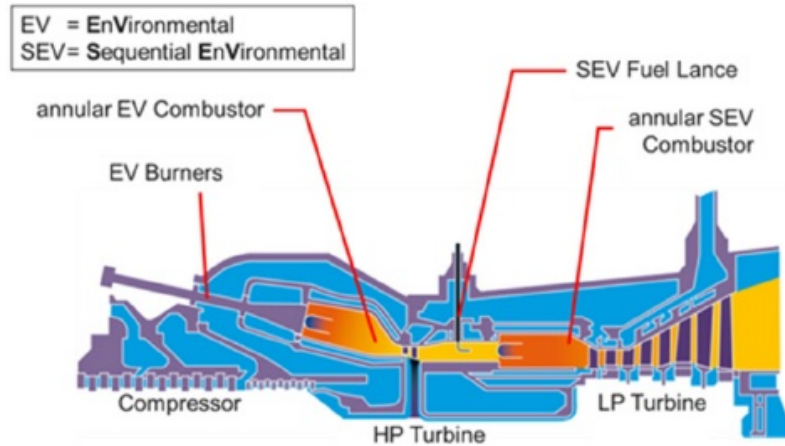


*Figure 2.5.2: Alstom GT26 sequential combustor schematic (gas flow from left to right), reproduced from [131].*

In the case of an open cycle gas turbine (OCGT), the heat is dumped and gross GT efficiencies are reported to be 41% [130]. Under CCGT configuration, the GT26 can offer efficiencies as high as 61% [130].

### 2.5.1.1 Benefits of Reheat Cycle

The reheat cycle in the GT26 enhances specific work and offers practical advantages. Achieving remarkably low NO<sub>x</sub> emissions is possible due to a lean premixed EV combustor, as reported by Biagioli et al. [132] and 2011 burner aerodynamic improvements for sequential combustion in the SEV as reported by Düsing et al. [133] [131].

The reheat concept significantly reduces NO<sub>x</sub> by limiting oxygen (O<sub>2</sub>) in the SEV environment, minimising thermal NO<sub>x</sub> formation. The stabilisation of the flame through autoignition in the SEV contributes to excellent emission performance across the GT26's operational range, effectively mitigating excessively high flame temperatures [129].

In addition to its impact on NO<sub>x</sub> emissions, the adoption of the reheat concept positively affects CO emissions by pushing combustion efficiency closer to comple-

tion. The GT26 exhibits an unparalleled ability to adjust its output, facilitated by the complete shutdown of the SEV combustor during periods of low load operation [133]. This exceptional turndown capability enhances operational flexibility, enabling the provision of ancillary services required by the National Grid, thus rendering the machine a commercially desirable asset [131].

Furthermore, the GT26's operational flexibility is complemented by its high operational efficiency, both at full and partial load conditions [131].

## 2.5.2 EV Burner

The EV burner is a lean premixed swirl combustor. A swirling flow is induced by its geometry that causes vortex breakdown which enables the stabilisation of the premix flame without the need of a physical device, as described by Döbbeling et al. [134]. The burner is comprised of two half cone shells that have two tangential slots generated as the cones are offset parallel to the axis [135]. Air is introduced into the combustor and swirled via the slots to induce the described vortex breakdown. Fuel gas is injected into the air stream in a cross flow configuration which in turn provides low emission levels due to effective mixing [135].

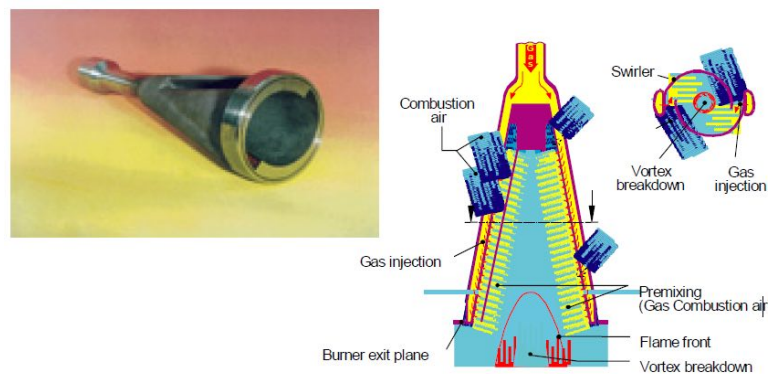


*Figure 2.5.3: EV burner system, reproduced from [135]*

## 2.5.3 SEV Burner

As described, the SEV burner is situated after the HPT. Hence, its inflow is a vitiated flow that has been partially expanded through the HPT. The operational

principles of the SEV are illustrated in Figure 2.5.4. Attention should be given to the vortex generator depicted in Figure 2.5.4. These vortex generators are strategically employed to improve the mixing of fuel and hot gas [131].

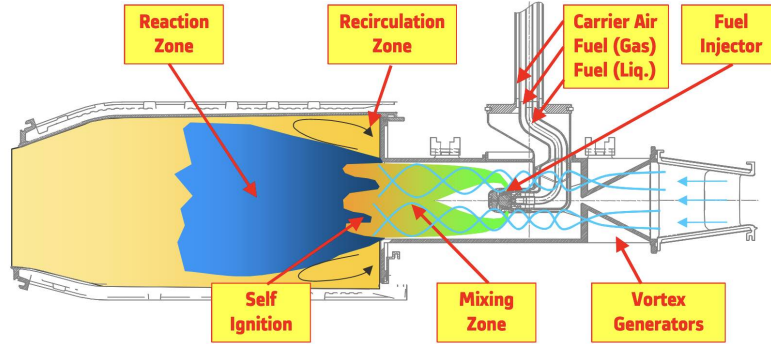


*Figure 2.5.4: Working principles of SEV combustor, with flow going from right to left, reproduced from [136].*

Vortex generators (VG), depicted in Figure 2.5.5, employ delta-wing-shaped ramps inducing 4 pairs of streamwise vortices just before the secondary fuel injection, as described by Eroglu et al. [137]. This differs from a swirling flow that is characterised by a larger flow structure that is rotational in nature, whereas the flow structure induced by the VG is the introduction of streamwise vortex structures. These streamwise vortices enhances turbulence dissipation, crucial for molecular-level mixing of fuel and oxidant [138]. Extensive studies optimised vortex generator designs for maximum mixing with minimal pressure drop, evaluating single VGs, pairs, and the two pairs in the configuration found in the GT26 [139].

A lance, strategically placed in the flow, injects fuel into the SEV combustor using four fuel and shielding air injectors. These injectors deliver fuel and air into four vortex pairs within the chamber. The shielding air serves the role of preventing premature ignition, acting as an “ignition controller” by preserving fuel jet momentum. The injection system is optimised for effective mixing, ensuring large-scale distribution and fine-scale mixing [138].

The injection strategy, along with high-velocity flows, prevents flashback in the SEV combustor by delaying autoignition. Flame stabilisation occurs through a sudden expansion in the combustor, creating recirculation zones at the outer and central regions of the flame. These zones result from velocity gradients induced by

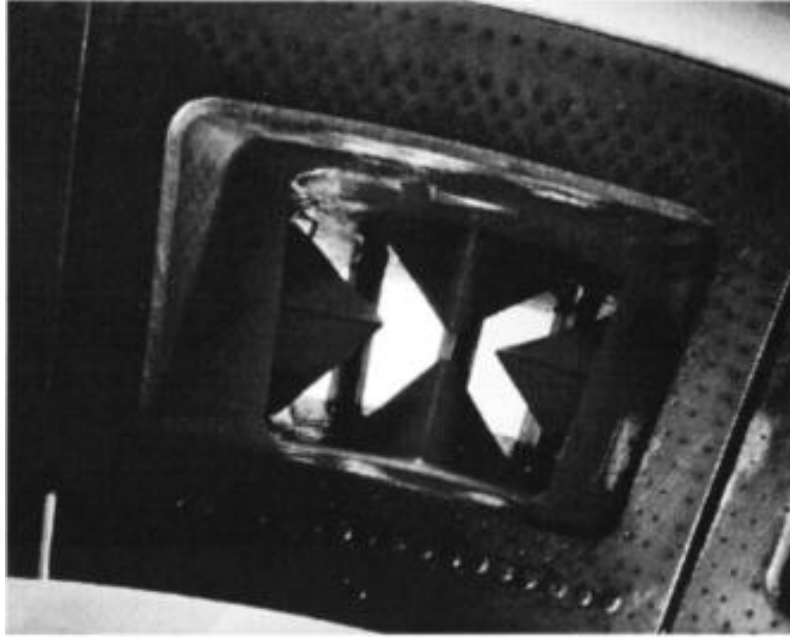


*Figure 2.5.5: SEV Vortex Generator, reproduced from [140].*

shear layers and vortex breakdown [137].

As a positive consequence of the utilisation of a reheat Brayton cycle, the GT26 is highly reputable in regards to fuel flexibility [129], which is considered a necessity in today's energy landscape. Under baseload conditions the fuel delivery between the EV and SEV is equal [129]. However, in a bid to improve the fuel flexibility of the GT26 for operating with high hydrocarbon ( $C_2+$ ) containing fuels and those of a low Wobbe Index [131], the "Wide  $C_2+$  Logic" control system was developed [141] [142] [136]. This control system was devised to account for the increased reactivity of natural gas fuels with a higher proportion of  $C_2+$ .

The control system utilises the reheat concept and the availability of two combustors. Since the SEV is reliant on the autoignition mechanism of combustion, it is highly sensitive to the inlet temperature of the vitiated flow entering the SEV. Hence, the "Wide  $C_2+$  Logic" works on the premise of reducing the firing temperature in the EV, by reducing fuel flow to the EV burner. The proportion of fuel reduced in the first stage is then fed into the SEV with the remainder of the fuel to achieve full power [141] [142]. The proportion of which the fuel flow is reduced in the EV and increased in the SEV is variable, dependent on the fuel blend used, it is also not documented in the literature and hence it is considered proprietary infor-



mation. The working principles of the deployment of this protocol is captured by Figure 2.5.6 below.

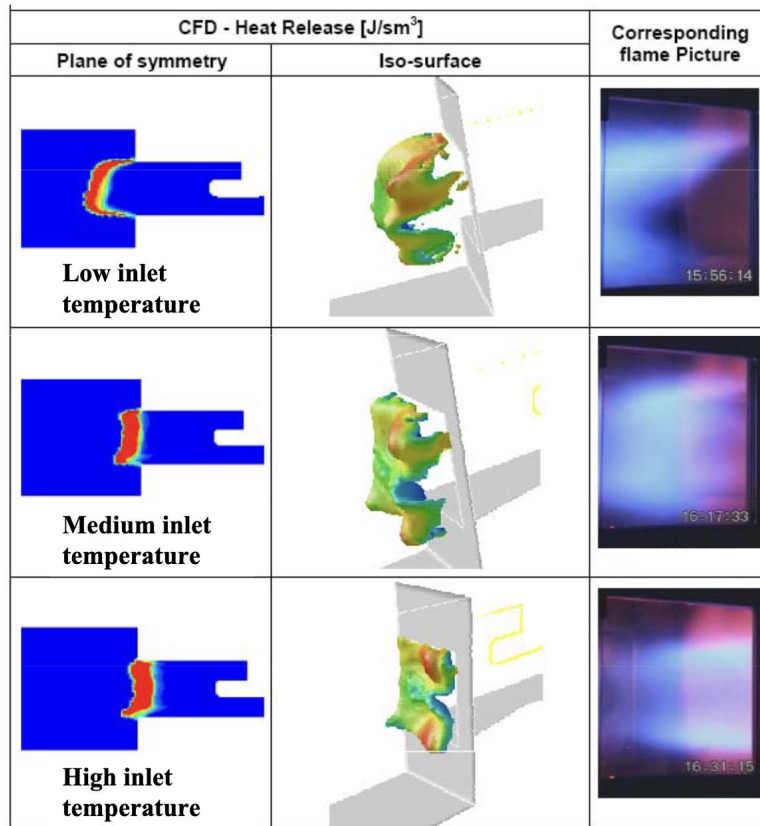


*Figure 2.5.6: Comparison between CFD calculations and flame imaging at atmospheric pressure as a function of the SEV inlet temperature, reproduced from [136]*

## 2.5.4 Hydrogen Capabilities of the GT26

The EV burner has been reported to have successfully operated with a 45/55 [%vol] H<sub>2</sub>/NG blend, at pressure [142],. This is the highest proportion of hydrogen achievable in the EV found in the literature. However, access to confidential information regarding the achievable hydrogen content in the EV burner was granted and protected by the studentship agreement relating to this project. The challenge pertaining to the GT26’s ability to operate with high-hydrogen fuels is associated with the SEV burner. Thus, resulting in the SEV becoming the sole focus of this thesis henceforth.

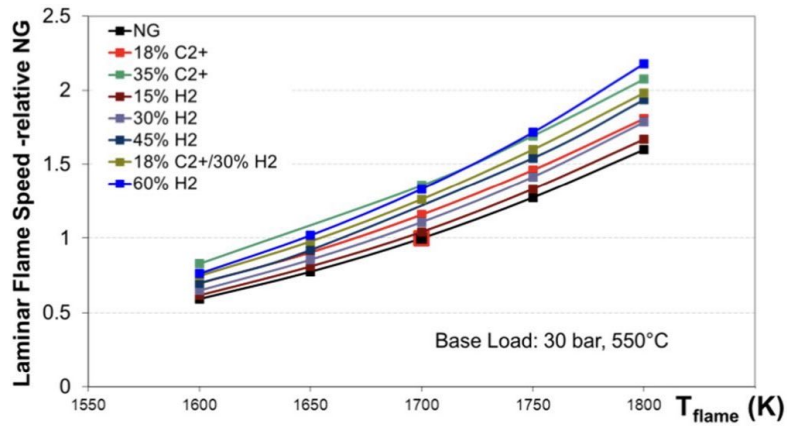
Since the “Wide C<sub>2</sub>+ Logic” control system was originally devised for the accommodation of more reactive natural gas blends, it functions as a method of addressing

the heightened reactivity induced by blending hydrogen into natural gas blends [129]. This principle is also established in a preliminary chemical kinetics model performed by Poyyapakkam et al., where the temperature dependence of fuel's autoignition was computed [102].

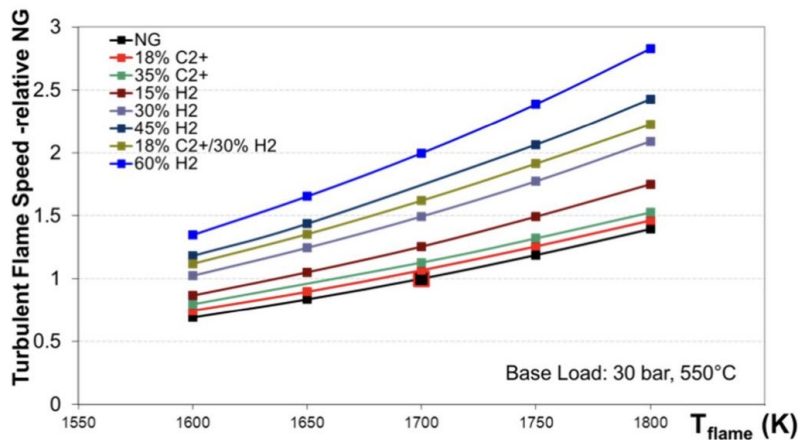
Despite the high-velocity flow in the SEV, there's concern about flashback when burning hydrogen fuels in the GT26. The elevated flame temperature in the EV, along with a shorter autoignition delay for hydrogen, moves the flames closer to the SEV burner and lance, risking issues like excessive thermal loading or flame tracking up the fuel line. These pose catastrophic failure risks, incurring commercial penalties. To mitigate this, a constant safety margin by limiting SEV inlet temperatures when burning hydrogen fuels is recommended [143].

It is also stated by Joos et al [138] that if the flow velocity of the injection of the hydrogen-containing fuel is increased to account for the reduction in autoignition delay time associated with hydrogen enriched fuels, this would induce a heavy pressure drop penalty, which is already a likely outcome owing the reduction in hydrogen's density when compared to natural gas.

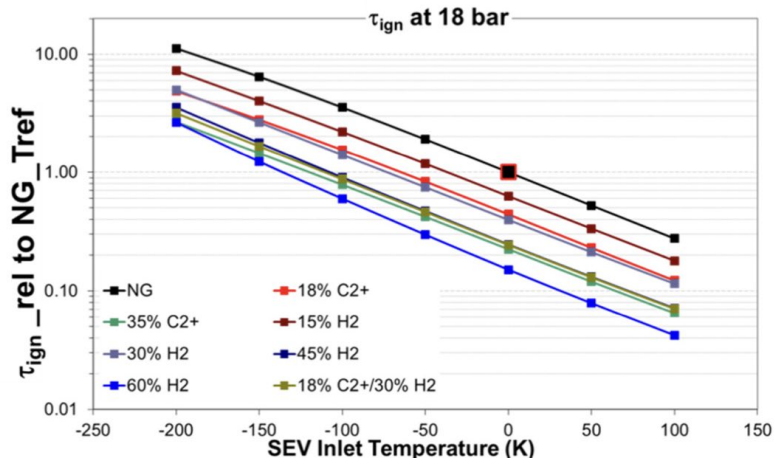
The potential of the Wide C<sub>2</sub>+ logic for hydrogen utilisation had been investigated through a numerical study by Wind et al. [142], in which the effect of the firing temperatures in both the EV and SEV combustors was evaluated on the Flame Speed and ignition delay time relative to a reference natural gas fuel, with fuels containing high C<sub>2</sub>+ content and hydrogen up to 60% by volume. As illustrated by Figure 2.5.7a, the firing temperatures necessary for equal laminar flame speeds are shown, the challenge of reducing turbulent flame speeds sufficiently is also illustrated in figure 2.5.7b. Notably, the turbulent flame speed surpasses laminar flame speed due to the increased intensity of mixing, which enhances heat and mass transport within the reaction. Additionally, flame wrinkling induced by turbulence at the flame front augments the flame's surface area, consequently increasing the reaction rate. Figure 2.5.7c then displays the necessary SEV inlet temperatures for achieving the same ignition delay time across the aforementioned fuel blends. These



(a) Normalised Laminar Flame Speed under EV relevant conditions, reproduced from [142].



(b) Normalised Turbulent Flame Speed under EV relevant conditions, reproduced from [142].

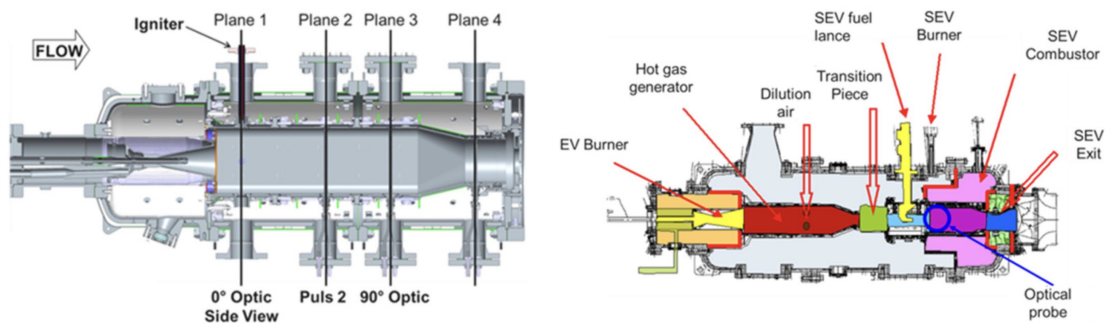


(c) Normalised ignition delay time in reference to natural gas under SEV combustor conditions, reproduced from [142].

**Figure 2.5.7:** Chemical Kinetic results relating to the GT26  $C_2+$  control system operation with hydrogen and or  $C_2+$  containing fuel blends fuels normalised against Natural Gas, [142]

studies being chemical kinetic studies, will have limitations in regards to the consideration of turbulent-chemistry effects. Hence, the study continues to undertake experimental testing of both the EV and SEV burners at field relevant conditions,

in the respective test rigs detailed in Figure 2.5.8.



(a) Schematic of EV single can high pressure test rig. (b) Schematic of SEV single can high pressure test rig

**Figure 2.5.8:** EV and SEV single can high pressure test rigs, respectively, reproduced from [142]

From this testing, it was shown that the EV burner displayed no indications of flashback when operating with a NG/H<sub>2</sub> fuel blend containing 45% hydrogen at base load (30bar pressure conditions). At part-load (16bar), fuel mixtures containing as much as 60% hydrogen were tested, where a single instance of flashback occurred in a off-design condition (hotter gas temperatures). Another positive outcome was the reduced pulsations during idle operation, which is considered to be the result of hydrogen's ability to extend the lean-blow off limit of a fuel blend [142].

In this study [142] both the 2006 and 2011 SEV upgrades were evaluated. The 2006 upgrade was unable to maintain its NO<sub>x</sub> emission performance with fuel blends containing more than 15% hydrogen without the reduction of the SEV exit temperature, which subsequently led to a reduction in power output and therefore a reduction in thermal efficiency [142]. However, it was shown in Figure 2.5.9 that the 2011 upgrade performed better in terms of flashback risk and NO<sub>x</sub> emissions as a result of its reduced cross-sectional area and increase in gas flow velocity for fuel blends of up to 30% hydrogen by volume [142].

Subsequently, Ansaldo Energia announce that the GT26 has the capability to operate with a hydrogen content of 45% by volume without any discernible impact on performance, provided that the MXL3 upgrade has been implemented [144], which has been supported by a study by Bothien et al [145].

In an effort to address the need for flashback protection while simultaneously maintaining low NO<sub>x</sub> levels, Poyyapakkam et al. conducted a comprehensive study,

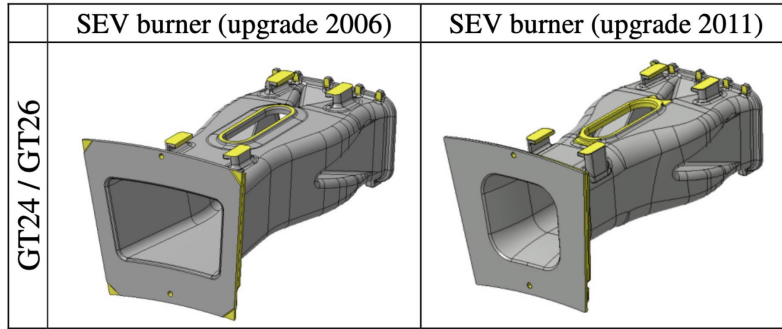


**Figure 2.5.9:** Schematics of the 2006 and 2011 SEV upgrades, reproduced from [131]

which delved into the challenges associated with the conventional radial fuel injection approach. The study also involved the development and testing of an innovative design. The fuel blend under consideration was a  $H_2/N_2$  fuel of 70%/30% that was identified by the European Commission as a representative fuel from a integrated gasification combined cycle that is coupled with CCS [102].

The research revealed that the existing radial fuel injection method, despite its commendable performance in terms of fuel distribution and mixing, resulted in the formation of a wake region. This wake region, in turn, led to relatively prolonged residence times, causing autoignition in regions where the fuel and oxidant were not optimally mixed. This phenomenon ultimately resulted in elevated  $NO_x$  emissions [102].

As a result of the aforementioned considerations, an innovative in-line injection design, presented in Figure 2.5.10, was developed. This revised design incorporates axial fuel injection aligned with the flow direction, accompanied by the introduction of multiple vortex generators. These vortex generators serve to induce a streamwise pattern of vortices, thereby enhancing the turbulent mixing process. It is noteworthy that these newly implemented vortex generators are of smaller dimensions compared to the existing concept. Therefore, the characteristic turbulent length-scale is reduced, facilitating the mixing of fuel and oxidant within shorter timescales, that is within the decreased autoignition delay times [102].

Whilst this paper denotes the success of achieving optimum combustion of a  $H_2/N_2$  fuel of 70/30 [%vol] [102], this fuel blend will not be as reactive as a 70/30



*Figure 2.5.10: Image of SEV in-line solution as reported by Poyyapakkam et al, reproduced from [102].*

[%vol]  $H_2/CH_4$  blend resulting from the inert content of  $H_2/N_2$ . Additionally, this study is limited in its investigation into the characterisation of the turbulence and the mixture fraction field of the fuel/oxidant. No further publications considering this in-line design were found.

A comprehensive series of studies, primarily led by Fleck, J. (2008 - 2012) has been carried out at Deutsches Zentrum für Luft- und Raumfahrt (DLR) Stuttgart to explore the ignition behaviour of hydrogen-enriched fuels within a generic reheat combustor. These investigations extend beyond chemical kinetics, with the specific aim of applying the findings to the GT24/GT26 gas turbines, funded by ALSTOM Power Generation AG [146] [147] [148] [149] [150] [151].

The study is initialised by the characterisation of a generic reheat combustor, operating at SEV relevant conditions of 15 bar [146]. The generic burner employs a modified FLOX burner (as described in [147]) to generate a vitiated gas mixture that closely resembles the gas entering the SEV, both in terms of gas temperature and  $O_2$  content. The vitiated hot gas enters a mixing duct (25x25mm), that has optical access via a quartz window, followed by a sudden expanse akin to the reheat combustor of the GT26. Fuel is then injected as a single jet in cross flow, analogous

to the multipoint fuel injection deployed by the SEV lance, as described above [146].

The initial characterisation of the flow field, accomplished through Particle Image Velocimetry (PIV), revealed a uniform velocity distribution and a fuel injection pattern consistent with a typical Jet-in-crossflow (JICF) configuration. Furthermore, the hot-gas generator exhibited performance levels that met its intended design specifications.

In the initial benchmark tests conducted with natural gas, no instances of autoignition were observed. However, when subjected to testing with hydrogen-enriched fuels, the rig consistently operated reliably up to a hydrogen content of 76% by volume in the fuel mixture. Beyond this threshold, the occurrence of autoignition in the mixing duct became evident, which was considered an undesirable outcome.

This study's scope was expanded, and the findings were presented at the fifth "The Future of Gas Turbine Technologies" conference [148]. During this extension, successful ignition of a natural gas case was achieved. However, this accomplishment required several notable operational adjustments, including significant reductions in pressure, mixing duct inlet temperature, and velocity, along with increases in oxygen content and equivalence ratio [148]. A series of "off spec" natural gas fuels were also evaluated, showing that increasing proportions of  $C_3H_8$  (up to 25%) reliably showed earlier autoignition. The campaign was finalised by evaluating an 80/20 [%vol]  $H_2/N_2$  fuel blend which reliably showed autoignition further upstream in the mixing duct once again [148]. This work is limited by its consideration of the fuel/oxidant mixedness and the global/local equivalence ratio, this was acknowledged by the authors and proposed for further investigation.

In the work conducted by Fleck et al. [149], their research delved deeper into the combustion of hydrogen under reheat conditions. The study encompassed two distinct  $H_2/N_2$  fuel blends, namely 70/30 [%vol] and 80/20 [%vol]. Notably, the research underscored the significant influence of temperature on autoignition. In instances where the gas velocity was at its highest, a mere 2% increase in temperature resulted in a substantial 16% reduction in the maximum achievable hydrogen content

by volume for stable combustion [149].

The test points included various fuels with equal hydrogen content but differing levels of dilution. For these test cases, it was demonstrated that despite variations in dilution levels, their ignition characteristics remained independent of the global equivalence ratio and macro-mixing [149]. The developments in study methodology introduced in [149] was extended in [150] where it was applied to H<sub>2</sub>/NG/N<sub>2</sub> fuel blends with varying level of inerts (80-95% non-inert). Two penetration depths were evaluated and no observable difference was shown in their ignition characteristics. The authors stipulate in their conclusion that the difference induced in fluid dynamics and mixing field do not play a crucial role in the ignition of the fuel. The conclusion is not congruent with the findings of more foundational studies on inhomogeneous autoignition discussed later in this literature review. However, this contradiction may be explained by the specific elevated pressure conditions under investigation here, as detailed in Section 2.2.2 and connected to hydrogen's non-monotonic pressure dependency [150].

In summary, under widely applied variations of the GT26 designs and upgrades, it is clear that the EV burner is robust in its ability to operate with highly reactive fuels when compared to the SEV. Hence, there has been a commensurate focus given to the SEV hydrogen's capabilities. It is clear that inlet conditions into the SEV are critical for the stable combustion of the SEV burner using highly reactive fuels. Although this work is limited in aiming to understand how the GT26's behaviour will change in closer increments of hydrogen-hydrocarbon fuel blends. Whilst this body of work has made strident efforts to understand the operational capability of the SEV, the majority of this work overlooks the fundamental principles underlying the stable combustion mechanisms in desired regions of the burner. The closest study to think beyond the current design of the GT26 was by Poyyapakkam et al. [102]; whilst they begun to investigate the effect of changing turbulent characteristics through the re-design of the vortex generators, they omit any attempt of characterising the mixing field or any turbulent property of the flow.



### 2.5.5 High Efficiency Upgrade Relevance for Hydrogen Capabilities

As of 2021, the worlds first offering of the GT26 High Efficiency (HE) upgrade by GE had come to completion at Uniper’s Enfield Power Station in North London. The upgrade offers the following key performance benefits:

- 2% increase in base load efficiency in closed cycle configuration.
- A 1% increase in part load efficiency in closed cycle configuration.
- Increased plant output from 15MW to 55MW per unit.
- Extended inspection intervals up to 32,000 hours.

Enhancing commercial performance involves increasing power per unit fuel and reducing long-term maintenance costs. As discussed in the literature review, achieving high hydrogen utilisation in the GT26 is hindered by the reactive conditions in the SEV. This subsection explores publicly available information on the HE upgrade [152], deducing features and their potential to increase the GT26’s hydrogen capability.

#### Components Changes

1. Improved Liner Material: Efficiency gains in a combustion system demand a proportional rise in firing temperature. Assuming the pre-upgrade firing temperature was optimised for peak efficiency, any post-upgrade increase relies on enhanced combustor materials supporting higher temperatures. Which is likely to induce an increase in NOx emissions via the Zeldovich mechanism.
2. Changes to SEV Burner: As the EV burner elevates temperatures, the SEV transforms into a more reactive reheat environment. This results in an undesirable reduction in autoignition delay time. To mitigate this, enhancing gas flow velocity in the SEV might involve an upgrade, reducing cross-sectional

area to increase velocity (akin to 2006 to 2011 upgrades), aligning with mass conservation principles.

3. Fuel Lance Design: To prevent flashback, a fuel lance redesign is anticipated. Currently, radial injection ensures mixing within residence and autoignition delay time criteria. However, with reduced autoignition delay time using hydrogen-enriched fuels, similar to the SEV burner redesign, addressing fuel residence time is crucial. It is posited that this is achieved by injecting the fuel in the axial direction to the gas flow through the SEV burner.
4. Thermoacoustic Dampening: As temperatures and reactivity rise, thermoacoustic instability becomes more likely. To counter this, a “high frequency damping front panel” and a “low frequency damper” (depicted in Figure 2.5.11) are included. The high-frequency damper manages flame and acoustic fluctuations, preventing potential damage from their alignment. Lower frequencies, associated with lean conditions near blow-off, can lead to periodic flame extinction and reignition. Hydrogen’s flame stretching under lean conditions enhances turndown capability but may increase the risk of low-frequency oscillations. The frequency dampening systems are predicted to address these issues by absorbing pressure oscillations associated with the resonance frequency of the GT.

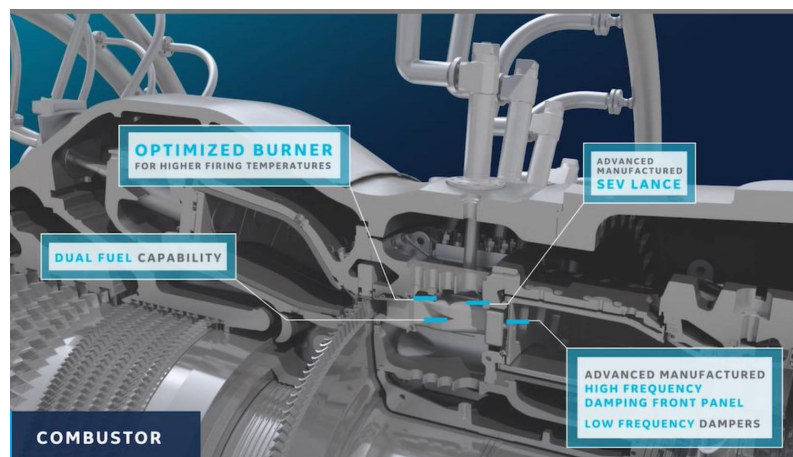


*Figure 2.5.11: Schematic of the inclusion of vibrations dampeners introduced as a part of the GT26 HE upgrade, reproduced from [152]*

Although the HE upgrade does not explicitly claim to enhance the GT26's hydrogen capacity, the described design changes could be effective in doing so.

The heightened firing temperature in the EV increases the reactivity of the SEV environment. Consequently, the aforementioned design alterations to the SEV burner and the SEV lance hold the potential to increase the range of hydrogen volumes operable in the GT26.

## 2.6 Hypothesis

Since limitations have been met with hydrogen capability of the GT26 when utilising the Wide C2+ logic in the SEV and that the EVs capacity to operate on hydrogen far surpasses current SEV capabilities, other means of improving the hydrogen capability of the GT26, or more specifically the SEV, should be investigated.

A design feature that is highly apparent in the SEV is the presence of the vortex generators that induce the mixing of the hot vitiated flow and the fresh fuel in the sequential stage. Hence, it is clear that turbulence and the mixing of the vitiated flow and fuel were key to the successful operation of the GT26. From the above literature review of GT26 relevant research, it is clear that further work is required to illuminate any possible design solutions for enabling high-hydrogen capability in the GT26. Hence, the following hypothesis has been devised:

*“What effect do turbulent characteristics have on the ignition of hydrogen enriched fuels under reheat combustion conditions?”*

The study by Poyyapakkam et al study [102] was particularly encouraging as it indicated that the geometry and turbulence characteristics are considered to effect the ignition of hydrogen enriched fuels, but lack of characterisation of the turbulence characteristics resulted in no development in the quantitative understanding of the affect of the turbulence on the ignition of hydrogen enriched fuels. This has in turn incurred a motivation to seek an understanding of the fundamental principle that is dictating the increase or decrease in the rate of the ignition reaction.

Hence, this thesis is focused on isolating the the phenomena of turbulent inhomogeneous autoignition, and investigating the effect of turbulence on the ignition of hydrogen enriched fuels.

The desired outcome is to acquire knowledge of a turbulent design parameter and its influence on the reactivity of the SEV environment to enable the realisation of high hydrogen use in the SEV, and therefore drive the hydrogen capability of the GT26 in its entirety.

## 2.7 Turbulent Autoignition Literature

As indicated above, a study investigating the relationship between the turbulent characteristics with the ignition behaviour of hydrogen-enriched fuels at reheat combustion conditions was pursued. The direction of this Literature Review now moves from direct GT26 research and its hydrogen capability to the relevant phenomenon under investigation to elucidate a path to higher hydrogen capability in the GT26, that being; the ignition of turbulent inhomogeneous fuel oxidant mixtures.

Through detailing the studies below, this Literature Review aims to provide an understanding of methodologies deployed and common findings, that may appear counter-intuitive at first. The analysis conducted aligns with the principles discussed in this review, albeit adapted to the context of the GT26, with the ultimate goal of increasing the GT26s hydrogen capabilities.

An extensive body of work has been produced by the Hopkins Laboratory at Cambridge University under the direction of Mastarakos and Markides that investigated experimentally the effect of turbulence on the autoignition of inhomogeneous fuel mixtures [88] [153] [154] [155]. Markides [88] offers a comprehensive account of the research conducted and the outcomes derived from a series of studies. It provides detailed information about the newly established experimental facility, as well as an extensive characterisation of the flow within the setup. Through characterisation of the flow field, the following turbulent characteristics were devaluated:

- Turbulence intensity, which accounts for the fluctuations in the measured value of velocity compared to the mean measured velocity and is calculated by:  

$$TI = \frac{u_{RMS}}{U_{mean}} \times 100\%.$$
- Integral Lengthscale which refers to the largest lengthscale of the turbulent flow i.e. the geometry of the largest vortex.
- Kolomogorov lengthscale, which refers to the smallest lengthscale of turbulence in the flow.

Within turbulent flows a range of lengthscales exist, however, the Integral lengthscale and the Kolmogorov lengthscale denote the extremities in the flow being evaluated. Turbulent theory describes how the vortices of an integral lengthscale transfer kinetic energy from the larger scale eddies to smaller scales via an energy cascade, which eventually leads to the dissipation at the Kolmogorov lengthscale, where the energy is converted to heat due to viscosity [156]. Whilst these properties of the flow are characterised, there is no offer of evaluating their impact since there is only a singular turbulence grid used in their analysis.

The book also details methods for measuring (i) autoignition frequency, (ii) autoignition length (the distance from the fuel nozzle to ignition events), and (iii) autoignition delay time (calculated by variations of  $\tau_{IDT} = \int \frac{L_{IGN}}{t} dt$ ) for various fuels investigated throughout the research campaign [88].

The four fuels tested were hydrogen, acetylene, ethylene and n-heptane. These studies showed that an increase in air temperature had a significant effect on the decrease of autoignition length and therefore a decrease in ignition delay time. It was also shown that as the levels of turbulence increased, so did the autoignition delay time (ADT). Thus, indicating that turbulence has an *inhibiting* effect for inhomogeneous mixtures. Much value is found in this body of work. However, the temperature conditions pertaining to this work were undertaken at temperatures far below that of a GT reheat combustor ranging from  $784K - 912K$  [157], hence its direct relevance is limited to the GT26. Of particular value from this work is

the extensive characterisation of the mixing field, which was performed through the planar laser induced fluorescence (PLIF) of acetone - this work was done at cold conditions using the principles of dynamic similarity scaling via the Reynolds number [88]. The discovery of this body of work was of great inspiration as it confirmed early iterations of the design considerations and experimental methodology of this doctoral project that was created in isolation.

The experimental studies performed at Cambridge was also included in a review paper undertaken by Mastarakos [157] that takes an extensive view of the ignition of turbulent non-premixed flames. It is highlighted that autoignition events typically occur away from stoichiometry at cases denoted as “most reactive mixture fraction” which are found in regions of low scalar dissipation within the turbulent flows [157].

The studies presented by Cabra et al. [158] and [159], stand as an early insight into mixture field characterisation relating to the autoignition of inhomogeneous mixtures. The primary objective of Cabra, et al. was to gain insights into the behaviour of mixture fraction when employing nitrogen-diluted hydrogen blends as observed in [158], followed by subsequent investigations involving methane, as outlined in [159]. The experimental apparatus employed for these investigations is detailed in Figure 2.7.1. Noteworthy operational parameters included a  $H_2$ /air vitiated co-flow, with co-flow velocities of approximately  $5.4m/s$  and fuel jet velocities reaching  $100m/s$ . This specific configuration was designed to facilitate mixing by shear effects generated by the velocity gradient induced by the relative velocities of the coflow and fuel jet.

These publications [158] [159] elaborate on the sensitivity of lifted flame height (LFH) to various conditions, including jet velocity, coflow velocity, and coflow temperature. They reveal a near linear relationship between LFH and each of these parameters, at least within the range studied. Notably, the LFH exhibited the highest sensitivity to changes in coflow temperature

At a similar time, Oldenhof et al. investigated the effect of the fuel jet’s Reynolds number on the LFH of various natural gas flames [160] [161]. It was shown that

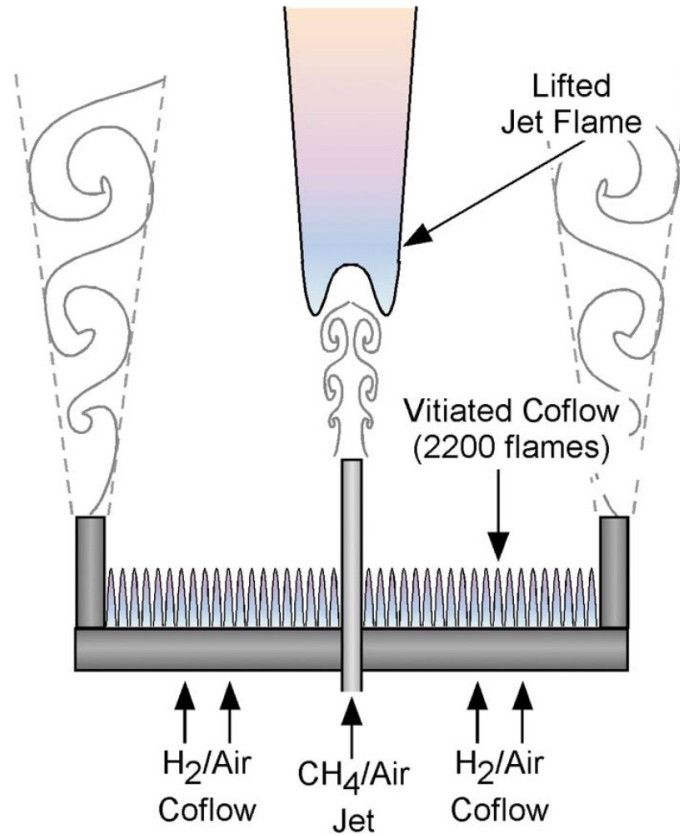


**Figure 2.7.1:** Schematic of test case of Cabra et al. experimental work, reproduced from [159]

the lift off height would increase at Reynolds number 3000-5000, suggesting that the high inertial forces are increasing mixing and maintaining strain rates below a critical number. Furthermore at a Reynolds number greater than 5000 indicated that the increased inertial forces have surpassed a critical point in which the turbulence is now having an inhibiting effect. This non-monotonic trend has been reconciled as the effect of enhanced entrainment of the hot coflow into the fuel jet due to the velocity gradient. Yet again, this is another study detailing the effect of turbulence of flame ignition and LFH's emphasising how its extensive study is required [160] [161].

Research conducted at Tsinghua University in Beijing, performed by Li et al. [162] and Liu et al. [163], has unveiled three distinct categories of autoignited flames. These categories encompass an attached flame, a lifted flame exhibiting reigniting spots, and a lifted flame, all of which are visually represented in Figure 2.7.2. The experimentation entailed the evaluation of fuels diluted with both  $N_2$  and

CO<sub>2</sub> across varying degrees of dilution. The findings indicated that the LFH was notably higher for CO<sub>2</sub>-diluted fuel blends. The experimental apparatus employed for this investigation featured a co-flow test rig equipped with a turbulence grid, as elaborated upon by Li et al. [162] and Liu et al. [163]. LFH measurements were acquired using a digital camera, and subsequent analysis was carried out in MATLAB to discern the flame edge. This analytical procedure closely adhered to the method outlined by Van et al. [164]. To further enhance the visualisation of flame structure, OH\* chemiluminescence data was collected as well.

The importance of developing understanding the flame stabilisation mechanisms for designing advanced combustors is considered crucial, hence, a numerical model is developed to assist in elucidating parameters associated with design [163]. It was found that there was poor-fitting of hydrogen LFH between experimentally derived data and from an existing mixing-strain model. Hence, adaptations to the model were performed, where the non-dimensional Damköhler and Karlovitz numbers were used to identify the flame stabilisation mechanism at play [163]. Damköhler and Karlovitz number's are described by the following equations:

$$Da = \frac{\textit{Mixing Timescale}}{\textit{Chemical Timescale}} = \frac{t_{mix}}{t_{chemical}} = \frac{1}{Ka} \quad (2.2)$$

Both Karlovitz and Damköhler numbers provide insights into the interplay between the interactions of the turbulence in the flow field and the rate of the chemical reaction. When Damköhler numbers are greater than unity, it signifies that the mixing of the fuel and oxidant outpace the rate of the chemical reaction. This observation highlights the dominance of turbulent mixing in governing the reaction rate. Conversely, Damköhler numbers of less than unity indicates that the chemical reactions occur more rapidly than the mixing of the fuel and the oxidant and is characterised as a chemistry-dominant regime. Since Karlovitz number is the inverse of Damköhler, the opposite is true for the conditions described above.

In this study [163] it was concluded that the sensitivity to turbulence was weak. This observation is ascribed to the method by which turbulence was induced, pri-



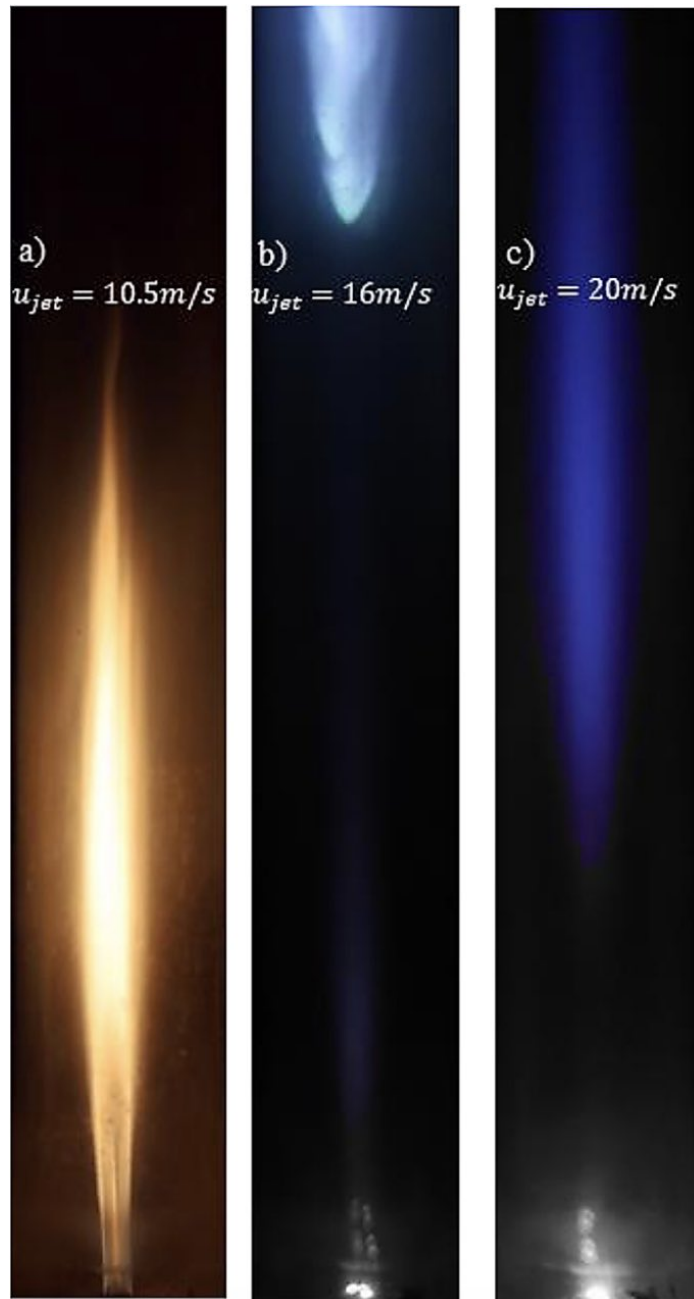


*Figure 2.7.2: Image of the three lifted flame types observable from Li et al. testing, reproduced from [162].*

marily through alterations in the hot air flow. These alterations predominantly affected turbulence intensity while exerting minimal influence on turbulent length scales. Consequently, it is postulated that adjustments to the turbulence grid geometry would introduce variations in turbulent length scales, thereby inducing a more pronounced impact on the ignition of lifted flames.

### 2.7.1 GT36 - Industrially Relevant Turbulent Autoignition

The CAPS lab at ETH Zurich have been investigating the ignition of autoignited flames in the context of the GT36 since 2018 through studies led by Schulz et al. [165] [166]. A modular sequential combustor has been used extensively to investigate various fuels blends, injector configurations and oxidants, as detailed by Solana-Perez et al. [167] [168] [169].

Where the GT26 and GT36 differ mostly is that the GT36 only has one turbine stage, as opposed to the GT26's HPT and LPT. In recent years, there has been more depth of research pertaining to the GT36, as opposed to the GT26, as a result of Ansaldo Energia's focus on the GT36. Notably, there may be an attraction to operating the GT36 with higher hydrogen as the sequential combustor is still at the elevated pressure conditions of the first stage, unlike the GT26. Hence, the non-monotonic trend of hydrogen's reactivity under pressure may play kindly to the operators desire for high hydrogen realisation in the GT36. A series of studies conducted at ETH Zurich encompassed a combination of experimental work undertaken by Solana-Perez et al. [167] [168] [169] and numerical modelling by Schulz et al. [166] [165].

The initial study led by Schulz [165] investigated the effect of thermoacoustic instabilities through means of a Large Eddy Simulation and experimentation. The combustion model as it relates to the sequential combustor accounted for different combustor modes, (ambient and elevated temperature propagation and autoignition) and included semi-detailed chemistry in the model. The model was compared to hydroxide planer laser induced fluorescence (OH-PLIF), OH\* chemiluminescence and acoustic pressure measurements. The goal of the study was to capture the thermoacoustic instabilities observed experimentally and account for them in the CFD model [165].

The subsequent numerical study [166] identified that 3 sequential flames coexist (1) autoignition (2) flame propagation (3) flame propagation assisted by autoignition. This work indicated the heavily reliance on the recirculation zones for the

stable operation of propagating flames. Whereas autoignited flames only required continuous self-ignition to sustain combustion. This work laid the foundations for further depth of study to the realisation of hydrogen combustion in the GT36.

Experimental work was continued by Solana-Perez et al. by investigating the effect of introducing increasing hydrogen content as a jet in cross flow injection, into a vitiated flow from a first stage combustor (burning NG in air, fully premixed,  $ER = 0.7$ ) [167]. The study showed how increasing the hydrogen content of the flame decreased the flame length significantly. It's region of  $\text{OH}\cdot$  intensity was also closer to the nozzle, although the displayed iso-contour map indicates that the intensity of  $\text{OH}\cdot$  signal declines with increasing hydrogen content. The threshold for flame edge detection was given as 30% of the maximum  $\text{OH}\cdot$  signal intensity, as is displayed in the relevant figures within the study [167].

Additional experimental work performed by Solana-Perez et al. [168] [169] was performed, where the fuel injection method develops to consider fuel inlet configurations and its effect on mixing and flame morphology. Despite the expressed interest in investigating the behaviour of pure hydrogen fuel under reheat conditions, the vitiated flow generated from the first-stage combustor employed natural gas as a fuel source. Using natural gas in the initial stage produced a vitiated gas flow that does not accurately represent the vitiated flow resulting from the use of hydrogen in the first stage. This discrepancy in flue gas composition may significantly impact mixing quality due to differing physical properties under these conditions and alter flame morphology due to changes in the composition of the flue gas.

Nevertheless, it is noteworthy that this study made commendable efforts to establish industrial relevance for the GT36. These efforts included the incorporation of vortex generators into the rig design, maintaining a constant rig exit temperature across various test points during operation, incorporating a backward-facing step to stabilise the flame, and introducing dilution air following the first-stage combustion [168] [169].

The findings of this study [168] demonstrated that the two tested inlet configu-

rations, which induced different flow regimes (as depicted in Figure 2.7.3), yielded insightful results. Specifically, excellent mixing was associated with reduced NOx emissions, while suboptimal mixing exhibited a more robust flame anchoring characteristic [168].

The other study [169] undertaken described the flame stabilisation regimes were identified under various points of steady operation. The study also validated various temperature measurement techniques, that further supported the use of a 0-D reactor simulation. Interestingly the 0-D reactor showed that there was not a significant impact upon the dominant flame regime in the sequential flame when using hydrogen as the first stage fuel [169]. This assertion requires experimental validation.

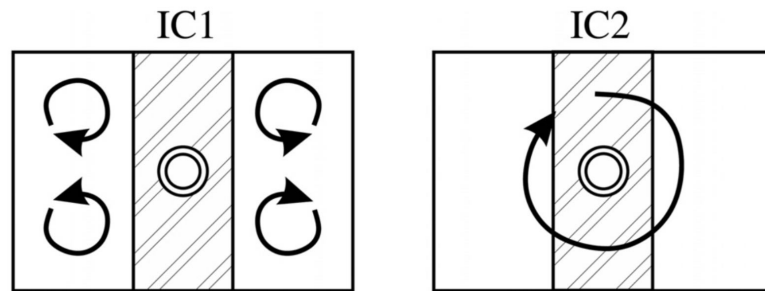


*Figure 2.7.3: Schematic of mixing patterns induced for the two inlet configurations (IC) utilised in works undertaken at ETH Zurich's CAPS lab, reproduced from [168].*

## 2.8 Literature Review Conclusion

This thesis occupies a unique position in the current literature, bridging the gap between the GT26 reheat combustion testing detailed in Section 2.5.4 and the research on turbulent inhomogeneities described in Section 2.7. This research will extend upon the fundamental laboratory-based experimentation discussed in Section 2.7 by working with elevated temperatures and utilising relevant CH<sub>4</sub>/H<sub>2</sub> fuel blends of interest to operators, designers and researchers of the GT26 Gas Turbine. The findings of this work will be valuable for SEV combustion investigations, contributing to the knowledge developed through the studies in Section 2.5.4.

### 2.8.1 Project Objectives

To achieve the stated Project Aim in Section 1.7.2, the following objects are pursued:

- An experimental test campaign will be devised to evaluate the impact of turbulence of fuel blends with varying hydrogen concentrations. In regards to turbulence, interest lied with the impact of Turbulence Intensity and Turbulent Lengthscales, as they were merely characterised in a small proportion of the works reviewed in the literature search. This project aimed to assess the impact of varying such variables.
- A new test facility is to be designed, manufactured and commissioned to enable the experimental evaluation of the above point.
- A suite of non-intrusive diagnostic techniques will be developed to enable appropriate measurements to address the stated hypothesis in Section 2.6. Measurements of Lifted Flame Height and a novel parameter called Flame Establishment Time were undertaken. This further supported the calculation of Ignition Delay Time and Damköhler. All four parameters and how they are evaluated is introduced in Chapter 4.
- Data analysis will be performed following the data acquisition to determine the impact of turbulence and hydrogen concentration on these variables.
- Temperature effects will also considered experimental to assess the impact of changing operating conditions on the parameters considered.
- CFD analysis will also be performed to enhance the understanding of the findings elucidated during the experimental campaign.

# Chapter 3

## Design and Commissioning of Novel High Temperature Inhomogeneous Mixture Autoignition Facility.

In this Chapter, the design process of the Turbulent Inhomogeneous Mixture Autoignition Rig (TIMAR) is presented followed by a description of its commissioning. Initially, the essential criteria and their manifestations are described. Subsequently, design choices related to the TIMAR's fundamental aspects are delineated, which has led to its current configuration. Additionally, the auxiliary components and their respective designs are presented. When relevant, the Chapter describes design calculations, the reasoning behind material selection, and other pertinent details.

Furthermore, a description of the commissioning of the TIMAR is presented, describing the operation of the TIMAR. The functionality of the TIMAR holds significance importance, as it forms the foundation upon which the experimental philosophy is developed to test the hypothesis of this thesis. Hence, the commissioning outcomes influence the methodologies adopted in conducting the experimental work.

## 3.1 Essential Criteria of Design

In the pursuit of emulating the operational conditions observed in the GT26 SEV, certain criteria were requisite. Foremost among these criteria was the need to attain elevated temperatures to ensure fuel autoignition. Given the SEVs operation as a flow-through burner, a similar principle was adopted for the TIMAR. As the hypothesis aims to assess the impact of turbulence on the ignition of hydrogen-enriched fuels, the controlled variation of turbulence characteristics emerged as an essential requirement.

Given the non-intrusive nature of the diagnostic methodologies employed to evaluate parameters such as the Lifted Flame Height (LFH) and Flame Establishment Time (FET), the inclusion of optical access was imperative. The working fluid within the GT26 SEV is a vitiated high-temperature flow from the primary stage, with secondary fuel injection into the vitiated flow. Therefore, considerations were made in generating representative gas mixtures akin to the operational environment of the GT26 SEV, in the design of the TIMAR.

### 3.1.1 Flow through Rig

Due to the project sponsor and previous site experience with the GT26, details regarding geometry and engine parameters are known. This enabled the scaling of flows from the GT26 to the TIMAR designed for testing at Cardiff University's Gas Turbine Research Centre (GTRC), which is described herein.

Considering conservation of mass through the GT26, it was necessary to begin calculations at the first stage EV combustor. Hence, the power output of the GT26 engine was established [130], and an equitable power distribution between the EV and the SEV combustors was assumed as reported by Güthe et al. [129]. Given the annular arrangement of 24 combustor cans within the GTs structure, the power allocation per combustor was derived. Furthermore, estimations of the equivalence ratio (ER) were performed through use of plant data including compressor flows,

cooling air requirements, and fuel mass flow rates.

Knowing the total cooling air requirements and the compressor’s air output facilitated determining the available air for combustion in the EV stage. This allowed establishing the required air-to-fuel ratio for a standard natural gas blend at RWE’s Pembroke site, as detailed in Table 3.1. The analysis resulted in an estimated ER of 0.55, where estimation considered specific locations of air inlets into the EV combustor.

While the global ER within the EV combustor is around 0.3, it’s crucial to acknowledge that a significant portion of the introduced cooling air is not localised near the flame and doesn’t contribute to its local ER. Additionally, under Lean Premixed (LPM) conditions, a natural gas flame operating at an ER of 0.3 is likely to have surpassed the lean blow-off threshold. Hence, an ER of 0.55 was utilised in the design. Using a calculated lower heating value for the described natural gas blend, detailed in Table 3.1 below, the volumetric flow rate of fuel for each individual combustor was determined.

**Table 3.1:** *Typical Natural Gas Fuel Blend composition operated at RWE’s Pembroke Power Station*

Constituent	CH <sub>4</sub>	C <sub>2</sub> H <sub>6</sub>	C <sub>3</sub> H <sub>8</sub>	N <sub>2</sub>
[% vol]	95.2	4.0	0.2	0.6

This resulted in determining the fuel and air flow rates for the entire engine and on a per-can basis. Knowing the SEVs geometry and the calculated flow rates, an estimated SEV burner inlet velocity of approximately 125m/s and a throat velocity of 157m/s within the SEV were calculated. This throat velocity serves as a benchmark, aligning with the gas flow velocity of approximately 150m/s in DLR Stuttgart’s reheat combustion rig [151] — a test rig developed to operate under conditions akin to the GT26. This alignment instilled a high degree of confidence in the design calculations.

As an initial design point for the TIMAR it was first considered that a first stage combustor would be used to provide the hot vitiated flow required for the attainment



of reheat combustion conditions, similar to approaches take by Fleck et al. [146] [147][148] [149] [150] [151] and Solana-Perez et al. [168] [169]. The air-fuel ratios calculated from the operation of the GT26 were considered for use in the Generic Swirl Burner (GSB) operational at the GTRC, targeting a max power output from the first stage of 200kW. The necessary equivalent flows indicated that a reheat combustion zone or ‘mixing-duct’ was to have a cross sectional area of  $0.000625m^2$ .

### **3.1.2 Optical Access**

As detailed in Section 3.1, optical access to the reheat combustion zone was necessary to undertake non-intrusive diagnostics of the flame. Since the diagnostic techniques being used require the use of lasers and the refraction of light would ideally be minimised, a square mixing duct (MD) was decided upon. Considering the cross-sectional area determined above, a  $25mm \times 25mm$  square tube was decided upon.

### **3.1.3 Change in Turbulence**

In order to test the hypothesis stated in Section 2.6, there must be a means of altering the turbulence characteristics within the fluid flow. Hence, a modular design of the TIMAR was incorporated to enable interchangeable turbulence devices to provide variation in the turbulence characteristics of the flow.

## **3.2 Design Decisions**

In this section, design decisions are detailed alongside supporting engineering calculations. Each major component of the TIMAR will be discussed and calculations will be detailed where necessary. A General Assembly drawing is provided in Figure A.0.1 found in Appendix A, to provide a point of reference for the components that are specified in this section.

### 3.2.1 Air Heater vs GSB

As described above, it was initially considered that the hot vitiated flow would be supplied by the Generic Swirl Burner (GSB) that is frequently operated at the GTRC. The GSB, is a first stage premixed combustor that is modelled upon a commonplace industrial GT burner. The GSB was commissioned during Runyon's PhD project [113] and has been used extensively at the GTRC since, supporting a number of studies [170] [171] [172].

Despite the extensive knowledge and operational experience in-house regarding the GSB and its capability to produce the desired flue gas compositions, including the relevant intermediates and free radicals, it became apparent there were obstacles in its deployment in the context of this study. Therefore, rendering it unfavourable for use in the the TIMAR configuration. At this point in the design it was considered that equal flow fields and thermal power between the fuel blends was to be maintained (more detail on this philosophy in Section 4.1.1). If the same thermal power was desired in the first stage combustor across the fuel blends under consideration (100/0 [%vol] CH<sub>4</sub>/H<sub>2</sub> through to 0/100 [%vol] CH<sub>4</sub>/H<sub>2</sub>), the flow rates for each fuel blend or test case would vary widely, as detailed in Table 3.2 below. Hence, maintaining a comparable flow field between the fuel blends tested would not be feasible when the GSB is being used.

This resulted in the decision to pursue the use of an electric air heater. Through using an electric air heater, a synthesised oxidant representative of the flue gas from the EV combustor would be derived. The composition of the synthesised oxidants needed to be determined, the methodology is introduced in Section D.5.2.

**Table 3.2:** Gas flow in the MD calculations for equal Power and ER from GSB.

CH4 [%vol]	H2 [%vol]	Power [kW]	ER [-]	Stoichiometric Air Fuel Ratio	Air mass Flow [g/s]	Fuel Mass flow [g/s]	MD Velocity [m/s]
100%	0%	41	0.6	17.19	23.50	0.82	129.20
90%	10%	41	0.6	17.40	20.61	0.72	113.34
80%	20%	41	0.6	18.23	18.45	0.64	100.94
70%	30%	41	0.6	18.03	16.54	0.58	90.99
60%	40%	41	0.6	18.48	15.06	0.53	82.82
50%	50%	41	0.6	19.07	13.82	0.48	76.00
40%	60%	41	0.6	19.87	12.77	0.45	70.22
30%	70%	41	0.6	21.04	11.87	0.41	65.26
20%	80%	41	0.6	22.88	11.08	0.39	60.95
10%	90%	41	0.6	26.25	10.40	0.36	57.17
0%	100%	41	0.6	34.32	9.79	0.34	53.84

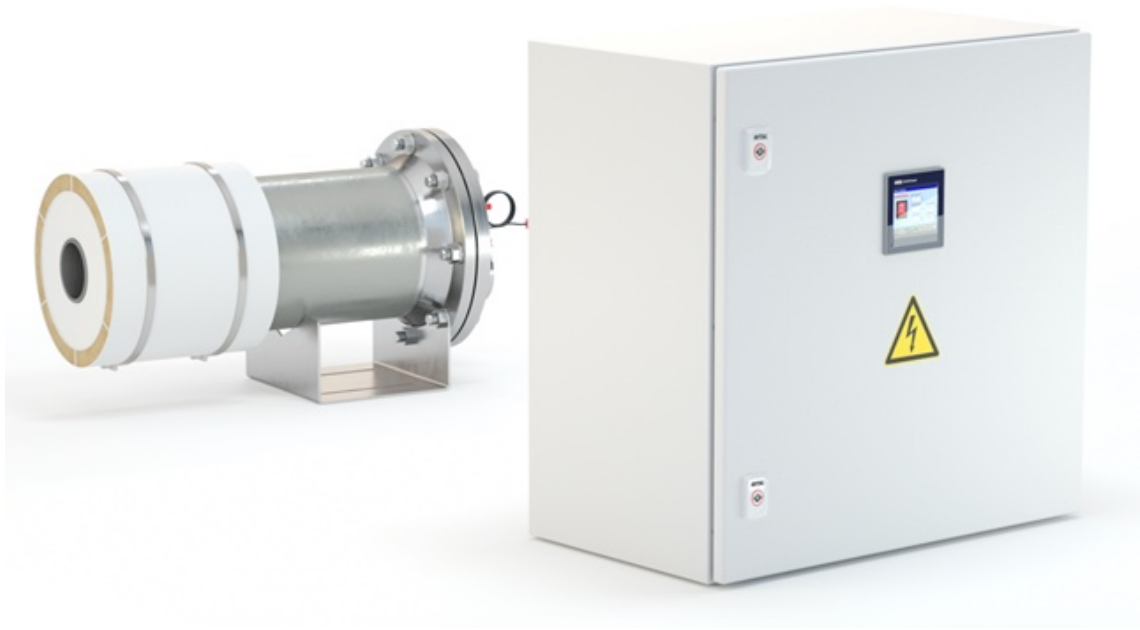


*Figure 3.2.1: Kanthal heater and corresponding control unit, image reproduced from [173].*

### 3.2.2 Electric Air Heater Detail

Following a tender process, Kanthal's 30 kW Flow Air Heater (KFH-2-30-400) and its accompanying control unit (CC-KFH-2-30-400-CE), depicted in Figure 3.2.1, was purchased. This heater was selected due to its superior ability to achieve elevated temperatures compared to competitors. The 30kW option was selected due to its operational range of flows i.e.  $\dot{m}_{min} = 4.53g/s$  to  $\dot{m}_{max} = 45.28g/s$  covering the range of flows of interest in the TIMAR. At the heater's nominal flow an air flow velocity within the  $25mm \times 25mm$  MD of ca.  $140m/s$  was determined.

### 3.2.3 Fuel Delivery

The following means of fuel delivery were considered for the design of the TIMAR:

- Jet-In-Cross-Flow
- Radial Injection
- Co-flow Axial Injection

From the literature review, it was shown that a Jet-In-Cross-Flow had been considered for study at DLR Stuttgart [151] and CAPS lab in ETH Zurich [167], with the former citing its choice of fuel injection as a crude representation of one (out of four) of the fuel/air injection points found in the standard SEV fuel lance design. However, these studies quickly built upon these initial fuel injection methodologies to include axial fuel delivery, which is more in-keeping with the direction fuel injection architecture of the GT26 will take with highly reactive fuels, as stipulated by the prototype design developed by Poyyapakkam et al [102].

For the TIMAR design, the decision was made to incorporate fuel injection via a co-flow axial injector, despite the GT26 operating a radially injected fuel delivery system in the SEV. This choice was influenced by the complexity of the SEV fuel delivery system, which involves carrier air and introduces numerous variables when employing a jet-in-cross-flow fuel delivery. Considerations such as jet penetration depth, orifice diameter, and the potential for uneven heat distribution in the MD prompted the decision. Therefore, to maintain flow field symmetry, a co-flow axial injection of the fuel into the hot oxidant was chosen.

In addition, this design decision was reinforced by the similar designs employed by the Hopkins Lab at Cambridge in their turbulent autoignition studies [88] and by Li et al. [162] in their investigation into flame lift off height. Schematics of the designs from both campaigns are presented below, where the commonalities are clear.

The main features of the TIMAR had been developed independently of these studies. It was reassuring that the initial design iterations of the TIMAR were consistent with the literature.

### **3.2.4 Turbulence Devices**

Three turbulence devices (TDV) were selected for use within the test campaign. These TDVs were designed with modularity in mind to enable interchangeability between experimental tests. Table 3.3 details the geometry of the TDVs, including

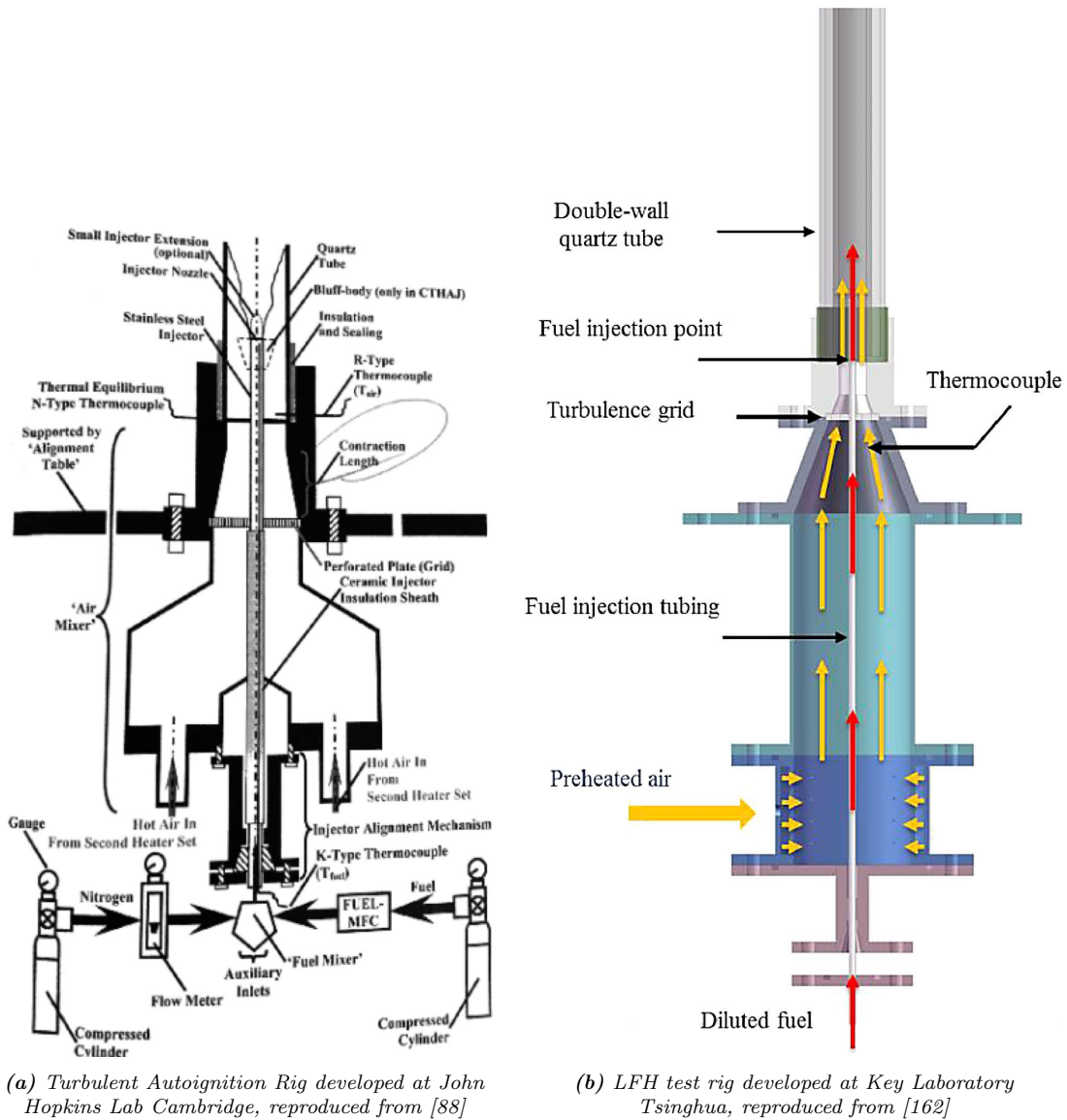


**Figure 3.2.2:** Schematics of respective test rigs, detailed by their caption.

the flow blockage ratio. The blockage ratios were selected to be within a relatively close range of one another with the aim of having a similar impact to the velocity in TIMAR as a result of the near-equitable reduction of the cross sectional area as whilst being mindful of manufacturing capabilities (i.e. standard drill sizes), yet will exhibit vastly different turbulence characteristics due to differences in geometry. Figure 3.2.3 below shows adapted versions of the technical drawings that illustrates the designs of the TDVs. The full technical drawings are found in Figure's A.0.2, A.0.3 and A.0.4 in Appendix A, reproduces the technical drawing supplied to the manufacturer. Each have the same design philosophy but differ primarily in terms of hole diameters and number of holes.

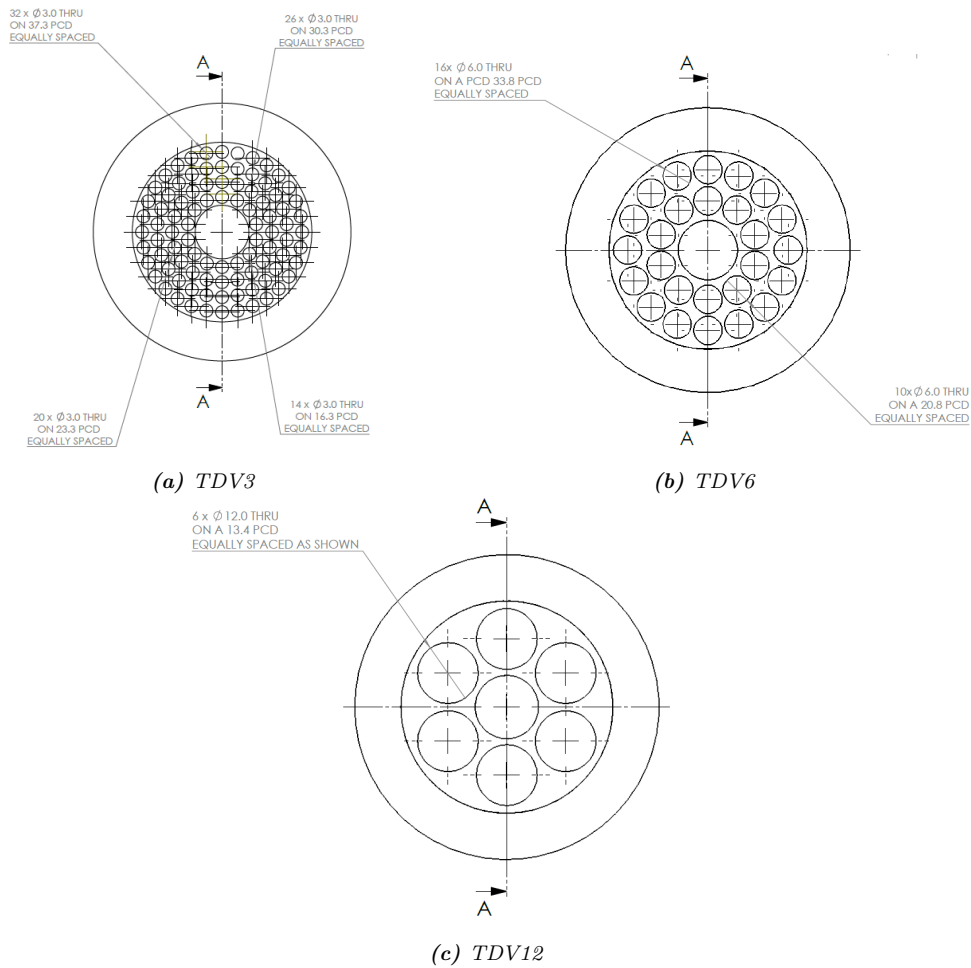


**Figure 3.2.3:** Adapted technical drawings illustrating the design of the three TDVs designed for the purposes of this doctoral project.

**Table 3.3:** Design details regarding the 3 interchangeable TDVs designed for their use in the TIMAR.

TDV	Characteristic Diameter [mm]	Number of Holes	Blockage Ratio
TDV3	3	92	47.40%
TDV6	6	26	53.58%
TDV12	12	6	49.46%

When designing the TDVs, a crucial consideration was the material choice of Inconel 625. This decision stemmed from the need for a dissimilar metal to interface with the transition piece, aiming to prevent the components from fusing together under elevated temperature conditions and thermal stress. The selection of Inconel for the TDVs, as opposed to the transition piece, was also based on the challenges as-

sociated with machining Inconel compared to stainless steels, as well as the differing sizes and machining requirements of the respective components.

## 3.3 Ancillary Components

In this section, ancillary components for the TIMAR are described.

### 3.3.1 Fuel Delivery

As indicated in Section 3.2.3, the chosen fuel delivery method for the TIMAR is co-flow axial injection. A description of both the fuel lance design and the fuel-steam flange (FSF-01) is found below.

#### 3.3.1.1 Fuel Lance

To maintain a consistent flame power and fuel velocity across various fuel blends, a parametric study was conducted to determine the optimum geometries for each test case.

The parametric study included the following:

- Fixing the fuel lance diameter: This study involved maintaining the fuel lance diameter constant while varying the mass flow rate of fuel to assess its impact on the fuel jet velocity and to determine the corresponding thermal power with that fuel flow rate. The aim was to determine what the thermal power of the various fuel blends would be whilst aiming to maintain constant velocity across the fuel blends considered.
- Fixing the thermal power: In this scenario, the thermal power remained constant (and therefore the fuel mass flow) while the fuel lance diameter was adjusted to observe its influence on the fuel jet velocity.
- Maintaining Fuel Jet Velocity: The fuel jet velocity was maintained at  $150\text{m/s}$  and alterations were made to the fuel lance diameter and fuel mass flow, ob-



serving its effect on thermal power and the determination of suitable fuel lance diameters.

The initial fuel calculations assumed ambient temperature conditions, introducing uncertainty that subsequent efforts aim to mitigate, as detailed in Section's 3.4.1 and 3.4.2.

This parametric study revealed the complexity of maintaining constant flow conditions across hydrocarbon-hydrogen fuel blends. Consequently, a thermal power of 36.5 kW was chosen, using three fuel lances with diameters of 3.00 mm, 3.6 mm, and 5.5 mm. This decision was guided by the calculated fuel velocity exhibiting the smallest percentage difference for the considered fuel blends compared to the target fuel jet velocity of  $150\text{m/s}$ . This decision was later revised based on outcomes from the commissioning phase.

Machining challenges arose in drilling the central hole of the  $250\text{mm}$  fuel lances due to their relatively small diameters (3mm, 3.6mm, and 5.5mm). A proposed solution involved cutting the rod into three lengths, drilling the fuel gas path, and welding the pieces back together. Additional design features included an M8 fine thread at the lance's bottom, a reduced cross-sectional area at the end, and flats on the external surface for spanner fitting.

Initially, Inconel 625 was considered for the fuel lance material so that dissimilar metals interfaced under elevated temperatures. However, challenges with the machining of the TDV's prompted 314 stainless steel to be chosen. This choice balanced thermal protection under elevated temperatures with practical advantages in ease and cost-effective manufacturing. Fig A.0.5 displays a drawing from the manufacturer, Metal Fabrication Co., illustrating the described manufacturing process.

### **3.3.1.2 Fuel-Steam Flange**

To introduce the fuel into the TIMAR and for the fuel to be injected in an axial direction, a dedicated fuel-steam flange (FSF-01) was designed. The fuel would be introduced into the rig via 4 equidistant tubes that entered the TIMAR via the

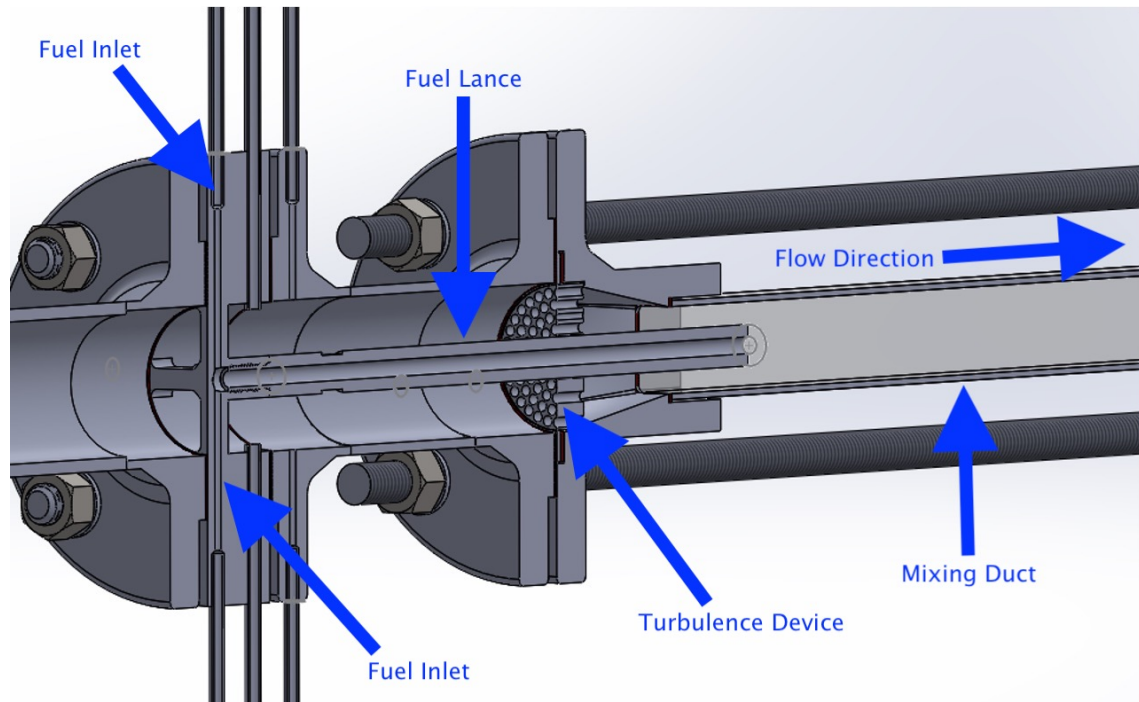


*Figure 3.3.1: Section view of CAD schematic depicting how the FSF-01, fuel lance and turbulence device interact with one another.*

fuel labyrinths within the flange where they would converge at a central point. The central point had a threaded section in which the fuel lance would be fitted, enabling the fuel to be injected into the turbulent flow downstream of the turbulence device. This design is illustrated by Figure 3.3.1. The fuel lance was sufficiently long to enable the fuel flow within to become fully developed (i.e.  $> 10D$ ).

### 3.3.2 Steam Injection

To produce synthesised oxidants it was necessary to include water or steam into the oxidant mixture to represent the flue gas from the EV combustor in the GT26. However, the introduction of water into the heater would have caused irreparable damage to the heating elements within the heater. Hence, the TIMAR was designed so that steam would be introduced downstream of the heater and upstream of the TDV so that the steam will mix effectively with the rest of the flue gas.

Therefore, additional tubes were added to FSF01 for the introduction of steam into the oxidant mixture. In the technical drawing illustrated in Figure A.0.6, the steam tube is positioned downstream of the fuel delivery labyrinths, where turbu-

lence will be introduced as a result of the labyrinths. The steam tubes also protrude 0.8mm into the flow. This was to account for the boundary layer height which the steam would now evade and mitigate the steam flow being entrained in the low flow region close to the wall. This was calculated through determining the Reynolds number and using the following equation to determine the boundary layer thickness, which accounts for turbulent flows of  $Re > 5 \times 10^5$ , over a flat plate:

$$\delta_T = \frac{0.37x}{Re^{0.2}} \quad (3.1)$$

where, the characteristic length in the consideration of Reynolds number is the internal diameter of TIMAR.

### 3.3.3 Transition Piece

The transition piece (TRN) played a pivotal role in the TIMAR system as it served as the interface for reducing the cross-sectional area from the rig upstream of the TDV to that of the MD. Its two primary functions were to accommodate the TDV for imparting turbulence to the flow and to house the quartz tube. During manufacturing, a notable challenge emerged in transitioning from the circular geometric profile of the rig upstream of the TDV to the square geometric profile of the MD. This obstacle was successfully addressed through the application of spark-erosion manufacturing techniques, enabling the production of unique and traditionally challenging geometries with ease.

Figure 3.3.2 depicts not only how the TDV sits within the TRN, but also how the quartz tube interfaces with the TRN. Not shown in this figure is the change in geometry in relation to the quartz tube seat. During commissioning, it was identified that the quartz tube was susceptible to damage despite the use of bespoke ceramic paper gaskets to prevent metal on quartz material interactions. Considering the expense and lead times associated with the quartz tubes, the TRN was adapted to then house bespoke graphite seats to act as the interface between the quartz and the

stainless steel (314) TRN. Since the tensile strength of the graphite was less than that of both the quartz and the TRN, the graphite became the sacrificial component and thus provided protection to the quartz tube, extending its operational life.

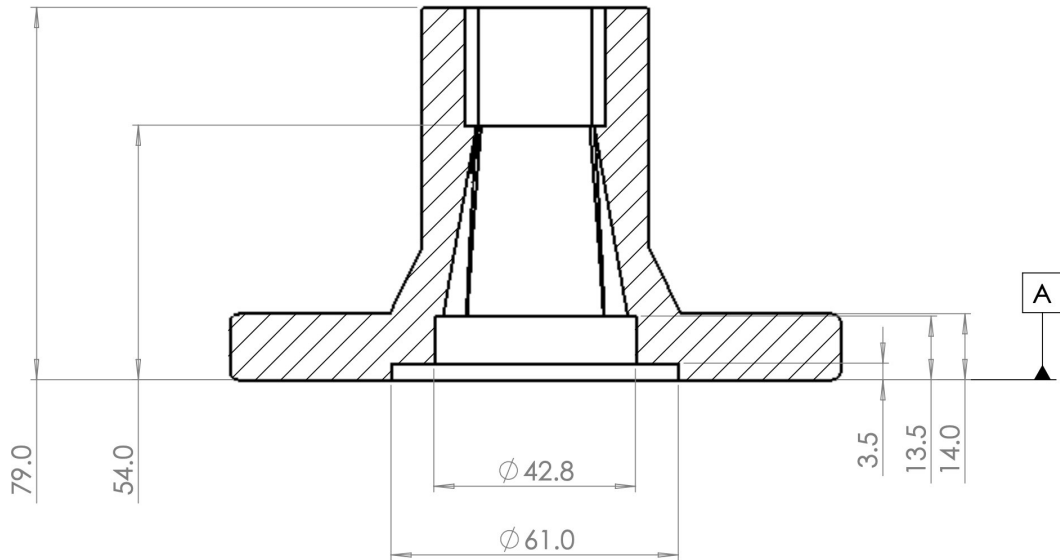


*Figure 3.3.2: Section View of Transition Piece reproduced from technical drawing, denoting its key geometric features.*

### 3.3.4 Quartz tube

In the design of the TIMAR, optical access to the flame was achieved through the use of Fused Quartz tubes. Specifically, Momentive Performance Material GE214 was chosen for its exceptional purity, which contributed to superior thermal stability, including resistance to thermal shock. Moreover, it boasted high optical transmissivity, as illustrated in Figure 3.3.3. Figure 3.3.3 describes the transmissivity of a 1mm sample. To adjust for different materials thicknesses the following equation can be deployed:

$$T = (1 - R)^2 e^{-at} \quad (3.2)$$

Where  $T$  is percent transmission,  $R$  is surface reflection loss for one surface,  $a$  is absorption coefficient [ $cm^{-1}$ ] and  $t$  is thickness [ $cm$ ]. Wavelengths of interest were 310nm and 525nm, in accordance with  $OH^*$  and laser light reflections related to the

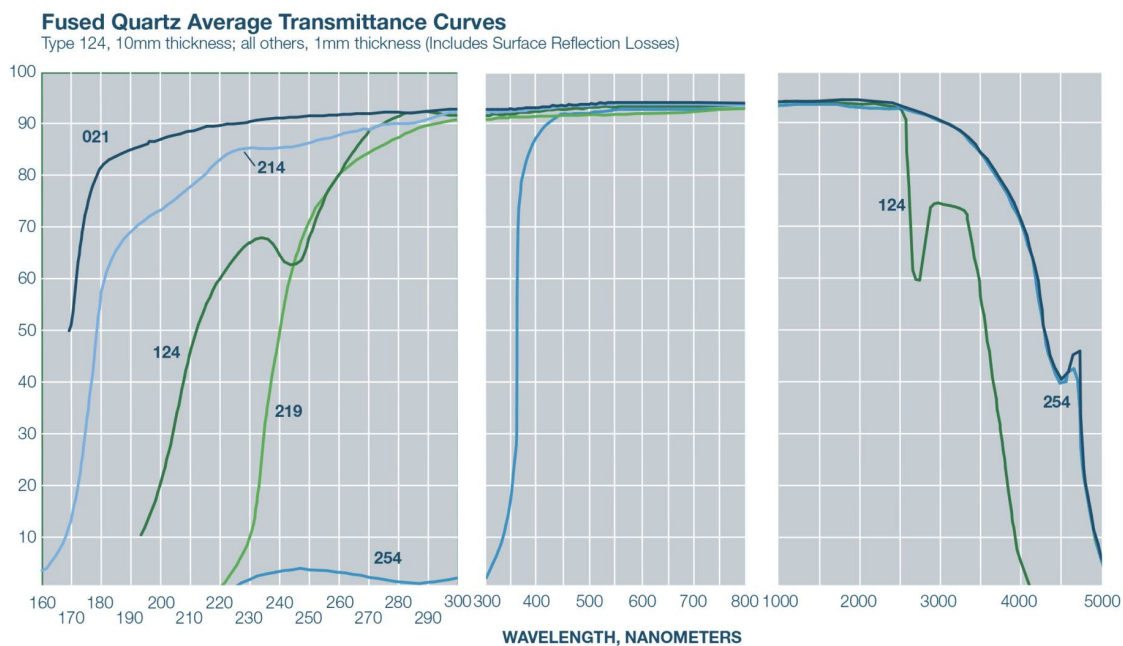


**Figure 3.3.3:** Transmissivity of Fused Quartz materials, 214 denotes the material used in the TIMAR. All values are absolute for a material thickness of 1mm, reproduced from [174].

OH· chemiluminescence and PIV analysis that will be introduced in Chapter 4.

In addition, borosilicate tubes were used during the commissioning stages of the TIMAR. This choice was motivated by cost-effectiveness and significantly shorter lead times, ensuring that any damage to these tubes during commissioning would not result in project delays or increased costs. It is important to highlight that borosilicate's optical transmissivity is inferior to that of Fused Quartz, limiting its use exclusively to the commissioning phase. It became evident that borosilicate's thermal stability would not suffice, as will be reported in Section 3.6.2.

To determine the length of the MD, a series of CHEMKIN simulations were performed, encompassing a range of anticipated operational conditions for the TIMAR. Among these scenarios, the least reactive case involved testing a pure methane flame. The Closed Homogeneous Reactor tool within CHEMKIN facilitated the analysis of ignition delay times. The marker used for the determination of ignition delay time was the determination of the time taken to reach peak temperature, related to methane under experimentally relevant conditions ( $T=1100\text{K} - 1400\text{K}$ , and an ER range of 0.3-1.5)), as depicted in Figure 3.3.4. For the purposes of evaluating the ignition delay time, GRIMECH 3.0 is used throughout [175]. The 1350K results

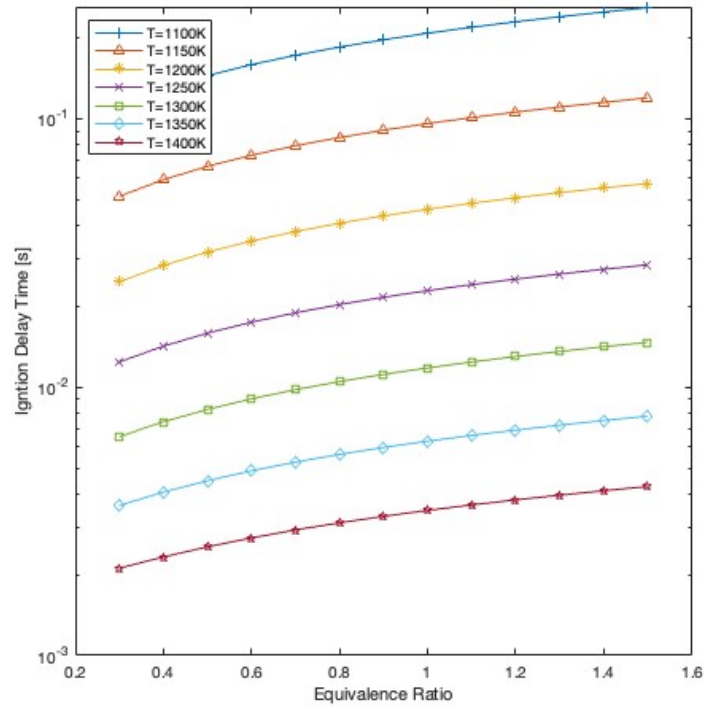


**Figure 3.3.4:** Results of CHEMKIN simulation of ignition delay time for pure methane at atmospheric pressure and elevated temperatures.

were focussed on in the analysis, as the project was initially operating on the assumption of rig temperatures near a maximum temperature of 1100°C due to a lack of information regarding rig heat loss.

Following the determination of the ignition delay time and prior estimations of flow velocities in the MD, an estimated distance between the point of fuel injection and the point of flame ignition in the MD was determined. It was shown that a distance of between 0.54m-1.17m was likely for the pure methane case.

Based on this analysis, the length of the tube was set to 0.6m. Whilst this length was shorter than that determined by the largest of the estimating calculations described above, this was a conscious decision, that was attributed to the idealised setting in which CHEMKIN operates, failing to account for the acceleration of the ignition event resulting from turbulence-chemistry interactions. Additionally, space limitations within the GTRC played a role in this decision.

In summary, a fused quartz tube of a square cross section area of 25mmx25mm, nominal wall thickness of 1.75mm and length was 0.6m was selected.

### 3.3.5 Insulation

Due to the elevated temperatures achievable by the electric air heater, and the temperature gradient between the hot air and the ambient environment, heat loss was likely to be prominent. Since temperatures greater than 900°C were desired to replicate the elevated temperature conditions of the GT26, it was necessary to insulate the test rig as far as reasonably practicable. Hence, the TIMAR was insulated in a Calcium-Magnesium Silicate thermal blanket that offered heat insulation at a continuous temperature of 1150°C and a thermal resistivity ranging from 0.04 – 0.48W/mK. No further detail on the range of thermal resistivities is provided by the supplier.

## 3.4 Instrumentation

The instrumentation protocol was intentionally simplistic with the primary objective being the mitigation of failures due to the elevated temperatures experienced in the TIMAR. K-type thermocouples were positioned in the TIMAR, as denoted by Figure ?? below. Type K thermocouples were selected due to their ability to operate continuously at 1,100°C ( $\pm 0.4\%$  of measured value) which coincides with the max temperatures attainable by the

### 3.4.1 Oxidant Flow Temperature Measurement

Thermocouples 1 and 2 were fed through the additional instrumentation tubes that were fitted to the assembly flanges, secured into place using Swagelok fittings. The thermocouples were placed perpendicularly to the direction of the flow. Hence, a thermocouple correction was performed to determine the real gas temperature value. This necessitated the development of an algorithm, detailed by B.1.2.01 in Appendix B.5.2 to determine the real gas temperature, which took the following steps:

1. Oxidant flow was inputted by the user.
2. The oxidant type was determined through selecting either air or flue gas. If

flue is selected, the oxidant composition is then determined by the fuel blend under investigation in any given case.

3. The heat supplied to the oxidant is determined through  $Q = \dot{m}_{oxi}C_{p_{oxi}}\Delta T$ . Where  $\Delta T$  is determined as the difference between ambient temperature and the measured value of temperature in the TIMAR.
4. Oxidant properties are determined from inputted conditions and use of lookup tables.
5. The heat transfer coefficient is determined, which required the determination of the oxidants dynamic viscosity, heat capacity and thermal conductivity (equations provided below).
6. Reynolds and Prandtl numbers were calculated and used in the Nusselt number correlation described below.
7. The heat transfer coefficient was calculated and used in a heat balance equation that was rearranged to return an iteration of the real gas value.
8. Steps 4 - 7 were repeated until convergence criteria of  $T_{iter} - T_{iter+1} < 0.000001$  was achieved.

The dynamic viscosity was determined through use of Sutherland's formula [176]. It is an approximation for how temperature affects the viscosity of gases by considering the intermolecular force potential. The equations used are as follows:

$$\mu = \mu_0 \frac{a}{b} \left( \frac{T}{T_0} \right)^{\frac{3}{2}} \quad (3.3)$$

$$a = 0.555T_0 + C \quad (3.4)$$

$$b = 0.555T + C \quad (3.5)$$

where,  $\mu$  is the viscosity in centipoise [cP] at temperature  $T$ ,  $\mu_0$  is the reference viscosity at the reference temperature  $T_0$  and  $C$  is the Sutherland constant. The



viscosity for individual constituents were calculated and the viscosity of the mixture was determined by the following equation, which is based on a method developed by Schmick [177]:

$$\mu_{mix} = \frac{y_i \mu_i \sqrt{M_i} + y_j \mu_j \sqrt{M_j} + \dots + y_n \mu_n \sqrt{M_n}}{y_i \sqrt{M_i} + y_j \sqrt{M_j} + \dots + y_n \sqrt{M_n}} \quad (3.6)$$

The Nusselt number correlation is given by equation 3.7. This correlation, originally described by Jimenez [178], was developed for the context of thermocouple heat transfer. It is an adaptation of the correlation established by Churchill [179] for heat transfer from cylinders in a cross flow. In the specific context of this study, it serves as a method for determining the heat transfer coefficient of a thermocouple in a cross flow, analogous to the conditions encountered in the TIMAR.

$$Nu_{cyl} = 0.3 + \frac{0.62 Re^{\frac{1}{2}} Pr^{\frac{1}{3}}}{\left(1 + \left(\frac{0.4}{Pr}\right)^{\frac{2}{3}}\right)^{\frac{1}{4}}} \left(1 + \left(\frac{Re}{282000}\right)^{\frac{5}{8}}\right)^{\frac{4}{5}} \quad (3.7)$$

Considerations for the uncertainty of the measurement is introduced in Section 4.6.

An additional thermocouple, denoted as T3 in Figure ??, was placed at the end of the MD. The function of this thermocouple was to measure the temperature of the gas flow exiting the MD. However, it was not uncommon during the operation of the TIMAR that the flame would extend out of the MD, destroying the thermocouple. Hence, little value was placed on this thermocouple as the test campaign progressed.

### 3.4.2 Fuel Flow Measurement

Since the mass flow rate of the fuel was known, knowing the fuel temperature was vital to determine the fuel's density and therefore determine its velocity. This measurement was not trivial. Due to the elevated temperatures in the TIMAR, the relative long length of the fuel lance and its relative thinness, heat would be conducted through the fuel lance and transferred to the fuel passing through the lance.

This presented difficulties because as the fuel temperature increased, its density proportionally decreased. In line with the principle of conservation of mass it caused a proportional increase in fuel velocity. Furthermore, each fuel blend tested had distinct heating characteristics owing to their respective heat capacities. This calculation required an iterative approach and was performed by an algorithm.

The algorithm, provided in Appendix B.2.2, was designed to determine the real gas temperature of the fuel by utilising the heat balance associated with equation 3.8 below. It assumed that the fuel lance wall was equal to the temperature of the oxidant, considering sufficient time was allowed for the TIMAR to reach thermal equilibrium before operation. The final heat balance for determining the fuel temperature was established between the radiative heat imparted onto the fuel gas from the lance and the convective heat loss of the gas travelling over the thermocouple, and it is given as:

$$T_{fuel} = T_{flc} + \left( \epsilon \sigma \frac{(T_{flc}^4 - T_{oxi}^4)}{h_{fuel}} \right) \quad (3.8)$$

Again, consideration for the uncertainty of this variable is introduced in Section 4.6.

### 3.4.3 Design Conclusions

The final design of the TIMAR constructed is shown by Figure 3.4.2, note gas flow goes from right to left. Its design successfully enabled high temperatures to result in combustion initiated by the autoignition mechanism. The ability to synthesise oxidants representative to the flue gas from a first stage combustor was present in the final design, in addition to the fuel blending capabilities facilitated by the ancillary equipment at the GTRC. The modular design of the TDVs enables the adaptation of the turbulence characteristics within the gas flow, essential for testing the proposed hypothesis. Finally, with the optical access given to the MD via the quartz tube, any flame exhibited can be analysed using the non-intrusive optical diagnostics suite. Hence, all essential criteria is met.

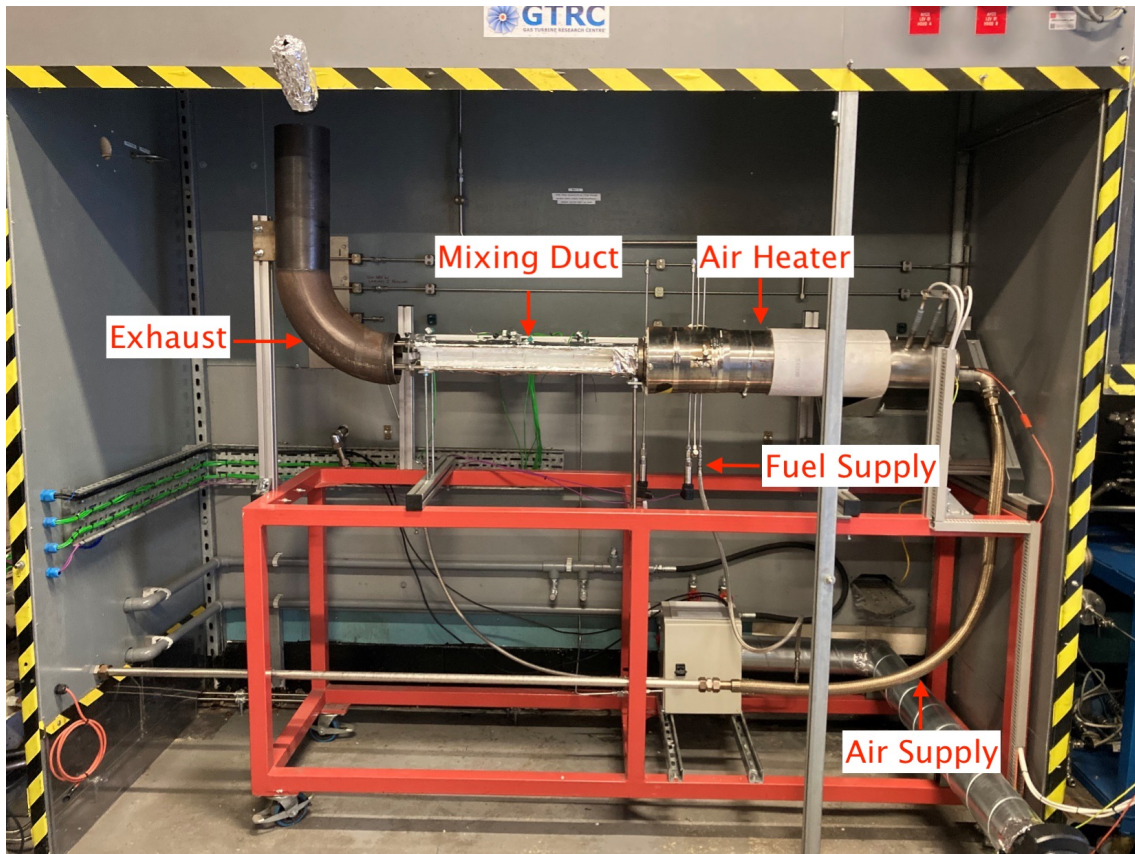


*Figure 3.4.2: Image of the TIMAR in the Left Hand Extraction Bay at the GTRC.*

### 3.5 Health & Safety

Prior to any commissioning, a Health & Safety assessment was undertaken. This required the inclusion of a general Risk Assessment (RA), a Control of Substances Hazardous to Health (COSHH) assessment and a zoning assessment in line with Dangerous Substances and Explosive Atmosphere Regulations (DSEAR). Additionally, a Safe Operating Procedure (SOP) was developed in accordance with the GTRC's protocols. All of which are found in Appendix C.

Whilst the considerations for Health & Safety are not typically introduced in academic literature, it has been included as supporting documentation to provide a framework for the safety assessments of other hydrogen related research activities. It is widely known that most hydrogen related incidents happen within lab settings [180], therefore, this serves as an example of safety considerations that should be made as a result of the extensive experience of operating with alternative fuels at

the GTRC.

## 3.6 Commissioning

The aim of the commissioning phase of the TIMAR was to understand how it operated, which informed the design of the experimental campaign. The commissioning objectives were to test the TIMAR through a parametric study of fuel blends and fuel and air mass flow rates to determine the optimum operational conditions for testing the hypothesis of this thesis.

Commissioning first began by operating the full construction of the TIMAR via temperature cycling. It was first temperature cycled to 500°C, increasing in 100 °C increments until the full operating temperature 1100°C was attained. The ability for the heater to control to its target temperature vastly improved the closer to maximum power the TIMAR was operated, where the advertised  $\pm 1^\circ\text{C}$  was achieved.

The initial commissioning described was performed using Borosilicate as the MD material of length of 500mm, which served its intended purpose, of a low consequence material in the event of a failure. Thermocouples were placed into the flow radially, to measure the axial temperature profile of the MD, the results of which are introduced in further detail in Section 3.6.6. In addition, the 3mm TDV was used throughout commissioning.

### 3.6.1 First Flame

The first fuel used to commission the TIMAR was a Coke Oven Gas (COG) mixture, as detailed in Table 3.4, that had a Lower and Higher Heating Value of 87.5MJ/kg and 102.2MJ/kg, respectively. COG was used as intermediary gas mixture of the fuel blends to be utilised in the experimental campaign and was readily available. To maintain simple operation in the initial stages of commissioning, air was used as the oxidant. At this point in the development and design of the experiment a thermal power of,  $P_{therm} = 36.5\text{kW}$ , was desired. Thus corresponding to a fuel flow

rate of  $\dot{m}_{fuel} = 0.42g/s$ .

**Table 3.4:** Coke oven gas fuel composition for commissioning.

	H2	CH4	CO	N2	CO2
[% vol]	61.0	26.0	7.0	4.0	2.0

An initial oxidant flowrate of 20g/s air was used and a heater set point temperature of 1050°C. At the first attempt, a flame was observed in the TIMAR, which is shown in Figure 3.6.1. Notably, the flame was attached to the nozzle. The image taken was taken from remote HD-CCTV camera within the rig room.

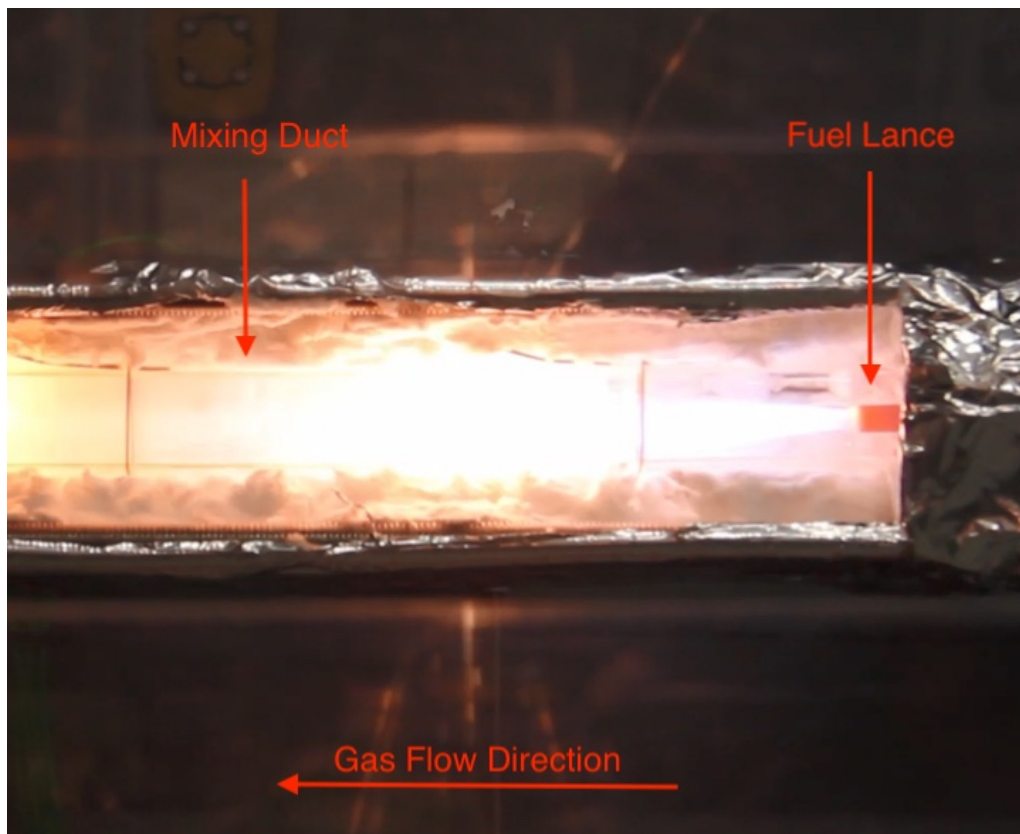


**Figure 3.6.1:** Image of first flame in the TIMAR, 20g/s air and 0.42g/s COG fuel.

Since the flame was attached to the nozzle it was clear that these initial conditions are too reactive to enable a lifted flame in this configuration. Thus, a series of combined flows were evaluated to realise a lifted flame within the MD. Initial attempts were made by reducing the fuel mass flow rate, thus reducing the reactivity of the fuel/air mixture. At the minimum attainable fuel flow rate of 0.1g/s, the flame persisted in its attachment to the nozzle.

### 3.6.2 Methane Testing

The subsequent commissioning activities aimed to evaluate the least reactive case of the reactivity spectrum by commissioning with pure methane. However, a borosilicate tube caused a failure resulting from the thermal stresses induced by the elevated temperature of combustion and the conduction of heat to and from the thermocouples. The consequence of which is captured by Figure 3.6.2. This initiated a revision of the set up to remove thermocouples from the flow.

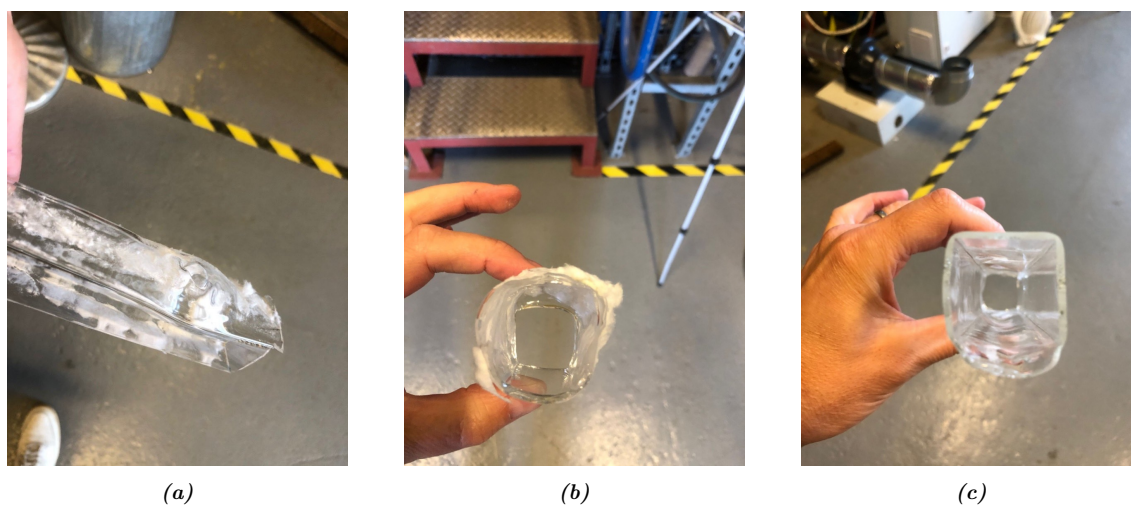


*Figure 3.6.2: Borosilicate failure resulting from thermal load.*

Following a rebuild, a parametric study of methane cases where the fuel and oxidant flows were varied to facilitate a range of ERs and residence times was performed to assess the operation of the rig with methane. Despite utilising the maximum flow temperature, minimal velocities and stoichiometric conditions the realisation of methane combustion was not possible under any conditions achievable within the operating limits of the TIMAR. It was considered that the reactivity of methane is insufficient to combust under the conditions achievable by the TIMAR. Adaptations that may have enabled the realisation of methane ignition in the TIMAR would be the extension of the mixing duct, to provide further residence time for the reaction to unfold, or to increase the reactivity of the case by preheating the fuel. These adaptations were not pursued as a result of resource and lab space restrictions.

### 3.6.3 Methane/Hydrogen Fuel Blend Testing

Testing progressed to incrementally introduce hydrogen into the fuel blend to determine a point of minimum reactivity which would enable combustion in the TIMAR. To test this principle, each methane-hydrogen fuel blend used would be tested at a stoichiometric condition. Air flow was set at  $8g/s$ . The following test points, detailed in Table 3.5 were considered. Combustion was achieved for a 90/10 [%vol]  $CH_4/H_2$  case at an air flow of  $8g/s$ , where the calculated MD velocity was ca.  $40m/s$ , based on continuity. Further trials were undertaken by increasing the hydrogen content. Testing concluded at a 25% by volume of hydrogen due to limitations on the mass flow controller (Bronkhorst M13) deployed for the hydrogen fuel flows.

**Table 3.5:** Test conditions evaluated for the commissioning of hydrogen and methane blends

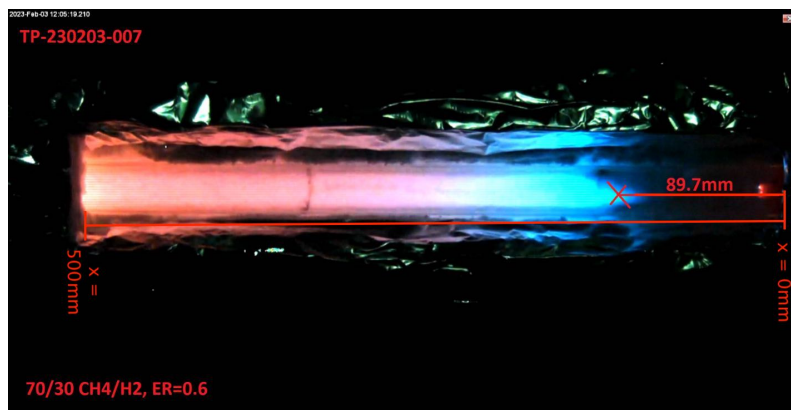
$\dot{m}_{air}$	CH4	H2	$\dot{m}_{fuel}$	ER	$T_{air}$	FLAME	$U_{MD}$	Residence Time
[g/s]	[vol%]	[vol%]	[g/s]	[-]	[degC]	[1/0]	[m/s]	[s]
20	100.0%	0.0%	0.47	0.40	1050	0	103.36	0.00484
8	100.0%	0.0%	0.47	1.01	1050	0	40.83	0.01225
8	90.0%	10.0%	0.46	1.00	1050	1	40.47	0.01236
8	90.0%	10.0%	0.46	1.00	1050	1	40.76	0.01227
8	80.0%	20.0%	0.44	1.00	1050	1	40.47	0.01236
8	70.0%	30.0%	0.44	1.00	1050	1	40.76	0.01227
8	75.0%	25.0%	0.44	1.00	1050	1	40.95	0.01221
8	77.5%	22.5%	0.44	1.00	1050	1	40.95	0.01221

As a result of the relatively low mass flow rate of air into the rig, testing evolved to determine whether any improvement in the resolution of the LFH for a given blend could be improved. This was achieved by inducing alterations to the air mass flow rate to achieve ERs ranging from 0.6-0.8. Fuel blends tested ranged from 90/10 [%vol] to 70/30 [%vol]  $CH_4/H_2$  - this was again limited due to the rating of the mass flow controller used. From this study, it was clear that the proportion of hydrogen

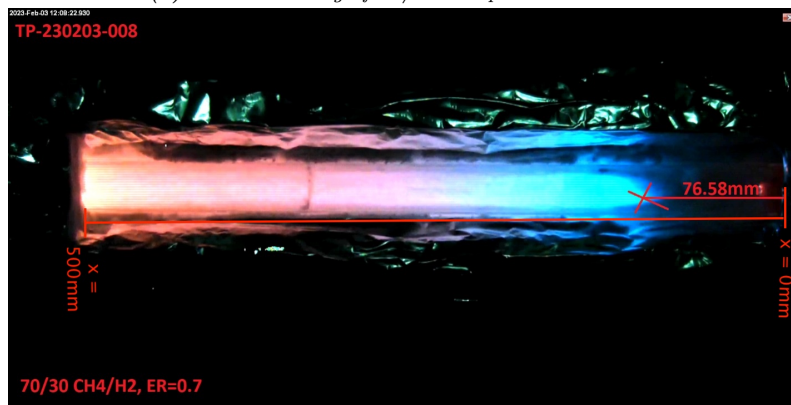


had a greater impact on the position of the flame within the MD than the ER.

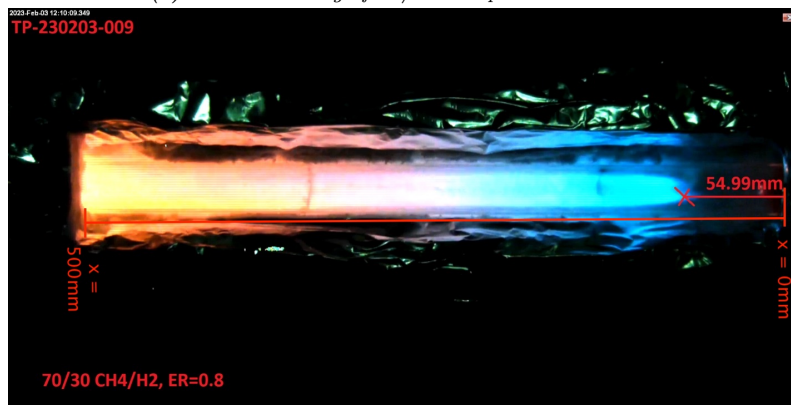
Interestingly, the effect of ER was more influential for the 70/30 [%vol] case than it was for the 80/20 [%vol], as it was observed that the increase of ER the more that the LFH reduced, which is expected since the velocity of the gas flow in the MD was reduced. This is illustrated in Figure 3.6.3 below.



(a) Commissioning of 70/30 test point at ER=0.6.



(b) Commissioning of 70/30 test point at ER=0.7.



(c) Commissioning of 70/30 test point at ER=0.8.

**Figure 3.6.3:** HD-CCTV images of 70/30 flames during commissioning, detailing effect of changing air flow on LFH.

When the ER of the 80/20 [%vol] case is increased (by reducing air flow) there is

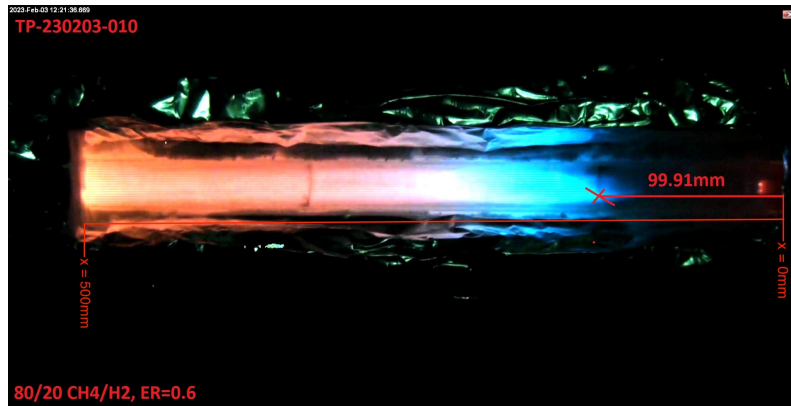


a negligible change in the LFH observed across the three cases (0.6 - 0.8), as shown in Figure 3.6.4. Thus indicating that the increased hydrogen in the 70/30 [%vol] is having a greater effect than that observed at 80/20 [%vol]. Furthermore, the 80/20 [%vol] at ER=0.8 showed excellent repeatability, with a mean value of  $97.71mm$  and a variability of  $\pm 1.42mm$  from 5 repeats. In this instance the method deployed to measure the LFH here is crude and does not represent that of the measurements found in later chapters of this thesis.

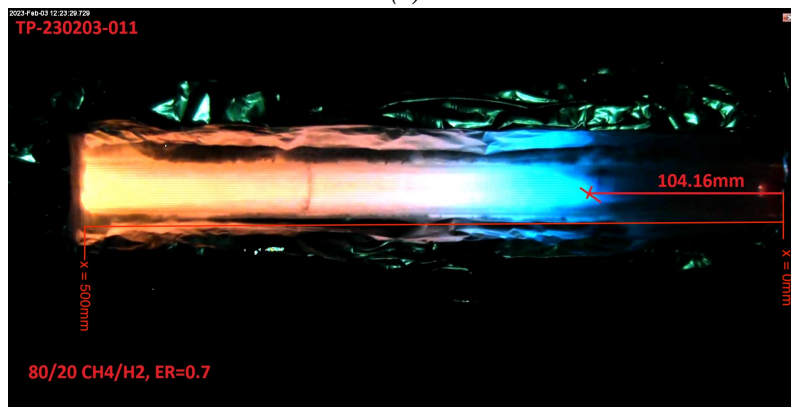
It was evident that altering the ER through adjustments in air flow had a discernible impact on flame height. It was also evident that this effect was not independent of the velocity of the gas within the MD and, consequently, the residence time. In light of this observation, commissioning was progressed by focusing on the impact of the reduction in fuel mass flow, not the increase in residence time.

This effect was tested and observations are presented in Figure 3.6.5, where it is shown, perhaps counter-intuitively, that the leaner the chemistry, the smaller the LFH is. It is shown in Figure 3.6.5a that the case with an ER of 0.5 has a smaller LFH than that of the richest case Figure 3.6.5d that has an ER of 0.8. This is due to the difference in fuel mass flow rates to achieve the varying ERs and hence, the smaller the ER, the smaller the fuel mass flow resulting in smaller LFH as a result of the reduced fuel gas velocity exiting the fuel lance.

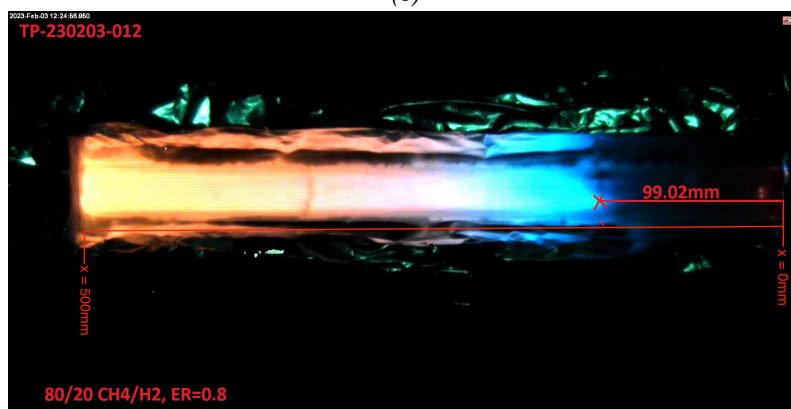
This phenomena was observed with all the other air mass flows considered and fuel blends. Notably there were limitations in ERs of some fuel blends that could be tested due to limitations of the capacity of mass flow controllers.



(a)

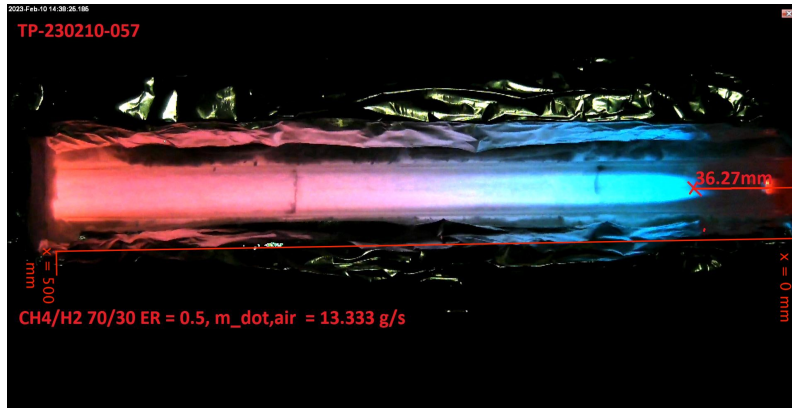


(b)

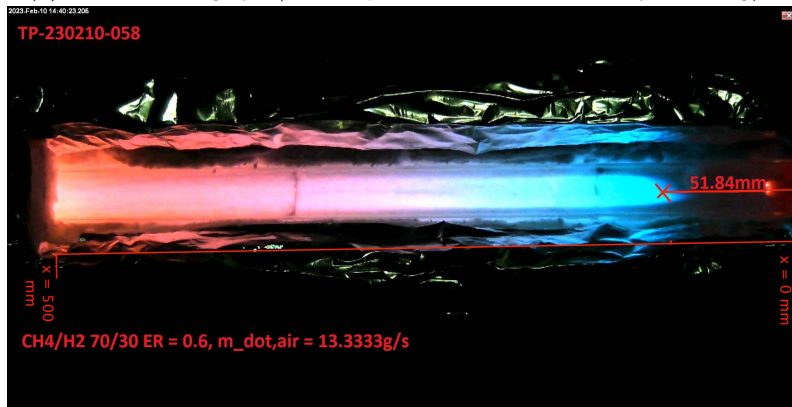


(c)

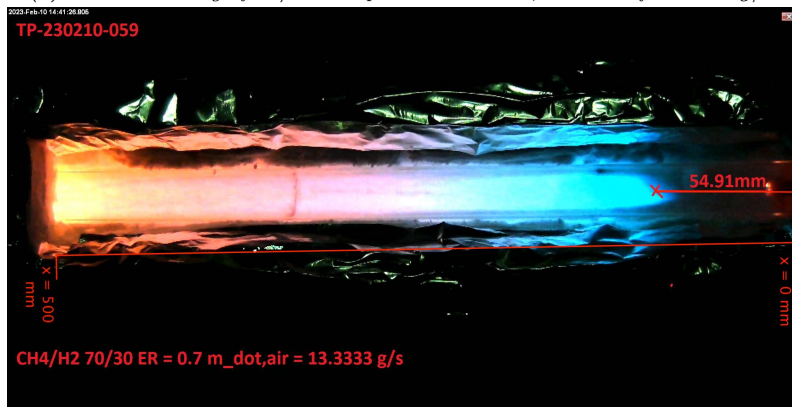
*Figure 3.6.4: HD-CCTV images of 80/20 [%vol] flames during commissioning, detailing negligible impact of changing air flow on LFH.*



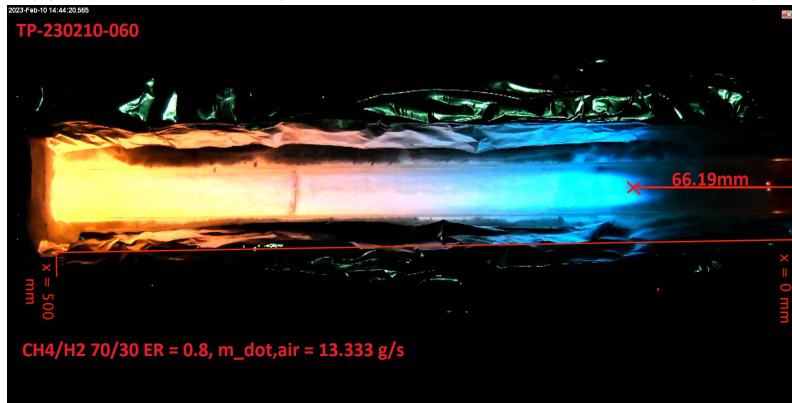
(a) Commissioning of 70/30 test point at  $ER=0.5$ , air mass flow 13.33g/s.



(b) Commissioning of 70/30 test point at  $ER=0.6$ , air mass flow 13.33g/s.



(c) Commissioning of 70/30 test point at  $ER=0.7$ , air mass flow 13.33g/s.



(d) Commissioning of 70/30 test point at  $ER=0.8$ , air mass flow 13.33g/s.

**Figure 3.6.5:** HD-CCTV images of 70/30 flames during commissioning, detailing effect of changing fuel flow, relating to the ER, on LFH.

Figure 3.6.6 is a graphical representation of the LFHs measured in the  $\text{CH}_4/\text{H}_2$  70%/30% commissioning cases with a constant air mass flow rate of  $\dot{m}_{air} = 13.33\text{g/s}$ . The trendline shows a near linear trend between the cases.

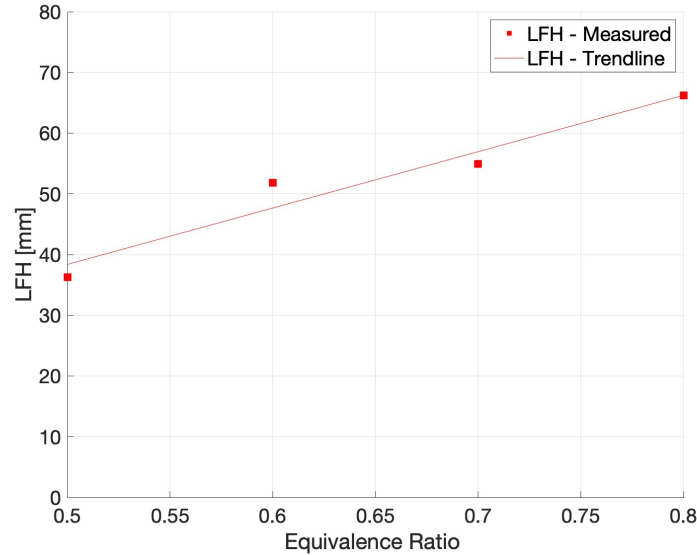


**Figure 3.6.6:** Graphical representation of the LFH associated with the  $\text{CH}_4/\text{H}_2$  commissioning cases at a constant  $\dot{m}_{air} = 13.33\text{g/s}$ .

As commissioning progressed, the hydrogen flow limiting M13 mass flow controller was replaced with a higher rated M14 mass flow controller. This modification facilitated the attainment of higher hydrogen flow rates. Therefore, higher hydrogen fuel blends were now able to be assessed.

As shown by Figure 3.6.7, which is a raw chemiluminescence image (chemiluminescence set up will be introduced in detail in Section 4.5.1) of a 25/75 [%vol]  $\text{CH}_4/\text{H}_2$  flame that the flame is attached to the nozzle exit, which was unanticipated. This was experienced for all fuel blends with more than half of the fuels volume containing hydrogen. Even when the air flow was increased to the maximum capacity (without performance degradation) of the electric air heater of  $23.75\text{g/s}$  there appeared to be an insufficient residence time in the MD, or delay in the ignition, for the flame to not be attached owing to the significant increase in the reactivity of the cases with high hydrogen content.

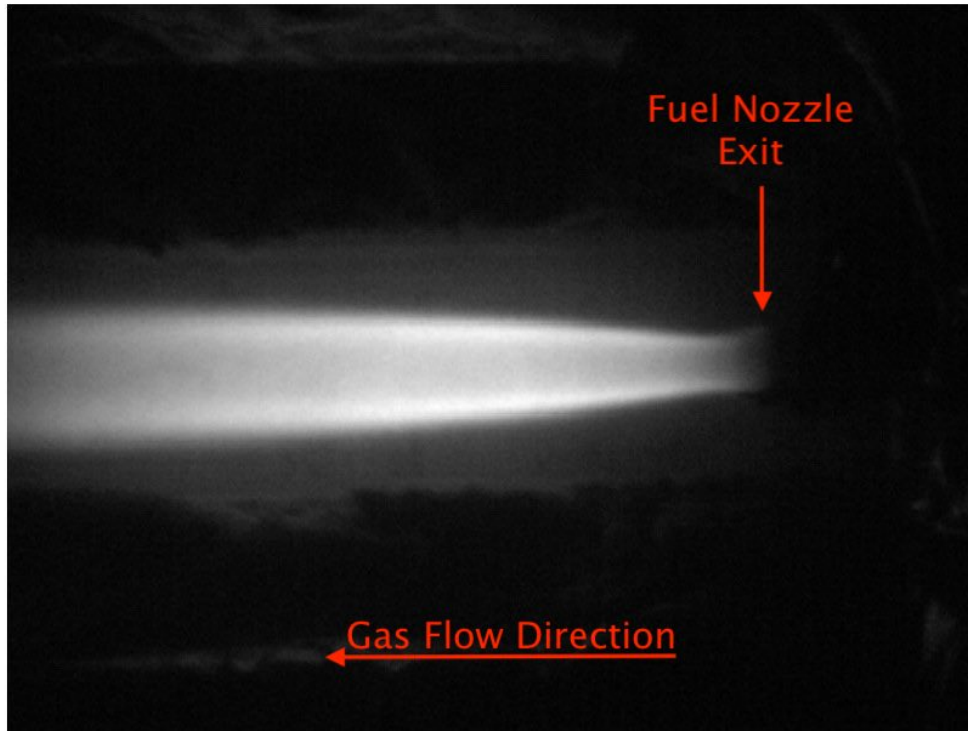


*Figure 3.6.7: Raw chemiluminescence image of 25/75 CH<sub>4</sub>/H<sub>2</sub> fuel blend.*

### 3.6.4 Pure Natural Gas Case

Since the pure methane case proved that it would not autoignite within the TIMAR under any flow condition, there was an attempt to ignite a natural gas blend of the composition described in the Table 3.6 below.

*Table 3.6: Composition of natural gas used in commissioning.*

	CH <sub>4</sub>	C <sub>2</sub> H <sub>6</sub>	C <sub>3</sub> H <sub>8</sub>	C <sub>4</sub> H <sub>10</sub>	C <sub>5</sub> H <sub>12</sub>	H <sub>2</sub>	N <sub>2</sub>
[mol%]	80.00%	9.00%	2.00%	1.50%	1.00%	3.50%	3.00%

A natural gas flame was achievable, owing to the inclusion of more reactive constituents within the fuel such as higher hydrocarbons (C<sub>2</sub><sup>+</sup>) and quantity of hydrogen. However, its stable operation necessitated an oxidant flow rate of 20g/s.

If all other test conditions were performed with an oxidant mass flow of  $20g/s$ , this would in turn offer a reduced resolution for higher hydrogen LFH measurements as a result of the increased residence time.

Due to the variability in natural gas blends available commercially, it was decided to omit its consideration from testing due to the resource limitations to account for the impact of hydrogen upon blending with the natural gas blend. It was considered that the best method for reporting to the wider research community was to maintain the use of methane to enable an accessible comparison of the results derived from this study.

### 3.6.5 Pure Hydrogen Case

During the commissioning of the fuels containing less than 25% hydrogen by volume testing was limited due to the M13 mass flow controller deployed. With the M13 mass flow controller still in service on the hydrogen line, a pure hydrogen flame was attempted for the first time. The relatively low hydrogen fuel flow was preferentially used in this initial investigation to minimise potential overpressures that may occur from hydrogen's detonation potential. Figure 3.6.8 below presents the hydrogen flame observed during this test. Due to the low maximum mass flow rate of hydrogen attainable by the M13 mass flow controller, a total fuel mass flow of  $\dot{m}_{fuel} = 0.031g/s$  was achieved, thus producing a flame with a thermal power of  $3.84kW$ .

In this test, a particularly intriguing observation is the visibility of the pure hydrogen flame, which emitted red light. Conventionally, it is thought that a pure hydrogen flame is not typically visible to the human eye due to its emission of light in the ultraviolet range of the electromagnetic spectrum. However, under certain conditions, it can manifest as a pale blue flame if the correct lighting conditions are present. Interestingly, in the captured image taken with an HD camera using a Bayer filter, the red flame is distinctly visible. This peculiarity raises questions about the nature of the red flame occurrence, as it was also observed with the naked eye that relies on the trichromatic structure of the eye.



*Figure 3.6.8: Image of pure hydrogen flame during commissioning,  $P_{therm} = 3.84kW$*

However, following research on the matter reveals otherwise. In a study conducted by Schefer et al. [181], the occurrence of invisible hydrogen flames is dispelled as a misconception. Their detailed study on the flame spectra which was performed to characterise the ultraviolet, visible and infrared emission bands showed a visible hydrogen flame. This study shows that the richer cases of pure hydrogen considered the more red light is emitted from the flame. This is however in complete contrast to the test case described above, where the air fuel ratio is exceptionally lean.

It is proposed by Muiy et al [182] that the emission of red electromagnetic radiation is a result of the hydrogen  $H - \alpha$  spectrum, which has a very close spectrum to the colours associated with sodium excitation. The theory of the presence of red in hydrogen combustion due to sodium content in the air was presented by Gaydon [183] which is dispelled as a result of Muiy et al's study [182]. Muiy et al's study also identify three other distinct peaks of emission within the red colour range; 656.5nm, 658.8nm and 660.6nm. The former is thought to be related to the water vibration-rotation spectrum band whilst the latter two wavelengths are considered unknown in the mechanism at play in the occurrence of its emission.

Whilst this is an aside from the objectives of the research pertaining to this thesis, it is an interesting observation nonetheless.

### 3.6.6 Axial Temperature Profile

To further the understanding of the conditions within the MD it was necessary to characterise the temperature profile resulting from the inevitable heat loss from the TIMAR, resulting from the high temperature differential between the working fluid and the ambient conditions.

Hence, the axial temperature profile was determined through the use of equi-spaced (100mm) thermocouples positioned along the centreline of the MD. The thermocouples were located at axial positions of 86mm, 186mm, 286mm, 386mm and 486mm away from the nozzle exit. The positioning of the thermocouples in the flow was only for purpose of this temperature characterisation.

The TIMAR was heated at maximum power for a sufficient duration to ensure that it had reached thermal equilibrium. The test was run for a duration of 30 minutes. The corrected (via the thermocouple correction algorithm introduced in Section B.1.2 temperature variation over time is presented by Figure 3.6.9a, and the temperature variation at different axial positions is depicted by Figure 3.6.9b, accompanied by the standard deviation of the temperatures at the given axial positions.

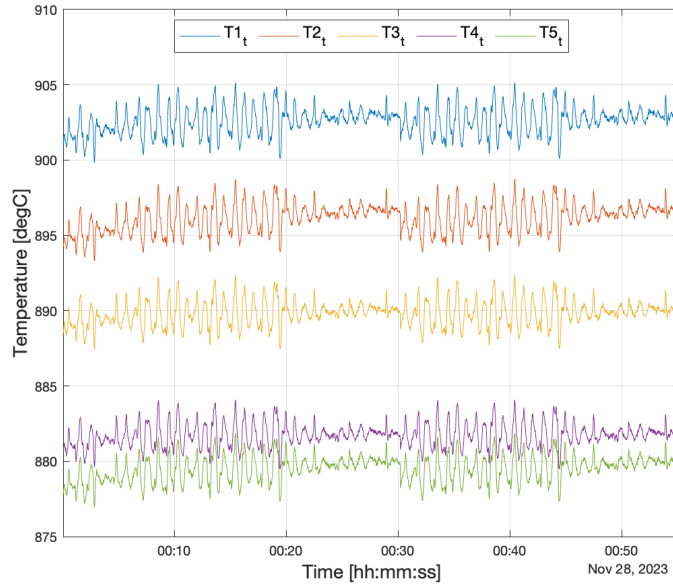
As anticipated, the temperature within the MD decreased with increasing axial distance. The temporal fluctuations observed in figure 3.6.9a, is considered to be the result of the fluctuations in heater power as it aims to maintain the set point value.

### 3.6.7 Commissioning Major Findings

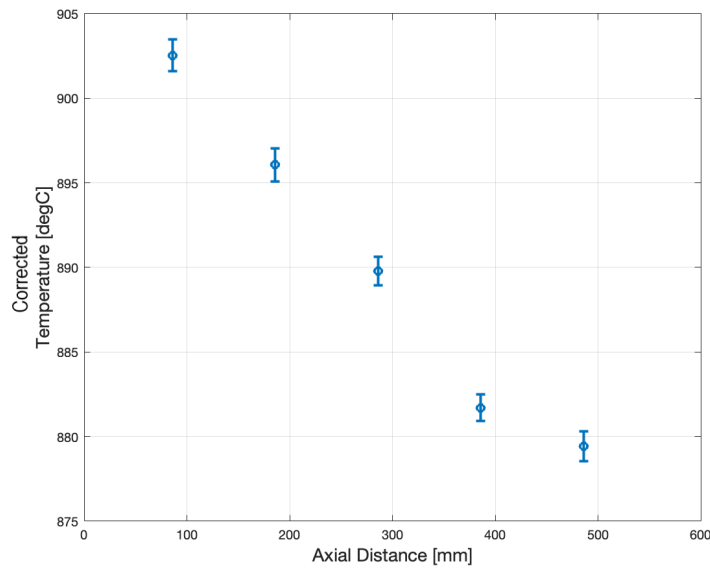
From the commissioning programme, the following major findings were deduced, which informed the experimental test programme and the methodologies to evaluate the fuel blends under their given turbulent conditions.

- Hydrogen had a significant impact on the reactivity of the fuel blends, with blends of 60% by volume or greater of hydrogen exhibiting attached flame





(a)



(b)

**Figure 3.6.9:** Temperature variations at in the TIMAR (a) over test duration, and (b) at different axial positions.

behaviour.

- The oxidant flow rate had a significant effect on the location of the lifted flame.
- Upper and lower limitations are now known for both the M13 and M14 mass flow controllers for both  $\text{CH}_4$  and  $\text{H}_2$  fuel mass flows.
- Altering the ER by adjusting air flow had an impact on flame height for the

same blend. This was found to be dependent on the velocity of the gas in MD.

- By altering the ER with the fuel mass flow, the leaner cases with less fuel injected into the system exhibited the smallest lifted flame, resulting from the reduced fuel mass flow rate.
- Commissioning also highlighted challenges in determining the temperature of the fuel and therefore its velocity, this in turn initiated the development of the MATLAB script discussed in Section 3.4.2.
- Temperature measurements within the TIMAR show a reading of  $932^{\circ}\text{C}$  at the inlet to the TRN.

### **3.7 TIMAR Development Conclusions**

In this chapter, a comprehensive review of the necessary design features required of the TIMAR are described followed by how these features were realised. Followed by a review of the commissioning activities undertaken in developing an understanding of the TIMARs operation which informed the development of the test campaign to be introduced in the next Chapter.

# Chapter 4

## Experimental Methodologies Pertaining to Novel Turbulent Inhomogeneous Mixture Autoignition Facility Testing.

This chapter outlines the development of the testing philosophy that guided the design of the experimental test campaign, as a result of the insights gained during the commissioning phase. The methodologies employed for measuring and calculating the dependent variables crucial for testing the hypothesis are introduced. This includes the methodology of the Particle Image Velocimetry (PIV) technique, which was used to determine the turbulence characteristics associated with each Turbulence Device (TDV). For continuity, the optimisation of the PIV settings are also introduced. Additionally, the methodology for measuring Lifted Flame Height (LFH) and Flame Establishment Time (FET) is discussed, along with the calculation of Ignition Delay Time ( $\tau_{IGN}$ ) and Damköhler Number. The determination of these variables contribute to understanding the impact of turbulence on the ignition of hydrogen-enriched fuel blends

## 4.1 Development of Experimental Philosophy

The development of the testing philosophy is detailed in this section. The findings from commissioning informed the capabilities of the TIMAR, and informed the experimental methodology derived. The philosophy developed is described chronologically below.

### 4.1.1 Decision Triangle

In designing the TIMAR, considerations around how to control the experiment were developed. It became apparent that a decision triangle was to be considered between fuel velocity, fuel lance diameter and flame power. This transpired into the following design/operating choices:

- Maintain constant flow field (velocity).
- Maintain constant geometry (fuel lance).
- Maintain chemistry/reactivity (flame power).

Initially, constant velocity and constant thermal power across the fuel blends was adopted. Hence, calculations were performed to determine the fuel lance diameters that would accommodate constant velocity and thermal power for the range of fuel blends considered. The following conditions were determined for a  $36.5kW$  flame across all fuel blends considered initially (0% H<sub>2</sub> through to 100% H<sub>2</sub> at increments of 25% [%vol]). Fuel velocity of  $150m/s$  was the target, as this was determined to be the velocity achievable in the air heater producing air at  $1100^{\circ}C$ . The target of having a fuel velocity equal to that of the oxidant,  $U = u_{fuel}/u_{oxidant} = 1$ , was considered the target as per the operating principles adopted by Markides [88]. As elucidated further in this thesis, the temperature of the fuel has a significant impact on the velocity of the fuel, resulting from the decrease in density associated with the increased fuel temperature.

**Table 4.1:** Fuel velocities associated for the given fuel blend under the methodology considered.

CH4	H2	Fuel Lance Diameter	Thermal Power	Velocity $U$ Percentage Difference
[%vol]	[%vol]	[mm]	[kW]	[-]
100	0	3	36.5	1.46%
75	25	3	36.5	-3.82%
50	50	3	36.5	6.04%
25	75	3.6	36.5	-0.15%
0	100	5.5	36.5	0.09%

As noted during commissioning, the maximum temperature achievable in the mixing duct (MD) was  $932^{\circ}C$ , which is significantly less than what was considered in initial design calculations. Upon discovering new temperature information to improve the assumptions made in flow field calculations, it was found that MD velocities are in the order of  $128m/s$ . The following calculations yielded the percentage difference between the oxidant velocity and the fuel velocity exiting the fuel lance. the purpose of this work was to attain conditions that would limit the percentage difference between the fuel and air velocity as far as reasonably practicable. Hence, it describes the difference between the fuel and air velocities whilst aiming to attain  $U = u_{fuel}/u_{oxidant} = 1$ , criterion conditions. Ambient temperature and pressure was considered for the fuel properties due to no fuel temperature data at this juncture. A selection of three fuel lance diameters are listed,  $3mm$ ,  $3.6mm$  and  $5.5mm$ , which proved to be the optimum compromise for meeting  $U = u_{fuel}/u_{oxidant} = 1$  criterion and the sufficient resource available to fund the manufacturing of the fuel lances.

Whilst the assumption of ambient conditions for the fuel seemed like a logical first step, it was clear during commissioning that it would not suffice. As described in the previous Chapter, the fuel lance would pick up significant heat as a result of its position and orientation in the hot oxidant flow. Thus, heat would transfer from the body of the fuel lance to the fuel as it travels through the lance. This increase

in the fuel temperature would in turn cause an increase in fuel velocity, resulting from its reduced density.

Thus, despite aiming to have an equal flow field and achieve the  $U = u_{fuel}/u_{oxidant} = 1$ , further work was necessary to determine the fuel velocity by considering the fuel temperature. In addition, properties such as the specific heat capacities and thermal conductivity introduced complexities. These all impacted the velocity of the fuel resulting from its heat pick up, thus, negating the  $U = u_{fuel}/u_{oxidant} = 1$  between blends test philosophy, *whilst* maintaining power.

### 4.1.2 Maintaining Flow Field Conditions

Due to the wide ranges of velocities that are adopted in an attempt at maintaining thermal power, it was decided to change tact and to prioritise the maintenance of the flow field conditions between test points coupled with the same diameter fuel lance. Maintaining the aim of  $U = u_{fuel}/u_{oxidant} = 1$  criterion. In addition, in the interest of maximising the resolution of the LFH, the maximum air mass flow of 23.75g/s is now used throughout.

The MATLAB script that was developed to determine the velocity of the oxidant and the fuel, detailed in Sections 3.4.1 and 3.4.2, was used to return a mass flow rate of fuel to attain  $U = u_{fuel}/u_{oxidant} = 1$  conditions. This necessitated a “probe point” where an initial estimate of the fuel mass flow was released. The lowest temperature recorded following the injection of fuel in the probe point was considered to be the fuel temperature. The fuel mass flow required to attain the  $U = u_{fuel}/u_{oxidant} = 1$  case was returned when the probe points measured temperature was used as an initialising value within the algorithm. Now with the returned mass flow of fuel, a “test point” was then taken.

Through testing this methodology it was shown that despite the flow velocities being assumed equal across all cases of the fuel blends, across all cases the mixing regime were found to be different. This was determined to be a result of the difference in the momentum flux between test points resulting from the different densities

and thus mass flows of fuel. The density values were inferred from the corrected temperature algorithm that was introduced in Section ??.

Hence, despite best efforts to maintain a similar flow field between the fuel blends by maintaining kinematic conditions, it is not possible to replicate flow fields between test points since the flow field is dependent on dynamic conditions. Even by recreating all possible similarities, it remains that the properties and molecule size of the fuels differ which renders it not possible to maintain flow field conditions between fuel blends.

### 4.1.3 Maintaining Thermal Power

There was no clear consensus on how the experiment would be controlled by maintaining dynamically similar flow fields. Where this thesis positions itself is studying the impact of hydrogen addition in a commercial engine, hence, the change to flow properties is inherent in the investigation as it will be inherent in the retrofit conversion of hydrocarbon-fuelled GTs to high hydrogen capability.

Hence, this resulted in omission of flow field considerations, and reflected a more practical approach. The methodology philosophy thereafter was based on maintaining the thermal power of the fuel blends, as this property could be controlled, regardless of the conditions, elevated or ambient.

Since the M14 mass flow controller was limited to  $0.185g/s$  of hydrogen, as determined through commissioning activities described above, the thermal power of each test condition was set at  $22.2kW$ .

Since different fuel blends are being considered, the only variables that could be described with a measurable uncertainty and enable comparison between conditions, was the inlet conditions to the MD and the thermal power of the flame.

## 4.2 Test Matrix Development

In the development of the test matrix, three campaigns were considered: (i) the use of air as the oxidant, (ii) varying the proportions of a given constituent within the oxidant to determine the effect of each constituent individually and (iii) applied test cases where the oxidant is synthesised and approximates the exhausted gas of a given fuel blend from a first stage combustor.

### 4.2.1 Fundamental Study of Each Constituent in the Oxidant.

In essence, the idealised oxidants to be synthesised would be varying combinations of  $N_2/O_2/CO_2/H_2O$  and an initial test campaign was considered to evaluate the effect of each constituent. The initial oxidant compositions to be tested were of nitrogen and oxygen, where their proportion in relation to one another is described by:

$$\beta = \frac{n_{O_2}}{\sum_n n_i} \quad (4.1)$$

The  $\beta$  values proposed for testing were: 0.1, 0.12, 0.15, 0.18 and 0.21.

It was proposed to build upon this testing by introducing  $CO_2$  into the oxidant mixture. The range of  $\beta$  values was maintained, in addition to testing with 4  $CO_2$  levels of 2.5%, 5.0%, 7.5% and 10.0% by volume. This range was chosen specifically as it captured the range of the predicted  $CO_2$  concentrations in the exhaust of the first stage combustor. The aim was to assess how  $CO_2$  affects the autoignition of the specified fuels.

Similarly, the percentage volume of  $H_2O$  was also considered in isolation with a  $N_2/O_2$  of the  $\beta$  values described. The percentage volumes of water vapour proposed were 5%, 10%, 15% and 20%. Again, these steam fractions are within the range of percentage volumes expected in the flue gas from a first stage combustion of the fuel blends under evaluation. Where the 5%  $H_2O$  percentage volume is the lower limit set



by the 100% [% vol] CH<sub>4</sub> case and the 20% H<sub>2</sub>O percentage volume is the upper limit set by the 100% [% vol] H<sub>2</sub> case. These value were calculated through by evaluating the Equivalence Ratio to attain a constant Adiabatic Flame Temperature in the first stage burner (using 100% CH<sub>4</sub> at engine relevant conditions as the base case) for the fuel blends considered. Furthermore, the products of the combustion reaction were determined through the balancing of chemical equations for the relevant ER according to the fuel blend under consideration.

#### **4.2.2 Applied Conditions Relevant to the Fuel Blend Under Evaluation.**

It was expected that from the fundamental study of varying each oxidant composition independently will have provided a foundation of knowledge to how each oxidant constituent affects the ignition of the fuel. The proceeding method aimed to build upon the initial foundation by considering an oxidant composition analogous to the SEV inlet oxidant composition for a given fuel blend.

The process of determining the applied test case was initialised by determining an adiabatic flame temperature (AFT) for the EV burner through use of confidential data and an equilibrium model in CHEMKIN for a methane flame. The determined AFT was subsequently used to determine the ER necessary for the different fuel blends and thus enabled the determination of the exhaust gas composition from the first stage combustor. Matching AFT across the fuel blends was considered as it is analogous to the desire of GT operators and designers to maintain turbine inlet temperature in operational GTs.

Due to the complexity of the GT26 operation, additional inclusions for cooling air was considered to approximate an oxidant mixture entering the SEV combustor, where a target of ca. 15% O<sub>2</sub> [%vol] was also a criterion to be met, as detailed by Gütthe et al. [129].

This process included the development of a MATLAB script and CHEMKIN models to calculate the required information. The outcomes of this analysis is given

in Table 4.2.

**Table 4.2:** *Determined flue gas compositions to synthesise for applied test cases.*

<b>CH4</b>	<b>H2</b>	<b>ER</b>	<b>CO2</b>	<b>H2O</b>	<b>O2</b>	<b>N2</b>
[%vol]	[%vol]	[-]	[%vol]	[%vol]	[%vol]	[%vol]
100%	0%	0.6	3.10%	6.20%	14.07%	76.64%
75%	25%	0.589	2.80%	6.55%	14.15%	76.50%
50%	50%	0.575	2.37%	7.11%	14.24%	76.27%
25%	75%	0.551	1.62%	8.09%	14.40%	75.88%
0%	100%	0.4925	0.00%	10.07%	14.82%	75.11%

A detailed account of this investigation is provided in Appendix ??.

### 4.2.3 Air as Oxidant

Due to limitations in both experimental time and availability of mass flow controllers, the consideration of synthesising a representative oxidant was excluded from the test campaign undertaken. While this was not ideal and did not recreate the oxidant conditions experienced in the GT26, it did enable the evaluation of the core hypothesis of this thesis: the impact of turbulence on hydrogen enriched fuel ignition.

Due to the reduction in test cases associated with the exclusion of the fundamental study of varying oxidant compositions and that of the applied cases, it enabled the a wider range of fuel blends to be tested. Hence, the fuel blends considered was 80/20 [%vol] CH<sub>4</sub>/H<sub>2</sub> to 0/100 [%vol] CH<sub>4</sub>/H<sub>2</sub> at 10% increments.

The test cases to be evaluating in this experimental campaign for the impact of temperature and turbulence are introduced in Table 4.3 and 4.4, respectively.

*Table 4.3: Experimental test cases for evaluating the impact of temperature.*

Fuel Blend		TDV	Air Temperature
CH4 [%vol]	H2 [%vol]	[mm]	[°C]
80	20	3	750
70	30	3	750
60	40	3	750
50	50	3	750
40	60	3	750
30	70	3	750
20	80	3	750
10	90	3	750
0	100	3	750
80	20	3	850
70	30	3	850
60	40	3	850
50	50	3	850
40	60	3	850
30	70	3	850
20	80	3	850
10	90	3	850
0	100	3	850
80	20	3	932
70	30	3	932
60	40	3	932
50	50	3	932
40	60	3	932
30	70	3	932
20	80	3	932
10	90	3	932
0	100	3	932

*Table 4.4: Experimental test cases for evaluating the impact of turbulence.*

Fuel Blend		TDV	Air Temperature
CH4 [%vol]	H2 [%vol]	[mm]	[°C]
80	20	3	932
70	30	3	932
60	40	3	932
50	50	3	932
40	60	3	932
30	70	3	932
20	80	3	932
10	90	3	932
0	100	3	932
80	20	6	932
70	30	6	932
60	40	6	932
50	50	6	932
40	60	6	932
30	70	6	932
20	80	6	932
10	90	6	932
0	100	6	932
80	20	12	932
70	30	12	932
60	40	12	932
50	50	12	932
40	60	12	932
30	70	12	932
20	80	12	932
10	90	12	932
0	100	12	932

## 4.3 Testing Methodology

In this section the methodology deployed for testing was undertaken following the completion of the prerequisite safety checklist ensuring safe operation with risk reduced as far as reasonably practicable.

Air flow at  $23.75\text{g/s}$  is passed through the TIMAR, and the air heater temperature is incrementally increased at intervals of  $100^\circ\text{C}$ , until  $900^\circ\text{C}$  where the interval drops to  $50^\circ\text{C}$ . Upon reaching maximum power of the air heater ( $1100^\circ\text{C}$ ) the TIMAR is left to reach thermal equilibrium by allowing sufficient time (ca. two hours) for it to heat soak whilst under direct supervision.

Once the TIMAR has reached thermal equilibrium, the rig room, where the experiments take place, is closed to personnel whilst the experiments are controlled from the remote location of the control room. This increased the safety margin of the experiment.

Upon taking a test point, the proportion of methane required for a given set point is flowed initially, followed closely by the hydrogen flow once the target methane flow is met. It was necessary to delay the delivery of the fuels due to difference in time taken to achieve set point. Methane was chosen to flow first due to its inability to ignite which would not influence the measurement of the dependent variables, as opposed to hydrogen which was known to ignite under all conditions considered in the TIMAR. Once both components of the fuel were at set point, the fuel was flowed a maximum of 10 seconds or until the operator was satisfied with the flame stability and the necessary data was acquired.

During experimental testing, data was acquired by use of the techniques that will be described in Section 4.5, where a total sum of five repeats were taken for a robust statistical spread of the acquired data.

## 4.4 Flow Field Particle Image Velocimetry

As a means of assessing the turbulent flow field conditions of the experimental test conditions, Particle Image Velocimetry (PIV) was performed. Due to constraints related to resources and equipment, the 80/20 [%vol] CH<sub>4</sub>/H<sub>2</sub> case is analysed via PIV only. PIV is performed for all three TDVs used within the experimental programme. The data obtained from the PIV analysis enabled a quantifiable means of evaluating the turbulence characteristics imparted by the TDVs case. The PIV analysis facilitated the determination of the Turbulence Intensity (TI) at the fuel and air inlets and the characteristic lengthscales of turbulence of the flow fields for the three turbulence devices evaluated in this study.

### 4.4.1 PIV Operating Principles

PIV is an imaging technique employed for the quantitative assessment of fluid flow velocities within a designated imaged window. This process started with the introduction of very small seeding particles into the fluid under examination. It was imperative that these seeding materials possessed a low or comparable density to the fluid being assessed. Owing to the negligible mass of individual particles, they exerted a minimal influence on the fluid's flow and closely track the fluid particle motion. Moreover, these seeding materials exhibit reflectivity, as a laser sheet is introduced into the fluid to illuminate the seed particles. Within this study Titanium (IV) Dioxide seed particles with a diameter of  $5\mu m$  were used.

A high-speed camera was utilised for the acquisition of images of the illuminated flow field. Crucially, the camera and the laser were synchronised to ensure that image capture coincides precisely with the laser pulse initiation. The camera exposure was set to a short duration to prevent image blurring caused by the rapid motion of illuminated particles. Detail regarding the settings used is introduced in Section 4.4.5.

Synchronisation was realised through the implementation of precise timing con-

trols, by triggering the camera upon the laser pulse initiation. This guaranteed that the camera’s lens opened immediately after the laser illuminates the fluid flow. The resulting images were obtained in pairs, commonly referred to as “image pairs” in the context of PIV. A schematic of the image synchronisation is provided in Figure 4.4.1.

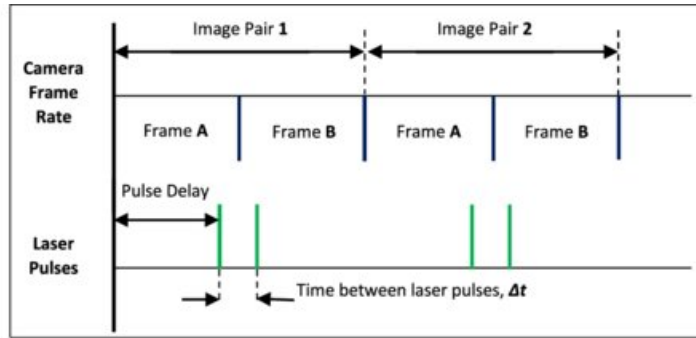


*Figure 4.4.1: Schematic illustrating the procedure of timing laser pulse and camera triggers, reproduced from [184].*

After image acquisition, a cross-correlation analysis was conducted. This analysis involved statistically evaluating the change in particle position within a predefined correlation window between the first and second image within each pair. The outcome of this analysis provides the most probable displacement of the particles. The time interval between successive images was used to calculate the time taken for the particle to travel the displacement measured between the image pair. This facilitated the determination of the particles velocities.

The entire process of cross-correlation, velocity determination, and the generation of resultant vector fields was performed in PIVlab, which is a dedicated PIV post-processing software developed by Thielicke et al [185] [186].

## 4.4.2 PIV Setup

To enable the capture of images a Phantom V1212 Ultra High-speed  $4kHz$  camera was used with a NIKKOR Micro AF 105mm f 1:2:8 lens. To only capture the reflected wavelengths of the laser light, a 525nm Central Wavelength filter was also used with a bandpass of 25nm and an optical density of 4.0.

In terms of lasers utilised, a Litron LD30-527, diode pumped solid state Nd:YLF laser was used to illuminate the particles. The laser light was directed by a ILA5150 articulate mirror arm to direct the laser light from the laser to emit down the length of the MD, following it being conditioned into a sheet using a ILA5150 light sheet optic filter.

PIV analysis was performed retrospectively to the experimental studies discussed later in this thesis. Hence, the region of interest was known to be within the first 200mm of the length of the MD. To ensure favourable resolution of the images, the camera was set up to capture data in an imaging window of 100mm in length and ensure the total height of the tube is included. Hence, a traverse was used to accurately move the camera between the two imaging windows of 0 – 100mm and 100 – 200mm.

The described PIV setup is depicted in Figure 4.4.2, below.

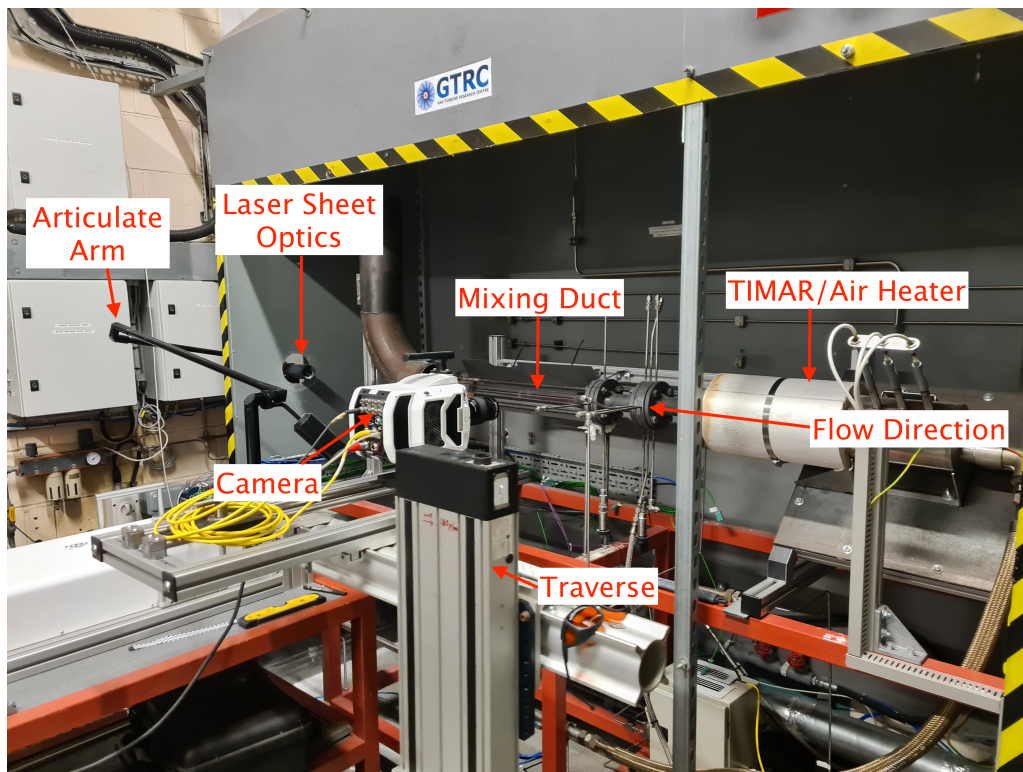


*Figure 4.4.2: Image illustrating the PIV setup used in this analysis.*



### 4.4.3 Dynamically Similar Conditions

Performing PIV at experimental conditions, i.e. under combustion and therefore high temperatures, would introduce a number of challenges such as the particle seed sintering and fouling of the optical access and the inability to work in close proximity to the rig to operate the PIV setup. Hence, PIV testing was performed under dynamically similar isothermal conditions, in which the Reynolds number for the hot and cold cases are equal. This method is consistent with that adopted by Markides [154] in their characterisation of the Turbulent Autoignition Rig at the John Hopkins lab.

Due to the same geometry and the ratio of inertial to viscous forces being equal at a given location in the hot and cold flows it is considered that geometric flow field will be replicated. In addition, this analysis elucidated the fact that only a singular cold flow, simulating the CH<sub>4</sub>/H<sub>2</sub> 80/20 [%vol] case, was attainable as a result of the operating range of the facilities at the GTRC. Hence, it was considered that Reynolds scaling was the most appropriate method.

$$Re_{hot} = \frac{\rho_{hot} U_{hot} D}{\mu_{hot}} = \frac{\rho_{col} U_{cold} D}{\mu_{cold}} = Re_{cold} \quad (4.2)$$

where,  $\rho$  is the fluid density,  $U$  is the fluid velocity,  $D$  is the internal diameter of the mixing duct and  $\mu$  is the fluid viscosity.

Notably, the Reynolds number will change between fuel cases, as thermal power of the test cases is maintained. However, it was deemed sufficient for a reference case that could be evaluated with the resource available.

#### 4.4.3.1 Air Flow

Through use of the relationship denoted in equations 4.2, to replicate the Reynolds number under experimental conditions (i.e. 932°C and  $\dot{m}_{air} = 23.75g/s$ ) a cold flow of 9g/s at ambient conditions is desired.

#### 4.4.3.2 Fuel Flow

Due to the heat transferred to the fuel as it travelled through the fuel lance, the fuel under combustion test conditions was subject to a temperature increase. The measured gas temperature from combustion testing was inputted into the thermocouple correction MATLAB script which yielded a corrected temperature. The determined temperature enabled the calculation of the fuel Reynolds number.

This hot fuel Reynolds number was also reproduced for cold conditions to enable dynamically similar conditions of the fuel flow. It was determined that the hot 80/20 [%vol] CH<sub>4</sub>/H<sub>2</sub> case of a  $\dot{m}_{fuel,hot} = 0.4259g/s$  could be modelled by a cold flow of air at a mass flow of  $\dot{m}_{fuel,cold} = 0.3000g/s$ . Other cases proved to be outside of the operable range achievable at the Gas Turbine Research Centre as gas flows would have been too low to control with the mass flow controllers available.

Through conservation of mass and flow calculations a bulk velocity from the isothermal substitute fuel jet of  $U_{bulk} = 34.69m/s$  was derived. Considering that the fuel lance is sufficiently long for a turbulent flow velocity profile to develop, the max velocity is considered to be  $U_{max} = 2U_{bulk} = 69.34m/s$ .

#### 4.4.4 PIV Methodology

In the following subsection, a description of the PIV methodology is presented, providing an account of the procedures employed in the analysis. The execution of PIV analysis is not trivial and demands careful consideration.

Since an air flow of  $9g/s$  is required for the appropriate recreation of dynamically similar conditions, and the passing of seed through the heater would incur irreparable damage, there was need to bypass a degree of air through a dedicated seeder downstream of the heater. After a short duration of commissioning, it was determined that a minimum flow of  $0.4g/s$  of air was required to pick up the seed within the seeding air flow. Hence, an air flow of  $8.6g/s$  was required to pass through the TIMAR, coupled with an additional  $0.4g/s$  through the downstream seeder.

Similarly, an additional seeder was introduced for the fuel line, to ensure that

the fuel flow was also represented within the PIV analysis. This necessitated no bypass since it avoided any heating elements relating to the TIMAR.

Considering that the air flow of  $8.6g/s$  through the TIMAR had already been established the following steps were taken to ascertain data for a given test point.

1. The remainder of the air flow ( $0.4g/s$ ) was introduced through the air/seeder bypass line to entrain the seed into the flow.
2. Once this condition was met, the fuel seeder was initialised to introduce the fuel seeder flow into the MD. Manual agitation of the seeder was requisite to ensure appropriate seed levels.
3. Simultaneously, the laser was initiated via an accompanying software installed on the PC controlling the data acquisition and laser, which triggered the camera to take image pairs at a defined time interval (as will be described in Section 4.4.5).
4. The test point was performed over a duration of 5 seconds.
5. The captured data was analysed qualitatively where batches of a minimum of 500 to a maximum of 2,000 images were saved. The number of images was dependent on the duration of sequential images of sufficient quality for analysis.
6. These images were imported into PIVlab, where the images were organised into image pairs.
7. The image pairs are analysed in PIVlab, where an interrogation window is applied to the imaged window.
8. The most statistically likely displacement of the seed particles between image A and image B of an image pair is calculated. Moreover, following appropriate specification of the calibration settings, the velocity of the given particles is determined.

9. Following this analysis across the image pairs, a mean value for the velocity vectors is determined.
10. The analysis produces contours of the instantaneous velocity contours (determined between the image pairs) and a mean velocity contour is also determined.
11. PIVlab provides the opportunity to extract derived data for further analysis which is delineated in Section 4.4.7

#### **4.4.5 Particle Image Velocimetry Settings Optimisation for Data Acquisition**

As described in 4.4.1, the appropriate selection of capture rates and image timings is paramount to derive appropriate images for analysis. In this section, initial images are taken and evaluated, comparing against one another to determine optimum equipment settings.

The PIV images included in this section relate to the MD as highlighted by the annotated Figure 4.4.3, below.

##### **4.4.5.1 PIV Image Timings**

Four timing intervals are evaluated and compared to determine the optimum timing conditions, being  $35\mu s$ ,  $50\mu s$ ,  $70\mu s$  and  $90\mu s$ . These values were selected on the basis of the expected bulk flow velocities within the TIMAR during cold operation and selecting a time period that would enable the seeded particle to travel 10 pixel within the optical domain. The range of timings considered both the fuel and air flows, whilst also allowing for contingency of faster and slower image timing as a means of validating the selected image timing. The operating conditions of a  $9g/s$  air flow, with a substitute fuel air flow of  $0.3g/s$  at ambient conditions are maintained throughout, along with the same TDV (TDV6). In this section, only the first imaging window of  $0 - 100mm$  from nozzle exit is region of interest (ROI)



*Figure 4.4.3: Annotated image of the TIMAR, highlighting the region of interest in the PIV analysis.*

as this is the flow region with the greatest level of transient events and therefore the region of highest interest. Figure 4.4.4 is raw PIV image that serves as a reference image.

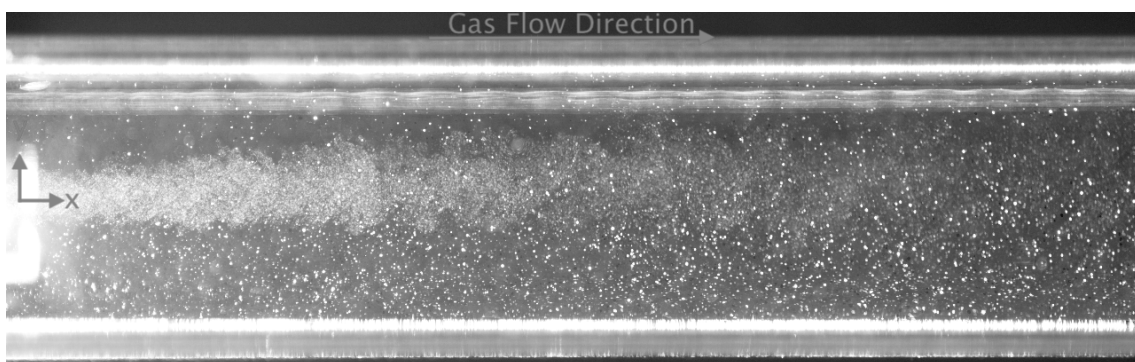


*Figure 4.4.4: Raw PIV image of 0-100mm region with fluid flow from left to right. ROI 0-100mm.*

Comparison of the image timings is presented by Figure 4.4.5 that were captured using the same operating conditions. All images shown in Figure 4.4.5, are described by the same velocity contour scale.

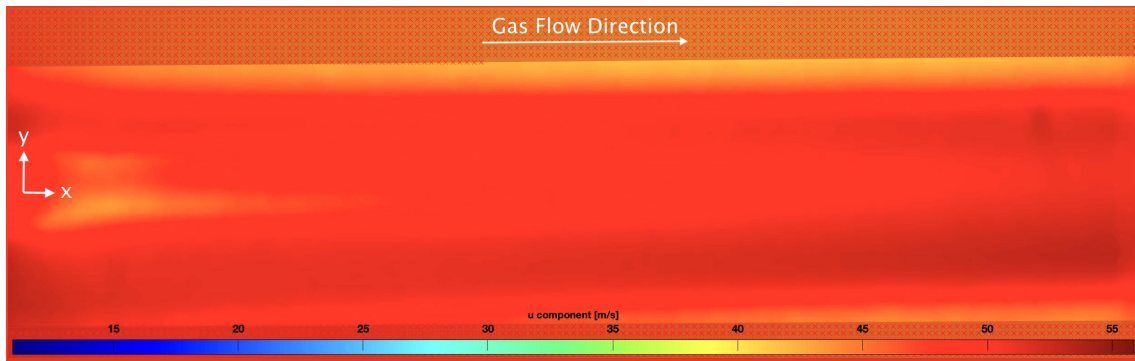
Figure 4.4.5a shows an over-prediction of the velocities within the whole domain relating to the  $35\mu s$  time interval. This is a result of the time interval being too small and therefore only capturing a small displacement of the seed particles within the correlation window used for the velocity analysis, hence, a reduced measurement precision is experienced leading to decreased velocity resolution limiting the analysis' ability to accurately detect velocity variations in the flow.

Figure 4.4.5b depicts the presence of a high velocity jet, which is the expected flow patterns from the set up analysed. With max velocity experienced on the centre line and a minimum at the wall boundaries, these settings are considered optimum for analysis under these conditions presently.

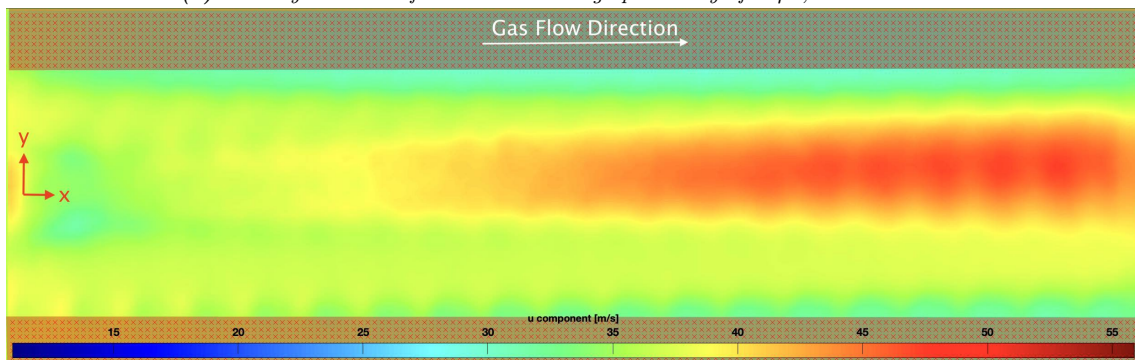
Figure 4.4.5c and 4.4.5d show regression in the analysis output following the progress observed between  $35\mu s$  and  $50\mu s$ . It is clearly observed that the presence of the central jet is weaker in the  $50\mu s$  case and is undetectable in the  $90\mu s$  case. The velocities are also shown to under-predict the flow velocities of the flow field. This is considered to be the result of reduced temporal resolution, which fails to capture any rapid changes in the flow velocity therefore leading to a reduction in flow detail. This has also lead to a decreased accuracy for the high-velocity flow regions, which is the results of the extended time between image pairs enabling particles to travel distances that exceed the correlation window size. Velocity field smoothing is also observed in these cases, with the issue becoming more prevalent in the  $90\mu s$  case. This is incurred by the temporal smoothing that is introduced, effectively averaging the flow information over the longer time period therefore obscuring the presence of fluctuations in the flow.

As a result of this analysis,  $50\mu s$  is considered to be the optimum timing for the test points that follow in the proceeding tests. This case is displayed within the test points own auto-scaled velocity contour range ( $u_{min} = 36.12m/s$  to  $u_{max} = 55.87m/s$ ) in Figure 4.4.6.

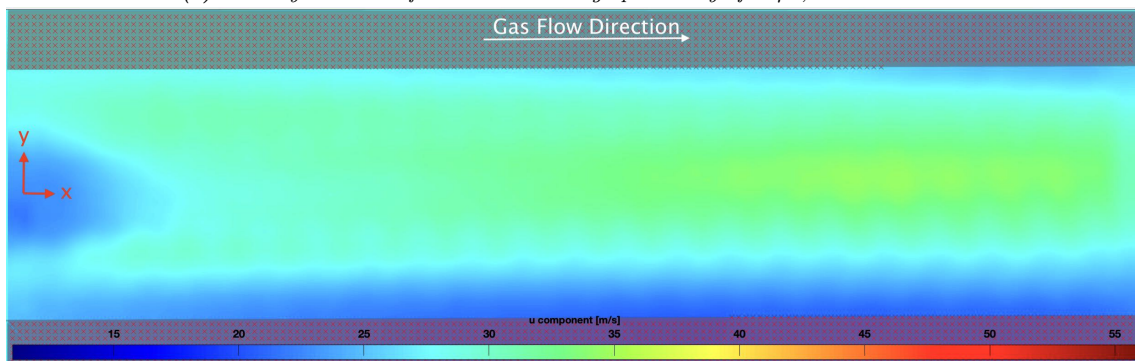




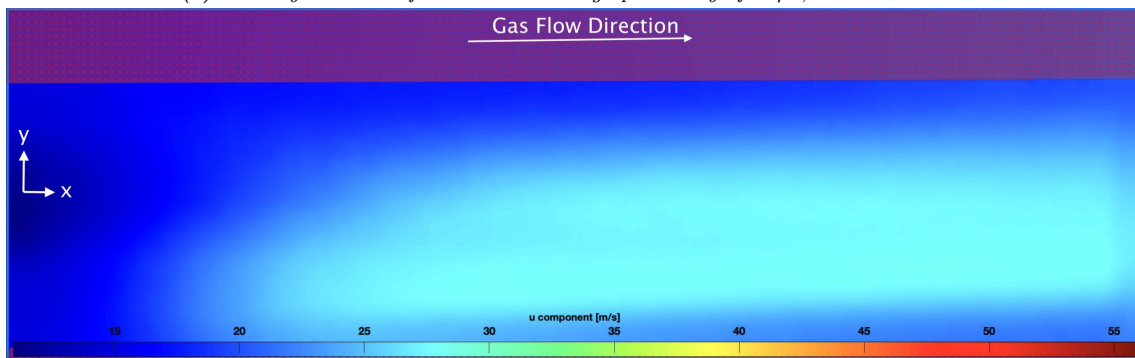
(a) Velocity Contour of TDV6 at an image pair delay of  $35\mu\text{s}$ , ROI 0-100mm.



(b) Velocity Contour of TDV6 at an image pair delay of  $50\mu\text{s}$ , ROI 0-100mm.



(c) Velocity Contour of TDV6 at an image pair delay of  $70\mu\text{s}$ , ROI 0-100mm.



(d) Velocity Contour of TDV6 at an image pair delay of  $90\mu\text{s}$ , ROI 0-100mm.

**Figure 4.4.5:** Velocity contours of four image pair delay times, contour range  $u_{min} = 10.96\text{m/s}$  -  $u_{max} = 55.87\text{m/s}$ .

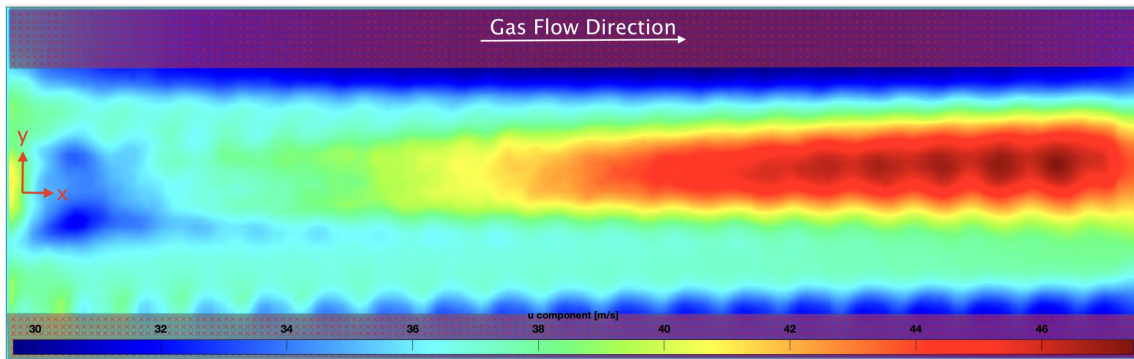


*Figure 4.4.6: Velocity contour of TDV6 at an image pair delay of  $50\mu\text{s}$  under its own auto scaled velocity contour. ROI 0-100mm.*

#### 4.4.5.2 PIV Capture Rate

The capture rate in PIV analysis refers to the rate at which pairs of images are acquired during the experiment. Selecting an appropriate capture rate is crucial to ensure short duration, allowing for effective temporal resolution in capturing rapid changes in fluid flow over time. This enables a higher degree of sensitivity to transient flow phenomena. Having a capture rate that is too high can also induce impacts regarding data overloading which increase processing demands. In a similar vein to effective mesh size in CFD analysis, there is an effective trade off between accuracy of analysis and increased computational expense as well as considerations for an appropriate resolution. It can also introduce a reduction in spatial resolution of the velocity field by limiting the particle displacement.

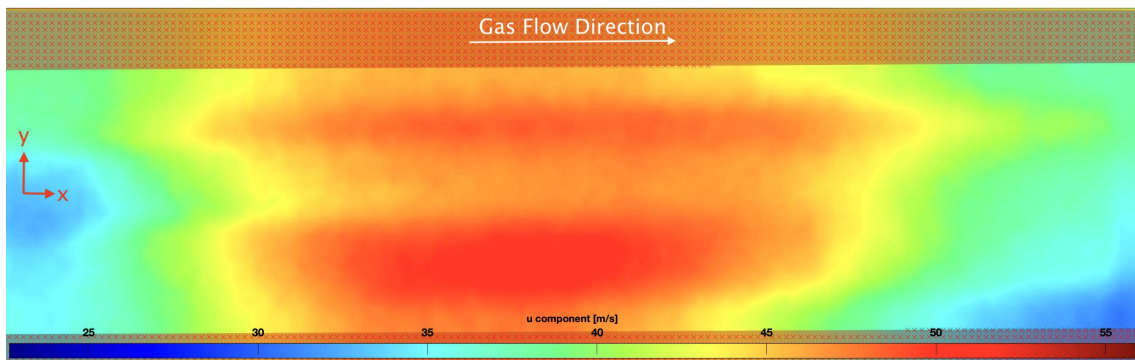
In Figure 4.4.7 below, the results of capturing rates equalling 3kHz, 4kHz and 5kHz respectively is shown. As is observed in Figure 4.4.7a, the capture rate is considered too slow to capture the fluid flow dynamics due to the longer time interval between successive image pairs. The analysis at  $3\text{kHz}$  overlooks changes in the fluid flow that occur resulting in an absence of critical flow features and dynamic behaviours.

Conversely, 4.4.7c depicts the expected fuel jet flow, yet due to the increased capture rate there is a reduction in the accuracy of the particle tracking. Due to the increased capture rate and the associated smaller time interval between images, a minimal particle displacement is observed, thus resulting in the lower velocities

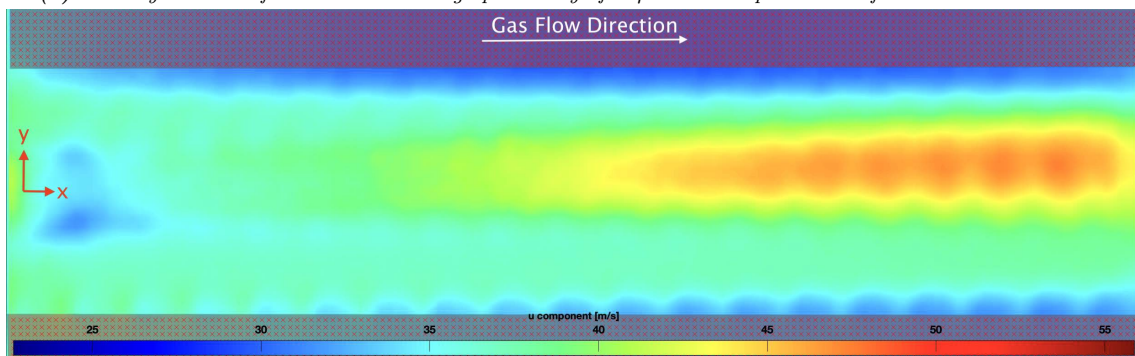


observed in Figure 4.4.7c and the lack of detail regarding the core jet of fuel in the flow.

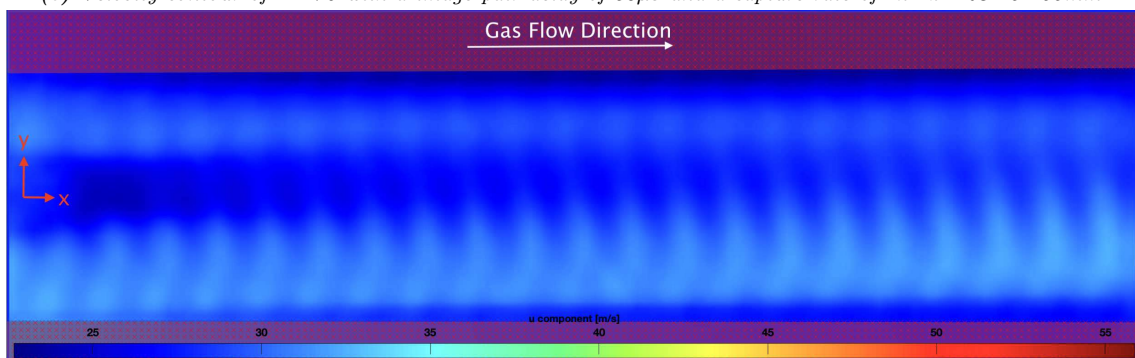
Thus, it was determined that a  $4kHz$  capture rate was optimum for the needs of this analysis of the fuel jet and oxidant flow mixing. This suggests that the temporal resolution and particle displacement is optimum for the analysis at hand by capturing this critical phenomenon in the flow, therefore, all analysis hereafter is performed at the capture rate of  $4kHz$ .



(a) Velocity contour of TDV6 with a image pair delay of  $50\mu s$  and a capture rate of  $3kHz$ . ROI 0-100mm.



(b) Velocity contour of TDV6 with a image pair delay of  $50\mu s$  and a capture rate of  $4kHz$ . ROI 0-100mm.



(c) Velocity contour of TDV6 with a image pair delay of  $50\mu s$  and a capture rate of  $5kHz$ . ROI 0-100mm.

**Figure 4.4.7:** Velocity contours of 3 capture rates, contour range  $u_{min} = 22.66m/s$  -  $u_{max} = 55.87m/s$ . ROI 0-100mm.

Observed in both Figure's 4.4.7b and 4.4.7c is the appearance of a repetitive flow

structure characterised by equispaced and periodic regions of velocity fluctuations. If this was a feature of the flow, it would decay in the downstream direction of the flow as the fuel and air flows homogenise. Recalling Figure 4.4.4, reflection in the quartz tube are observed where the density of light reflects the pattern observed in the processed image. Therefore, care must be taken to not mistake this as a flow feature when in actuality it is evidence of optical patternisation.

#### **4.4.6 Optimisation of Image Pre-Processing and Analysis Settings.**

Vital to the processing of the PIV data, image pre-processing and analysis settings are optimised. Given their interdependence in producing results of varying quality, their evaluation is conducted in tandem. This was performed through a parametric study of pre-processing and analysis settings, which are described in Table 4.5 and Table 4.6, respectively. Throughout this analysis the two sets of images were taken for each test point where the capture window included the following axial positions: (i) 0 – 100mm from nozzle exit and (ii) 100 – 200mm from the nozzle exit. This was chosen to ensure good continuity of data across the test point and to ensure that the settings evaluated were suitable for both the highly transient region between 0 – 100mm and the more developed flow associated with 100 – 200mm.

The calibration values used throughout were a Reference Length of 360.56px, that equated to a real distance of 28.5mm, with a time step of 0.05ms. This in turn produced a pixel/frame movement equal to 1.5809ms<sup>-1</sup>. The pre-processing test conditions are reported in Table 4.5, below.

**Table 4.5:** Table representing the PIV pre-processing settings.

PIV_EVAL#	CLAHE [1/0]	CLAHE [px]	High pass [1/0]	High pass [px]	Intensity Capping [1/0]	Wiener denoise [1/0]	Wiener denoise [px]	Background subtraction [1/0]
PIV_EVAL1	0	0	0	0	0	0	0	0
PIV_EVAL2	0	0	0	0	0	0	0	0
PIV_EVAL3	0	0	0	0	0	0	0	1
PIV_EVAL4	1	64	0	0	0	0	0	1
PIV_EVAL5	1	64	1	15	0	0	0	1
PIV_EVAL6	1	64	1	15	0	1	2	1
PIV_EVAL7	1	32	1	15	0	1	2	1
PIV_EVAL8	1	64	1	32	0	0	0	1

**Table 4.6:** Table representing the PIV analysis settings.

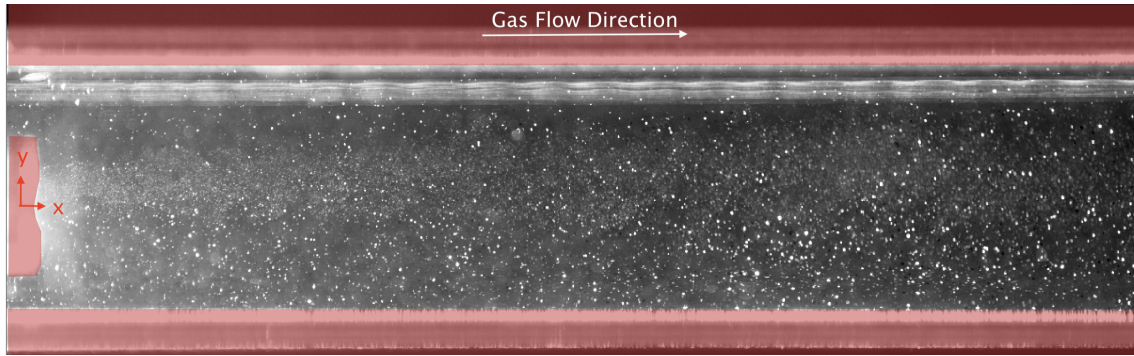
PIV_EVAL#	Algorithm	Pass 1 [px]	Pass 2 [px]	Pass 3 [px]	Pass 4 [px]
PIV_EVAL1	FFT	64	32	16	0
PIV_EVAL2	FFT	128	64	32	16
PIV_EVAL3	FFT	128	64	32	16
PIV_EVAL4	FFT	128	64	32	16
PIV_EVAL5	FFT	128	64	32	16
PIV_EVAL6	FFT	128	64	32	16
PIV_EVAL7	ENSEMBLE	128	64	32	16
PIV_EVAL8	ENSEMBLE	128	64	32	16

Furthermore, the settings for the PIV analysis also required assessment. The settings considered are reported in Table 4.6, below.

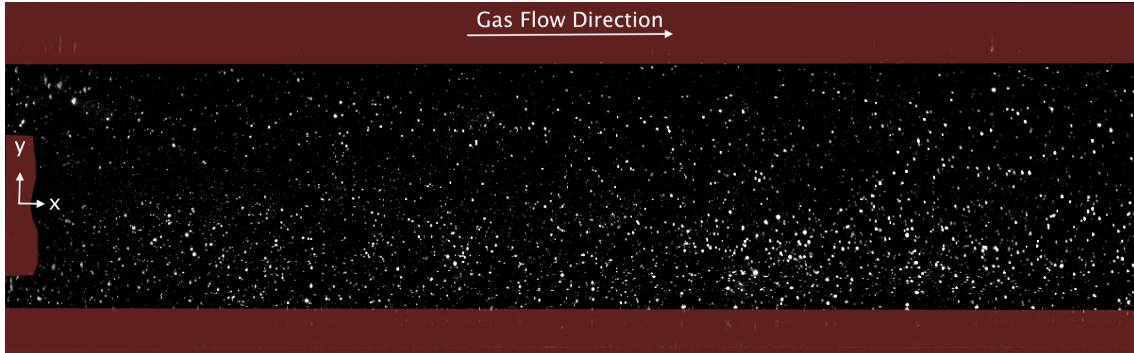
Through the evaluation of PIV\_EVAL1, it was determined that the analysis settings relating to the various passes of the interrogation window were not suitable due to an error warning describing that the interpass-validation discarded a proportion of the vectors in a given pass. This was coupled with the suggestion to increase the interrogation area size of Pass 1 to 128 pixels. As is described by Table 4.6, this was altered for the subsequent test points where the error was no longer present.

Highly discernible between Figures 4.4.8a and 4.4.8b, the inclusion of the background subtraction was very powerful for the processing of the image to ensure clear particles are seen by the PIVlab analysis operation. The omission of light reflections within the tube that are observable in Figure 4.4.8a and are not within Figure 4.4.8b.

As detailed in Table 4.5, the inclusion and adjustment of other filters such as CLAHE (contrast-limited adaptive histogram equalisation - that acts by enhancing the contrast within the images locally), High Pass (omitting particles of a given upper threshold in pixel size, that would impact the correlation signal [187]) and Wiener Denoise (purpose is to identify noise in the acquired images and remove it) were also evaluated. Their comparison is omitted at the pre-processing stage due



(a) Pre-processed PIV image without any background subtraction. ROI 0-100mm.



(b) Pre-processed PIV image with the inclusion of background subtraction. ROI 0-100mm.

**Figure 4.4.8:** Comparison between pre-processed images using the background subtraction function.

to the relative indifference shown in the pre-processed images, although, they did impact the results of the subsequent analysis.

After reviewing the pre-processing settings, test point PIV\_EVAL6, depicted below in Figure 4.4.9, was chosen due to its ability to yield the most relevant results in the FFT analysis.

This prompts the question: should any pre-processing of the images be undertaken? To address this, an examination of velocity contours from PIV\_EVAL2 and

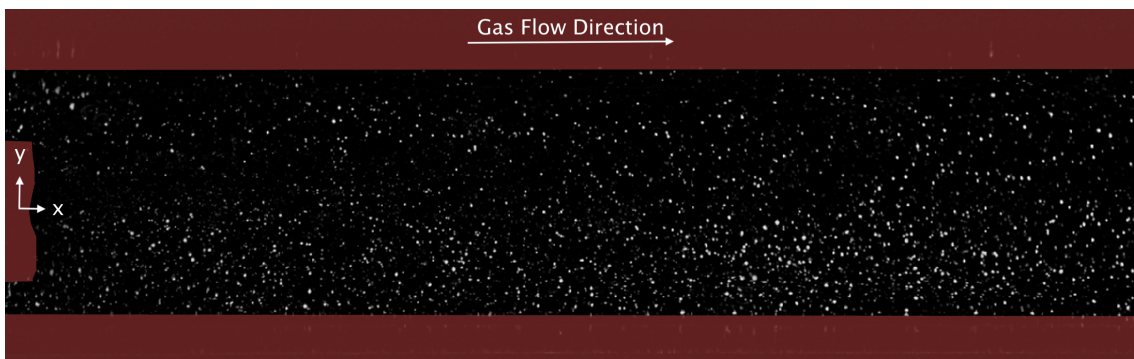
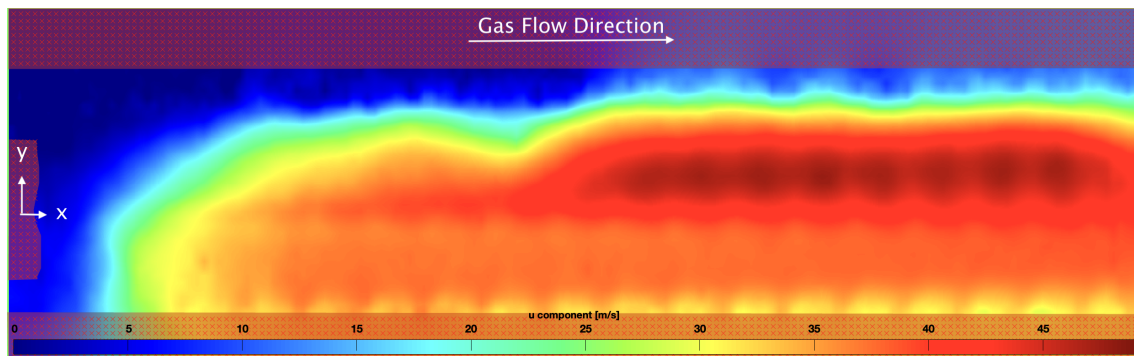
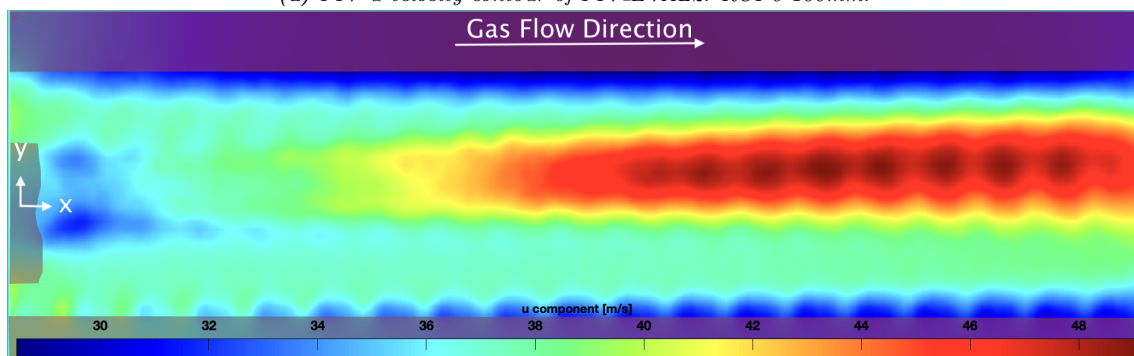


**Figure 4.4.9:** Pre-processed image of PIV\_EVAL6. ROI 0-100mm.

PIV\_EVAL6 was performed, maintaining identical analysis settings. In the absence of image pre-processing (PIV\_EVAL2), velocities at the nozzle exit were noticeably underestimated, and the rest of the flow lacked the same level of detail in flow dynamics compared to optimal pre-processing results (PIV\_EVAL6). This discrepancy is illustrated in Figure 4.4.10.



(a) PIV  $u$ -velocity contour of PIV\_EVAL2. ROI 0-100mm.



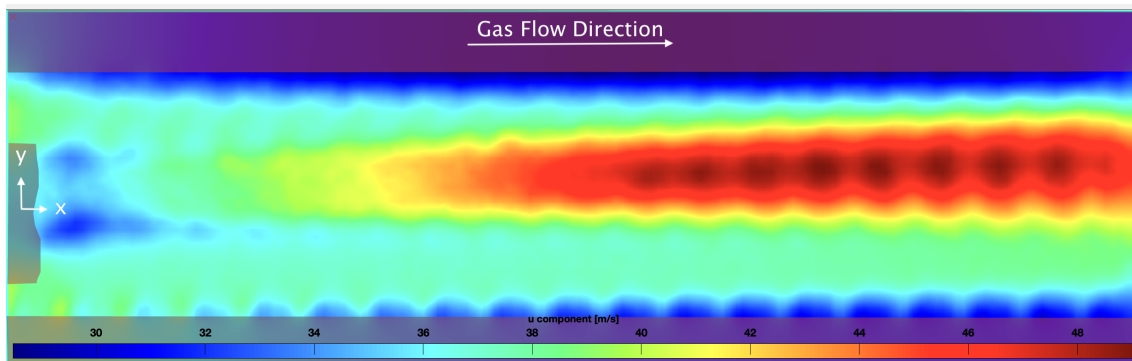
(b) PIV  $u$ -velocity contour of PIV\_EVAL6. ROI 0-100mm.

**Figure 4.4.10:** Comparison between  $u$ -velocity contours, under the same contour limits.

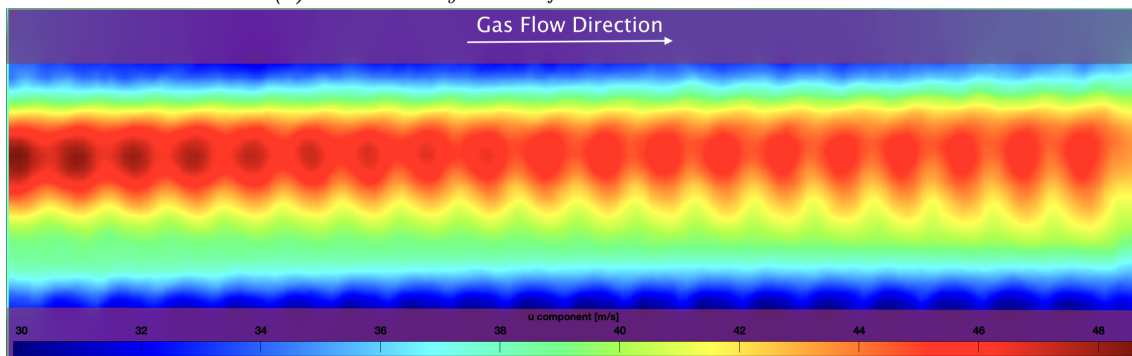
Since the necessity of image pre-processing had now been determined a refinement of the analysis settings was investigated, as detailed in Table 4.5. This necessitated the inclusion of both captured regions, i.e. 0 – 100mm and 100 – 200mm to determine the coherence between the two image sets. The ability to stitch images together is limited by the inclusion of images in PIVlab, hence, the following Figures display the first 0 – 100mm and the second 100 – 200mm range separately, as (a) and (b) within their own Figure environment, respectively.

Whilst there are marginal observable differences between them, PIV\_EVAL6 showed the best continuity between the extractable velocity fluctuation data from the PIV analysis from the two imaging windows that would later be used for data



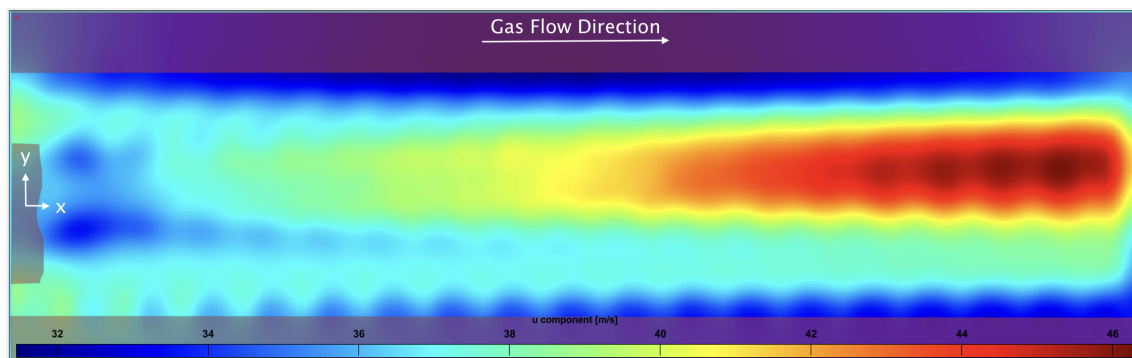


(a) PIV u-velocity contour for PIV\_EVAL3. ROI 0-100mm.

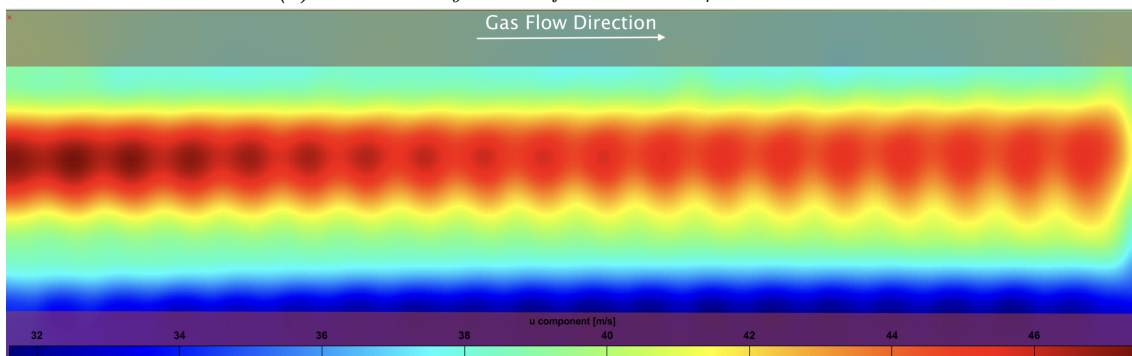


(b) PIV u-velocity contour for PIV\_EVAL3. ROI 100-200mm.

Figure 4.4.11: PIV u-velocity contour for PIV\_3 across both imaging windows.

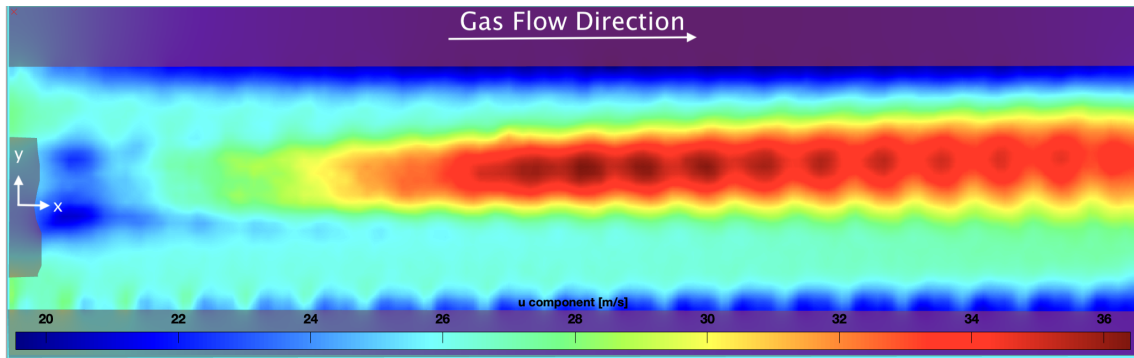


(a) PIV u-velocity contour for PIV\_EVAL4 ROI 0-100mm.

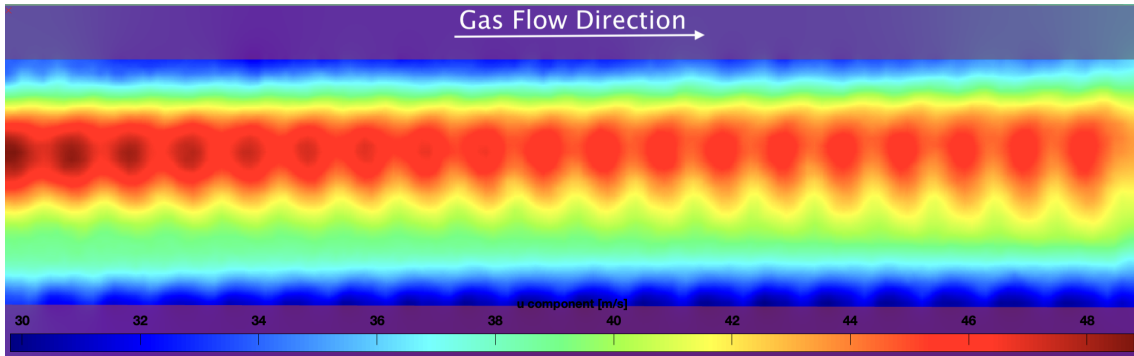


(b) PIV u-velocity contour for PIV\_EVAL4 ROI 100-200mm.

Figure 4.4.12: PIV u-velocity contour for PIV\_4 across both imaging windows.

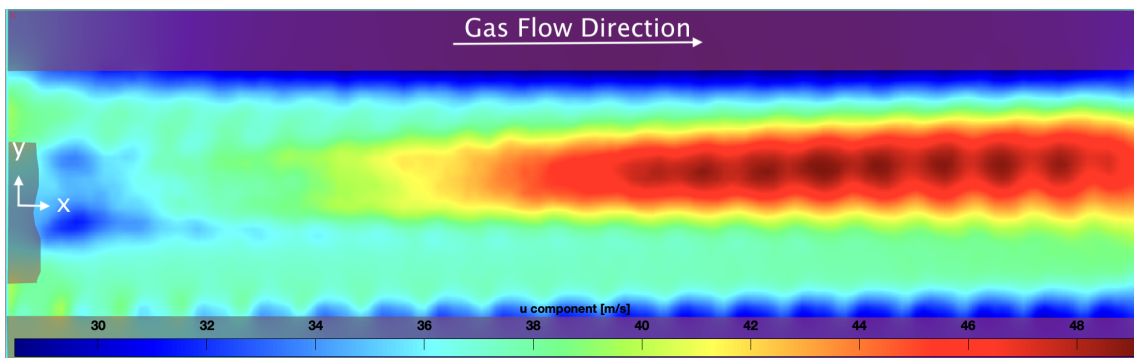


(a) PIV u-velocity contour for PIV\_EVAL5 ROI 0-100mm.

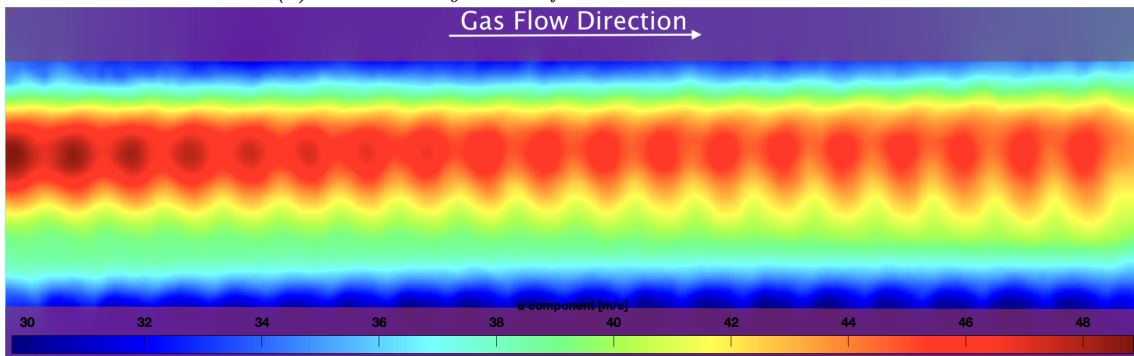


(b) PIV u-velocity contour for PIV\_EVAL5 ROI 100-200mm.

Figure 4.4.13: PIV u-velocity contour for PIV\_5 across both imaging windows.



(a) PIV u-velocity contour for PIV\_EVAL6 ROI 0-100mm.



(b) PIV u-velocity contour for PIV\_EVAL6 ROI 100-200mm.

Figure 4.4.14: PIV u-velocity contour for PIV\_6 across both imaging windows.



processing, hence, PIV\_EVAL6 was selected as the optimum conditions through the FFT analysis.

Furthermore, the ensemble analysis method was also analysed. However, when the extractable data was subsequently used for analysis (as will be described in Section 4.4.7), the ensemble method of analysis only returned a mean data set when extracted. Since the following analysis would include the determination of the turbulence intensity that relies on velocity fluctuation data, the consideration of ensemble analysis was excluded.

#### 4.4.7 Methods of PIV Analysis of Varying Turbulence Devices

PIV analysis was performed in order to distinguish a difference between the turbulence characteristics of the different turbulence devices deployed in the experimental campaign. This involved determining the Turbulence Intensity (TI) at the inlet to the MD and assessing the turbulent lengthscales resulting from the three TDVs considered.

##### 4.4.7.1 Turbulence Intensity

TI is determined through the Reynolds decomposition described by equation 4.3 below.

$$u(t) = U_{mean} + u'(t) \quad (4.3)$$

where  $U_{mean}$  denotes the mean velocity of the flow and  $u'(t)$  denotes the given velocity fluctuation at a given time  $t$ . Hence, it was necessary to determine the mean velocity of the flow, which was provided by PIVlab and subsequently determine  $u'(t)$  by determining the instantaneous velocity provided by the image pairs. This enabled the determination of the TI by the following equation:

$$TI = \frac{u_{RMS}}{U_{mean}} \times 100\% \quad (4.4)$$

Similarly, analysis was also replicated for the radial velocity profile in the  $v$  direction.

This was achievable by the fact that the FFT analysis of the capture PIV data would return instantaneous velocity values across the imaged window for a given image pair. Hence, if 1,000 images were taken, this returned 500 image pairs which would provide 500 instances of instantaneous velocities. The analysis of which to determine the TI was performed by a developed MATLAB script, that is given in Appendix B.4.2, and is described by the following steps:

1. From the PIV data, u- and v-velocity components were determined for both the instantaneous and mean velocities, across the two imaged windows and are imported into MATLAB.
2. Since the data for the velocities of a given image pair and the mean are provided in a singular matrix cell, it was necessary to remove the mean velocity matrix of a given cell and assigned to its own matrix.
3. Following the removal of the mean flow values, the matrices from the two imaged windows were concatenated to present the data across the  $200mm$  domain considered.
4. The resulting fluctuating components were determined by using the ‘if’ loop function to subtract the instantaneous velocity from the mean velocity, in accordance with the Reynolds decomposition described above, for both u- and v-velocity components.
5. The root-mean squared of the fluctuating velocities was determined using  $u_{RMS} = \sqrt{\frac{\sum u_i^2}{N}}$ , where  $N$  denotes the number of samples taken.
6. The root-mean squared values of the velocity fluctuations were used in Equation 4.4 to ascertain the directional TI.
7. The resulting TI from both the u- and v-velocity components were combined to produce a resultant TI.

8. This MATLAB script returned a TI contour, radial velocity and TI profiles; and centreline profiles for both the TI and the velocity.

#### 4.4.7.2 Turbulent Lengthscales

In addition to TI, determining the turbulent lengthscales in the flow was desirable. The lengthscales of interest were the Integral Lengthscale and the Kolmogorov lengthscale, representing the largest and smallest characteristic lengthscales within a turbulent flow, respectively.

These lengthscales were determined through use of the MATLAB script detailed in Appendix B.5.2. It operates on the following principles:

1. The determination and separation of the fluctuation velocities and mean velocity matrices is performed.
2. FFT analysis was performed on the fluctuating velocity matrices through use of a 'for' loop.
3. A power spectra of the velocities analysed by FFT is performed following this equation:  $PowerSpectra = u_{FFT}^2$
4. The power spectra was summed together and divided by the number of velocity matrices analysed to provide a time average power spectra.
5. The associated wave numbers was calculated by:  $k = 2\pi f$ , where  $f$  is the sample rate of the PIV data taken.
6. Furthermore, the peak wavenumber  $k_{peak}$  in the power spectra is determined and corresponds to the integral length scale by the following equation:  $L = \frac{2\pi}{k_{peak}}$ .
7. The power spectra is then plotted against the wavenumber, in which the minimum wavenumber is determined.
8. The Reynolds number of the flow is determined. Which enabled the use of the following equation to determine the Kolmogorov lengthscale:  $\eta = \frac{L}{Re^{3/4}}$ .

#### 4.4.8 PIV Methodology Conclusions

This section introduces PIV as a technique, along with the equipment used for analysis. The methodology, including the use of scaling through dynamically similar conditions, is described. A parametric study of data acquisition and image processing settings is presented, outlining how the optimal settings were determined. Furthermore, the methods employed in analysing the acquired data are introduced.

### 4.5 Data Acquisition Techniques

In order to characterise the influence of turbulence on the ignition of hydrogen-enriched fuels, two non-intrusive diagnostics were developed. These techniques were employed to determine the LFH, FET and a calculated Ignition Delay Time ( $\tau_{IGN}$ ). Damköhler Numbers are also derived to inform upon the role of the fluid mixing rate and the chemical reaction rate and their relative influence within the test points analysed.

The apparatus used to ascertain LFH has been previously utilised in other studies conducted at Cardiff University's Gas Turbine Research Centre (GTRC). However, modifications were introduced to the methodology regarding data acquisition and image processing, which will be covered in the subsequent sections. The apparatus employed to determine FET was specifically designed and implemented for the experimental campaign relating to this thesis. In this analysis emphasis was placed on the Hydroxyl OH\* free radical for the following reasons [188]:

- The presence of the OH\* radical signifies the initiation of the combustion reaction, as hydroxyl is among the initial stages in the combustion chain reaction. Its presence indicates consumption of reactants, notably H and O, and thus confirms the occurrence of combustion.
- Many of the chemical pathways that are taken by reactants as they are processed into products are sustained or initiated by the OH\* radical as an inter-

mediary.

### **4.5.1 Measured Lifted Flame Height**

As a measure of the reactivity exhibited by a specific fuel blend within distinct turbulent conditions, the concept of LFH was employed for assessment. Given that achieving autoignition in non-uniform mixtures requires sufficient time for both mixing and chemical processes of combustion to reach critical conditions, it is anticipated that fuel blends with lower reactivity, will result in a flame stabilising at a greater distance downstream in the MD, compared to more reactive blends. Consequently, instances characterised by lower reactivity, whether due to the type of fuel blend used or the turbulence present, will manifest longer LFHs.

#### **4.5.1.1 LFH: Measuring Equipment and Experimental Set-up**

To determine the LFH a High Speed OH\* Chemiluminescence imaging system was deployed comprised of a Phantom v1212  $4kHz$  high-speed Complementary Metal-Oxide-Semiconductor (CMOS) camera, Specialised Imaging SIL40HG50 high-speed image intensifier, UV lens (78mm, f/11), and a TECHSPEC 10nm Bandpass Filter with a Centre Wavelength of  $310 \pm 2nm$ . The optics set up had the following settings; capture rate of 4000 frames/second, gain of 3dB, exposure time of  $10\mu s$  and a delay of  $55ns$ .

The imaging set up was also focused onto a target focal point in the centre of the MD that would enable the correct imaging to take place under experimental conditions.

#### **4.5.1.2 LFH Measurement and Data Processing Methodology**

Within the body of research literature, an array of methodologies relating to the acquisition of chemiluminescence measurements exists. These encompass diverse techniques, including the calculation of time-averaged intensity values, application of background corrections, utilisation of deconvolution algorithms, and implementation

of Abel transformations.

Considering the nature of chemiluminescence as a line-of-sight technique, the measured light intensities are inherently integrated. This integration encompasses signals originating both behind and ahead of the focal plane, established by the practice of focusing onto a predefined target during the experimental setup. Consequently, to extract spatially-resolved information concerning the localisation of heat release zones, the images must undergo a deconvolution process. The Abel Deconvolution process works on the basis of a Fourier series-like expansion that projects the radial pixel intensity onto a theoretical 2D plane by use of a cosine expansion, as described by Runyon [113]. During the Deconvolution process, symmetry is assumed around the central axis. Therefore, the geometry of the MD that is square and the lack of a swirling component in the flow makes the case considered in this experimental campaign ideal for Abel Deconvolution analysis.

This process involves the application of a modified algorithm within MATLAB, composed of functions specifically developed by Runyon [113] and Killer [189]. A copy of the modified algorithm can be found in Appendix B.3.2. A large number of images are taken during the relatively short duration of a test point ( $\approx 10$ s), however only the first 2,000 images of the last 3,000 were typically used for analysis, as this was deemed as point of stability with the flame. This corresponded to performing the analysis over 0.5s of the flame's operation. Operator experience was used to determine whether a test point, by qualitatively determining whether seed densities were appropriate for further in the captured images were suitable for analysis i.e. there were no misfiring of the seeding system and that flow patterns were identifiable.

Prior to the processing of data, a background image of the TIMAR was used to determine the pixel location of the fuel lance tip. The background image would be taken when the test rig is hot to account for any thermal expansion of the material.

The algorithm itself worked on the following principles:

- Flame images were called into the algorithm in Multi-TIFF format.
- Prompts required the user to input the traverse position of a given test point.

- The x pixel position of the lance tip is also inputted, as determined from the aforementioned background image analysis.
- The additional number of columns to introduce into the image matrix was discerned and added to the image which depended on the traverse position to provide scaled images.
- A mean image was determined by creating a zeroed matrix of equal size to the image, reading in all the images and adding them to the zeroed matrix. The image matrix was then averaged by the number of pictures used to provide a mean image. The mean image is also treated with a median filter and a sharpening function to highlight finer details, reduce impulse noise and preserve edges. The Mean Image was converted into an 8-bit integer and greyscaled.
- The Abel Deconvolution function developed by Killer [189] determines a matrix size for analysis from the mean image. The centreline of the image was determined to perform the deconvolution around the central axis. This function utilises ‘`compute_expansion.m`’ ‘`solve_lsq.m`’ and ‘`generate_test_data.m`’ also developed by Killer [189]. The image is processed where each image is converted into double precision.
- The image size was adjusted and converted to greyscale.
- The flame edge was then determined which was defined as the boundary in which the OH\* threshold is 30% of the max intensity, as per studies undertaken at ETH Zurich [167] [168] [169]. Whilst it is acknowledged that OH\* intensities vary for the evaluated fuel blends, it was deemed highly valuable to maintain consistency in measurements across the experimental campaign.
- The LFH was then calculated as the distance from the fuel lance tip to the 30% OH\* threshold.
- An image was processed for display.

## 4.5.2 Measured Flame Establishment Time

As a means of determining the time for the flame to establish, a photomultiplier tube (PMT) setup was deployed. Its aim was to support conditions in which the LFH may be similar, or even attached flame, (i.e. higher H<sub>2</sub> cases) and aims to discern a difference between the blends with respect to the time taken for the flame to establish. It is emphasised that due care must be taken over the description of the parameter that the PMT setup is measuring. The PMT measures the time taken for the OH\* signal to pass a noise threshold, to the time of the first significant peak of the OH\* signal.

Ignition is defined as the process of initiating the combustion of a given substance, under particular conditions, resulting in the production of heat and light that results in a self sustaining release in the form of a flame. This includes the mixing timescales, the initial slow low-temperature ignition chemistry, followed by thermal runaway that is very notable characteristic of ignition events.

Since this measurement does not take into account the mixing or low-temperature chemistry, it cannot be defined as the ignition delay time. Since the PMT setup is limited to measuring the time from initial OH\* signal to first significant peak, it is measuring the time taken for thermal runaway to initiate and for the flame to establish itself. Hence, the parameter is defined as the “*Flame Establishment Time [FET]*” – which is defined as the following: “*Flame Establishment Time is defined as the time taken from the initial voltage reading to surpass the noise level threshold to the first significant peak in the OH\* intensity recorded by the PMT*”. This method was deployed for all fuel blends evaluated in the experimental campaign.

To the authors knowledge this a novel means of evaluating the character in which the thermal runaway facet of the ignition process unfolds as this body of work aims to address the impact of turbulence on the ignition of hydrogen enriched methane fuel blends.



### 4.5.3 FET: Measuring Equipment and Set-up

The emitted light from the flame was detected through use of a Hamamatsu H9306-09 PMT, that is comprised of a multialkali photocathode. The PMT has a 20kHz capture rate and a spectral response of 185nm to 900nm. The PMT was powered by a Hamamatsu C7169 power supply which drove the voltage to obtain a voltage signal from the PMT. Both PMT and PMT Power supply are shown in Fig 4.5.1.

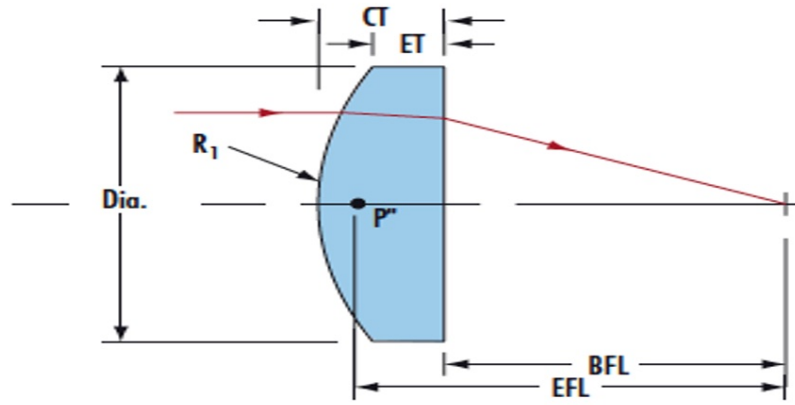


(a) Hamamatsu H9306-09b PMT set-up within the Rig Room (b) Accompanying Power Supply - Hamamatsu C7169, image reproduced from [190]

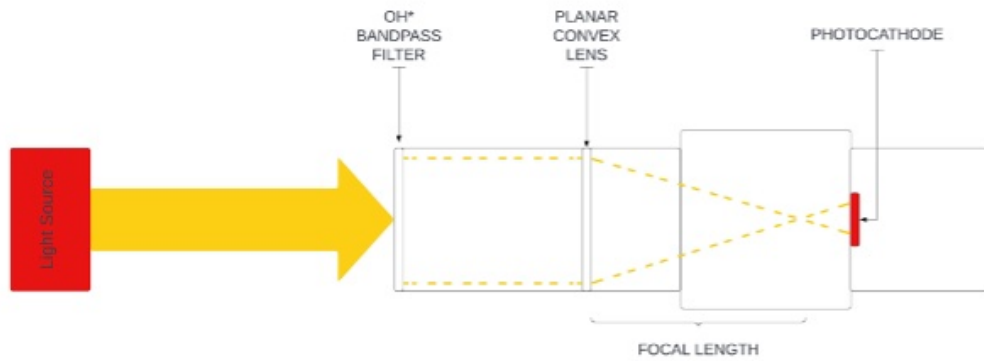
**Figure 4.5.1:** Hamamatsu PMT Components

A bandpass filter lens (centre wavelength of  $310 \pm 2 \text{nm}$ ) was placed in front of the PMT set up to only capture the light of the  $\text{OH}^*$  radical when combustion is taking place.

A set of UV Plano-Convex (PCV) Lenses (TECHSPEC UV Fused Silica Plano-Convex - Corning 7980 material) were been positioned in such a way as to collimate the filtered light onto the PMT to achieve max signal to noise ratio when a measurement was being taken. The setup was determined through careful selection of a PCV lens with an appropriate focal length. A depiction of focal length and other important PCV lens parameters is presented in Figure 4.5.2a, where  $R_1$  denotes the radius of curvature of the PCV lens,  $CT$  and  $ET$  denote to the central and edge thickness of the lens,  $EFL$  and  $BFL$  denote the effective and the back focal length, respectively. Figure 4.5.2b shows the process of the light passing through the filter and its interaction with the planar convex lens.



(a) Schematic of important geometry of the PCV lens



(b) Schematic of light path taken by the light as it interacts with the PMT set up.

**Figure 4.5.2:** Schematics of PCV lens geometries and PMT-light interactions.

Since combustion occurred at various lengths along the MD and given that both the chemiluminescence and PMT have a restricted field of vision, it was necessary to house both measurements devices on a remote control traverse. It was vital to ensure that the chemiluminescence camera was perpendicular to the MD, and considering the PMT only required to detect light, the PMT was oriented so that the PMT would detect light at the centre of the chemiluminescence camera's imaging window, as described by Figure 4.5.3.

#### 4.5.4 Calculated Ignition Delay Time

Since there are the deficiencies in the use of the PMT setup for the FET in establishing an ignition delay time, a calculated ignition delay time ( $\tau_{IGN}$ ) was determined.

And is described by the following equation:

$$\tau_{IGN} = \frac{U_{MW}}{LFH} \quad (4.5)$$

where LFH denotes the measured LFH from the chemiluminescence technique described above and  $U_{MW}$  denotes a mass weighted velocity of the bulk flow, inclusive of the oxidant velocity and the calculated fuel velocity, described by the following equation:

$$U_{MW} = \frac{\dot{m}_{fuel}u_{fuel} + \dot{m}_{air}u_{air}}{\dot{m}_{fuel} + \dot{m}_{air}} \quad (4.6)$$

The determination of the mass weighted velocity is an approach developed by the author to account for the average bulk velocity in the mixing duct. Whilst this method may underpredict the centreline velocity resulting from the high flow velocities of the fuel jet, it was deemed a good account of the average bulk velocity experienced within the mixing duct. The calculated  $\tau_{IGN}$  now has the means of describing the whole ignition process inclusive of the mixing and initial slow chemistry that was absent the in the FET analysis.

#### 4.5.5 Calculated Damköhler Number

Furthermore, the determination of  $\tau_{IGN}$  enabled the calculation of the non-dimensional Damköhler number that is defined by the following:

$$Da = \frac{\text{Mixing Time Scale}}{\text{Chemical Reaction Time Scale}} = \frac{|\tau_{IGN} - FET|}{FET} \quad (4.7)$$

Which describes the ratio between the transport mixing time scales and the chemical reaction time scales [191]. Its significance in the context of combustion is that it describes whether the combustion is being driven by the chemical time scales ( $Da < 1$ ) of the reaction since the reaction proceeds faster than the reactants can mix, or whether it is diffusion controlled ( $Da > 1$ ), where the rate of the reaction is primarily controlled by the mixing or transport to the reaction sites.

## 4.6 Uncertainty Analysis

An uncertainty analysis was conducted on the forthcoming experimental results to be presented in Chapter 5. While the uncertainty analysis encompassed all conducted test points, for the sake of brevity, the maximum uncertainty value identified for each parameter is reported. This approach aims to describe the most significant uncertainties associated with the operation of the TIMAR and the derived results.

### 4.6.1 Direct Measurements

The uncertainty associated with the direct measurements in the TIMAR are now described. Not only do they offer measured values, but they are also subsequently used in the calculation of other parameters that will be introduced in Section 4.6.2, and hence, their uncertainty must be known.

To measure the air flow into the electric air heater, a SICK FTMG-ISD20AXX volumetric flow meter was combined with a type-K thermocouple to perform air mass flow calculations for the air flow into the heater. The measurement accuracy of the volumetric flow meter is  $\pm 3\%$  of the measured value. The type-K thermocouple offers a measurement accuracy of  $\pm 1.5^\circ C$  over the range  $-40^\circ C$  to  $+375^\circ C$ , which is within the range of air temperature's delivered to the heater inlet. Temperatures outside of this operating range, that is,  $375^\circ C$  to  $1100^\circ C$  are subject to an uncertainty of  $\pm 0.4\%$  of the measured value. It should be noted that if the extended test matrix with the varying of the singular flue gas component and the industrial relevant conditions are evaluated, then the uncertainty would propagate further due to the inclusion of additional instrumentation to control the experiment.

The uncertainty associated with the LFH is a function of both the resolution of the chemiluminescence images and the accuracy of the traverse that houses the camera, since the traverse would be repositioned to capture the flame in the mixing duct in the less reactive cases. The resolution of the chemiluminescence image is  $6.82 \text{ px/mm}$ , and therefore has a resolution  $\sigma_{chemi} = \pm 0.1466 \text{ [mm]}$ . The resolution

of the traverse is governed by the number of pulses per millimetre that the traverse operates upon. This was set to 160 pulses per millimetre, hence the resolution of the traverse  $\sigma = \pm 0.00625 [mm]$ . To obtain the uncertainty of LFH measurement, the uncertainties of the chemiluminescence and traverse were combined following a root-squared sum, that take the following form:

$$\sigma_{RSS} = \sqrt{\sum_{i=k}^k \sigma_i^2} \quad (4.8)$$

where  $\sigma_i$  is the uncertainty associated with given variable  $i$ . Hence, the uncertainty of the LFH measurements is given as:  $\sigma_{LFH} = \pm 0.1467 [mm]$ .

The uncertainty of the FET measurements is a function of the capture rate of the PMT. Since the capture rate is set to  $20kHz$  throughout the test campaign the uncertainty associated with FET measurements is given as:  $\sigma_{FET} = \pm 0.00005 [s]$ .

The operation of mass flow controllers for the fuel delivery also carried an uncertainty of  $\sigma_{MFC} = \pm 0.5\%$  of the measured values, whether the M13 or M14 mass flow controller was utilised.

## 4.6.2 Calculated Variables

All other reported variables are a function of some form of calculation. Hence, their combined uncertainty is determined through use of the Gaussian uncertainty propagation formula, which is described in its general form as:

$$\sigma_q = \sqrt{\left(\frac{\partial q}{\partial x_1} \sigma_{x_1}\right)^2 + \left(\frac{\partial q}{\partial x_2} \sigma_{x_2}\right)^2 + \dots + \left(\frac{\partial q}{\partial x_n} \sigma_{x_n}\right)^2} \quad (4.9)$$

The uncertainty associated with the  $\tau_{IGN}$  results is a function of the mass-weighted velocity described by equation 4.6. Hence, the uncertainty associated with the mass flow of fuel and air; and the air and fuel velocities were calculated to enable the determination of  $\sigma_{\tau_{IGN}}$  which was calculated to be  $\sigma_{\tau_{IGN}} = \pm 0.006663 [s]$ .

Furthermore, the determination of Damköhler Number was subject to the uncer-

tainty of the FET and  $\tau_{IGN}$  measurements. Hence, using equation 4.9 its maximum uncertainty was determined to be  $\sigma_{Da} = \pm 0.1774$ .

### 4.6.3 Uncertainty Analysis Conclusion

All the uncertainties associated with the measured values and the described calculations are provided in Table 4.7, below. The uncertainties reported denote the highest value of uncertainty for any given test point studied within the experimental campaign, emphasising the conservative approach taken in quantifying and presenting the potential variations in the data. This comprehensive overview enables a thorough understanding of the potential variability in the results, supporting robust interpretations and decisions based on the experimental findings.

## 4.7 Experimental Methodologies Conclusions

This chapter details the development of the test philosophy, which informed the testing methodologies applied in this study. The evaluation of flow fields concerning the three TDVs used in the experimental campaign is introduced through PIV. Additionally, the techniques and methodologies developed within the experimental campaign to either measure or calculate the dependent variables for assessing the impact of turbulence on the ignition of hydrogen-enriched fuels are described. Furthermore, an analysis of the largest uncertainties associated with all direct measurements and calculated variables is introduced.

**Table 4.7:** Table of the largest uncertainties associated with each parameter considered by the experimental study relating to the TIMAR.

Variable	Symbol	Uncertainty	Unit	Measured or Calculated
Fuel Mass Flow	$m_{fuel}$	$\pm 0.5$	%	Measured
Temperature	$T$	$\pm 1.5$	$^{\circ}C$	Measured (-40 $^{\circ}C$ to +375 $^{\circ}C$ )
Temperature	$T$	$\pm 0.4\%$ of measured value	%	Measured (375 $^{\circ}C$ to 1100 $^{\circ}C$ )
Air Volumetric Flow	$Q_{air}$	$\pm 3.0\%$ of measured value	%	Calculated
LFH	$LFH$	$\pm 0.1467$	$mm$	Calculated
FET	$FET$	$\pm 0.00005$	$s$	Measured
Air Mass Flow	$\dot{m}_{air}$	$\pm 0.7125$	$g/s$	Calculated
Air Velocity	$u_{air}$	$\pm 0.01947$	$m/s$	Calculated
Fuel Velocity	$u_{fuel}$	$\pm 1.72$	$m/s$	Calculated
Mass-Weighted Velocity	$U_{MW}$	$\pm 0.0003724$	$m/s$	Calculated
Ignition Delay Time	$\tau_{IGN}$	$\pm 0.006653$	$s$	Calculated
Damköhler Number	$Da$	$\pm 0.1774$	[-]	Calculated

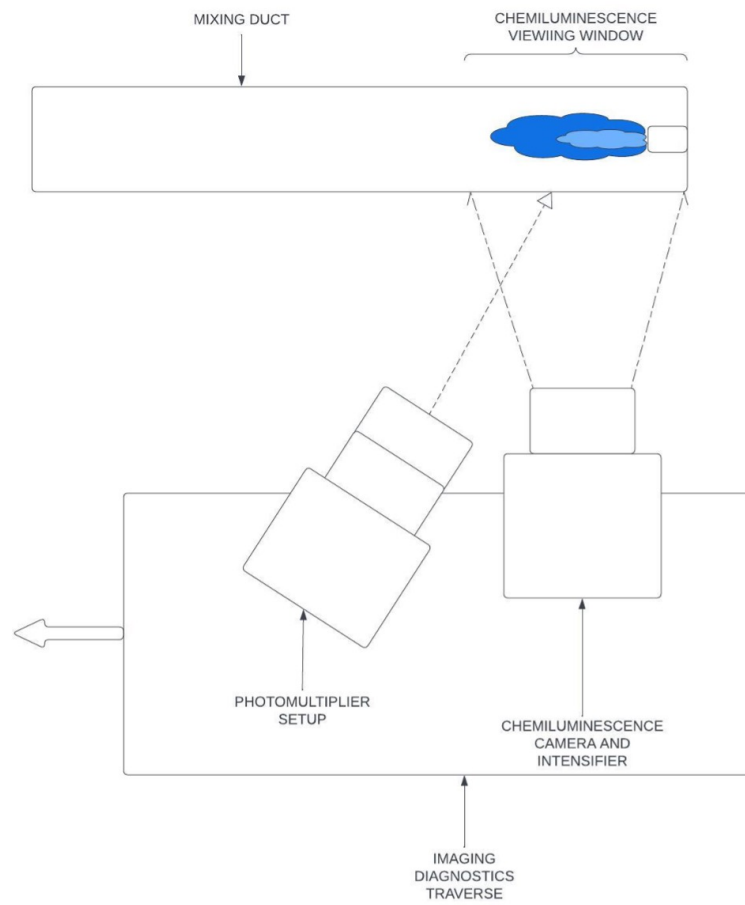


*Figure 4.5.3: Plan view of PMT and chemiluminescence camera set up on the traverse, schematic not to scale.*



# Chapter 5

## Turbulence and Temperature Effects on Autoignition of Hydrogen Enriched Fuels

In this chapter, the experimental testing results are analysed, firstly presenting the results of the PIV analysis followed by the results of investigating the influence of the oxidant temperature and the effects of turbulence as the controlled variables on the ignition of hydrogen enriched fuel blends. The PIV results inform the turbulence characteristics that were present in the use of the three Turbulence Devices (TDV) used in this study. The combustion experimental results describes the impact of the controlled variables on various dependent variables, including Lifted Flame Height (LFH), Flame Establishment Time (FET), the calculated Ignition Delay Time ( $\tau_{IGN}$ ), and the Damköhler number of the flame, determined through the methodology presented in Chapter 4. In each case the fuel blends considered range from 80/20 [%vol] to 0/100 [%vol] ( $\text{CH}_4/\text{H}_2$ ) and an air mass flow of 23.75g/s is maintained throughout.

## 5.1 Particle Image Velocimetry - Results

Herein, the results of the PIV analysis are presented, where the TI and lengthscales of turbulence for each TDV are described. This culminates in figure's presenting the centreline profiles of the velocities and the TIs. Following the results, a discussion on the limitations of the technique are described, along with the major findings of this study.

### 5.1.1 Turbulence Intensity and Lengthscales

Following the procedures described in Chapter 4, the TI and turbulent lengthscales evaluations were performed for all three TDVs. The results of which are displayed in Table 5.1, alongside the determined velocity range within the individual test points considered.

**Table 5.1:** Table of Velocity Components, Resultant TI's and Lengthscales for the 3 different TDV's from PIV analysis.

TDV	Axial Position [mm]	u_min [m/s]	u_max [m/s]	v_min [m/s]	v_max [m/s]	Resultant TI_air [%]	Resultant TI_fuel [%]	L_integral [mm]	L_η [mm]
3	0-100	33.35	44.06	-5.011	5.239	7.588	12.050	7.95	0.0263
3	100-200	34.21	43.45	-1.102	0.089				
6	0-100	29.04	48.96	-5.270	4.006	8.472	16.397	7.95	0.0272
6	100-200	30.37	47.57	-1.230	0.850				
12	0-100	29.28	44.40	-4.976	3.002	6.964	9.290	7.95	0.028
12	100-200	28.80	43.83	-0.850	0.280				

As displayed in Table 5.1, the velocities for the given test conditions showed a

decay in velocities when considering the maximum u- component velocities across the analysed regions and a narrowing of the velocity ranges as the analysis moves from the first imaging window of 0-100mm to the second imaging window 100-200mm, which describes how the flow field developed as the fuel and oxidant flows mix. Notably, there is also an increase in TI between TDV3 and TDV6 resulting from the larger geometry of the TDV6 that enabled a greater capacity to introduce more disturbances into the flow field. A decrease in Turbulence Intensity (TI) is shown when comparing TDV12 to TDV3 and TDV6.

### **5.1.2 Centreline Velocity**

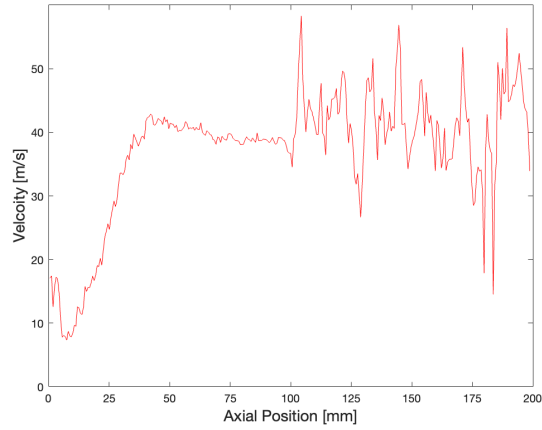
The centreline velocities of the three TDV cases are presented in Figure 5.1.1 below, where the centreline denotes the central position of the fuel lance. The centreline velocity was evaluated to ensure that no wall or boundary layer effects impacted the velocity profile.

As shown in the u-velocity centreline plots, there is a clear distinction as to where the two data sets of the two imaging windows are concatenated with one another at 100mm. In Figure 5.1.1a, there is an increase in the velocity fluctuations as the data set from the second imaging window is introduced due to the two different data sets captured from the two imaging windows.

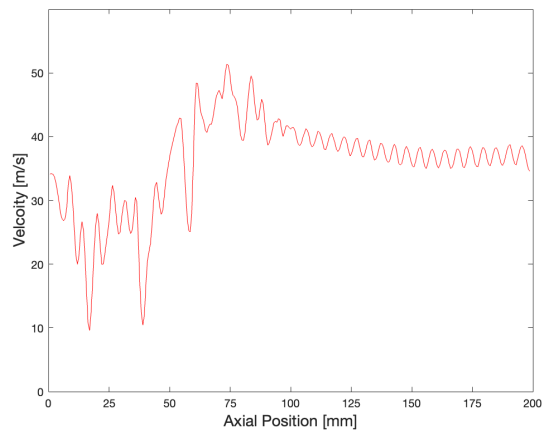
Conversely, Figure 5.1.1b illustrates that the fluctuations in the first imaging window are the largest. Whilst Figure 5.1.1c shows the smallest variation between the TDVs with a reduction of approx. 5m/s at the interface of the two data sets. The minimal fluctuations shown by Figure 5.1.1c coincides with the lowest TI level at the air inlet, as does the increased fluctuations at the inlet coincide with the increase TI for the air inlet in the TDV6 case.

### **5.1.3 Centreline Turbulence Intensity**

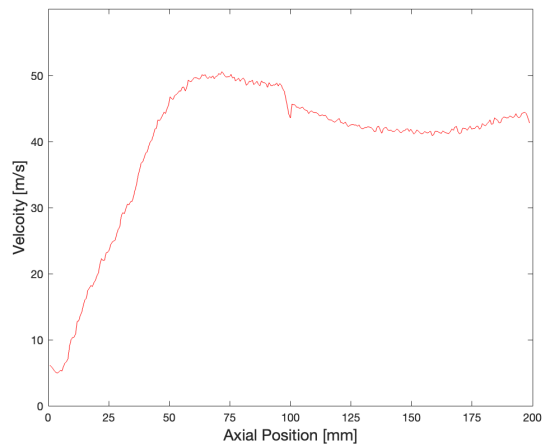
The centreline profile of the TIs relating to each TDV are presented in Figure 5.1.2, below. The centreline profile was considered for two purposes: (i) to evaluate the



(a) *U-velocity profile for TDV3 centreline.*



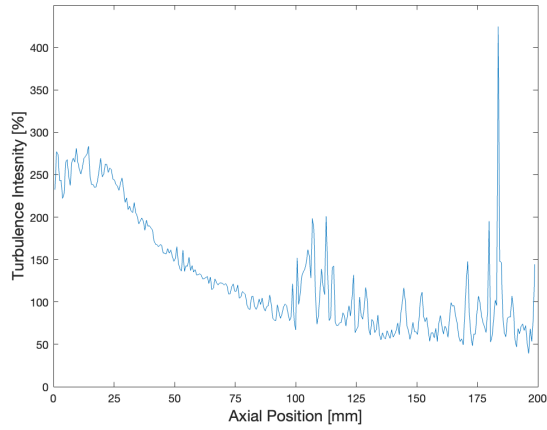
(b) *U-velocity profile for TDV6 centreline.*



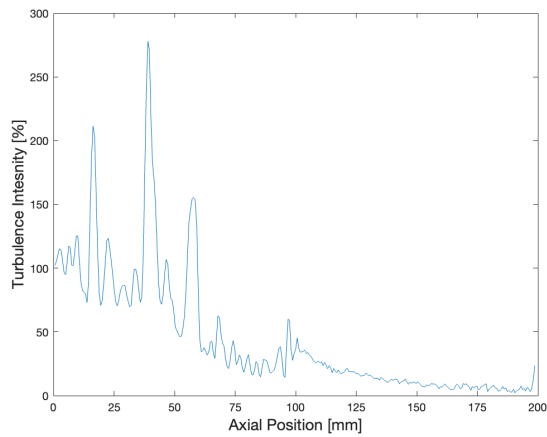
(c) *U-velocity profile for TDV12 centreline.*

**Figure 5.1.1:** Comparison between centreline *u*-velocity profiles of TDV3, TDV6, and TDV12, respectively.

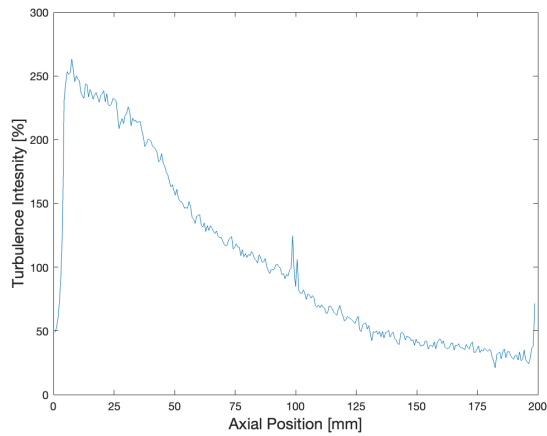
impact of turbulence characteristics of the oxidant flow on the fuel jet flow profile and (ii) to not unintentionally introduce wall effects or flow artefacts associated with the flow close to the wall into the analysis.



(a) *TI profile for TDV3 centreline.*



(b) *TI profile for TDV6 centreline.*



(c) *TI profile for TDV12 centreline.*

**Figure 5.1.2:** Comparison between centreline TI profiles of TDV3, TDV6, and TDV12, respectively.

The step change in fluctuations shown in Figures 5.1.1a and 5.1.1b is also observed for the TI centreline profiles illustrated in 5.1.2. These plots suggest that the greater TI at the air inlet for TDV6 is inducing a broader fluctuation on its centre-

line velocity which impacts the centreline TI. This suggests that the fluctuations in the outer regions of the flow are impacting the mixing of the fuel and oxidant.

The distinction of the two data sets from the given imaging windows, despite the optimisation of the pre-processing and analysis settings of the PIV data, is a limitation of this analysis. Throughout all the plots displayed between Figures 5.1.1 and 5.1.2, there is also a notably low value of both U and TI at the nozzle exit, where maximum velocities should be observed. This is due to limitations associated with the challenges of seeding the fuel flow close to the nozzle.

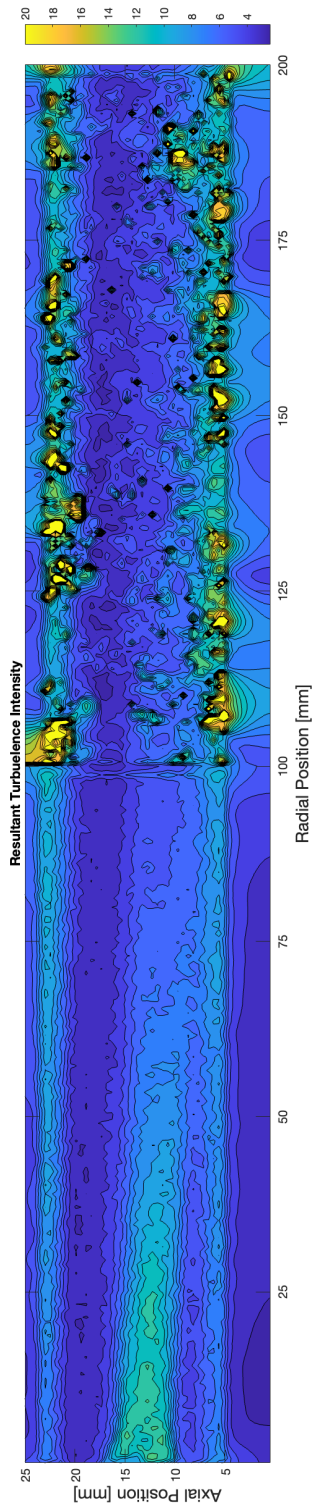
#### 5.1.4 Turbulence Intensity Contours

To consider the flow field as a whole, rather than specific point values or centreline profiles of TI, Figure 5.1.3 illustrates the TI contours for the three cases considered.

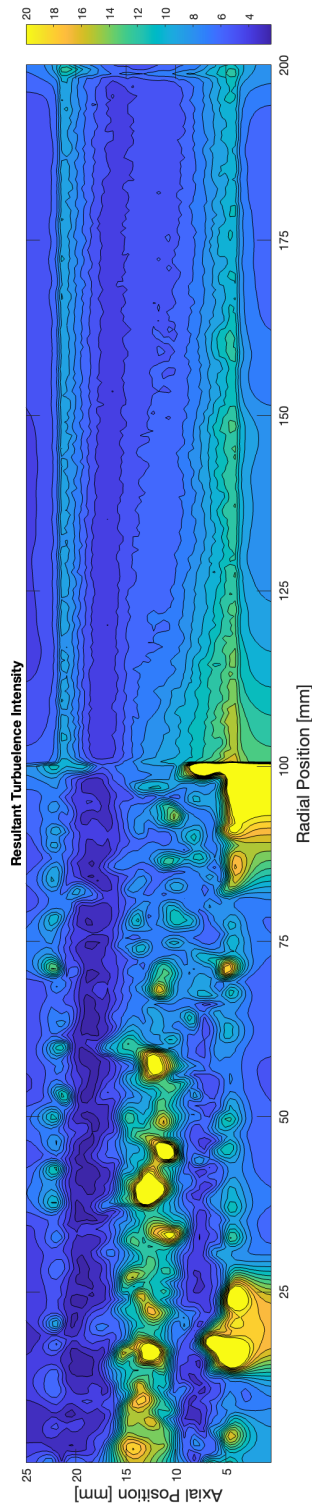
Figures 5.1.3a and 5.1.3b illustrate the challenge of the obtaining two cohesive data sets from the separate imaging windows. Whilst Figure 5.1.3c illustrates a near ideal case of the two data sets concatenating with reasonable success. This is due to the relatively low fluctuations in the the flow when TDV12 is in use compared to TDV3 and TDV6.

In the TI contours depicted in Figure 5.1.3, a discernible flow pattern is evident across all cases, illustrating a difference in the airflow above and below the fuel lance. For each case, a region of low TI ca. 4% is present above the fuel lance with its cross sectional area increasing at an angle as the flow develops downstream.

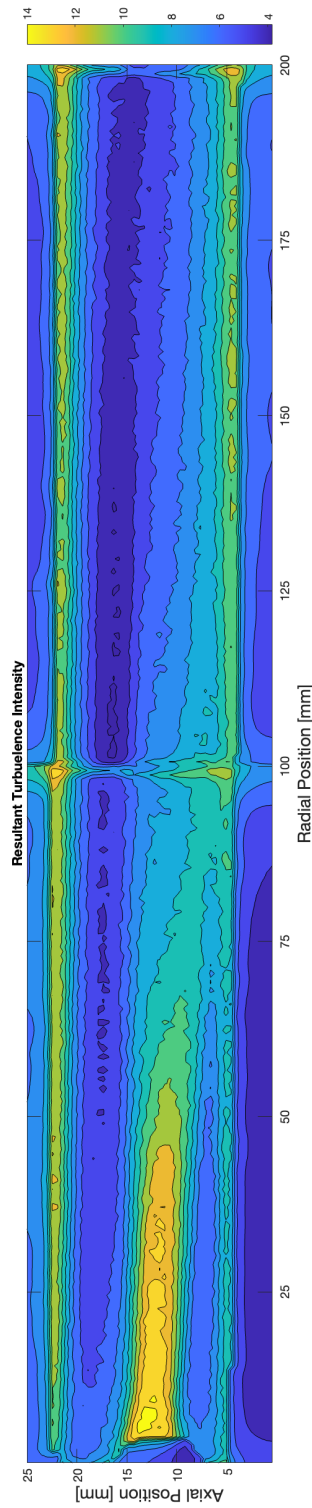
It is observed that TDV6 imparted a greater degree of turbulent fluctuations in the first imaging window whereas TDV3 depicts a reduced impact of TI at the inlet, comparatively. This is considered to be the result of the smaller geometry dampening the effects of turbulent fluctuations, which induces a more rapid dissipation of the turbulent kinetic energy, thereby contributing to the observed trend of decreased turbulence levels and faster decay rate in the smaller scale geometry of TDV3.



(a) TI Contour - TDV3, flow direction left to right.



(b) TI Contour - TDV6, flow direction left to right.



(c) TI contour - TDV12, flow direction left to right

Figure 5.1.3: TI contours for the complete consideration of the imaged windows for TDV, TDV6 and TDV12, respectively.

## 5.2 Particle Image Velocimetry Discussion

Discussion of the results is provided that describes the limitations of the methods and the significance of the results follows.

### 5.2.1 Fuel Jet Seeding

Despite optimising the image capturing and data-processing settings, no condition predicts  $U_{max} = 69.32m/s$ , as described in Section 4.4.3, close to the nozzle exit. This is most likely due to the excessive density of fuel seed particles exhibited at the exit of the nozzle, evidenced by the raw image taken in Figure 5.2.1.

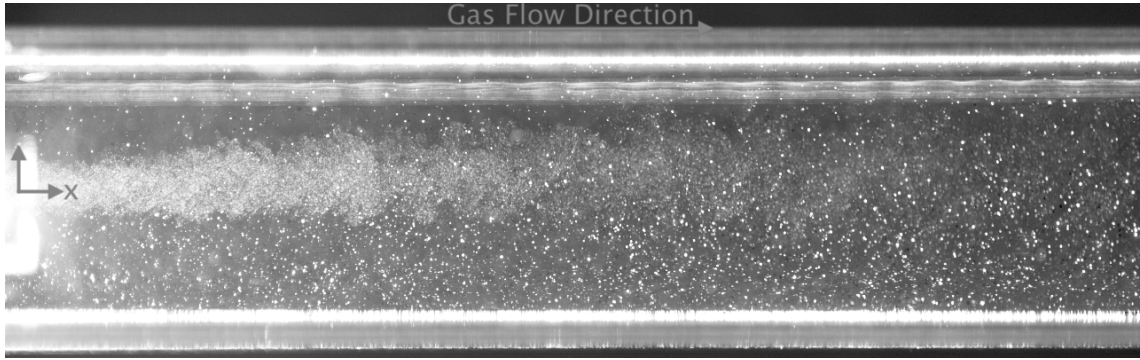


*Figure 5.2.1: Raw image of seed flow from the fuel nozzle exit which depicts the high density seed flow.*

When reviewing Figure 5.2.1, there is a difference in terms of the seed density at the nozzle exit when compared to further downstream. Hence, the under-prediction of velocity at that location shown by Figure 4.4.9. Notably, this pre-processing was performed without a Weiner Denoise filter, the function of which is to remove any particles under a given pixel size that would contribute to noise in the acquired image, yet they were still omitted from the analysis.

PIVlab did not identify the finer seed flow at the nozzle exit, hence, the velocity of the seed particles at the nozzle exit was determined manually. The displacement of a given particle was measured and the time delay between the images was used to determine a velocity of  $83.7m/s$ . This analysis was limited to the resolution ( $\pm 0.1mm$ ) of the measuring device used. Hence, the velocity determined may po-



tential lay in the range of  $73.2m/s$  to  $94.1m/s$ . The accuracy of this manual method is limited, however, it does show the inability of PIVlab to identify the velocities close to the nozzle exit in this test case and how they are under-reported throughout the data set taken. Consequently, there is an uncertainty in the velocity, or the velocity profile, in that axial position is likely to arise.

## 5.2.2 Air Flow Seeding

The air flow pattern above and below the fuel lance described in Section 5.1.4 is attributed to the manner in which the air seed is introduced into the TIMAR. Given that the air seed is introduced through a singular inlet at the bottom of the TIMAR, a preferential flow of seed particles toward the upper region of the imaged window occurs. Consequently, owing to the uneven distribution of seed particles in the examined cases, this results in an uneven distribution within the velocity field.

## 5.2.3 Variation in Velocity Between Air and Fuel Flows

Due to the fact that there are two flows that are being seeded in this PIV analysis, and that their velocities vary relatively substantially ( $U_{bulk,air} = 12.78m/s$  and  $U_{bulk,fuel} = 34.65m/s$ ), determining an effective image timings proved to be a limitation of this analysis. This impacts both the temporal and spatial resolutions and therefore inducing difficulties in analysing transient phenomena and fine scale flow structures in both flows. Since the fuel velocity is quicker than the air velocity, it's image timing would be required to be quicker to capture the displacement of seed particles across the same distance when compared to the air velocity.

This may have also induced a cross-correlation error in the analysis of the captured images, where the assumption made by the cross-correlation of particle displacement that particles in the fluid flow move linearly may have been incorrect. In addition, if the capture rate is insufficient in capturing a particular flow feature temporal aliasing can occur, leading to misinterpretation of particle displacements from the cross correlation process.

However, to analyse the two flows simultaneous a hybrid image timing of  $50\mu s$  was used as a compromise of detecting the flow features between the air and fuel flow. This enabled the flow to be analysed with a degree of accuracy for the two flows through this methodology.

Ideally, there would be separate analysis of the air and fuel flows by seeding them and acquiring data independently of one another. Post-processing analysis would then include combining the two data sets to account for the difference in the flow velocities and the optimal timing settings for each flow. This procedure was not investigated in this study due to limitations in laboratory resources. The process of combining the acquired from the two flows is not trivial. Hence, it is suggested that further work should investigate the potential of performing PIV analysis of both the fuel and air flows independently, with their specific image timings and combining the results for analysis.

#### **5.2.4 PIV Analysis Outcomes**

As detailed by Table 5.1, the Integral Lengthscale of turbulence in each case is equal across the test conditions. This is due to that the larger geometry of the mixing duct (MD) inlet is independent of the TDVs used and therefore the TDVs do not impact the overall Integral Lengthscale of the flow. However, the Kolmogorov Lengthscales that were calculated show an increase in their value as the relative dimensions of the TDVs increase. Thus supporting that the different TDVs introduced different turbulent characteristics upon the flow. It has also described how the TI increases between TDV3 and TDV6, whilst TDV12 shows a minimal impact upon the flow comparative to the other TDV considered.

Ultimately, this analysis showed that the TDV3 and TDV6 impact the flow greatly by introducing different levels of turbulence intensity and turbulent length-scales. Due to TDV12's relatively large geometry, its impact upon the flow in terms of TI is minimal. The larger turbulence device, TDV12, creates larger eddies. These larger structures tend to dissipate energy more slowly compared to smaller eddies,

which can lead to a lower overall turbulence intensity downstream. In contrast, smaller turbulence devices, TDV3 and TDV6, create a greater disturbance on the flow and generate smaller eddies that dissipate energy quickly, leading to higher localised turbulence intensity.

## 5.3 Temperature Effects - Results

The temperatures chosen for this phase of the test campaign were  $T = 750^{\circ}C$ ,  $T = 850^{\circ}C$  and maximum temperature of  $T = 932^{\circ}C$ . Throughout this phase of the experimental programme the turbulence characteristics were maintained constant through the consistent use of TDV3, to independently evaluate the impact of temperature. Air mass flow was also maintained at  $23.75g/s$  throughout.

As will be illustrated in the Figures following, no combustion event was realised for the  $T = 750^{\circ}C$  case until a  $H_2$  content of 40% [%vol]. This is a result of the reduced reactivity of the MD environment associated with this temperature case.

### 5.3.1 Temperature Effects: Lifted Flame Height vs Hydrogen Content

The impact of oxidant temperature on the LFH for the fuel blends considered is illustrated in Figure 5.3.1. As observed in Figure 5.3.1, the  $750^{\circ}C$  case presents the largest LFH heights throughout this phase of the test campaign until the 80%  $H_2$  [%vol] case, where the LFH is surpassed by the  $T = 932^{\circ}C$  case.

The  $T = 850^{\circ}C$  case shows how combustion of the 80/20%  $CH_4/H_2$  is realised, as was achieved during commissioning and with the  $T = 932^{\circ}C$  case. As expected, the values of LFH were greater for the  $T = 850^{\circ}C$  case up to 50%  $H_2$  [%vol]. At this threshold point, interestingly the  $T = 850^{\circ}C$  case exhibits shorter LFH than that of the  $T = 932^{\circ}C$  case where the MD environment is considered to be more reactive. For the 80%  $H_2$  [%vol] case, counter-intuitively, the  $T = 932^{\circ}C$  case reveals the longest LFH, seconded by the  $T = 750^{\circ}C$  case and followed by the  $T = 850^{\circ}C$  case.

The data displayed in Figure 5.3.1 shows a consistent concentration of data points for each test point. This indicates that the data points taken exhibit good repeatability.

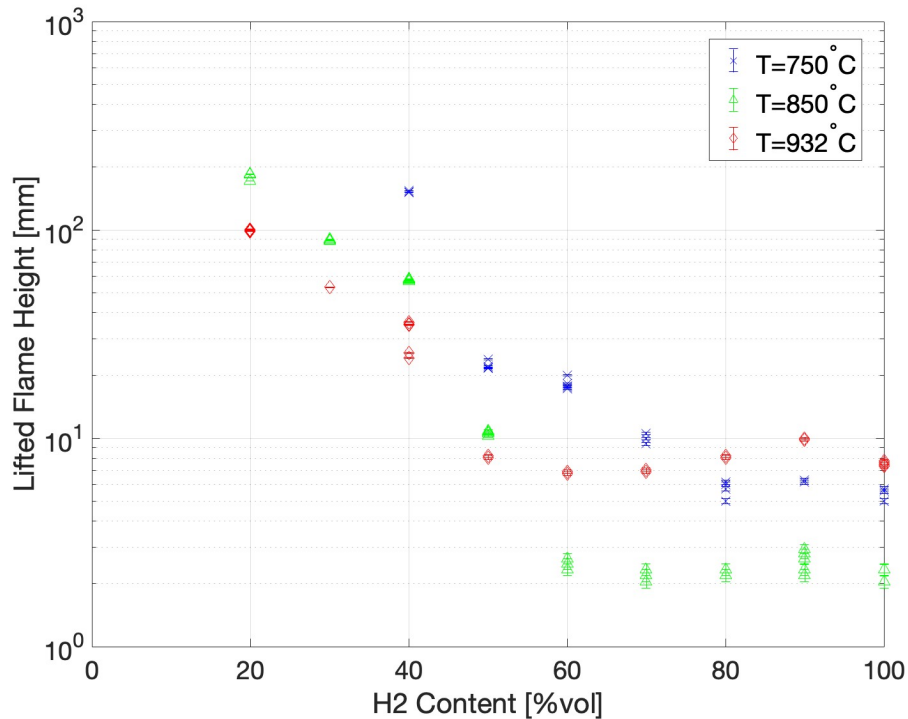


Figure 5.3.1: Temperature effects on the LFH of the fuel blends.

### 5.3.2 Temperature Effects: Flame Establishment Time vs Hydrogen Content

Figure 5.3.2 describes how the earliest instance of combustion in the TIMAR for an oxidant temperature of  $T = 750^{\circ}\text{C}$  is at 40%  $\text{H}_2$  [%vol]. The measured FET for the  $T = 750^{\circ}\text{C}$  case was measured to be approximately 65 times shorter in duration than that of the  $T = 932^{\circ}\text{C}$ . The  $T = 750^{\circ}\text{C}$  case also returns the shortest FET for all the temperature cases considered at 40%  $\text{H}_2$  [%vol]. Thereafter, the  $T = 750^{\circ}\text{C}$  case returns the largest FET results from 50%  $\text{H}_2$  [%vol] onward.

The  $T = 850^{\circ}\text{C}$  plot shows a wide spread of FET measurements for the 20% and 50%  $\text{H}_2$  [%vol] cases, whilst the remaining test cases have a far tighter spread. Between 20% and 40%  $\text{H}_2$  [%vol] the  $T = 850^{\circ}\text{C}$  cases exhibit a shorter FET than

that of the  $T = 932^\circ\text{C}$  cases. However, at the 50%  $\text{H}_2$  [%vol] threshold, the  $T = 932^\circ\text{C}$  case shows a sharp decline in FET, where the FET is at its minimum for the cases considered until 100%  $\text{H}_2$  [%vol] where the  $T = 850^\circ\text{C}$  case returns the smallest FET.

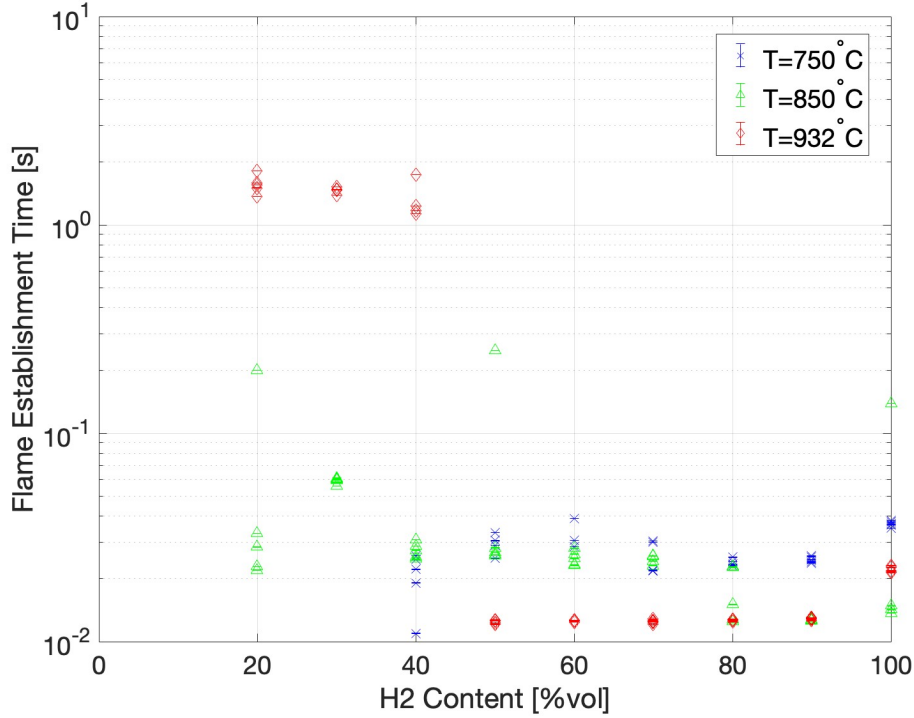


Figure 5.3.2: Temperature effects on the FET of the fuel blends.

### 5.3.3 Temperature Effects: Ignition Delay Time vs Hydrogen Content

Since the calculation of the  $\tau_{IGN}$  utilises the LFH for its calculation and that the boundary condition of the MD inlet is constant for the three temperature cases, its trend is near identical to that of the LFH.  $T = 750^\circ\text{C}$  trends a longer  $\tau_{IGN}$  than the other two temperature cases until 80%  $\text{H}_2$  [%vol], where it is surpassed by the  $T = 932^\circ\text{C}$  case. Between 20% and 50%  $\text{H}_2$  [%vol], the  $\tau_{IGN}$  for  $T = 850^\circ\text{C}$  is longer than that of the  $T = 932^\circ\text{C}$  case. From 50%  $\text{H}_2$  [%vol] onward, the  $T = 850^\circ\text{C}$  case describes the shortest  $\tau_{IGN}$ .

Again, due to the reliance of the  $\tau_{IGN}$  calculation on the measurement of LFH

and the consistent oxidant flow conditions for the given temperature cases, the data points displayed depict good repeatability with a relatively tight spread across for the repeated test points.

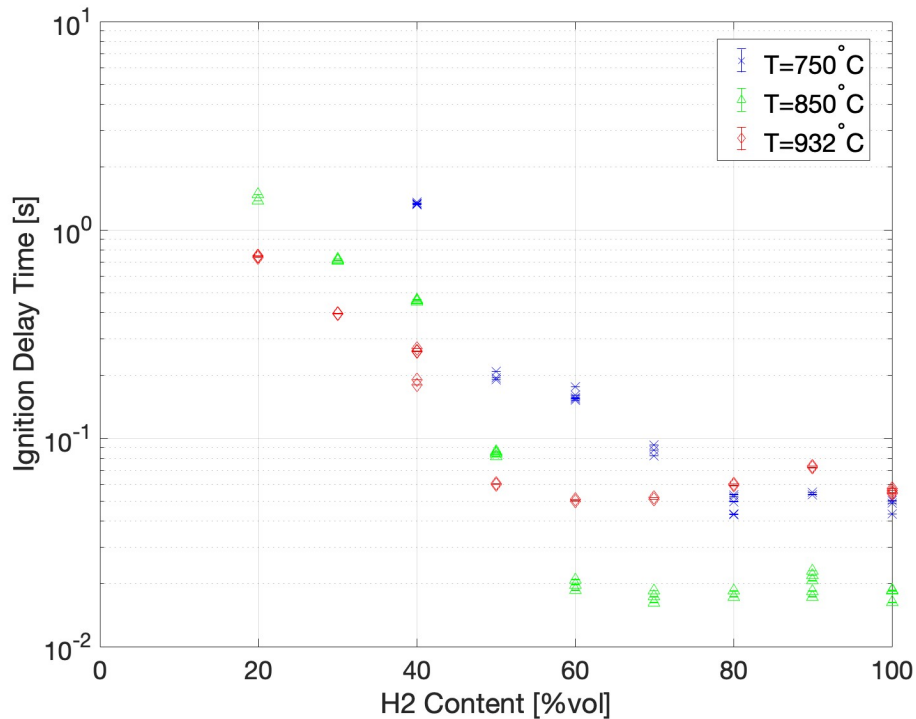


*Figure 5.3.3: Temperature effects on the  $\tau_{IGN}$  of the fuel blends.*

### 5.3.4 Temperature Effects: Damkhöler vs Hydrogen Content

Damköhler Number is considered in this temperature effect study to identify whether the reaction rate is being governed by the rate of the fuel and air mixing, or the reaction rate of the chemistry. Figure 5.3.4 illustrates how the  $T = 750^{\circ}\text{C}$  Damköhler Number decreases with a quasi-linear trend, demonstrating an exponential decay. The  $T = 750^{\circ}\text{C}$  Damköhler Number data points are repeatable.

The  $T = 850^{\circ}\text{C}$  case also shows a decrease in Damköhler Number with increasing  $\text{H}_2$  content in the fuel. The range of Damköhler Number for the  $T = 850^{\circ}\text{C}$  case shows far greater variability. The trend displayed on this semilog figure is not linear, with a considerable reduction in Damköhler Number for the 90%  $\text{H}_2$  [%vol]

case compared with its neighbouring 80% and 100% H<sub>2</sub> [%vol] cases.

The  $T = 932^{\circ}\text{C}$  case is characterised by a very consistent Damkhöler Number across all the fuel blends, showing very good repeatability. Thus describing the smallest impact of the H<sub>2</sub> content on the Damkhöler Number for this case of the highest evaluated temperature. At the threshold of 50% hydrogen in the fuel blend and higher, the Damkhöler Number is consistently greater than unity, evidencing the reaction rate being governed by the mixing rate.

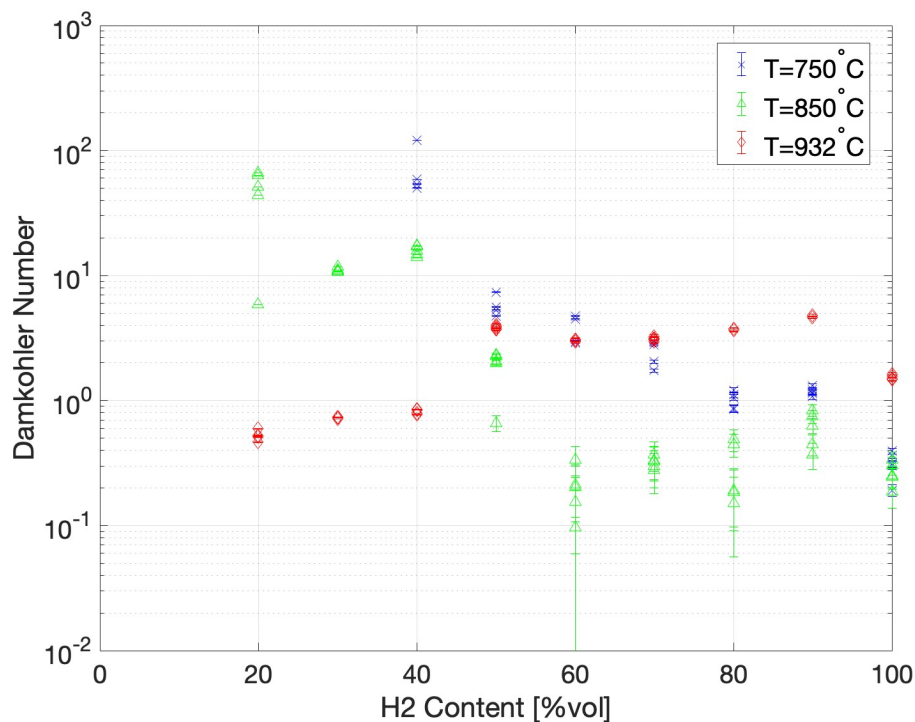


*Figure 5.3.4: Temperature effects on Damkhöler Number of the fuel blends.*

## 5.4 Temperature Effects Discussion

The impact of temperature has been illustrated through the description of the results above. Their significance is discussed and the mechanisms at play are postulated hereafter.

### 5.4.1 Temperature Effects: Lifted Flame Height vs Hydrogen Content

As detailed in the presentation of the LFH results in Figure 5.3.1, the regression in the results of LFH for the three temperatures is as one would intuitively expect between 20% and 50% H<sub>2</sub> [%vol], that is, the higher the temperature the smaller the LFH.

At the threshold of 60% H<sub>2</sub> [%vol] and beyond, the findings exhibit unexpected trends, particularly in the case of  $T = 850^{\circ}C$ , which yields the smallest LFH values. It is postulated that this outcome arises from the diminished air velocity resulting from the equal mass flow rate of air and the lower temperature conditions observed in both the  $T = 750^{\circ}C$  and  $T = 850^{\circ}C$  test cases.

The distinguishing factor between the  $T = 750^{\circ}C$  and  $T = 850^{\circ}C$  cases lies in the heightened impact of elevated temperatures on the reactivity of the environment. This effect significantly enhances the propensity for ignition of the hydrogen content in the fuel, particularly in the  $T = 850^{\circ}C$  case compared to the  $T = 750^{\circ}C$  case. Whereas due to the increased velocity associated with the  $T = 932^{\circ}C$  case provides sufficiently higher oxidant flow to enable an increased resolution and overall value of its associated LFH results.

### 5.4.2 Temperature Effects: Flame Establishment Time vs Hydrogen Content

The results presented in Figure 5.3.2 describing the impact of temperature on FET showed for the 20% - 40% H<sub>2</sub> cases appear to present anomalies since the higher the temperature exhibit an elongated FET. However, this phenomenon does not stem from a longer duration for the flame to initiate but rather arises as a consequence of the definition of FET. Specifically, FET is defined as *"the time taken from the initial voltage reading to surpass the noise level threshold to the first significant peak in the OH intensity recorded by the PMT."* Given that all the values of FET ascertained



were at the first significant peak of the  $\text{OH}^*$  value which was a minimum of 90% threshold of the maximum  $\text{OH}^*$  value, it is proposed that the time taken to reach the defined threshold for the lower temperature case was less than that observed for the higher temperature cases resulting from an overall reduction in the  $\text{OH}^*$  intensity for the lower temperature's. Hence, the FET was evaluated to be shorter.

At the threshold of 50%  $\text{H}_2$  [%vol], the time taken for the ignition of the fuel to occur surpasses the variability in the time taken to reach the first significant peak of  $\text{OH}^*$  intensity for the different temperatures considered. The outlier in this instance however is the 100%  $\text{H}_2$  [%vol] case where the  $T = 850^\circ\text{C}$  case exhibits a shorter FET than the  $T = 932^\circ\text{C}$  case where the  $\text{OH}^*$  threshold of the first significant  $\text{OH}^*$  peak at 60% and 70% respectively and thus requiring a shorter time duration to achieve this first significant peak of  $\text{OH}^*$  intensity as per the definition of FET.

### 5.4.3 Temperature Effects: Ignition Delay Time vs Hydrogen Content

Figure 5.3.3 displays the impact of temperature on the  $\tau_{IGN}$  of the various fuel blends under consideration, a trend analogous to that depicted in Figure 2.2.4 is present. Notably, the work undertaken by Eroglu et al. [97] is performed at significantly higher temperature's than those evaluating in the experimental work relating to this project.

Hence, the notable difference between the study undertaken by Eroglu et al. and this study is at what  $\text{H}_2$  [%vol] that the sudden reduction in  $\tau_{IGN}$  occurs. For the  $T = 750^\circ\text{C}$  case in this study, that sudden reduction and flattening of the trend occurs at 70%  $\text{H}_2$  [%vol]. At  $T = 850^\circ\text{C}$  and  $T = 936^\circ\text{C}$  this occurs at 60% and 50%  $\text{H}_2$  [%vol], respectively, whereas the sudden reduction in the study conducted by Eroglu et al.[97] is occurs at ca. 20%. Notably, a major differentiator between these studies is the fact that this study is reporting experimental results whilst Eroglu et al. [97] reports on chemical kinetic modelling. Hence, this is considered to be the reason as to why the trends highlighted by Eroglu et al. [97] are far more

homogeneous than what is described by the experimental results of this study, due to their lack of the inherent uncertainties associated with experimental undertakings.

#### 5.4.4 Temperature Effects: Damkhöler Number vs Hydrogen Content

Figure 5.3.4, it shows that for the  $T = 750^{\circ}C$  and  $T = 850^{\circ}C$  cases that at the lower  $H_2$  content of the fuel that the mixing of the fuel and oxidant dominates in the rate of reaction. However at a threshold's of 80% and 60%  $H_2$  [%vol] for  $T = 750^{\circ}C$  and  $T = 850^{\circ}C$ , respectively, the rate of the chemistry begins to dominate the rate of the reaction. This coincides with the fact that the higher temperatures and higher  $H_2$  content increases the rate of the reaction of the fuel blends.

Conversely, the  $T = 932^{\circ}C$  cases are characterised by the dominance of the mixing in the rate of reaction for the high hydrogen containing fuels of 50%  $H_2$  [%vol] threshold onward. This is due to the relative increase in the fuel jet velocity experienced by the higher hydrogen containing fuels resulting from their reduced density. The range in the Damkhöler Number, spanning from the minimum to maximum, is narrower for the  $T = 932^{\circ}C$  case compared to other temperature cases. This is attributed to the concurrent increase in the mixing rate, driven by the heightened velocity of the fuel jet. Additionally, the influence of the chemical reaction rate curtails how much the mixing dominates the reaction due to the enhanced reactivity of the MD environment stemming from elevated temperature and the increased reactivity associated with rising  $H_2$  content.

#### 5.4.5 Temperature Effects Conclusion

Throughout this analysis it is clear that the operating temperature has a significant effect on all the variables evaluated. The different temperatures incur various levels of reactivity for the fuel blends, that is, the higher the temperature the more reactive the combustion reaction is. In addition, the increased oxidant temperature influenced the amount of preheating experienced by the fuel and hence, impacted

the transport properties of the fuel, namely the density and therefore the fuel jet velocity. Hence, a major finding from this sections is the way the reaction rate is dominated by either the mixing rate or the chemical reaction rate, as characterised by Damköhler Number.

## 5.5 Turbulence Effects Results

In this section, the results pertaining to the influence of turbulence on the ignition of the fuel blends is considered under constant temperature conditions. Herein, the three TDVs are considered at a of  $T = 932^{\circ}C$  with an air flow of  $23.75g/s$ . As in the previous section, LFH, FET,  $\tau_{IGN}$  and Damkhöler Number are considered. First, the results are presented and described, followed by a discussion of the significance of the results.

### 5.5.1 Turbulence Effects: Lifted Flame Height vs Hydrogen Content

Figure 5.5.1 shows the influence of the three TDVs on the LFH. Within the 20% to 50% H<sub>2</sub> [%vol] range, TDV6 demonstrates the greatest retardation of the combustion of the fuel blends. The data exhibits good repeatability until the 50% case, where a substantial increase in the standard deviation is observed. Within this range, TDV3 data mirrors a similar trend as TDV6, however has a consistently smaller value of LFH. The consistency of TDV3 data remains high, except for the 40% H<sub>2</sub> [%vol] case, where a relatively large variability is observed.

Parallel to the relationship observed between TDV3 and TDV6, TDV12 follows a comparable trend with a reduction in absolute values compared to the other two cases. Notably, the consistency of TDV12 data is generally high, with the exception of a singular case—the 30% H<sub>2</sub> scenario within the TDV12 data set.

From the 50% H<sub>2</sub> [%vol] case onward, there is a reversal of the inhibitory effect induced by the turbulence devices compared to that observed in the 20% to 50% H<sub>2</sub> [%vol] range. TDV3 and TDV12 exhibit nearly equivalent values in LFH, whereas the turbulence characteristics induced by TDV6 enhances the rate of the combustion, as evidenced by the observed reduction in LFH. The high consistency in the data from TDV3 and TDV12 enhances the reliability of the observed trends, supporting the theory that the turbulence exerted by TDV3 and TDV12 devices inhibits the

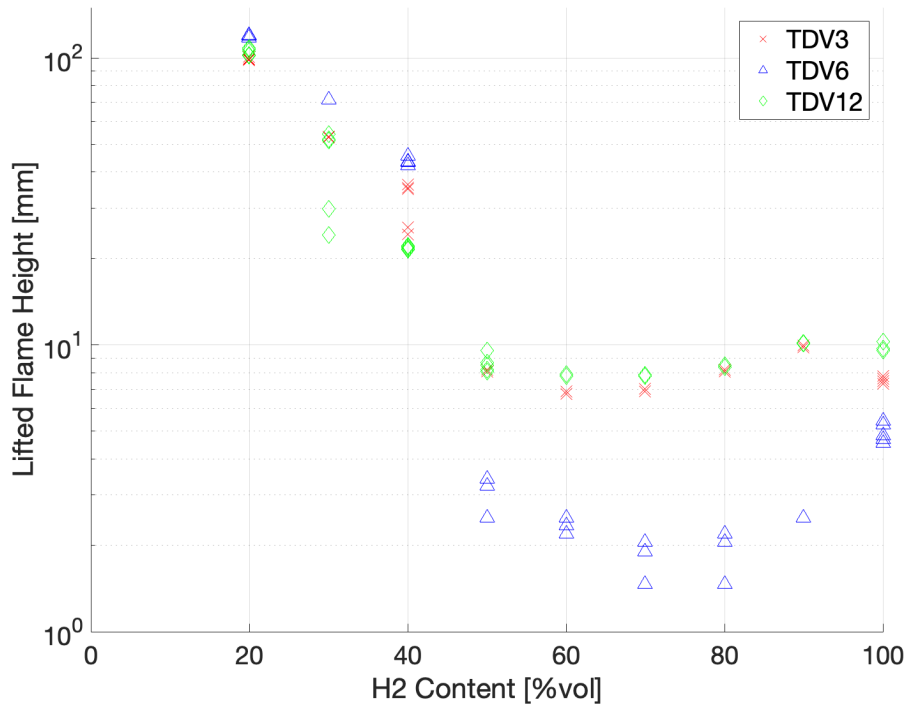


*Figure 5.5.1: Turbulence effects on LFH of the fuel blends.*

rate of the reaction within the 50% to 100% H<sub>2</sub> [%vol] range. In contrast, within the TDV6 data, the variability of LFH is notably greater in the 60%, 70%, and 80% H<sub>2</sub> [%vol] range.

### 5.5.2 Turbulence Effects: Flame Establishment Time vs Hydrogen Content

Figure 5.5.2 presents the results of Flame Establishment Time (FET) concerning the influence of turbulence. Within the range of 20% to 40% H<sub>2</sub> [%vol], notable variations exist in the FET results for the TDVs considered. TDV3 exhibits the highest FET times in this range, characterised by a closely scattered set of results indicative of reasonable data consistency. Conversely, TDV6 demonstrates an increase in FET as hydrogen content rises within this range. Its data spread is relatively wide for the 20% and 30% H<sub>2</sub> cases, while the 40% H<sub>2</sub> case is characterised by a tightly clustered data set. TDV12 shows an FET comparable to TDV6 for the 20% H<sub>2</sub> case but is significantly lower than that of TDV3 and TDV6 within the 20% to 40% H<sub>2</sub> range.

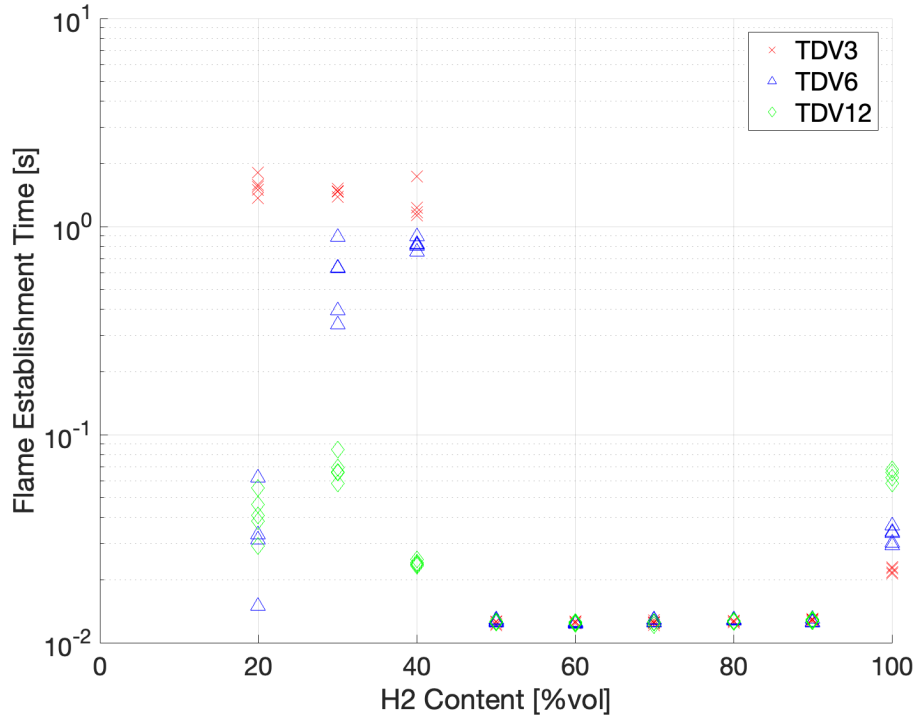


*Figure 5.5.2: Turbulence effects on Flame Establishment Time of the fuel blends.*

From 50% to 90% H<sub>2</sub> [%vol], the FETs for all TDV devices considered are nearly equal, with a tight scatter in the data sets indicating excellent repeatability. Furthermore, in the 100% H<sub>2</sub> case for the three TDVs, a longer FET is reported than any of the cases within the 50% to 90% H<sub>2</sub> range. The TDV12 case exhibits the longest FET, followed by TDV6, and TDV3 reports the shortest FET for the 100% H<sub>2</sub> case.

### 5.5.3 Turbulence Effects: Ignition Delay Time vs Hydrogen Content

The impact of turbulence on the  $\tau_{IGN}$  of the fuel blends considered is illustrated by Figure 5.5.3. In the 20% to 50% H<sub>2</sub> [%vol] range, TDV6 has the longest  $\tau_{ign}$  of the TDV's considered. Within this interval, TDV3 data mimics a parallel pattern to TDV6, with the distinction of a reduction in the determined value of  $\tau_{IGN}$ . The uniformity of TDV3 data remains robust, except for the 40% H<sub>2</sub> [%vol] scenario, where variability in the test point repeats is apparent when compared to any of the

other data sets associated with TDV3.

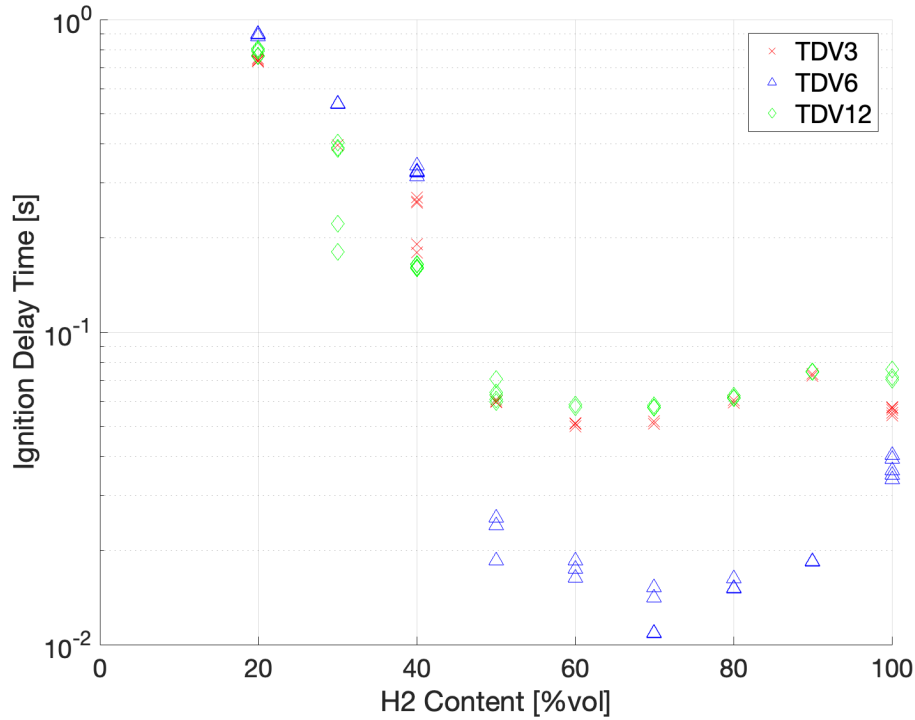


**Figure 5.5.3:** Turbulence effects on  $\tau_{IGN}$  of the fuel blends.

TDV12 shows a similar trend, but the values of  $\tau_{IGN}$  are smaller when compared to the other two cases. The TDV12 data set exhibited good repeatability between test points, as depicted by the tight scatter of data points, except for the singular case of 30% H<sub>2</sub> [%vol] scenario within the TDV12 data set, where the data scatter is at a maximum for the entire consideration of the turbulences influence on  $\tau_{IGN}$ .

Beyond the 50% H<sub>2</sub> [%vol] threshold, there is a reversal of the inhibitory impact induced by the turbulence devices compared to that observed in the 20% to 50% H<sub>2</sub> [%vol] range, as was also illustrated by Figure 5.5.1 for the LFH. TDV3 and TDV12 exhibit almost identical values in  $\tau_{IGN}$ , whereas the turbulence characteristics induced by TDV6 show an increased reaction rate, as evidenced by the smaller values of  $\tau_{IGN}$ .

The high uniformity in the data for all three TDV's enhances the reliability of the observed trends, instilling confidence in the inhibitory effects of TDV6 for fuel blends containing up to 50% H<sub>2</sub>, and for the TDV3 and TDV12 devices within the 50% to 100% H<sub>2</sub> [%vol] range. Other than the individual points highlighted above.

The data displays notable consistency for all the fuel blends evaluated for TDV6 in relation to  $\tau_{IGN}$ .

### 5.5.4 Turbulence Effects: Damkhöler vs Hydrogen Content

The Damkhöler Number trends concerning the influence of the TDVs are presented in Figure 5.5.4. For TDV3, between 20% and 40% H<sub>2</sub> [%vol], the Damkhöler Number is below unity, trending upwards with increasing H<sub>2</sub> content. From 50% H<sub>2</sub> onward, the Damkhöler Number consistently remains above unity, with a minor inflection between 50% and 90% H<sub>2</sub> [%vol] and a relatively sudden reduction at 100% H<sub>2</sub> [%vol], while remaining above unity. All the data points considered for TDV3 exhibits limited dispersion, indicating consistent values.

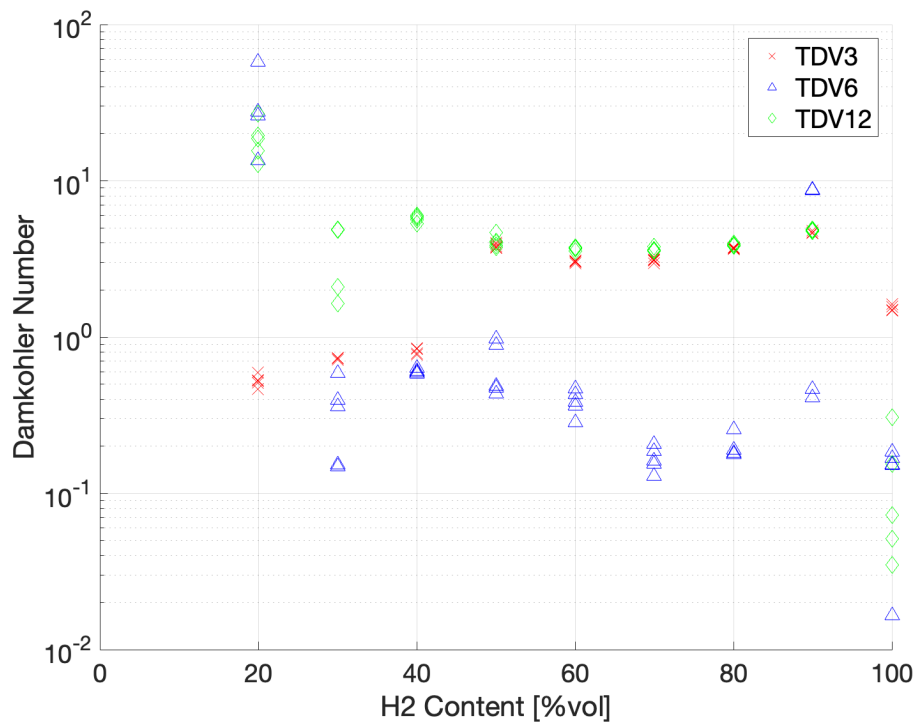


*Figure 5.5.4: Turbulence effects on Damkhöler Number of the fuel blends.*

For TDV6, the Damkhöler Number for the 20% H<sub>2</sub> case remains above unity, while all other fuel blend conditions remain below unity, except for a singular anomalous result related to the 90% H<sub>2</sub> case. The dispersion of data points throughout is reasonable, although greater variability is evident at 100% H<sub>2</sub> where the lowest



Damkhöler Number is recorded.

Conversely, the Damkhöler Number relating to the TDV12 test cases consistently remains above unity for fuel blends in the range of 20% to 90% H<sub>2</sub> [%vol], where the data indicates reasonable dispersion for 20% and 30% H<sub>2</sub> and very low variability for all other Damkhöler Numbers in that range. At 100% H<sub>2</sub>, the Damkhöler Numbers are below unity and are characterised by a considerable spread, highlighting a wider range of values within the data set compared to those ascertained in the range of 20% to 90% H<sub>2</sub> [%vol].

## 5.6 Turbulence Effects Discussion

The effect of turbulence on the ignition of the various fuel blends considered has been illustrated through the reporting of the results above. This discussion aims to elucidate the mechanisms underpinning the results described in the following subsections. Reference is made to the turbulence characteristics that were described in Chapter 4 relating to the PIV analysis performed in characterising the flow field of the TIMAR and will be solely referred to as “PIV analysis” herein.

### 5.6.1 Turbulence Effects: Lifted Flame Height vs Hydrogen Content

As illustrated by Figure 5.5.1, TDV6 exhibits an inhibiting effect on the combustion of the fuel blends from 20% to 40% H<sub>2</sub> [%vol]. This is a result of the higher Turbulence Intensities (TI) associated with the use of the TDV6 as determined through the described PIV analysis. It is postulated that the increased TI is disrupting the flames ability to stabilise due to increased strain rates, of which hydrocarbon dominant fuels are more susceptible to, compared to hydrogen dominant fuels [106] [192]. Where TDV3 and TDV12 differ in this range of fuel blends is that the TI intensities are less than that of the TDV6 case.

Beyond the 50% H<sub>2</sub>, the role of turbulence in this instance is reversed which is

considered to be a result of the turbulent lengthscales in regard to the TDV3 case and a result of less sufficient mixing in the case of the lower TI TDV12 case. Specifically to the TDV3 case, the relatively smaller lengthscales of turbulence cause an inhibiting effect resulting from the ability of the smaller lengthscales to impede the ignition kernels from reaching a critical volume for the propagation of the reaction to occur. Since the turbulence decays and the strain rates remain under a critical value the realisation of ignition kernels of a critical volume is achieved further downstream, hence increasing LFH in the case of TDV3.

### **5.6.2 Turbulence Effects: Flame Establishment Time vs Hydrogen Content**

The results detailed in Figure 5.5.2, highlight the need for a nuanced understanding of FET and the influence of the flow field conditions on the combustion reaction.

Considering 20% - 40% H<sub>2</sub> [%vol] fuel blends, a wide range of FET values across the TDV cases is observed. What these results show is that despite these fuel blends having a relatively close range of LFH as described above, the rate at which the thermal runaway part of the ignition process is influenced by the turbulence characteristics of the flow field is different for the TDVs considered. Where TDV6 and TDV12 exhibits chemistry with smaller timescales than that observed in the TDV3 cases, thus highlighting the influence of the flow field on the chemistry.

From the 50% H<sub>2</sub> [%vol] point onward, the variability in FET is imperceptible due to the highly reactive conditions of the high hydrogen containing fuels and the elevated temperature conditions associated with this phase of the experimental programme. The only exception to this is that of the 100% H<sub>2</sub> case which is supportive of the hypothesis, that the relative length of the Kolmogorov lengthscales associated with the given TDV act in an inhibiting capacity to the realisation of critical kernel volumes enabling ignition to propagate. Notably, the increase in FET at 100% H<sub>2</sub> [%vol] is due to the slower attainment of peak OH\*\* release compared to the high hydrogen (<50%) blends considered in this study. It is stipulated that OH\* release

is more prominent and its reaction rate is accelerated by the initiation of combustion of the hydrogen-containing proportion of the fuel blend when combined with hydrocarbons like  $\text{CH}_4$ . This results in a greater FET for the pure hydrogen case. However, further research is required to validate this claim, as no literature was found to support this theory.

FET measurements highlight the importance of introducing Damköhler Number in the analysis to characterise the flow field or the chemistry's relative influence on the rate of the combustion reaction.

### 5.6.3 Turbulence Effects: Ignition Delay Time vs Hydrogen Content

As the determination of  $\tau_{IGN}$  relies on the LFH, the proposed explanations for its observed trend are comparable. With the higher TI levels associated with TDV6, in the range of 20% - 40%  $\text{H}_2$  [%vol], the turbulent flow field acts by disrupting the stable formation of ignition kernels, with regions of higher strain rates acting to extinguish the initial ignition kernels. This is more pronounced in this fuel blend range, as previously described in Section 5.6.1, that hydrocarbon fuels are more susceptible to being extinguished due to higher strain rates in the flow field [106] [192]. Whilst the strain rates in the flow field are higher than the other TDV cases observed, they are not so high that they stop the fuel from igniting. Moreover, the higher strain rates act as an inhibitor.

As described in Section 5.6.1, once the hydrogen proportion reaches 50% by volume in the fuel blend, its presence in the fuel blend becomes more apparent and the influence of turbulence begins to alter since the higher TI case of TDV6 now describes a shorter  $\tau_{IGN}$  when compared to the other two TDV cases. This is considered to be the impact of hydrogen's improved ability to ignite and sustain a flame under the more strained flow field.

Conversely, the smaller Kolmogorov lengthscale associated with the TDV3 case then act as a combustion inhibitor by inhibiting the formation of ignition kernels

of a critical volume to propagate the combustion reaction and for the flame front to establish. Hence, the extended  $\tau_{IGN}$  when compared to that of the TDV6 case. The quasi-constant LFH corresponding to TDV12, when compared to TDV3, is postulated to be the result of the poorer mixing associated with this TDV. As previously described, the relative geometry of TDV12 to the geometry of the TIMAR is large and hence its impact upon the flow is diminished. The longer lengthscales of turbulence associated with TDV12 do mix the fuel and oxidant but at a slower rate than that of TDV6, resulting in the longer  $\tau_{IGN}$ . due to this an inhibiting effect as a result of the insufficient mixing, its combustion performance in terms of combustion efficiency and emission performance is likely to be impacted.

#### 5.6.4 Turbulence Effects: Damkhöler Number vs Hydrogen Content

As presented in Figure 5.5.4, for TDV3, the chemical reaction rate governs the overall reaction rate for fuel blends ranging from 20% to 40% [%vol]. Upon reaching the threshold of 50% H<sub>2</sub> and beyond, the influence of turbulence becomes more prominent, characterised by Damkhöler Numbers exceeding unity. This observation substantiates the hypothesis that turbulence significantly affects fuel ignition within this range of test conditions, exerting a more substantial influence than chemical reactions.

Subsequently, the interplay between flow field conditions and chemical conditions is upheld by the Damkhöler Numbers for TDV6, all of which are below unity, except for the 20% H<sub>2</sub> case. Damkhöler Numbers below unity indicate that the reaction rate is primarily governed by chemical reactions rather than the mixing of fuel and air. Considering that the LFH and  $\tau_{IGN}$  for TDV3 are longer than those for TDV6, it evidences that operating regimes with Damkhöler Numbers greater than unity are desirable to ensure that mixing timescales determine the reaction rate.

This is also supported by the Damkhöler Number results for TDV12, all of which surpass unity, except for the 100% H<sub>2</sub> case. This highlights the influence of the flow

field on the ignition of hydrogen-enriched fuels. However, a notable difference from the TDV3 case is that it is associated with inferior mixing rather than inhibitory effects of strain on the combustion reaction.

## 5.7 Results Conclusions

In the presented results, the influence of temperature on the ignition of hydrogen-enriched fuel blends is presented. Followed by the impact of turbulence on the ignition of the fuel blends evaluated, this study was supported by the PIV analysis that quantified the turbulence characteristics of the three TDVs used in the study. The PIV analysis highlighted the different TIs of the three TDVs. The integral lengthscale across the three TDVs were equal owing to the shared geometry of the MD inlet, yet exhibited different Kolmogorov lengthscales trending in the line with the TDV characteristic geometry size.

Concerning the influence of temperature within this experimental campaign, heightened temperatures were characterised by shorter LFH, FET, and  $\tau_{IGN}$  due to the increased reactivity of the environment. Notably, at  $T = 932^{\circ}C$ , a pronounced decrease in the dependent variables occurs around 50% H<sub>2</sub>. Conversely, at lower temperatures, this decline in the dependent variables shifts to higher hydrogen proportions within the fuel. A distinct flattening of the curve is observed in the  $T = 750^{\circ}C$  case at 80% H<sub>2</sub>, as corroborated by [97] in Section 5.4.3. The analysis of Eroglu et al. at higher temperatures exhibited a sudden drop in ignition delay time around 20% H<sub>2</sub>, with fuel blends from 20% onward returning similar results.

Additionally, variations in temperature impacted the velocity of the oxidant within the MD, affecting the residence time of the fuel-oxidant mixture and reducing measurement resolution. Whilst this effect is minimal for the  $T = 750^{\circ}C$  case, the increased reactivity of the  $T = 850^{\circ}C$  case has a greater impact on the measurement of dependent variables, resulting in values lower than those of the  $T = 932^{\circ}C$  case. Damkhöler Number determinations for the test cases reveal that the chemical reaction is the dominant mechanism governing the reaction rate for  $T = 850^{\circ}C$ , as

opposed to the other two temperature cases, which were characterised by mixing controlling the reaction rate.

In regards to industrial applicability and the impact to the GT26, it has shown that reducing the SEV temperature an impact on fuel jet temperatures and subsequently cause the fuel jet velocity to slow down, depending on the impact of heat transfer on the fuel temperature. This would result in a lower velocity fuel jet that would increase the likelihood of flashback from occurring. The  $850^{\circ}\text{C}$  results also suggest that there is a critical threshold where the fuel jet velocity is too low in comparison to the rate of the combustion reaction to maintain the design position of the flame within the SEV. Thus, it can be considered that the increased velocity associated with the  $932^{\circ}\text{C}$  results are an optimal balance, from the temperature's considered in this campaign, between the fuel jet velocity and the increased rate of the combustion reaction.

The assessment of turbulence impact demonstrates how TDV6 initially inhibits combustion due to higher Turbulence Intensity (TI) levels for fuel blends containing 20% to 40%  $\text{H}_2$ . However, beyond this threshold, TDV6 exhibits the smallest values of dependent variables analysed. For higher fuel blend ranges in TDV3 and TDV12 test cases, their values are comparable but governed by different mechanisms. TDV3, characterised by smaller turbulence length scales, delays the formation of critical ignition kernels, acting with an inhibitory effect. In contrast, TDV12 is characterised by less efficient mixing, resulting in longer values of dependent variables compared to TDV6.

The inclusion of the Damkhöler Number proved highly valuable, enabling the determination of whether the reaction rate was dominated by the transport of fuel and oxidant or by chemical kinetics. Cases characterised by Damkhöler Numbers less than unity, indicating dominant chemistry, exhibit results associated with highly reactive cases and low values of dependent variables. Conversely, cases with Damkhöler Numbers greater than unity demonstrate higher values of dependent variables. Since the highest LFHs and  $\tau_{IGN}$  are associated with Damköhler Num-

bers of greater than unity for the hydrogen rich fuel blends, it shows that varying turbulence conditions can enable control over the reaction rate.

This has considerable value for exerting control over the reaction rate in the retrofit designs of the GT26 SEV combustor for hydrogen enriched fuels, where its current configuration is limited. These results offer the insight that the influence of turbulence and therefore the design of the Vortex Generators, offer an avenue of investigation for the increased H<sub>2</sub> capability of the SEV combustor in the GT26.

# Chapter 6

## Computational Fluid Dynamic Simulations of Inhomogeneous Mixture Autoignition

A Computational Fluid Dynamics (CFD) investigation has been conducted to enhance the comprehension of the mechanisms observed in the experimental programmes. CFD offers insights via flow visualisation, that includes temperature distributions, concentration gradients and comprehensive data sets of velocity, pressure and temperature which were not able to be discerned via the methods deployed in the experimental testing. Two 2D models of the TIMAR is developed to undertake this analysis with a high level of computational efficiency, with the first being a pressure based model and the second taking into account compressibility effects. This study commenced with a mesh independence analysis, succeeded by the evaluation of turbulence models, both of which subsequently contribute to the formulation of the final CFD models employed in the combustion-enabled CFD test scenarios.

CFD analysis was performed within ANSYS Fluent 2023 R2, denoted as “Fluent” henceforth. For all the test cases considered a total of 36 processing cores were utilised, coupled with the parallel processing achievable by utilising an additional



GPU capabilities supplied by the addition of a NVIDIA RTX A5000 graphics card to maximise computational efficiency.

The outcomes of the Particle Image Velocimetry (PIV) analysis described in Chapter 4 provide inputs to the CFD model, in addition to temperature measurements of the fuel from the experimental test cases. Within this study, the chemiluminescence images of the experimental test cases associated with TDV3 derived from the experimental investigation described in Chapters 5 and 6 are compared with the results of this CFD study.

For methodological continuity, an estimation of the LFH is performed by locating the axial position of the OH\* threshold of 30% of its maximum value, as per the LFH-chemiluminescence methodology outlined in Chapter 5. To account for the OH\* radical, the reaction mechanism (GriMech3.0) was modified to include OH\* as a species and including reactions for OH\* along with their associated reaction rate parameters.

## 6.1 CFD Theory

CFD is a branch of fluid mechanics that employs numerical methods and algorithms to analyse and solve problems involving fluid flows and in this case, can be coupled with chemical reaction mechanisms to model combustion test cases where the impact of fluid flow, heat transfer and the chemical reactions are considered in unison.

When performing CFD analysis, it is necessary to define a fluid domain which is discretised by use of a mesh, which is the process of dividing the domain into small control volumes where the governing equations are applied.

Central to CFD analysis are the Navier-Stokes equations which describe the conservation of momentum of a fluid flow, which together with the conservation of mass, provide a description of how fluid velocities change with time and space, encompassing the impact of pressure, viscosity and any other external forces. The

2D Navier-Stokes equations are described by the following equations:

$$\frac{\partial u}{\partial t} + u \frac{\partial u}{\partial x} + v \frac{\partial u}{\partial y} = -\frac{1}{\rho} \frac{\partial p}{\partial x} + \nu \left( \frac{\partial^2 u}{\partial x^2} + \frac{\partial^2 u}{\partial y^2} \right) \quad (6.1)$$

$$\frac{\partial v}{\partial t} + u \frac{\partial v}{\partial x} + v \frac{\partial v}{\partial y} = -\frac{1}{\rho} \frac{\partial p}{\partial y} + \nu \left( \frac{\partial^2 v}{\partial x^2} + \frac{\partial^2 v}{\partial y^2} \right) \quad (6.2)$$

Specific to combustion CFD models is the inclusion of Transport Equations which describe the advection, diffusion and the chemical reaction terms. Where advection accounts for the convective transport of species in the fluid flow, representing how a given species is carried by the bulk motion of the flow. The diffusion term reflects the molecular diffusion of a given species due to concentration gradients within the fluid domain. The chemical reaction is represented by the source term, which describes the production and consumption of species due to the chemical reactions within the fluid domain. The inputs to the species transport equations are provided by an appropriately selected reaction mechanism. The species transport equation is given by:

$$\frac{\partial(\rho Y_i)}{\partial t} + \nabla \cdot (\rho \mathbf{u} Y_i) = \nabla \cdot (\rho D_i \nabla Y_i) + \dot{\omega}_i \quad (6.3)$$

where, the advection term is given by  $\nabla \cdot (\rho \mathbf{u} Y_i)$ , diffusion term is given by  $\nabla \cdot (\rho D_i \nabla Y_i)$  and the chemical reaction source term is represented by  $\dot{\omega}_i$ .

Since turbulence is characterised by a chaotic irregular flow with a wide range of length and time scales, this makes it is exceptionally computationally challenging to resolve directly. Hence, turbulence models are introduced to provide a means of closure for the system of equations. As is deployed in this study, Reynolds-Averaged Navier-Stokes (RANS) model is often utilised as a time averaged form of the governing equations, which in effect filters out the high-frequency turbulence events. RANS in turn, introduce additional terms to be resolved, known as Reynolds stresses that represent the effects of the unresolved turbulent fluctuations. Whilst it may offer the least detail in terms of turbulence characteristics, due to the averaging effect, it does provide a computationally effective means of evaluating a fluid flows.

In contrast to RANS, Direct Numerical Simulation (DNS) can be deployed to directly simulate the entire range of scales of the turbulent flow. Hence, it is characterised by a highly computationally intensive means of resolving the flow. To realise the computational efficiency of RANS and the high-fidelity of DNS, a hybrid method known as Large Eddy Simulation (LES) can be deployed where the larger scales of turbulence are resolved explicitly and the smaller scales of turbulence are modelled with the aim of capturing the most energetic scales of turbulence whilst achieving relatively good computational efficiency.

Throughout this study, RANS is deployed to increase computational efficiency. The selection of turbulence model will be delineated in Section 6.4.

## 6.2 CFD Geometry

A 2D CAD model of the TIMAR was produced as an input to the CFD environment of Fluent, benefiting from the symmetrical geometry of the TIMAR in an effort to reduce the computational expense. In addition, the model encompasses half the height of the MD where the whole 2D domain is subsequently represented by use of a symmetry line, again, for the purposes of minimising computational expense. Efforts in reducing computational expense were motivated by the increase in computational expense associated with the inclusion of species transport to model combustion. Therefore, the geometrical model is described by an analysis domain of a length of  $600\text{mm}$  and a height of  $12.5\text{mm}$ . Figure 6.2.1 illustrates the geometry of the model utilised within this study.

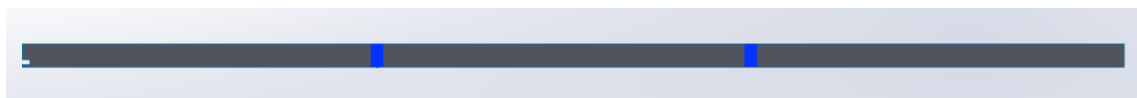


**Figure 6.2.1:** 2D geometrical CAD model developed in Solidworks for analysis in Fluent, three sections shown by blue vertical lines.

The CAD model is characterised by three separate surfaces of an equal length of  $200\text{mm}$  to enable the refinement of the mesh as will be described in Section 6.3.

In accordance to CFD best practices, the inlet for the fuel and air are separately

assigned. The outlet is defined as a gauge pressure outlet, hence, it was set to ambient pressure in accordance with the operating conditions of the TIMAR. Wall conditions are specified to be non-slip. And as aforementioned, a symmetry line is defined to enable analysis to be performed in the upper half of the fluid domain, and subsequently the full fluid domain is then able to be visualised in post processing.

### 6.3 Mesh Independence Study

As described in Section 6.1, the fluid domain under consideration must be discretised into a number of smaller control volumes where the governing equations are resolved. This process is achieved through so-called ‘meshing.’ Here lies, the mesh independence study, that aims to establish the optimum mesh density to effectively analyse the problem whilst minimising computational expense.

The mesh independent study was performed for the meshes described in Table 6.1. As aforementioned, the CAD model of the geometry was comprised of three regions of  $200mm$  in length. The first  $200mm$  was subject to a refinement of 2, meaning the specified element size is halved twice, the second  $200mm$  was subject to a refinement of unity, where the element size is halved once and the last  $200mm$  was not refined at all, maintaining its originally specified element size. This enabled the ability to capture the highly transient flow features near the inlet where the fuel and oxidant are mixing through the refined mesh, and enabled a high level of computational efficiency in the latter part of the geometry where the flow will have developed.

Due to the relative simplicity of the geometry deployed, the meshes in this study are characterised by quadrilaterals with uniform spacing within the three regions of refinement. Hence the omission of any other mesh parameters such as; edge and face curvature and proximity; sphere of influence or influence of a swept body etc. [193].

The parameter that was used in determining the efficacy of the mesh in this mesh independence study was the centreline velocity of the fluid domain under isothermal

**Table 6.1:** Mesh details for the meshes considered in the mesh independence study.

Element Size [mm]	Number of Elements
0.25	549,350
0.50	137,117
0.75	62,384
1.00	36,099
1.25	22,416

conditions. The centreline velocity profiles of the meshes considered in this study is presented in Figure 6.3.1, below.

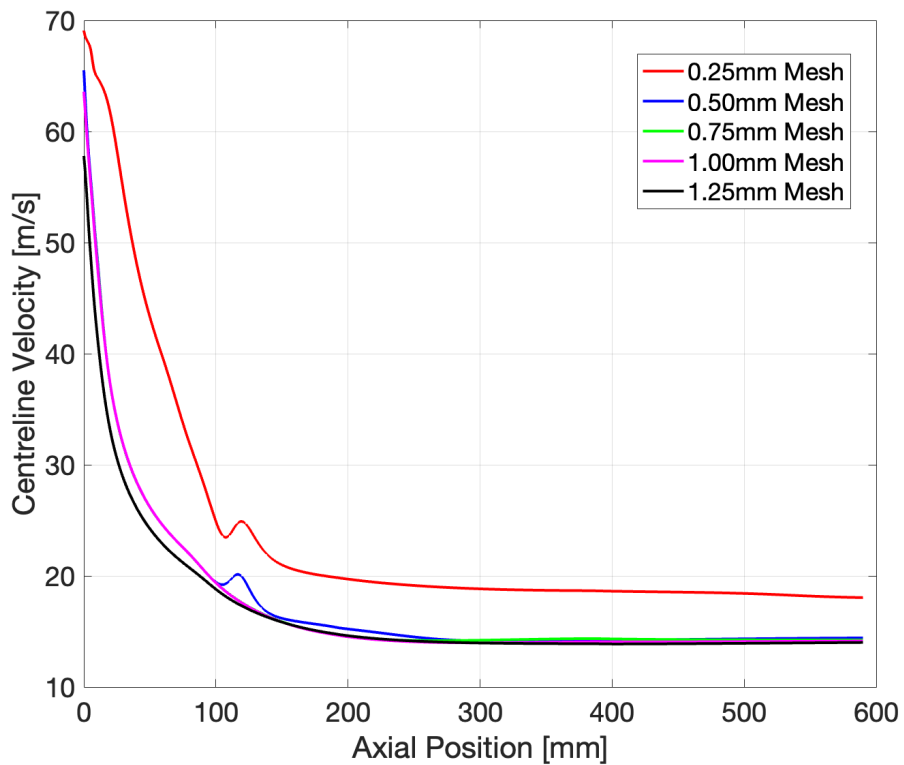
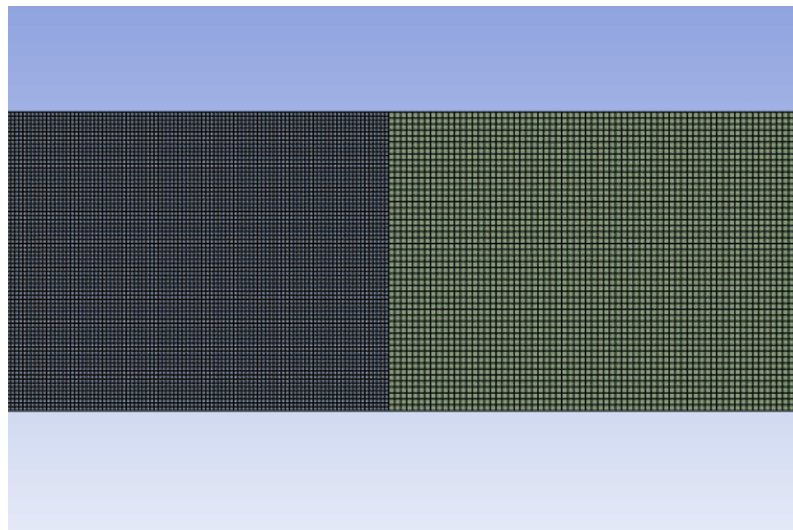


**Figure 6.3.1:** Centreline velocities,  $u$  velocity vector, of the mesh independence study.

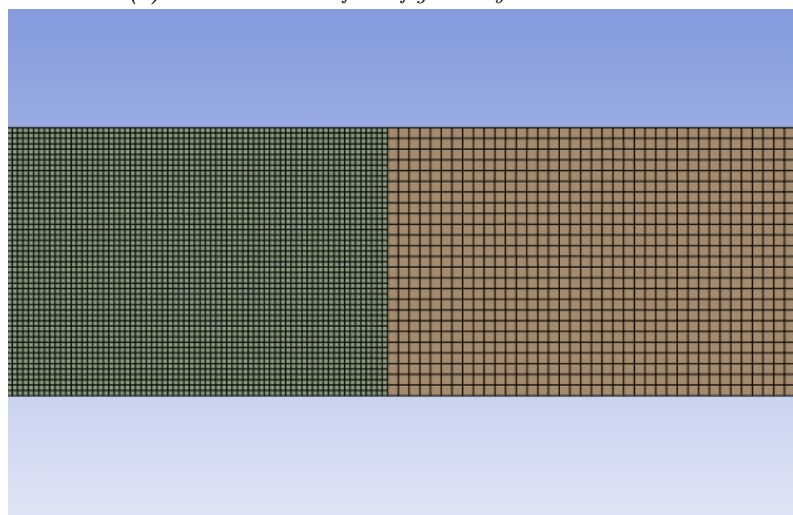
As illustrated in Figure 6.3.1, there is a notable difference between the 0.25mm mesh and the other meshes, it is considered that the small mesh size is causing numerical diffusion which relates to the consequence of using a mesh that is too fine. The mesh in this instance is excessively fine which in turn is in effect smoothing velocity gradients leading to an overestimation of the fluid velocities. Additionally

there is a notable increase in the otherwise uniform velocity profile at an axial position of  $100 - 120\text{mm}$ .

Whilst the other meshes are agreeable with one another, the  $0.50\text{mm}$  mesh is the only mesh size that capture's the increase in velocity in the  $100 - 120\text{mm}$  region. It is postulated that this feature in the flow is an effect of the two air and fuel flows mix with one another and are in turn leading to the change in the velocity profile. The lack of this velocity change in the meshes of  $0.75\text{mm}$  and larger is due to the relatively larger element size and the inability to capture the feature of the flow as a result of the loss of detail. Hence, this study concludes that a mesh size of  $0.50\text{mm}$  is optimal for the subsequent analysis.



*(a) Mesh at the interface of geometry sections 1 and 2.*



*(b) Mesh at interface of geometry sections 2 and 3.*

**Figure 6.3.2:** Mesh interfaces between the respective sections of CAD geometry, illustrating the impact of the mesh refinement.

## 6.4 Determining the Turbulence Model

As described in Section 6.1, the use of RANS models in CFD require the use of a turbulence model in order to resolve the turbulence closure problem. Careful selection is required for the turbulence model deployed as the accuracy of RANS simulations is sensitive to the choice of the turbulence model and its parameters.

Hence, a study was performed using isothermal flows to determine the most suitable turbulence model for use in the CFD model. The models considered are as follows, accompanied by a brief description:

- $k - \omega$  Standard: is a two equation closure model that solves two transport equations for turbulent kinetic energy ( $k$ ) and the specific rate of dissipation ( $\omega$ ). It is typically deployed for simulating boundary layer flows, and is known for its ability to handle adverse pressure gradients, yet is sensitive to far-field boundary conditions.
- $k - \epsilon$ : is another two equation closure model that solves two transport equations. This equation differs from the  $k - \omega$  case by modelling the turbulent kinetic energy ( $k$ ) and the rate of dissipation of the turbulent kinetic energy ( $\epsilon$ ). It is best applied to simulating internal flows, yet is deficient when modelling flows with adverse pressure gradients and near wall regions.
- $k - \omega SST$ : is an extension of the standard  $k - \omega$  turbulence model and combines elements of both the  $k - \omega$  and  $k - \epsilon$  models leading to improved accuracy and robustness for a wider range of flows. Whilst it also takes the turbulent kinetic energy, and the specific rate of dissipation, it also includes considerations of the shear stress transport by introducing it as a third transport equations. Hence, its computational expense is greater. Notable with  $k - \omega SST$  is the use of a blending function that is used to smoothly transition between the freestream where  $k - \omega$  is employed and the near wall regions where  $k - \epsilon$  is utilised. Thus, making it more applicable to a range of flows.

- Reynolds Stress: as described in 6.1, the application of RANS introduces Reynolds stresses. Where the two-equation models use additional transport equations for turbulence variables, the Reynolds stress model directly solve the transport equations for the individual Reynolds stress components which are; the transport term, production term, pressure-strain correlation term, diffusion term and the dissipation term. Hence, it is the most computationally expensive.

Similarly, the centreline velocity was the parameter utilised in determining the efficacy of the turbulence model to be utilised throughout. Figure 6.4.1 presents the centreline velocities relating to this study below, where the  $0.50mm$  mesh is used throughout.

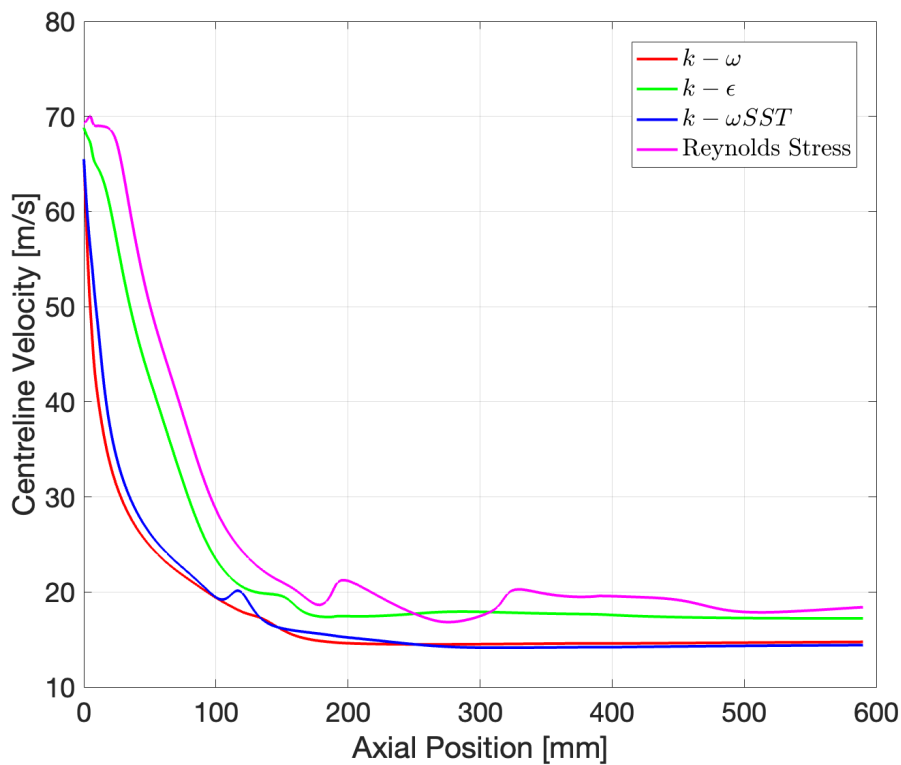


**Figure 6.4.1:** Centreline velocities,  $u$  velocity vector, of the turbulence model determination study.

As illustrated in Figure 6.4.1, both  $k - \omega$  models over predict the velocity decay of the centreline flow. There is a notable improvement of the  $k - \omega SST$  model due to its ability to capture the flow feature ca.  $100 - 120mm$ . The  $k - \epsilon$  model seems an improvement in the modelling of the velocity profile at the centreline due to its



strength of modelling internal flows. The Reynolds stress model is the model that captures more of the flow field patterns that are caused by the two flows mixing as is illustrated by the unsteady trend from 180 – 320mm axial position. The velocity profile becomes more uniform downstream as the mixing of the air and fuel transitions to homogeneity.

Hence, due to the Reynolds stress models ability to capture the centreline velocity profile with the most detail, it is utilised throughout the combustion models in this study hereafter.

## 6.5 Combustion Model Inputs

Two CFD models are used to evaluate the range of fuel blends considered in this study: (i) a pressure based model and, (ii) a model that accounts for compressibility effects. Whilst pressure based models are typically sufficient for most general cases, due to the exceedingly high velocities and temperature's experienced in the experimental cases, it was found necessary to account for compressibility effects. The use of both models is included to investigate the impact of compressibility on the test cases considered. The common inputs into both models are described in this section.

### 6.5.1 Species Transport PDF Table

Non-premixed combustion species transport was deployed throughout with a steady diffusion flamelet and a non-adiabatic energy treatment. Hence, the combustion was model through use of the Probability Density Function (PDF). PDF models models take a statistical approach, therefore it determines the likelihood of a particular scalar variable (e.g. mixture fraction, temperature, reaction progress variable) at a given spatial location. This achieved through importing a chemical kinetic mechanism, of which GriMech3.0 [175] was used throughout, which is widely considered as a robust chemical reaction mechanism applicable to a wide range of applications.

A flamelet was generated for each fuel blend with a number of grid points in the flamelet and the maximum number of flamelets set to 64 from which a PDF table was calculated.

### 6.5.2 Materials

Within the CFD model, the ability to specify materials was realised. The walls of the mixing duct (MD) were specified as “glass-silica-fused-SiO<sub>2</sub>” with a specific heat capacity of 754.47,  $J/kgK$  and a thermal conductivity of 1.3787  $W/mK$ . A wall thickness was not specified as only the fluid domain was considered in the model following the fluid domain extraction process. Correspondingly, the walls of the fuel lance were specified as “stainless-steel-314,” consistent with the material employed in the TIMAR. The specified stainless steel material exhibited a specific heat capacity of 509.61  $J/kgK$  and a thermal conductivity of 16.826  $W/mK$ . The assigned wall temperature for both the MD and the fuel lance was established at 932°C, under the assumption of thermal equilibrium within the TIMAR.

### 6.5.3 Inlet Conditions

The air inlet velocity was defined as 128.879  $m/s$  as per the velocity of air at 932°C and a mass flowrate of 23.75  $g/s$  entering the MD, taking into account the reduction of the cross sectional area due to the presence of the fuel lance in the centre of the MD inlet. As described above, it was necessary to convert the mass flow rate at the inlet to the TIMAR from the experimental work to a velocity resulting from the nature of 2D CFD modelling. The TI at the inlet was defined as 7.588% as per the results derived from the PIV analysis in Chapter 4. A hydraulic diameter of 8.5  $mm$  was also defined, again, considering the reduction in cross sectional area in the flow domain from the presence of the fuel lance at the MD inlet.

The velocity of the fuel inlet was defined by the following equation that uses the  $\frac{1}{7}$  power law that describes developed turbulent velocity profiles which is assumed

due to the length of the fuel lance:

$$u(y) = u_{max}[ms^{-1}] \left(1 - \frac{y}{y_{max}}\right)^{\left(\frac{1}{7}\right)}$$

For each fuel blend considered in this analysis, the fuel temperature's and velocities profiles utilised are detailed by Table 6.2 below, as per the data derived from the experimental component of this study.

**Table 6.2:** Table of temperature and velocity profile inputs for the CFD models for the range of fuel blends considered.

Fuel Blend [CH <sub>4</sub> /H <sub>2</sub> %vol]	T [°C]	Velocity Profile
80/20	647.46	$u(y) = 690.62[ms^{-1}] \left(1 - \frac{y}{1.5[mm]}\right)^{\left(\frac{1}{7}\right)}$
70/30	630.70	$u(y) = 735.27[ms^{-1}] \left(1 - \frac{y}{1.5[mm]}\right)^{\left(\frac{1}{7}\right)}$
60/40	620.04	$u(y) = 797.70[ms^{-1}] \left(1 - \frac{y}{1.5[mm]}\right)^{\left(\frac{1}{7}\right)}$
50/50	609.17	$u(y) = 873.50[ms^{-1}] \left(1 - \frac{y}{1.5[mm]}\right)^{\left(\frac{1}{7}\right)}$
40/60	590.57	$u(y) = 959.06[ms^{-1}] \left(1 - \frac{y}{1.5[mm]}\right)^{\left(\frac{1}{7}\right)}$
30/70	580.64	$u(y) = 1075.15[ms^{-1}] \left(1 - \frac{y}{1.5[mm]}\right)^{\left(\frac{1}{7}\right)}$
20/80	563.34	$u(y) = 1210.32[ms^{-1}] \left(1 - \frac{y}{1.5[mm]}\right)^{\left(\frac{1}{7}\right)}$
10./90	534.27	$u(y) = 1397.25[ms^{-1}] \left(1 - \frac{y}{1.5[mm]}\right)^{\left(\frac{1}{7}\right)}$
0/100	512.39	$u(y) = 1669.04[ms^{-1}] \left(1 - \frac{y}{1.5[mm]}\right)^{\left(\frac{1}{7}\right)}$

## 6.5.4 Radiation Modelling

Whilst diatomic gases such as H<sub>2</sub>, O<sub>2</sub> and N<sub>2</sub> have a negligible effect on radiative heat transfer, combustion products such as H<sub>2</sub>O and CO<sub>2</sub> have a significant impact. Hence, it was necessary to include the impact of the absorption and scattering of the radiation of gases within the model.

The Radiative Transport Equation is described by the following:

$$\nabla \cdot (I(r, s)s) + (\alpha + \sigma_s)T(r, s) = an^2 \frac{\sigma T^4}{\pi} + \frac{\sigma}{4\pi} \int_0^{4\pi} I(r, s')\Phi(s, s') d\Omega' \quad (6.4)$$

where,  $\nabla (I(r, s) s)$  is the rate of change of the radiation intensity,  $(\alpha + \sigma_s) T(r, s)$  denotes the absorption term,  $an^2 \frac{\sigma T^4}{\pi}$  is the emission of radiation term and  $\frac{\sigma}{4\pi} \int_0^{4\pi} I(r, s') \Phi(s, s') d\Omega'$  represents the scattering. As described by equation 6.4, this equation is challenging to solve due to the scattering integral and the directional variable  $s$  and that radiation in a real system has an infinite number of beam angles incident at any given point in the fluid domain.

Hence, a Discrete Ordinate (DO) radiation model is applied. Whilst radiation is omnidirectional in nature, the DO model will discretise the number of beam directions, thus, simplifying analysis to a given number of beam directions that are separated by a wave angle of  $\Delta\omega = \frac{360^\circ}{N_{directions}}$ , as presented in Figure 6.5.1 below [194].

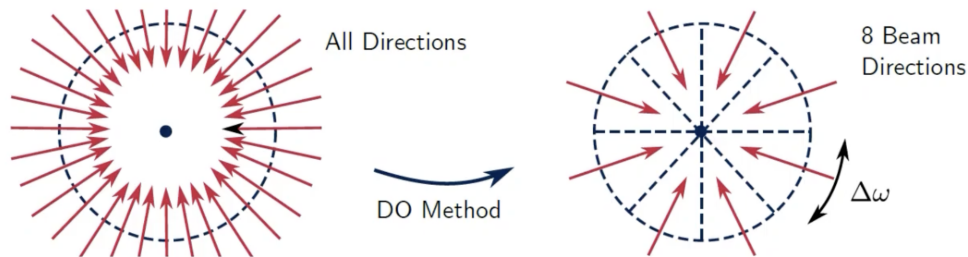


**Figure 6.5.1:** Impact of Discrete Ordinate method discretisation, reproduced from [195].

This impacts the equation by reducing the integral by numerical integration, thus, reducing the scattering term to the following:

$$\frac{\sigma}{4\pi} \sum_{j=1}^N I_j \Phi_j \Delta\omega \quad (6.5)$$

where  $N$  is the number of discrete directions we consider using within the DO model.

In DO modelling the radiation intensity is assumed constant over the wave angle, which is defined as the angular distance between the discretised beams ( $\Delta\omega$ ). Within FLUENT, the DO method will discretise the control volume into octants and will require a number of segments per octant to be defined ( $N_\theta$ ). Therefore, the total number of beam angles resolved for is  $8 \times N_{theta}$ . In addition, the DO model utilises

symmetry in its calculations, thus, only four octants are solved for, thus, reducing computational time [194], as is illustrated in Figure 6.5.2, below.

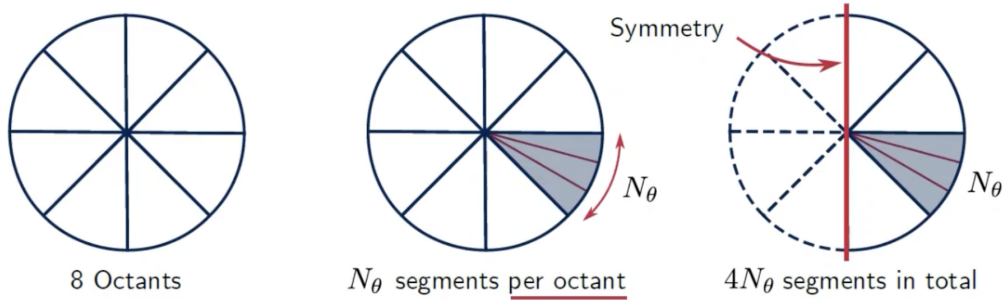


**Figure 6.5.2:** Use of octants and segments in the angular discretisation employed in DO method, reproduced from [195].

It is important to acknowledge that the inclusion of the DO method will require a transport equation for every beam direction defined. Hence, in this 2D analysis, with the use of symmetry and a  $N_{theta} = 2$ , an additional eight equations must be resolved to account for the eight beam directions specified. Thus, resulting in increased computational expense.

However, since radiations coupling with energy is weak as radiation is a function of temperature only, to reduce computational time, the radiative transport equations are specified within this model to be resolved for every ten iterations of the energy equations.

### 6.5.5 Convergence Criterion

Coupled with the convergence criteria of the residuals within the calculation of the model, an additional three convergence conditions were applied to the the points illustrated in Figure 6.5.3 and detailed in Table 6.3, below. Their placement was based on three regions in the flow that saw the highest level of transients and were defined as (from left to right) “fuel lance wall”, “centreline mixing” and “shear layer mixing region.” The criterion for their convergence was a  $1 \times 10^{-6}$  maximum difference between values of the iterations.

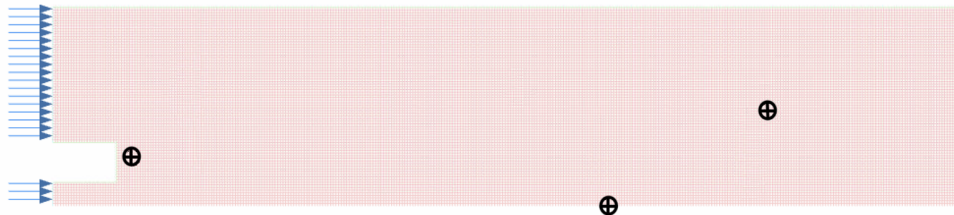


**Figure 6.5.3:** Location of convergence criterion points within CFD model.

**Table 6.3:** Location of the convergence criterion points.

Point Name	x Location [mm]	y Location [mm]
Fuel Lance Wall	5	3
Centreline Mixing	35	0
Shear Layer Mixing	45	6

### 6.5.6 Solution Controls

When running the model an initial time scale factor of unity was applied. Every 300 iterations the time scale factor was reduced by a factor of ten until a time scale factor of  $1 \times 10^{-6}$ . The reasoning being was to enable the solution to initiate with stability, minimising the potential for divergence in processing the solution. As the solution develops and residuals reduce, it enabled the reduction in the time scale factor and thus improve the accuracy of transients and the temporal resolution, thus capturing rapidly evolving turbulent structures.

### 6.5.7 Inclusion of Compressibility Effects

Due to the operation of the TIMAR includes gas flows at high temperature and velocity it is necessary to consider the impact of compressibility effects as each fuel blend was determined to exhibited a  $Mach > 0.3$ , where the non-compressible assumption is no longer considered [196].

The consideration of compressibility effects was incorporated into the species transport specification and the resultant PDF table for chemical kinetics, as illus-

trated in Figure 6.5.4 below. The incorporation of compressibility effects accommodates alterations in both density and temperature in the transport equations. Compressibility effects become prominent as velocities approach or exceed the speed of sound. Consequently, the inclusion of compressibility effects addresses changes in gas density resulting from fluctuations in temperature and pressure, thereby influencing species transport.

In the evaluation of compressible flows, temperature and pressure exhibit coupling, reflecting their interconnected relationship. Additionally, the local speed of sound is ascertained, exerting influence on species advection locally if surpassed at a given point in the flow. Accounting for the speed of sound facilitates the identification of shockwaves, which profoundly impact local conditions of pressure, temperature, and velocity, consequently affecting the rate of reaction, if present.

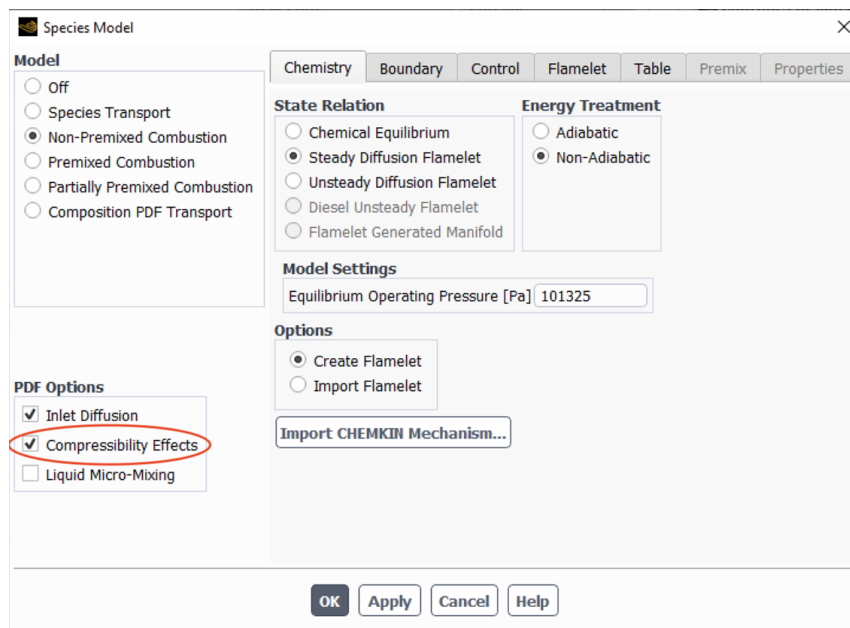


*Figure 6.5.4: Specifying compressibility effects to be included in the calculation of the PDF table.*

## 6.6 Combustion CFD Results

The results of the CFD models are now presented. Each model utilised the settings detailed in Section's 6.5, with the exception of the fuel blend, fuel temperature and velocity input specified for the inlet, as described by Table 6.2. Each fuel blend

had a corresponding flamelet and PDF table generated. Chemiluminescence images from the experimental section of this study are presented in this section, derived via the methodology described in Section 4.5.1, to enable comparison of the CFD model and the experimental results.

The OH\* contour plots from the two CFD models and the OH\* chemiluminescence of the experimental test case for the all the fuels blends are found in the Appendix, however the contour plots of 80/20 [%vol] CH/H<sub>2</sub>, 40/60 [%vol] CH/H<sub>2</sub> and 0/100 [%vol] CH/H<sub>2</sub> are presented at the end of this Chapter. Due consideration must be given to the OH\* chemiluminescence plots that clearly do not exhibit the same level of OH\* concentration downstream of the initial flame, as this is a result of the limited length of the imaging window captured by camera set up used in the experimental section of this project. The image has been post-processed to establish the flames relative position in the MD to serve as comparison between the experimentally derived results and the results of the CFD study.

Figure 6.7.1 describes the LFH from the three means of evaluating the 80/20 [%vol] CH<sub>4</sub>/H<sub>2</sub> case. The CFD model (Figure 6.7.1a) that considered pressure effects only returns the largest LFH of the test cases presented. The CFD model that considers the impact of compressibility effects (Figure 6.7.1b) has a LFH of approximately half that of the pressure-based CFD model. Furthermore, the processed experimental chemiluminescence image in Figure 6.7.1c, derived the experimental campaign exhibits a LFH of approximately half that of the compressible-CFD model and three times smaller than the pressure based CFD model.

Illustrated in Figure 6.7.2, the CFD model that considered pressure effects only, depicted in Figure 6.7.2a, returns the largest LFH of the test cases considered for the 40/60 [%vol] CH<sub>4</sub>/H<sub>2</sub> fuel blend. The compressibility-effects CFD model, presented in Figure 6.7.2b, has a smaller LFH compared to the pressure-based CFD model. The difference between the two CFD models has reduced compared to the 80/20 [%vol] CH<sub>4</sub>/H<sub>2</sub> case described above in Figure 6.7.1. Furthermore, the processed experimental chemiluminescence image from the experimental campaign exhibits a



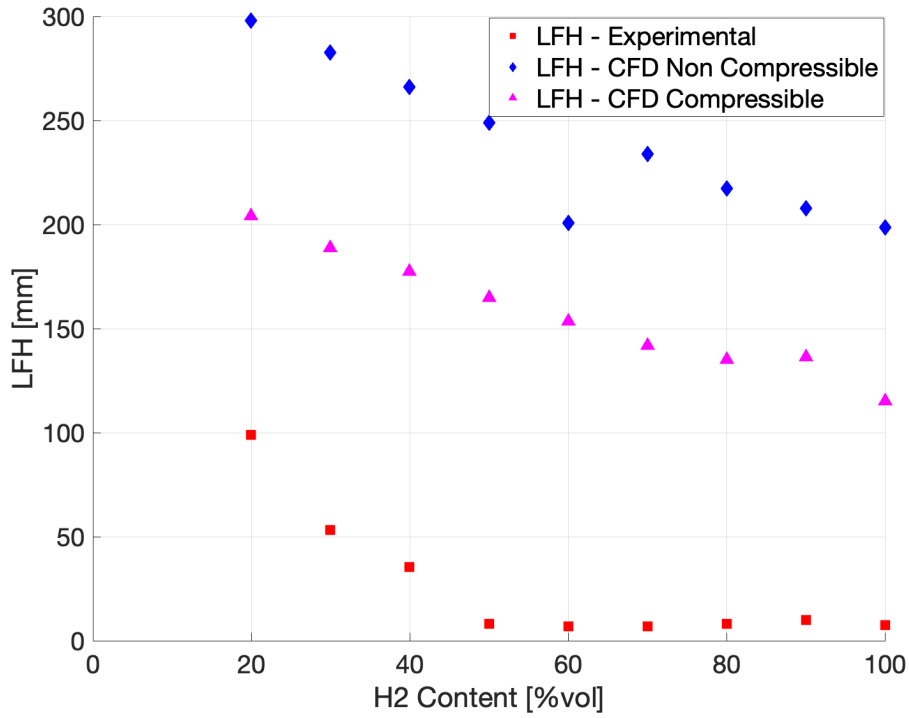
far smaller LFH when compared to the pressure based and compressible-CFD model.

Figure 6.7.3 below, depicts the difference in results for the pressure-based and compressibility-based CFD models and compares against the processed chemiluminescence image from the experimental campaign. Consistent with the cases above, the pressure-based model shows the longest LFH of the three methods considered, as depicted in figure 6.7.3a. The compressibility-based model's LFH, presented in Figure 6.7.3b, also predicts a reduction in the LFH when compared to the other fuel blends cases considered above and is less than the LFH exhibited by the pressure-based model. The experimentally derived chemiluminescence image of Figure 6.7.3c shows a LFH that is considerably smaller than either of the CFD models again. The value of the LFH is larger than that observed in the 40/60 [% vol] CH<sub>4</sub>/H<sub>2</sub> case, as was discussed in Section 5.5.1.

Discernible between the experimental and CFD results is the topology of the OH\* contour. The CFD results depict an OH\* contour that initially establishes itself either side of the centre of the fluid domain with a shape akin to an inverted quadratic polynomial where gradient reduces the further downstream the tube the contour is as the OH\* concentration increases. The experimental results exhibit an OH\* concentration representative of a diffusion flame.

Figure 6.6.1, presents the LFH values derived from each method. There is a considerable difference in the LFH between each of the methods. The CFD model considering only pressure and radiation exhibits the largest LFH values across the range of fuel blends considered in this study. Followed by the CFD model taking compressibility effects into consideration. Subsequently, the experimentally derived LFH results return the smallest LFH across the fuel blend range by a considerable amount.

Since compressibility effects were apparent and the high temperature and velocity nature of the cases considered, Mach number analysis was undertaken. Mach number is a function of the speed of sound, therefore the speed of sound of each case was considered using the inputs into the model described in Table 6.2, through use of



**Figure 6.6.1:** Lifted Flame Heights of the fuel range of fuel blends considered attained through the experimental campaign and the CFD study, where the Lifted Flame Height is determined to be 30% of the max  $OH^*$  intensity.

equations 6.6 and 6.7, below:

$$c = \sqrt{\frac{\gamma RT}{MW}} \quad (6.6)$$

$$Mach = \frac{u_{max}}{c} \quad (6.7)$$

where,  $c$  is the speed of sound of the fuel blend,  $\gamma$  is the adiabatic index of the fuel blend at the corrected measured fuel temperature denoted by  $T$ ,  $R$  is the universal gas constant,  $MW$  is the molecular weight of the fuel gas blend, and  $u_{max}$  is the maximum fuel velocity specified in Table 6.2.

Two cases of Mach number were evaluated, for the flow conditions of the fuel prior to combustion and a case of the combustion products of the reaction at an adiabatic flame temperature at the equivalence ratio of the case determined through using the equilibrium tool within CHEMKIN. The results of the Mach analysis is presented in Figure 6.6.2 below.

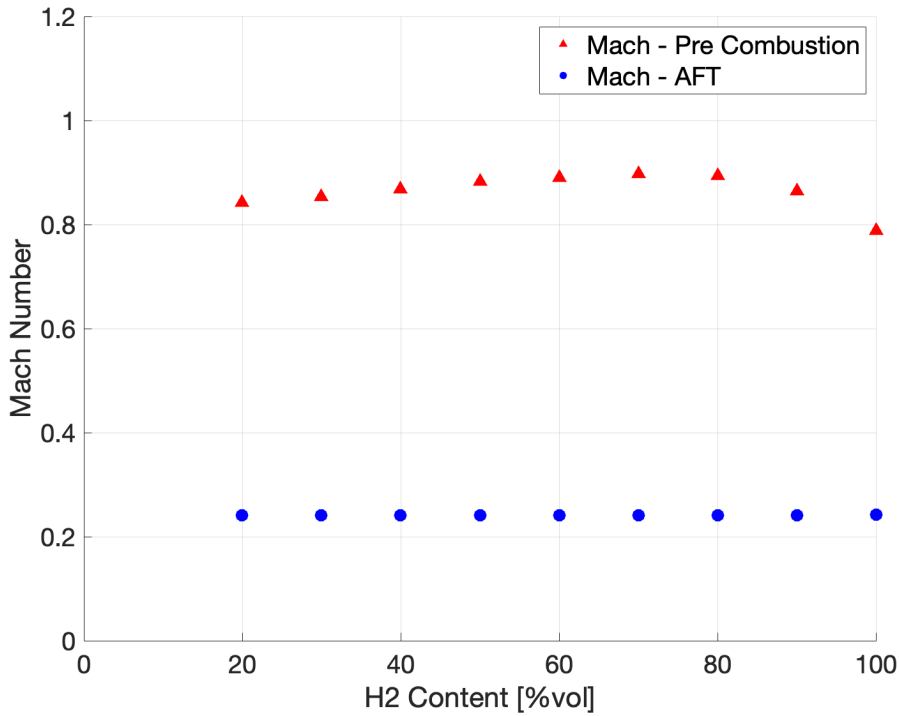


*Figure 6.6.2: Mach number analysis from experimental campaign.*

## 6.7 Combustion CFD Discussion

Throughout this study, the impact of hydrogen was evident across all test cases showing a consistent decrease in LFH as the hydrogen content of the fuel increased regardless of the method used, other than the anomalous pressure-based case of 40/60 [%vol]  $\text{CH}_4/\text{H}_2$  which exhibits a LFH similar in magnitude to the 0/100 [%vol]  $\text{CH}_4/\text{H}_2$ , as shown in Figure 6.6.1. This point is considered anomalous due to the trend of all other LFH considered through the pressure-based model trend consistently otherwise. It has been retrospectively theorised that the anomalous result is a result of a user error in inputting the test case conditions.

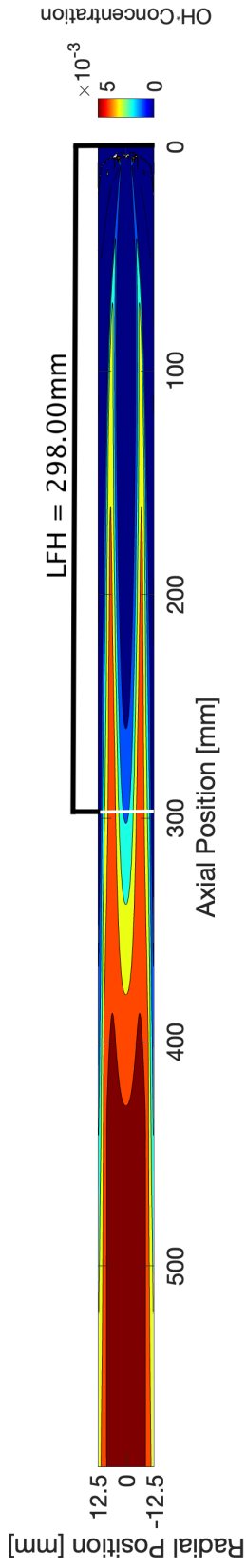
There was a difference in the LFHs observed from the three methods considered across the fuel blend range, where the pressure-based CFD model returns the longest LFHs, followed by the non-compressible model and the smallest LFHs are presented by the LFHs derived from the experimental campaign.

As the compressibility-based model was the more comprehensive CFD model

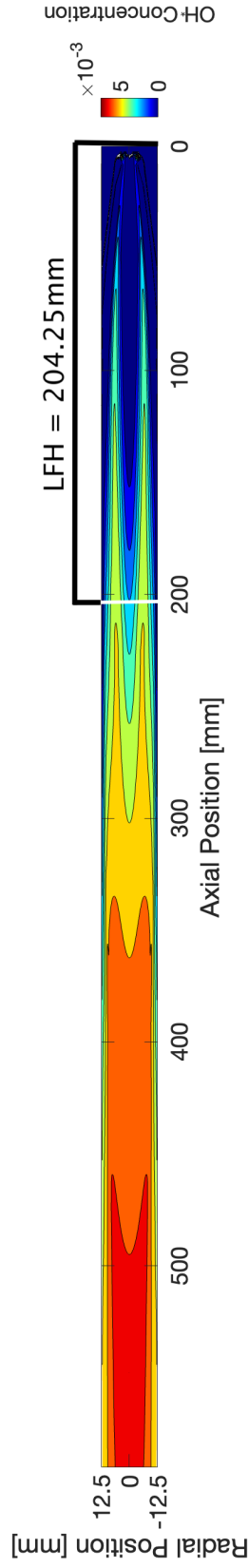
of the two, it suggested under the experimental conditions that the reduced LFH could have been caused by the occurrence of shockwaves increasing the reaction rate due to the flow entering the supersonic regime. However, the Mach number analysis, presented in Figure 6.6.2, using the corrected fuel temperatures and fuel velocities from the pre-combustion conditions detailed in Table 6.2 and those of the combustion reactants at a determined AFT, indicated that the conditions remained within the subsonic range throughout.

Consequently, the difference between the CFD models and the experimental test case was attributed to the limitations of PDF tables in modelling chemistry. PDF tables assume local thermodynamic and chemical equilibrium within a computational cell, where the time scales for chemical reactions are assumed to be much faster than the fluid mixing process. However, as determined through the Damköhler Number analysis in Chapter 5, this assumption did not hold for every considered case. PDF tables also simplified chemical kinetics by assuming a finite number of PDF shapes, leading to inaccuracies in capturing the complex nature of combustion chemistry in high-velocity turbulent flows. Sensitivity to grid resolution was another challenge for PDF tables, as regions of high gradient between parameters and within turbulent flows, present in the considered cases, led to errors in predicting combustion behaviour. PDF tables considered the most probable route of the chemistry of the inputs provided to the model, but they were unable to accurately model the experimental cases.

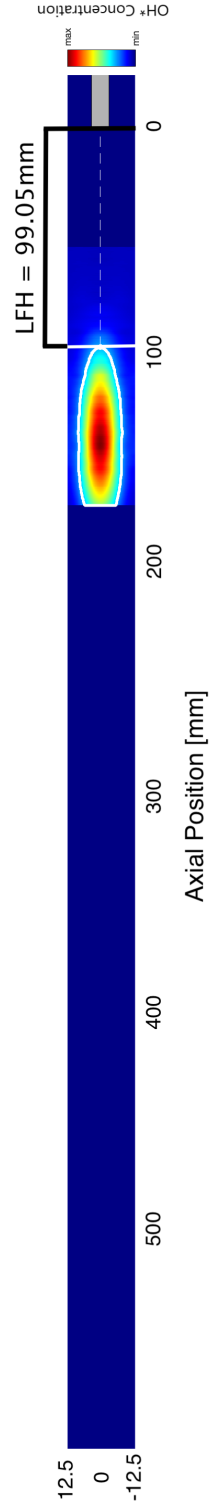
Progression of this CFD study in future work would entail utilising detailed chemistry to model the species transport. This progression in this CFD study was unattainable due to resource limitations.



(a) CFD: Pressure based and effects  $CH_4/H_2$  80/20 [%vol] OH concentration contour for the TDV case.



(b) CFD: Pressure based, radiation and compressibility effects  $CH_4/H_2$  80/20 [%vol] OH concentration contour for the TDV case.



(c) Experimental derived  $CH_4/H_2$  80/20 [%vol] chemiluminescence processed image for the TDV3 case.

**Figure 6.7.1:** LFH analysis from both the CFD and experimental analysis for the  $CH_4/H_2$  80/20 [%vol] TDV3 case. Gas flow is from right to left.

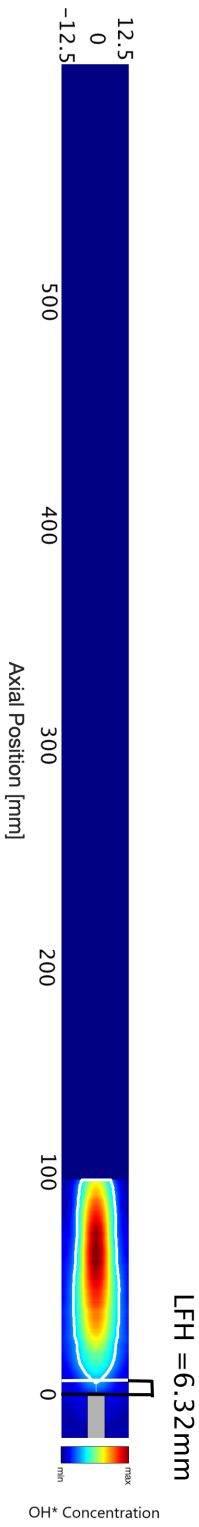
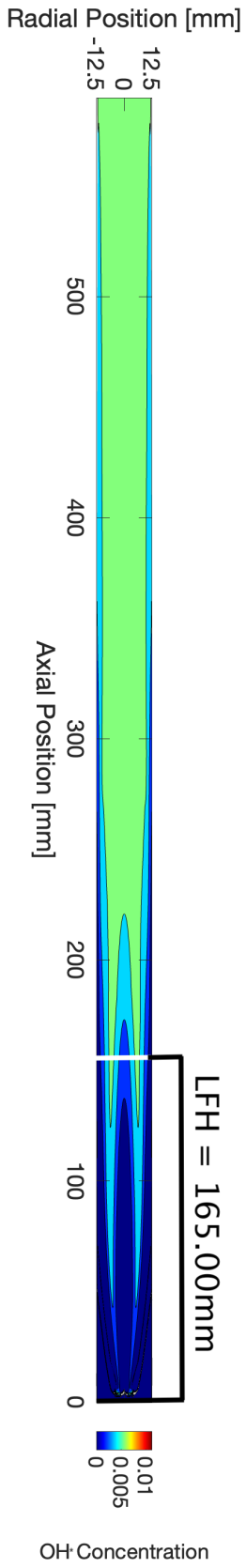
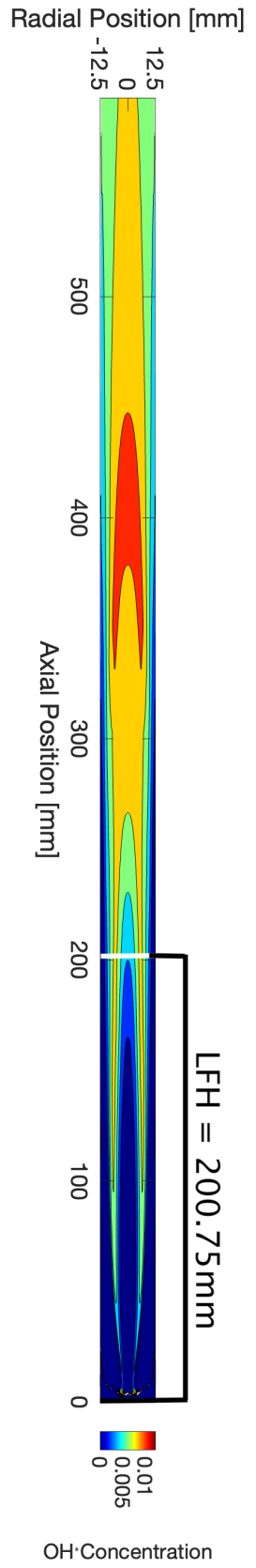
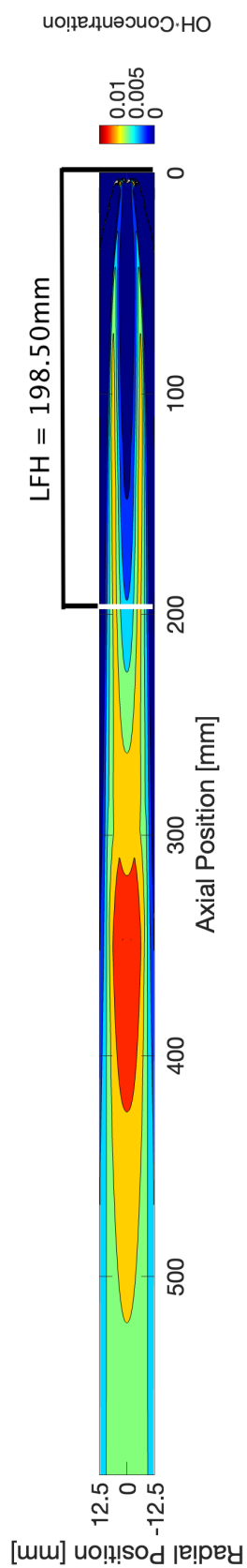
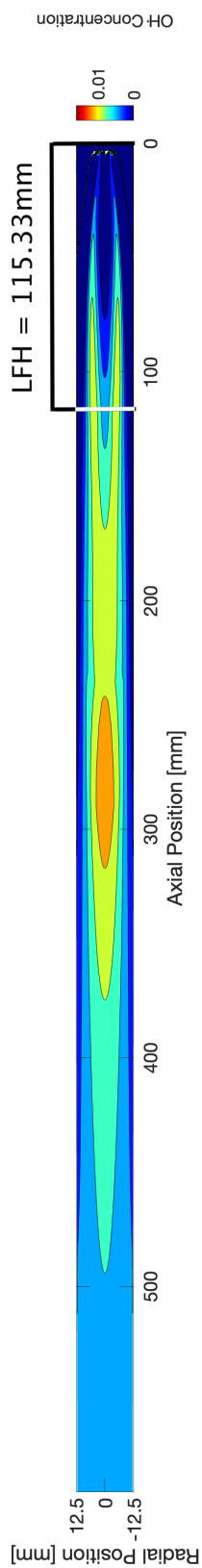


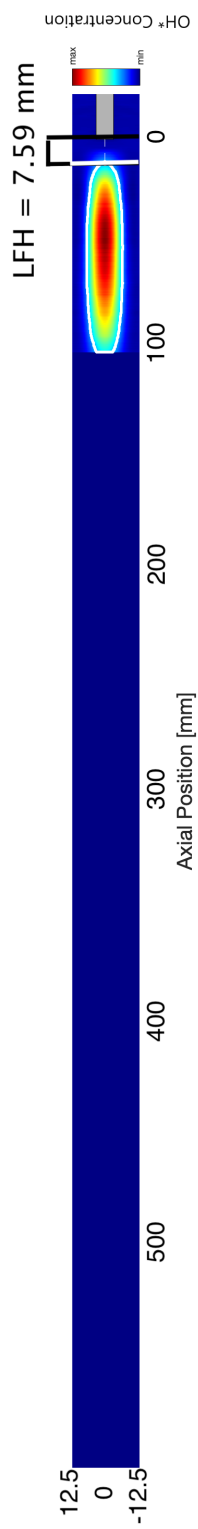
Figure 6.7.2: LFH analysis from both the CFD and experimental analysis for the  $CH_4/H_2$  40/60 [%vol] TDV3 case. Gas flow is from right to left.



(a) CFD: Pressure based and effects  $CH_4/H_2$  0/100 [%vol] OH concentration contour for the TDV case.



(b) CFD: Pressure based, radiation and compressibility effects  $CH_4/H_2$  0/100 [%vol] OH concentration contour for the TDV case.



(c) Experimental derived  $CH_4/H_2$  0/100 [%vol] chemiluminescence processed image for the TDV3 case.

**Figure 6.7-3:** LFH analysis from both the CFD and experimental analysis for the  $CH_4/H_2$  0/100 [%vol] TDV3 case. Gas flow is from right to left.

# Chapter 7

## Conclusions and Future Work.

The need to decarbonise heavy-emitting assets is becoming increasingly important as a result of the continued development of humankind and our increasing needs for energy. The role of power in the future of energy will also increase as many more processes become electrified. Hence, the need to decarbonise flexible generating assets to support the ever increasing utilisation of RES is paramount. Whilst protection of our environment is primary, it can not be achieved without a period of transition in which the conversion of generating assets using carbonaceous fuels to operating with alternative fuels such as hydrogen will be vital. Hence, the expressed interest of power industry players, such as the sponsor of this doctoral project RWE, in adapting their current assets to maintain their economic viability.

As described throughout this thesis, the challenges of operating with hydrogen are numerous and highly consequential in the event of system failures. A thorough approach to understanding the impact of hydrogen in power generating assets is key to the successful implementation of hydrogen in assets originally designed for natural gas, as is undertaken in this doctoral project for the adaption of the GT26 GT to operate on either pure hydrogen or hydrogen fuel blends with natural gas. Whilst RWE are the main benefactors of this research, it is not limited to other operators of the GT26 or either GE or Ansaldo Energia who now own the intellectual property of the engine.

In this conclusion section, the key findings of this study are highlighted with



a view of both the fundamental mechanisms underlying the ignition of hydrogen enriched fuels and how they can be considered in the retrofit of future designs to the GT26. Such conclusions are followed by suggestions for future work that will increase the depth of study achievable with the TIMAR and elucidate further considerations for the utilisation of high hydrogen containing fuels in the GT26.

## **7.1 Conclusions**

### **7.1.1 Development of Experimental Test Campaign**

In this study a thorough test campaign was developed which considered the impact of temperature and turbulence on the ignition of inhomogeneous hydrogen enriched fuel mixed with (i) air (ii) air with varying proportions of a single main constituents of a flue gas (i.e.  $\text{CO}_2$  or  $\text{H}_2\text{O}$  and (iii) industrially applied conditions where the fuel gas composition was pertaining to the fuel blend operated in the first stage, as described in Chapter 4. Due to restraints in time and resource, the test campaign was unable to extend past the considerations for air. However, these efforts were not futile, as they provide a natural progression point for future research in this area.

The impact of turbulence was successfully evaluated due to the design, development and implementation of the Turbulence Devices (TDVs). Which offered different Turbulence Intensities and Kolmogorov lengthscales imparted on the oxidant flow into the mixing duct where the reaction took place. Thus, successfully addressing the proposed hypothesis in Section 2.6.

### **7.1.2 The TIMAR Development**

In this study a novel combustion facility for investigating the impact of turbulence on the ignition of inhomogeneous hydrogen enriched fuel and oxidant mixtures is developed for use at Cardiff University's Gas turbine Research Centre. Through commissioning and characterisation of the TIMAR, its operating principles were understood which contributed to developing the experimental campaign conducted

and described in this thesis. The TIMAR was a repeatable and reliable combustion facility that was supported by the precise control of mass flow rates of both fuel and air, and the oxidant temperature's attained through this study. Thus, enabling a comprehensive investigation into the effect of turbulence on the ignition of hydrogen enriched fuels.

### 7.1.3 Methodologies

Within this study, four experimental outputs were achieved either through direct measurement or inferred by calculation. Chemiluminescence imaging was utilised in the determination of lifted flame heights from the experimental campaign, where the least reactive cases were characterised by longer LFH. Its determination will prove valuable in the development of retrofit designs of the GT26's SEV combustor.

A technique was developed in determining a parameter defined as the "Flame Establishment Time" which described the rate of the ignition reaction that is characterised by the thermal runaway aspect of the reaction. This was enabled by determining the rate of the hydroxyl radical in achieving a peak value for a given case. This method was limited by the varying  $\text{OH}^*$  profiles of the test cases considered, which returned different rates at which the first significant peak of  $\text{OH}^*$  was achieved.

Furthermore, a calculated ignition delay time was determined through the ascertained LFH and the oxidant flow in the mixing duct. In turn enabled the determination of the duration of the mixing and slow ignition chemistry that inhomogeneous oxidant fuel mixtures exhibited.

The determination of FET and the ignition delay time enabled the calculation of the non-dimensionless number Damköhler which described whether the combustion reaction was being driven by the chemical or mixing timescales, which proved to be invaluable when considering the impact of turbulence on the ignition of the inhomogeneous mixtures of the fuel and oxidants evaluated in this study. It is suggested that the consideration of Damköhler Number should be included in the

design of combustors that aim to utilise high proportions of hydrogen in its fuel supply.

#### **7.1.4 Impact of Turbulence**

From this study it was shown that for high proportions of hydrogen, two turbulence states were identified to inhibit the ignition of such fuels.

It was shown that inducing a turbulent flow characterised by relatively small lengthscales of turbulence had an inhibitory effect on the ignition of highly enriched hydrogen fuel blends which results from the disturbances induced by the turbulent flow on the production of ignition kernels reaching a critical volume to enable the ignition reaction to propagate. This was supported by the Damköhler numbers of greater than unity that were ascribed to the TDV3 cases for high hydrogen containing fuels, when compared to TDV6, which exhibited shorter LFHs which is associated with an increased reaction rate.

In addition, it was also evidenced that poor mixing also induced an inhibitory effect resulting from the insufficient concentrations of reactive species in local regions of the flow. As was showcased by the TDV12 results. Similarly, the LFH for the TDV12 cases compared to the TDV6 cases were longer.

#### **7.1.5 Industrial Relevance**

As demonstrated in this study, it is crucial for GT Original Equipment Manufacturers to ensure that the combustion resulting from a autoignition-governed combustor is dominated by the rate of mixing rather than chemistry timescales in the combustor. This objective can be achieved by developing autoignition-governed combustors that consider Damköhler numbers greater than unity for combustion in their respective combustors.

Considerations for the strategic redesign of the vortex generators in the SEV combustor, along with ensuring sufficient fuel jet velocities, should be carefully evaluated. This research demonstrates that turbulence characteristics, such as intensity

and lengthscale, can significantly impact the ignition time of hydrogen-enriched fuels in an inhomogeneous mixture with an oxidant. Future SEV combustor designs must ensure that the reaction rate is governed by the mixing rate of the fuel and oxidant, rather than the combustion reaction rate.

## **7.2 Future Work**

Since this is the first investigation into the impact of turbulence on the ignition of hydrogen enriched fuels within the TIMAR, the number of possible routes to extend this study is considerable and their pursuit would be highly beneficial for extending the understanding developed in this doctoral thesis.

### **7.2.1 Synthesised Reheat Oxidant Compositions**

Due to the resource limitations noted above, this study evaluated the effect of turbulence on the ignition of inhomogeneous air fuel mixtures. Whilst this represents a more reactive case than the vitiated flow from the first stage combustor in the GT26, it is recommended to pursue further study with the TIMAR with the use of synthesised oxidants as described in Section D.5.2 to account for the  $\text{CO}_2$  and  $\text{H}_2\text{O}$  contents of the vitiated flow that enters the SEV of the GT26.

### **7.2.2 Fuel Lance Design**

In this study, the heat transfer from the fuel lance to the fuel introduced complexities in the treatment of the fuel temperatures which were accounted for with the use of the thermocouple correction algorithm developed for this study. However, to minimise the impact of heat transfer to the fuel, it is suggested that the fuel lance should be redesigned to consider the use of a material with a lower thermal conductivity such as ceramic.

### 7.2.3 Emission Analysis

When using a combustion system in an industrial context, emissions are often limited resulting from permitting agreements with environmental agencies. Hence, it is proposed that in future studies with the TIMAR that the emissions are also evaluated as it is known widely in combustion research that the strategies of mixing fuel and oxidants impacts the concentration of pollutants. This will prove to be of high importance when larger proportions of hydrogen are used in the fuel blend, naturally leading to the occurrence of higher NO<sub>x</sub> emissions. Investigating means of minimising the formation of NO<sub>x</sub> is considered to be of high value for the utilisation of hydrogen in combustion systems.

### 7.2.4 Turbulence Devices

From the experimental campaign of this study it was shown that TDV3 and TDV6 impacted the flow field sufficiently to assess the impact of turbulence on the ignition of fuels considered. However, due to the larger characteristic geometry of TDV12 it had a minimal impact. Therefore, it is suggested that other turbulence devices should be considered in future studies with the TIMAR to provide larger turbulent lengthscales to elucidate the impact of turbulence in the range of TDV6 and TDV12. It is also suggested that other turbulence devices should be employed such as the use of delta wings akin to the vortex generators present in the GT26.

In addition, to enable continuous investigation of different turbulent characteristics without the need for rig rebuilding, as was performed in this study, it would be advantageous to develop an air driven turbulence device where the change in air flow conditions of the TDV would induce different turbulence characteristics on the flow.

### **7.2.5 Elevated Pressure**

The work undertaken in this thesis is all performed at ambient conditions, however, the SEV combustor in the GT26 operates at an elevated pressure of ca. 15bar. Hence, the principle of this study can now be developed to consider elevated pressure conditions to account for the impact of pressure on the ignition of hydrogen enriched fuel in inhomogeneous fuel and oxidant mixtures. Thus, leading to further knowledge on the possible routes to inhibiting the ignition of such fuels, and therefore increasing the hydrogen capability of the GT26.

### **7.2.6 CFD**

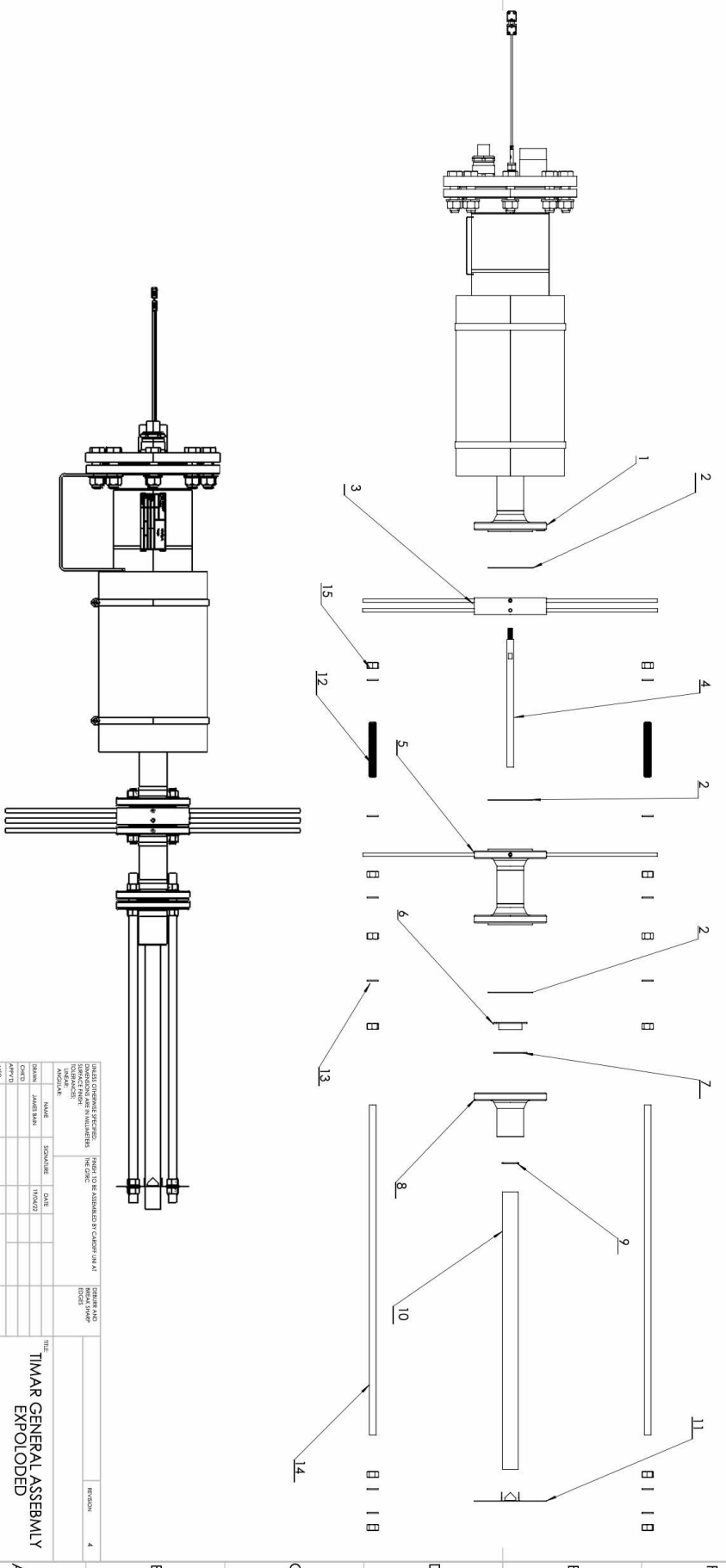
Due to resource limitations, the CFD aspect of this thesis was limited to 2D modelling with the use of PDF tables to resolve for the chemistry. Further work is recommended to develop the CFD models by accounting for detailed chemistry and to deploy a 3D model to account for the impact of turbulence in all directions.

# Appendix A

## APPENDIX A: Technical Drawings

ITEM NUMBER	PART NUMBER	DESCRIPTION	MATERIAL	QUANTITY
1	H-KFH01	KANITHAL FLOW HEATER	-	1
2	G-USG01	UPSTREAM GASKET	CALCIUM-MAGNESIUM SILICATE	3
3	F-FSFO1	FUEL STEAM FLANGE	310 STAINLESS	1
4	F-FLC51	FUEL LANCE (5mm ID)	INCONEL 625	1
5	F-FHN01	INSTRUMENTATION FLANGE	310 STAINLESS	1
6	F-TDV	TURBULENCE DEVICE (1 of 3)	INCONEL 625	1 of 3
7	G-TDGO1	TURBULENCE DEVICE GASKET	CALCIUM-MAGNESIUM SILICATE	1
8	F-FRN01	TRANSITION PIECE	310 STAINLESS	1
9	G-QTG01	QUARTZ GASKET	CALCIUM-MAGNESIUM SILICATE	1
10	Q-QRT01	QUARTZ TUBE	QUARTZ GLASS	1
11	F-FPI01	DOWNSTREAM FINGER PLATE	INCONEL SHEET	1
12	X-SS12	SHORT M12 STUD	INCONEL 625	4
13	X-WSH12	M12 WASHER	316 STAINLESS	24
14	X-STD12	M12 STUD BAR	INCONEL 625	4
15	X-NUT12	M12 NUT	316 STAINLESS	20

NOTES:  
 > EXPLODED VIEW OF THE TIMAR RIG PROVIDED TO ILLUSTRATE THE SETUP OF COMPONENTS  
 > DRAWING IS NOT TO SCALE  
 > FASTENERS HAVE BEEN LABELLED ONCE FOR BREVITY



SOI IDWORKS Educational Product: for Instructional Use Only.

TITLE: TIMAR GENERAL ASSEMBLY EXPLODED		SHEET NO: 1 SHEET OF: 1	
PROJECT: TIMAR_GA		REVISION: 4	
DRAWN BY: JAMIR BANI		DATE: 17/03/23	
CHECKED BY:		APPROVED BY:	
DATE:		MATERIAL:	
SIZE:		WEIGHT:	
C/N:		NUMBER:	
THIS DRAWING IS THE PROPERTY OF SOI IDWORKS. IT IS TO BE ASSUMED BY CUSTOMER THAT IT IS TO BE USED FOR THE PURPOSES AND MATERIALS SPECIFIED HEREIN. IT IS NOT TO BE REPRODUCED OR TRANSMITTED IN ANY FORM OR BY ANY MEANS, ELECTRONIC OR MECHANICAL, INCLUDING PHOTOCOPYING, RECORDING, OR BY ANY INFORMATION STORAGE AND RETRIEVAL SYSTEM.			

Figure A.0.1: General Assembly of TIMAR provided for context when referring to design decisions.





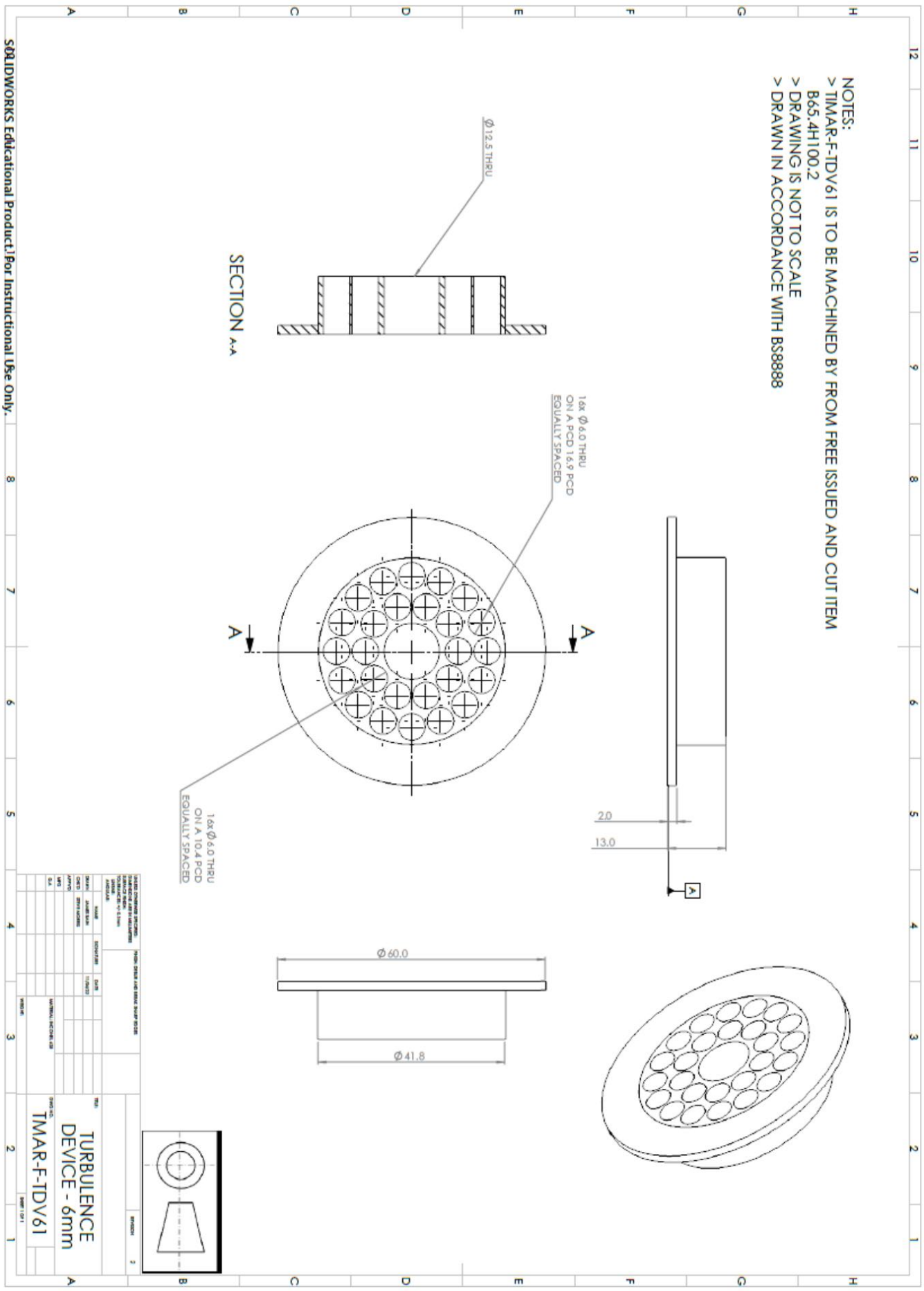
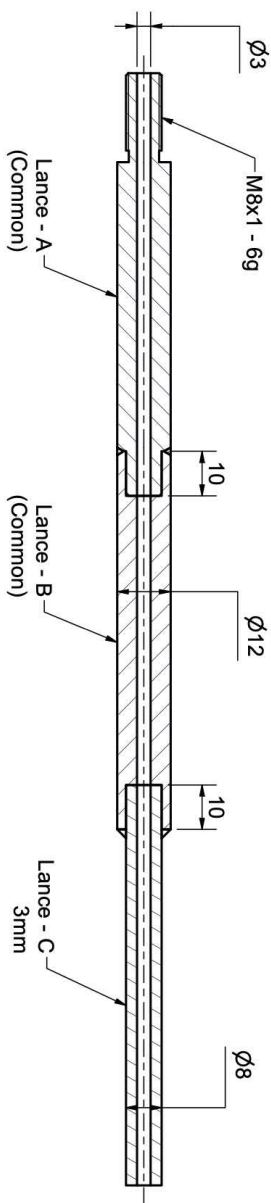
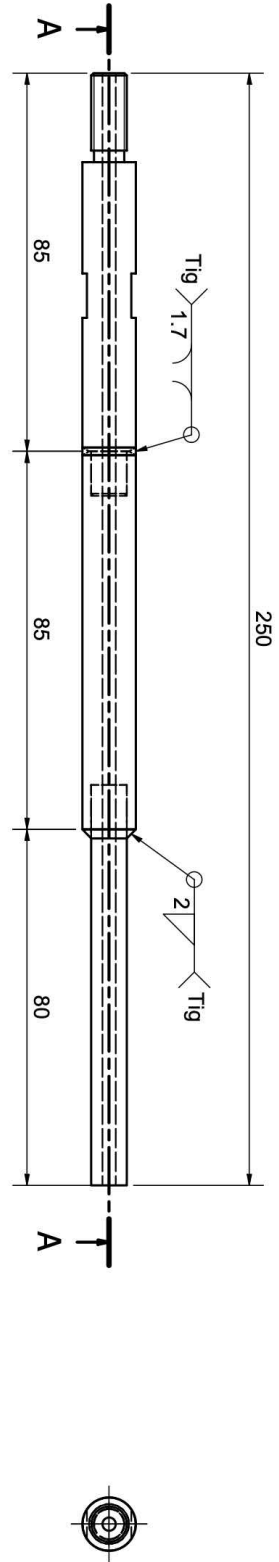


Figure A.0.3: Technical Drawing of TDV6 as supplied to manufacturer.



REQ'D BY \_\_\_\_\_ JOB No. \_\_\_\_\_



A-A ( 1 : 1 )

All fillet weld leg length to be 26mm UNO. All butt welds to be full penetration UNO. All weld symbols to be in accordance with BS EN ISO 2553. Functional tolerances class 1 UNO. Execution class to be EXC 2. Fabrication tolerances to be in accordance with BS EN1090-2. Weld acceptance criteria to be BS EN 5817 class C. Supplementary NDT to be in accordance with table 24 UNO. Hold times to be in accordance with table 23 UNO

Remove All Burrs & Sharp Edges  
 Material: Free Issue  
 Stainless Steel 316 - 314  
 Inconel 6225  
 All Welds tig z2mm Fillet UNO  
 Individual items and type to be identified to worker, for batch tracing

IF IN DOUBT ASK		Quantity	Material	Finish	Drawn	Scale	Date
A3		1	Inconel SIS	S/C	MP	1:1	21/10/2022
		Title	Fuel Lance		Drg No.	E66889/1	Rev. A

General Tolerance (Unless Noted Otherwise):

Range(mm)	Machined	Fabricated
0 - 6	±0.1	±0.2
6 - 100	±0.2	±0.5
100 - 1000	±0.5	±1.0
1000 - 5000	±0.8	±1.5
5000+		

**metal FABRICATION**  
 www.metal-fab.co.uk  
 East Moors Road, Cardiff CF24 5EE  
 Tel (029) 2048 9767  
 E-Mail sales@metal-fab.co.uk

Figure A.0.5: Technical Drawing of Fuel Lance, supplied by manufacturer Metal Fabrications Ltd.



# Appendix B

## APPENDIX B: MATLAB Scripts

### B.1 Oxidant Thermocouple Correction.

#### B.1.1 Oxidant Thermocouple Correction Description.

In the following section, a copy of the oxidant thermocouple correction script is provided. The purpose of this script was to determine a real oxidant temperature, which necessitates a correction due to convection losses of the flowing gas. This script utilises a heat energy balance between the heat in the oxidant flow and the convective heat transfer resulting from the fluids flow. Upon the input of the oxidants conditions and the fuel blend, the script deduces further properties such as, thermal conductivity and heat capacity via look up tables. These values are further used to determine the Reynolds number of the flow, which is then used to determine the correct Nusselt number to determine a heat transfer coefficient suitable for the flow conditions at hand. The determined heat transfer coefficient is subsequently used to determine a real oxidant flow temperature.

#### B.1.2 Oxidant Thermocouple Correction Script.

Provided overleaf.

```

%% This script works out the real oxidant temperature flow in the rig
%% this further informs the fuel mas flow as we seek an equal flow
velocity
%% between both the oxidant and the fuel gas

% this work is based on a heat balance between the heat supplied to the
air
% and the convective heat tranfer over the thermocouple. i.e.
%  $Q_{heater} = m_{dotoxi} * C_{p,oxi} * \Delta T$ 
%  $Q_{conv} = h(T_{oxi} - T_{tc})$ 
% equate the two eqn's and rearrange to give
%  $T_{oxi} = Q_{heater}/h + T_{tc}$ 

%% Constants
R = 8314.472; % [J/mol] universal gas constant
CSA = 0.25*pi()*(0.0483^2); % [m2]
D = 0.0483; % [m]
N2_vol = 0.79;
O2_vol = 0.21;
N2_MW = 28.01348; % [g/mol]
O2_MW = 31.9988 ; %[g/mol]

%% Part (i) Heat Supplied to Oxidant
prompt0 = "AT PRESENT, THIS SCRIPT ONLY ACCOUNTS FOR AIR!!!";
prompt1 = "Oxidant Mass Flow Velocity [g/s] ="; %g/s
m_dotair = 23.75/1000; %input(prompt1)/1000; %kg/s
prompt2 = "Heater Set Point Value [degC] = "; %degC
T_sp = 1373; %input(prompt2)+273; %degK
prompt3 = "Temperature Measured by TC2 [degC] =";%degC
T_tc = input(prompt3)+273; %degK
T_h_in = 323; %degK
deltaT = T_sp-T_h_in;
T_film = (T_sp+T_h_in)*0.5;

%% Data Loading

%Part (i) Calcs
load Air_CP.txt
Cp_Air0 = Air_CP(:,2);
tempAirCp = Air_CP(:,1);
Cp_Air = interp1(tempAirCp,Cp_Air0,T_film);

%Part (ii) Calcs
load k_air_data.txt
tempOxik = k_air_data(:,1);
kOxi = k_air_data(:,2);

%% Part (i) Heat supplied to Oxidant
Q_heater = m_dotair*(deltaT)*Cp_Air;

%% Part (ii) Determination of convective heat transfer coefficient

%Outside of while loop, anything without an iteration
% PART(i)-viscosity
T_0N2 = 540.99; %[degR] T_0 value in the viscosity calculation, this
is a standard property of the gas
T_0O2 = 526.05; % [degR]
a_N2 = 0.555*T_0N2+111;

```

```

a_02 = 0.555*T_002+127;
mu0_N2 = 0.01781; % [cP]
mu0_02 = 0.01254; % [cP] note: do the calcs in cP and once the mixture
has been determined we can then convert to Pa*s or kg/ms
mu_fuelblend_denomenator= (N2_vol*sqrt(N2_MW))+(02_vol*sqrt(02_MW));

% initialising the while loop
tol=4;
iter=1;
T(iter)=1100; %degK
h(iter)=20;
% while loop begins to iterate the result for the heat transfer
coefficient
while tol>0.0000001

% Oxidant density
rho_oxi(iter) = 101325/((R/28.98)*T(iter)); %note that the
temperature for the density calculation has to be in Kelvin
% Oxidant vel
U_oxi(iter) = m_dotair/(rho_oxi(iter)*CSA);

% Oxidant Viscosity
T_oxiR(iter) = T(iter)*(9/5)+273; %converting into degree
Rankine

%visc coeffs
b_N2(iter)=0.555*T_oxiR(iter)+111;
b_02(iter)=0.555*T_oxiR(iter)+127;

%viscosity of constiutents, mu= mu_0(a/b)*(T/T0)^3/2.
mu_N2(iter)=mu0_N2*(a_N2/b_N2(iter))*((T_oxiR(iter)/T_0N2)^(3/2));
mu_02(iter)=mu0_02*(a_02/b_02(iter))*((T_oxiR(iter)/T_002)^(3/2));

%viscosity of blend %fuel beInd viscosity is mu_mix =
%(y_i*mu_i*SQRT(M_i)+.....)/(y_i*SQRT(M_i))

mu_oxi_numerator(iter) =
(N2_vol*mu_N2(iter)*sqrt(N2_MW))+(02_vol*mu_02(iter)*sqrt(02_MW));
mu_oxicP(iter) =
mu_oxi_numerator(iter)/mu_fuelblend_denomenator;
mu_oxi(iter) = mu_oxicP(iter)/1000;

% Oxidant Heat Capacity
Cp_oxi(iter)=interp1(tempAirCp,Cp_Air0,T(iter)-273);

% Oxidant thermal conductivity
k_oxi(iter) = interp1(tempOxik,k0xi,T(iter)-273);

%% Non-Dimensional Flow Relationships

% Reynolds Number
Re(iter) = (rho_oxi(iter)*U_oxi(iter)*D)/mu_oxi(iter);

% Prandtl Number
Pr(iter) = (Cp_oxi(iter)*mu_oxi(iter))/k_oxi(iter);

%% Nusselt number correlation

```



```
% S Jimenez [2022], relevance of heat conduction.... combustion  
and flame Nu_cyl eq4
```

```
%  
Nu(iter)=0.3+((0.62*(Re(iter)^0.5)*(Pr(iter)^(1/3)))/((1+(0.4/Pr(iter))^(2  
/3))^0.25))*((1+(Re(iter)/282000)^(5/8))^(4/5));
```

```
NuPrt1(iter) = 0.62*((Re(iter))^0.5)*((Pr(iter))^(1/3)); % as  
described in xls
```

```
NuPrt2(iter) = (1+((0.4/Pr(iter))^(2/3)))^0.25;
```

```
NuPrt3(iter) = (1+((Re(iter)/282000)^(5/8)))^0.8;
```

```
Nu(iter) = 0.3+((NuPrt1(iter)/NuPrt2(iter))*NuPrt3(iter));
```

```
h(iter+1) = (Nu(iter)*k_oxi(iter))/(D); %[W/mK]
```

```
T(iter+1)=Q_heater/h(iter) + T_tc;
```

```
tol(iter)=abs(h(iter+1)-h(iter));
```

```
iter=iter+1;
```

```
end
```

```
T_oxi = ((Q_heater/h(iter))+T_tc)-273
```

```
rho_oxi_fin = 101325/((R/28.98)*(T_oxi+273));
```

```
U_oxi_fin = m_dotair/(rho_oxi_fin*(0.025^2))
```

## B.2 Fuel Lance Thermocouple Correction.

### B.2.1 Fuel Lance Thermocouple Correction Description.

This algorithm operated, in three parts, as follows:

1. Part 1: Introduction of Constants and Look Up Tables.
  - (a) Constant values are saved to the workspace such as: Gas constants, geometry constants, molecular weights and viscosity constants.
  - (b) Matrices of conditionally dependent variables, such as specific heat capacity and thermal conductivity are also saved to the workspace.
2. Part 2: Determination of the oxidant conditions.
  - (a) The user is prompted to input whether the oxidant is air or flue gas. The composition of which is determined accordingly.
  - (b) The measured oxidant temperature is also inputted by the user, subsequently the oxidants heat capacity is determined via interpolation of the look up tables. The properties of the oxidant mixture are determined on a mass basis due to the units of heat capacity.
  - (c) The heat supplied to the oxidant is determined through use of  $Q_{oxi} = \dot{m}_{oxi}Cp_{oxi}\Delta T$ , where  $\Delta T$  is the difference between the ambient temperature of fuel in and the measured oxidant temperature.
  - (d) The viscosity of the oxidant is determined as outlined by the procedure in Section 3.4.1, using equations 3.3, 3.4, 3.5 and 3.6.
  - (e) A iterative loop is initiated using the while function in which the oxidants density, velocity, viscosity, thermal conductivity, heat capacity, Reynolds number and Prandtl number is calculated upon an initiated temperature value.

- (f) These fuel properties are further used to determine which Nusselt number correlation is appropriate for use, which is further used to deduce the heat transfer coefficient (Nusselt number correlations will be detailed below).
- (g) Convergence criteria of which is reliant on the tolerance of the oxidant temperature being within 0.000001.
- (h) Thus, providing a final oxidant temperature that in turn provides a density and a velocity.

### 3. Part 3: The determination of the fuel gas temperature.

- (a) Here, the user is prompted to enter the proportion of the fuel blend that is hydrogen, on a volumetric basis, and the temperature measured by the thermocouple in the fuel lance.
- (b) Subsequently, the fuels molecular mass and mass fractions are determined, as is the fuels thermal conductivity.
- (c) Another iterative loop is initiated in which the fuels viscosity, heat capacity, Reynolds number and Prandtl number are once again determined.
- (d) The determination of Reynolds number and Prandtl number in turn determine which Nusselt number correlation is used to determine the heat transfer coefficient.
- (e) The heat transfer coefficient is further used to determine an iterative value of the fuel temperature by a heat balance between the convective heat flow and the radiative heat from the lance itself, as described by equation 3.8.
- (f) The calculated temperature was further used to determine the density of the fuel and therefore its velocity.

### **Nusselt Number Correlations**

As detailed above, in both Part 2 and Part 3 of the fuel temperature calculations, Nusselt number correlations were relied upon. Nusselt numbers are empirical rela-

tionships that are used to predict the convective heat transfer coefficient ( $h$ ) of a given system, which can be further used in heat transfer calculations. The selection of the specific Nusselt correlation hinges entirely upon the configuration under consideration and the dimensionless numbers pertinent to that configuration. The value of the Nusselt number in isolation does not convey information about the flow characteristics. Instead, it must be further employed within the following equation to ascertain the heat transfer coefficient:

$$Nu = hL/k \quad (\text{B.1})$$

Where  $h$  is the convective heat transfer coefficient [ $W/m^2K$ ],  $L$  is the characteristic length of the configuration [ $m$ ] and  $k$  is the thermal conductivity of the fluid [ $W/mK$ ]. The determination of the heat transfer coefficient now enables the user to perform heat transfer calculations.

As stipulated above, the means of determining which Nusselt correlation depends entirely on the configuration that is being analysed. Since the fluid passes through a circular pipe, Nusselt correlations for that geometry only are considered. The Nusselt correlations are as follows, with their applicable range:

For a Reynolds number of less than 2300 ( $Re < 2300$ ), the Nusselt correlation is given by the equation below and was first developed by Hagen, G. & Poiseuille, J.L. [197] and further modified by Sieder and Tate [198] to account for the Prandtl number:

$$Nu_{\text{fuel}} = 3.66 + \frac{0.06668 Re_{\text{fuel}} Pr_{\text{fuel}}}{1 + 0.04 Re_{\text{fuel}} (Pr_{\text{fuel}})^{\frac{2}{3}}} \quad (\text{B.2})$$

For Reynolds numbers between 2300 and 4000 ( $2300 < Re < 4000$ ), the Nusselt number was derived using a correlation developed Gnielinski [199], and is as follows:

$$Nu_{\text{fuel}} = 0.037 (Re_{\text{fuel}})^{0.6} (Pr_{\text{fuel}})^{\frac{1}{3}} \quad (\text{B.3})$$

And the final correlation considered here is the Dittus-Boetler [200] correlation which is applicable for smooth tubes over a wide range of Reynolds [201], it was

used for all flows that were characterised by Reynolds number greater than 4,000 ( $4000 < Re$ ), and is given by:

$$Nu_{\text{fuel}} = 0.023 (Re_{\text{fuel}})^{0.8} (Pr_{\text{fuel}})^{0.4} \quad (\text{B.4})$$

### **B.2.2 Fuel Lance Thermocouple Correction Script.**

Provided overleaf.

```
% The purpose of this script is to determine the corrected thermocouple
% temperature due to the heat loss via convection of the fuel gas over the
% thermocouple in the fuel lance.
```

```
% NOTE [01/03/23] At present, this script is used to determine the
velocity
% from inputting a given mass flow rate. In future, it can be adjusted to
% provide the mass flow required for a target u_fuel
```

```
%% FUEL BLEND IN USE
```

```
prompt1 = "H2 content in fuel blend [0.0-1.0] = ";
H2_vol = input(prompt1);
CH4_vol = 1-H2_vol;
H2_MW = 2.01588; %g/mol
CH4_MW = 16.04246; %g/mol
H2_mass = H2_vol*H2_MW; %g/mol
CH4_mass = CH4_vol*CH4_MW; %g/mol
sigmaMass = H2_mass + CH4_mass;
H2_massfrac = H2_mass/sigmaMass;
CH4_massfrac = CH4_mass/sigmaMass;
R = 8314.472; % [J/mol] universal gas constant
```

```
%Measured Temp
```

```
prompt2 = "Fuel Temperature Measured by TC [degC] = ";
T_tc = input(prompt2); %[degC]
prompt4 = "Wall Temperature Measured [degC] = ";
T_w = input(prompt4);
T_tck = T_tc+273.15; %change into degree Kelvin]
```

```
%% FUEL BLEND DENSITY
```

```
%
```

```
% ----> NOTE: an estimated of T_g will be given by T_tc+25degC, it is at
this
```

```
%initial estimated gas temperature that the fuel properties will be
%calculated for the fuel blend initially.
```

```
T_g0 = T_tck+25; %[degK]
% iter=1;
% T_g0(iter)=
% iterCounter = iterCounter+1;
```

```
T_g0C = T_g0-273.15;
rho_fuelblend = 101325/((R/sigmaMass)*T_g0); %[kg/m3]
```

```
%% Fuel Velocity in the Fuel Lance
```

```
prompt2 = "m_dot,fuel (g/s) = "; %input the mass flow of fuel
m_dotfuel = input(prompt2)/1000; % [g/m3 to keep units constant]
prompt3 = "Fuel Lance Diameter: 3mm, 3.6mm or 5.5mm? = ";
dia_flc = input(prompt3)/1000 ; % conversion to m from mm to keep
units consistent
CSA_flc = 0.25*pi*(dia_flc)^2;
U_flc0 = (m_dotfuel)/(rho_fuelblend*CSA_flc);
```

```

disp("Fuel Lance Vel = ");
disp(U_flg0);

%% Viscosity calcs, eqn is,  $\mu = \mu_0(a/b)*(T/T_0)^{3/2}$ . Method for
determining

%Viscosity temperatures
T_g0R = (T_g0C*(9/5))+491.57; %conversion into degree Rankine
T_0CH4 = 581.67; %[degR] T_0 value in the viscosity calculation, this
is a standard property of the gas
T_0H2 = 528.93; % [degR]

%viscosity Coefficients
a_CH4 = 491.82685;
a_H2 = 365.55615;
b_CH4 = 0.555*T_g0R + 169;
b_H2 = 0.55*T_g0R + 72;

%viscosity of constituents,  $\mu = \mu_0(a/b)*(T/T_0)^{3/2}$ .
mu0_CH4 = 0.012; % [cP]
mu0_H2 = 0.00876; % [cP] note: do the calcs in cP and once the mixture
has been determined we can then convert to Pa*s or kg/ms
mu_CH4 = mu0_CH4*(a_CH4/b_CH4)*((T_g0R/T_0CH4)^(3/2));
mu_H2 = mu0_H2*(a_H2/b_H2)*((T_g0R/T_0H2)^(3/2));

%viscosity of blend %fuel blend viscosity is  $\mu_{mix} =$ 
 $\frac{(y_i*\mu_i*\sqrt{M_i})+\dots}{(y_i*\sqrt{M_i})}$ 

mu_fuelblend_numerator =
(CH4_vol*mu_CH4*sqrt(CH4_MW))+(H2_vol*mu_H2*sqrt(H2_MW));
mu_fuelblend_denomenator =
(CH4_vol*sqrt(CH4_MW))+(H2_vol*sqrt(H2_MW));
mu_fuelblendcP = mu_fuelblend_numerator/mu_fuelblend_denomenator;
mu_fuelblend = mu_fuelblendcP/1000;

%% SPECIFIC HEAT CAPACITY DATA INPUT

%CP_CH4
load CP_CH4_data.txt
CP_CH4 = CP_CH4_data(:,1);
tempdegKCH4 = CP_CH4_data(:,2); %temp in degC is called from
CP_CH4.txt, giving all rows of data (denoted by :) and in column 2

%CP_H2
load CP_H2data.txt
CP_H2 = CP_H2data(:,2);
tempdegKH2 = CP_H2data(:,1);%temp in degK is called from
CP_CH4.txt, giving all rows of data (denoted by :) and in column 3

%interpolate the text files for the correct Cp value
Cp_CH4_i = interp1(tempdegKCH4,CP_CH4,T_g0);
Cp_H2_i = interp1(tempdegKH2,CP_H2,T_g0);

%mixture heat capacity, note, since Cp is mass based, rule of mixtures
%requires to be considered on mass basis
Cp_fuelblend = (Cp_CH4_i*CH4_massfrac)+(Cp_H2_i*H2_massfrac);

```

```

%% THERMAL CONDUCTIVITY
load k_fuelblend_data.txt
if H2_vol == 0
    kcol=2;
elseif H2_vol == 0.05
    kcol=3;
elseif H2_vol == 0.1
    kcol = 4;
elseif H2_vol == 0.15
    kcol = 5;
elseif H2_vol == 0.2
    kcol = 6;
elseif H2_vol == 0.25
    kcol = 7;
elseif H2_vol == 0.3
    kcol = 8;
elseif H2_vol == 0.35
    kcol = 9;
elseif H2_vol == 0.4
    kcol = 10;
elseif H2_vol == 0.45
    kcol = 11;
elseif H2_vol == 0.5
    kcol = 12;
elseif H2_vol == 0.55
    kcol = 13;
elseif H2_vol == 0.6
    kcol = 14;
elseif H2_vol == 0.65
    kcol = 15;
elseif H2_vol == 0.7
    kcol = 16;
elseif H2_vol == 0.75
    kcol = 17;
elseif H2_vol == 0.8
    kcol = 18;
elseif H2_vol == 0.85
    kcol = 19;
elseif H2_vol == 0.9
    kcol = 20;
elseif H2_vol == 0.95
    kcol = 21;
elseif H2_vol == 1
    kcol = 22;
else
    disp('Fuel blend in increments of 0.05 please!')
end

tempdegKk = k_fuelblend_data(:,1);
k_find = k_fuelblend_data(:,kcol);
k_blend = interp1(tempdegKk,k_find,T_g0);

%% Non-dimensional Flow relationships

%Reynolds Number_d
Re_d = (rho_fuelblend*U_flg0*(dia_flg))/mu_fuelblend;

%Reynolds Number_L
Re_L = (rho_fuelblend*U_flg0*0.25)/mu_fuelblend;

```



```

%Prandtl Number
Pr = (Cp_fuelblend*k_blend)/mu_fuelblend;

%RePr
RePr = Re_d*Pr;

%next step is to solve the viscosity, Cp and K of the fuel blend
% THEN, apply a Nusselt number correlation to determine heat transfer
% coefficient, then develop a loop for the determining the gas temperature

%% Nusselt number correlation

% S Jimenez [2022], relevance of heat conduction.... combustion and flame
Nu_cyl eq4

NuPrt1 = 0.62*(Re_d^0.5)*(Pr^(1/3)); % as described in xls
NuPrt2 = (1+((0.4/Pr)^(2/3)))^0.25;
NuPrt3 = (1+((Re_d/282000)^(5/8)))^0.8;
Nu = 0.3+((NuPrt1/NuPrt2)*NuPrt3);
h = (Nu*k_blend)/(dia_flg*1000); %[W/mK]

%% Real Gas Temperature Calc

emiss =1; %emissivity value used
SBC = 5.67e-8; %Stefan Boltzman constant
T_gi = T_tc + (emiss*SBC*((T_w)^4-(T_tc)^4))/h; %degC

```

## B.3 Chemiluminescence Image Processing.

### B.3.1 Chemiluminescence Image Processing Description.

The chemiluminescence image processing scripts purpose was to take the imaging data captured during the experimental campaign and to measure the Lifted Flame height, defined as, the distance between the nozzle exit and the stated 30% OH\* threshold. The script operated via the following steps:

1. Part 1: Data loading and Set-up.
  - (a) The raw images captured in the experimental campaign are selected and imported in mutliTIFF format.
  - (b) The resolution of the image is inputted, as per the calibration testing performed at the start of each test day.
  - (c) The traverse position, on which the camera was situated, in millimetres is input into the script in order to determine the Lifted Flame Height (LFH).
  - (d) The pixel number of the nozzle exit in the calibration image is also inputted to provide the datum point for the LFH measurement.
2. Part 2: Mean Image.
  - (a) The imported images are read into a matrix via a for loop, where image conditioning is performed, such as, filtering and sharpening.
  - (b) The images are further summed.
  - (c) The mean image is determined by the summed image divided by the number of imported images.
3. Part 3: Abel Deconvolution.
  - (a) The centre of the image is determine, which is then used to split the image.

- (b) A zero matrix is initiated for the output image that is of the same dimensions as the mean image.
- (c) The split mean image, is further converted into double precision and has the Abel inversion function performed on it.
- (d) The output of the Abel inversion is added to the zeroed matrix to build the Abel inverted image.
- (e) The image is subsequently saved.

#### 4. Part 4: Abel Normalisation.

- (a) The Abel inverted image is converted to grayscale with a scale of 0 (black) to 1 (white).
- (b) The number of additional columns to present the traverse position is determined.
- (c) The remaining length of the mixing duct is also added onto the end of the image matrix as zeros (black).
- (d) The image is subsequently saved.

#### 5. Part 5: Flame Edge Detection and Result

- (a) The image is further binarised, however, with a minimum threshold of 0.3, as per the 30% OH\* criterion. This provided an image that only showed the flame regions of interest.
- (b) The image described further used to measure the number of pixels between the fuel lance edge and the flame edge.
- (c) A final image is produced which shows the flame within the mixing duct with the addition of the fuel lance for reference. The LFH is also showcased on the final figure which is determined via the number of pixels between nozzle edge and the flame edge, multiplied by the pixel resolution in millimetre.
- (d) The image is subsequently saved.

### **B.3.2 Chemiluminescence Image Processing Script.**

Provided overleaf.



```

assignin('base','i',i);
assignin('base','j',j);
n = (j/2) + 1; %determine size of image and midline in the model
CentXPix=272; %%% Input the horizontal (left-right) central pixel location
assignin('base','CentXPix',CentXPix);

R=(j-CentXPix)*PixRes; %%% the radius of the image, R in mm
numColsToAdd = TRVposn/PixRes; % [mm]/[mm/pix]

%%% from the central pixel of the image to the right edge (WhichWay =1)
%%% from the left edge of the image to the central pixel (WhichWay = 2)
WhichWay=2; %%% Input Whichway 1 or 2
assignin('base','WhichWay',WhichWay);
if WhichWay == 1
    NewEdge = (2*(j-CentXPix));
    %%% Initialize output image matrix
    ImAbel = zeros(i, NewEdge);
    k = (NewEdge/2) - 1;
    %%% For loop cycles through each row of the input image
    for z = 1:i
        %%% Extract single image row
        A = Image(z, CentXPix:j);
        %%% Convert image row to double precision
        A2 = im2double(A, 'indexed');
        %%% Calls the Abel inversion function one row at a time with an
        %%% input of 5 cosinus expansions in the Fourier-series-like
        %%% expansion
        [f_rec , X] = abel_inversion(A2,R,5);
        %%% Add the Abel deconvoluted row to the output matrix
        ImAbel(z, (NewEdge/2):NewEdge) = f_rec(:,1);
        %%% Rotate the Abel deconvoluted row about the central axis
        f_rec = flipud(f_rec);
        ImAbel(z, 1:k) = f_rec(2:(NewEdge/2),1);
    end
end
if WhichWay == 2
    NewEdge = (2*CentXPix);
    ImAbel = zeros(i, NewEdge);
    k = (NewEdge/2) - 1;
    %%% For loop cycles through each row in the input image
    for z = 1:i
        %%% Extract single image row
        A = Image(z, 1:(CentXPix+1));
        A = fliplr(A);
        %%% Convert image row to double precision
        A2 = im2double(A, 'indexed');
        %%% Calls the Abel inversion function one row at a time with an
        %%% input of 5 cosinus expansions in the Fourier-series-like expansion
        [f_rec , X] = abel_inversion(A2,R,5);
        %%% Add the Abel deconvoluted row to the output matrix
        ImAbel(z, (NewEdge/2):NewEdge) = f_rec(:,1);
        %%% Rotate the Abel deconvoluted row about the central axis
        f_rec = flipud(f_rec);
        ImAbel(z, 1:k) = f_rec(2:(NewEdge/2),1);
    end
end
%%% Assign Abel Image to Workspace
assignin('base','NewEdge',NewEdge)
assignin('base','k',k)

```

```

assignin('base', 'ImAbel', ImAbel)
ImAbelRot=imrotate(ImAbel,-90);
assignin('base', 'ImAbelRot', ImAbelRot)
figure(3)
imagesc(ImAbelRot)
colormap("jet")
%% Set FileName and Save AbelImage
l=length(file);
FileName=['AbelDeconvImg -', 'WhichWay', num2str(WhichWay), '-', file(1:l-4),];
FullFileName=['C:\Users\c1421421\OneDrive - Cardiff University\CDT\REHEAT RIG\00_TEST_DATA\DATA PROCESSING\IMAGE PROCESSING CODE',FileName];
imwrite(ImAbelRot,FullFileName, 'tif')

%%%%%%%%%%%%%%%%%%%%%%%%%%%%%%%%%%%%%%%%%%%%%%%%%%%%%%%%%%%%%%%%%%%%%%%%%%%%%%
%%%%%%%%%%%%%%%%%%%%%%%%%%%%%%%%%%%%%%%%%%%%%%%%%%%%%%%%%%%%%%%%%%%%%%%%%%%%%% Adjust Image Size %%%%%%%%%%%%%%%%%%%%%%%%%%%%%%%%%%%%%%%%%%%%%%%%%%%%%%%%%%%%%%%%%%%%%%%%%%%%%%%
%%%%%%%%%%%%%%%%%%%%%%%%%%%%%%%%%%%%%%%%%%%%%%%%%%%%%%%%%%%%%%%%%%%%%%%%%%%%%%
ImAbel2=ImAbel;
[X2 Y2]=size(ImAbel2);
assignin('base', 'X2', X2);
assignin('base', 'Y2', Y2);
nshift=abs(Y2-j);
assignin('base', 'nshift', nshift)
if Y2-j>0
    ImAbel2(:,1:nshift)=[];
    AdjImAbel=ImAbel2;
else
    Nzero=zeros(X2,nshift);
    AdjImAbel=cat(2, ImAbel2, Nzero);
end
AdjImAbel=imrotate(AdjImAbel,-90);
assignin('base', 'AdjImAbel', AdjImAbel);
figure(4)
imagesc(AdjImAbel)
colormap('jet')
FileNameAdj=['AdjAbelDeconvImg -', 'WhichWay', num2str(WhichWay), '- ', file(1:l-4),];
FullFileNameAdj=['C:\Users\c1421421\OneDrive - Cardiff University\CDT\REHEAT RIG\00_TEST_DATA\DATA PROCESSING\IMAGE PROCESSING CODE',FileNameAdj];
imwrite(AdjImAbel,FullFileNameAdj, 'tif')

%%%%%%%%%%%%%%%%%%%%%%%%%%%%%%%%%%%%%%%%%%%%%%%%%%%%%%%%%%%%%%%%%%%%%%%%%%%%%%
%%%%%%%%%%%%%%%%%%%%%%%%%%%%%%%%%%%%%%%%%%%%%%%%%%%%%%%%%%%%%%%%%%%%%%%%%%%%%% Normalise Abel Image %%%%%%%%%%%%%%%%%%%%%%%%%%%%%%%%%%%%%%%%%%%%%%%%%%%%%%%%%%%%%%%%%%%%%%%%%%%%%%%
%%%%%%%%%%%%%%%%%%%%%%%%%%%%%%%%%%%%%%%%%%%%%%%%%%%%%%%%%%%%%%%%%%%%%%%%%%%%%%

%ImAbelN=AdjImAbel./(max(max(AdjImAbel))); %% Option1 giving negative values
ImAbelN=mat2gray(AdjImAbel); %% Option2 converts the matrix A to a grayscale image I that contains values in the range 0 (black) to 1 (white)
assignin('base', 'ImAbelN', ImAbelN)
numColsToAdd = round(TRVposn/PixRes);
assignin('base', 'numcolsToAdd', numColsToAdd);

zeroMatrix = zeros(size(ImAbelN, 1), numColsToAdd);

ImAbelNExtended = [ImAbelN, zeroMatrix];

```

```

figure(5)
%imshow(ImAbelN)
colormap('fire')
assignin('base','ImAbelNExtended',ImAbelNExtended);
figure(6);
%imshow(ImAbelNExtended);
colormap("fire")
FileNameN=['NormAbelDeconvImg -','WhichWay', num2str(WhichWay),'-
',file(1:l-4),];
FullFileNameN=['C:\Users\c1421421\OneDrive - Cardiff University\CDT\REHEAT
RIG\00_TEST_DATA\DATA PROCESSING\IMAGE PROCESSING CODE',FileNameN];
imwrite(ImAbelN,FullFileNameN,'tif')

%%%%%%%%%%%%%%%%%%%%%%%%%%%%%%%%%%%%%%%%%%%%%%%%%%%%%%%%%%%%%%%%%%%%%%%%
%%%%%%%%%%%%%%%%%%%%%%%%%%%%%%%%%%%%%%%%%%%%%%%%%%%%%%%%%%%%%%%%%%%%%%%% Flame Edge Detection %%%%%%%%%%%%%%%%%%%%%%%%%%%%%%%%%%%%%%%%%%%%%%%%%%%%%%%%%%%%%%%%%%%%%%%%%
%%%%%%%%%%%%%%%%%%%%%%%%%%%%%%%%%%%%%%%%%%%%%%%%%%%%%%%%%%%%%%%%%%%%%%%%
%%%%%%%%%%%%%%%%%%%%%%%%%%%%%%%%%%%%%%%%%%%%%%%%%%%%%%%%%%%%%%%%%%%%%%%% Whichway=1 %%%%%%%%%%%%%%%%%%%%%%%%%%%%%%%%%%%%%%%%%%%%%%%%%%%%%%%%%%%%%%%%%%%%%%%%%

%
figure(7)
assignin('base','ImAbelN', ImAbelN)
Y3= CentXPix;
BWImage=imbinarize(ImAbelNExtended,0.3); %binarise the image
se = strel('disk',15); %introduce the dot on the edge detected pixel
BWImage=imclose(BWImage,se);
%imshow(BWImage)
imedge = edge(BWImage, 'Roberts');
[rows, columns] = find(imedge==1);
X3=columns(find(rows==Y3,1,'last'));
X4 = numColsToAdd+608;
LFHa=((603-X3)*PixRes)+TRVposn
LFHarounded=round(LFHa,2);
txt=['LFH = ' num2str(LFHarounded) 'mm'];
imshow(ImAbelNExtended)
colormap("fire")
c=colorbar;
c.XTick=[0 1];
c.XTickLabel={'min','max'};
hold on
scatter(columns,rows,5,'MarkerEdgeColor','w')
hold on
plot(X3,Y3,'.','Color','w','MarkerSize', 15)
hold on
r=rectangle('Position',[X4 246 X2 52]);
r.FaceColor = [0.7 .7 .7];
r.EdgeColor = 'k';
line([X3 X4],[Y3 Y3],'Color','w','LineStyle','--')
text(X4-300,500,txt,'Color','w','FontSize',16,'FontName','Arial')
line([1 X4+X3],[Y3+round(14.25/PixRes)
Y3+round(14.25/PixRes)],'Color','w','LineWidth',2,'LineStyle','--')
hold on
line([1 X4+X3],[Y3-round(14.25/PixRes) Y3-
round(14.25/PixRes)],'Color','w','LineWidth',2,'LineStyle','--')
saveas(gcf,'230705_018_CHEMI_030THRSHLD','jpg')

```





## B.4 Turbulence Intensity and Radial Velocity Profile

### B.4.1 Turbulence Intensity and Radial Velocity Profile Description

The purpose of the Turbulence Intensity (TI) and radial velocity profile calculating script was to take the imaging data acquired during the PIV testing and to treat the data to derive instantaneous and mean velocities for the determination of the TI and radial velocity profile. The operating principles are described below.

1. The  $u$  velocity components, for the two imaging windows, are called into the workspace.
2. The last element of the image matrix was extracted, since this was the mean velocity determined in the PIV data analysis software, PIVlab.
3. The two mean velocity matrices of the two imaging windows are concatenated with one another.
4. The instant velocity matrices are further used to determine the magnitude of the velocity fluctuation from the mean value and is squared.
5. The Root-mean-squared velocity value is then calculated by  $u_{RMS} = \sqrt{\frac{u'^2}{N}}$ , where  $u'$  is the velocity fluctuations and  $N$  is the number of velocity data points.
6. The TI is further determined via:  $TI = \frac{u_{RMS}}{U_{mean}} \times 100\%$ .
7. The above process is repeated for the  $y$ -direction,  $v$  velocity components.
8. A resultant TI is subsequently determined.

9. Furthermore, the centreline TI and velocities are extracted from the processed data. Their profiles are subsequently plotted against the axial position in the mixing duct.

### **B.4.2 Turbulence Intensity and Radial Velocity Profile Script**

Provided overleaf.

```

%% This scripts purpose is to take u and v component data from the both
sets
% of 0-100mm and 100-200mm combine the two to give a complete 200mm of
% flow data. The mean flow data that is calculated in PIVlab is excluded
% for the extraction of transient PIV data values. However, it is
included
% for the determination of the fluctuating values. Turbulence intensity
% (TI) is further determined and plotted on a contour.

% NOTE: IMPORTANT! u_component and v_component data must be imported from
% PIV data files. Then they must be renamed u_component1 for 0-100mm and
% u_component2 for 100-200mm and the same for v, respectively.

%% _____ X DIRECTION _____%%

% Check the number of elements in each cell
num_elements_u_comp1 = numel(u_component1);
num_elements_u_comp2 = numel(u_component2);

% Reduce the larger cell to match the size of the smaller cell
if num_elements_u_comp1 > num_elements_u_comp2
    u_component1 = u_component1(1:num_elements_u_comp2);
elseif num_elements_u_comp2 > num_elements_u_comp1
    u_component2 = u_component2(1:num_elements_u_comp1);
end

%% Separate the mean value from the transient PIV data

% Extract the last element from u_component1 and assign to Umean1
Umean1 = u_component1(end);
% Extract the transient PIV data
U_fluc1 = u_component1(1:end-1);

% Extract the last element from u_component2 and assign to Umean2
Umean2 = u_component2(end);
% Extract the transient PIV data
U_fluc2 = u_component2(1:end-1);

%% Concatenate the mean velocity data and the transient PIV
% Concatenate the matrices from both cells by adding columns - mean
% velocity
Umean = cell(1, numel(Umean1));

for i = 1:numel(Umean1)
    Umean{i} = [Umean1{i}, Umean2{i}];
end
% assign Umean to a matrix as opposed to a cell
Umean = Umean{1};

% Concatenate the matrices from both cells by adding columns - transient
% velocity PIV data
u_component = cell(1, numel(u_component1));

for i = 1:numel(u_component1)
    u_component{i} = [u_component1{i}, u_component2{i}];
end

%% Determine velocity fluctuations in the transient PIV data

```

```

%initialising a clean matrix to input the summation of fluctuating values
u_matrixSize = size(u_component{1});
u_flucsqSum = zeros(u_matrixSize);

% a for loop to determine the sum of the flucuating values squared
u_numMatrices = length(u_component);

for i = 1:u_numMatrices %set the number of times to run the loop based
off of the size of the cell
    u_matrix = u_component{i}; % assign each matrix in the cell to
its correponding i value
    u_fluc = u_matrix-Umean; %determine the flucuating velocity
value
    u_flucsq = u_fluc.^2; %square the fluctuating velocity value
    u_flucsqSum = u_flucsqSum + u_flucsq; %assign the flucutating values
to the zero'd matrix above to have the sum of the squared fluctuating
values
end
% perform RMS calc: EQN => u_RMS = sqrt(u'^2/N)
u_RMS = sqrt(u_flucsqSum/u_numMatrices);

TI_x = u_RMS./Umean*100;

%% _____ Y Direction _____ %%

% Check the number of elements in each cell
num_elements_v_comp1 = numel(v_component1);
num_elements_v_comp2 = numel(v_component2);

% Reduce the larger cell to match the size of the smaller cell
if num_elements_v_comp1 > num_elements_v_comp2
    v_component1 = v_component1(1:num_elements_v_comp2);
elseif num_elements_v_comp2 > num_elements_v_comp1
    v_component2 = v_component2(1:num_elements_v_comp1);
end

%% Separate the mean value from the transient PIV data

% Extract the last element from u_component1 and assign to Umean1
Vmean1 = v_component1(end);
% Extract the transient PIV data
V_fluc1 = v_component1(1:end-1);

% Extract the last element from u_component2 and assign to Umean2
Vmean2 = v_component2(end);
% Extract the transient PIV data
V_fluc2 = v_component2(1:end-1);

%% Concatenate the mean velocity data and the trasient PIV
% Concatenate the matrices from both cells by adding columns - mean
% velocity
Vmean = cell(1, numel(Vmean1));

for i = 1:numel(Vmean1)
    Vmean{i} = [Vmean1{i}, Vmean2{i}];
end
% assign Umean to a matrix as opposed to a cell
Vmean = Vmean{1};

```

```

% Concatenate the matrices from both cells by adding columns – transient
% velocity PIV data
v_component = cell(1, numel(v_component1));

for i = 1:numel(v_component1)
    v_component{i} = [v_component1{i}, v_component2{i}];
end

%% Determine velocity fluctuations in the transient PIV data

%initialising a clean matrix to input the summation of fluctuating values
v_matrixSize = size(v_component{1});
v_flucsqSum = zeros(v_matrixSize);

% a for loop to determine the sum of the fluctuating values squared
v_numMatrices = length(v_component);

for i = 1:v_numMatrices %set the number of times to run the loop based
off of the size of the cell
    v_matrix = v_component{i}; % assign each matrix in the cell to
its corresponding i value
    v_fluc = v_matrix - Vmean; %determine the fluctuating velocity
value
    v_flucsq = v_fluc.^2; %square the fluctuating velocity value
    v_flucsqSum = v_flucsqSum + v_flucsq; %assign the fluctuating values
to the zero'd matrix above to have the sum of the squared fluctuating
values
end
% perform RMS calc: EQN => u_RMS = sqrt(u'^2/N)
v_RMS = sqrt(v_flucsqSum/v_numMatrices);
TI_y = v_RMS./Vmean*100;

%% _____ COMBINE FOR RESULTANT DATA _____ %%

VEL_FLUC = sqrt((1/2)*(u_RMS.^2)+(v_RMS.^2));
VEL_MEAN = sqrt(Umean.^2+Vmean.^2); % u = sqrt(u^2 + v^2)
TI = (VEL_FLUC./VEL_MEAN)*100;

% plot the TI contour : Create a filled contour plot using the contourf
function
% Define the fixed figure dimensions
figureWidth = 6000;
figureHeight = 750;

% Create a figure with the specified dimensions
fig = figure('Position', [100, 100, figureWidth, figureHeight]);
startValue = 0;
endValue = 20;
interval = 1;
rowMatrix = startValue:interval:endValue;
contourLevels = [rowMatrix];

subplot(3,1,1)
contourf(TI, contourLevels);
colorbar;
% Remove X-axis and Y-axis ticks
%xticks([0:25:200]);

```

```

%contourLabels = {'-10.0', '-9.5', '-9.0%', '-8.5%', '-8.0%', '-7.5%', '-7.0%', '-6.5%', '-6.0%', '-5.5%', '-5.0%', '-4.5%', '-4.0%', '-3.5%', '-3.0%', '-2.5%', '-2.0%', '-1.5%', '-1.0%', '-0.5%', '0.0%', '0.5%', '1.0%', '1.5%', '2.0%', '2.5%', '3.0%', '3.5%', '4.0%', '4.5%', '5.0%', '5.5%', '6.0%', '6.5%', '7.0%', '7.5%', '8.0%', '8.5%', '9.0%', '9.5%', '10.0%'};
%legend( 'Location','eastoutside')
title('Resultant Turbulence Intensity');

subplot(3,1,2);
contourf(TI_x,contourLevels)
colorbar;
%xticks([0:25:200]);

title('x-direction Turbulence Intensity')

subplot(3,1,3)
contourf(TI_y,contourLevels)
colorbar;
%xticks([0:25:200])

title('y-direction Turbulence Intensity')
%% _____ CENTRELINE EXTRACTIONS
%%
%%----- Centreline TI -----%%
middleRowIndex = ceil(size(TI,1)/2);
%extract the middle row
middleRowTI = TI(middleRowIndex, :);
desiredWidthMM = 200;

numColumns = u_matrixSize(:,2);

% Calculate the width of each column in millimeters
columnWidthMM = desiredWidthMM / numColumns;
x_dist = (1:numColumns) * columnWidthMM;
columnsToRemove = 2;
middleRowTI = middleRowTI(:,1:end - columnsToRemove);
x_dist = x_dist(:,1:end - columnsToRemove);
figure
plot(x_dist,middleRowTI)
xticks([0:25:200])
yticks([0:50:400])

%%----- Centreline Velocity-----%%

[rows, ~] = size(Umean);
% Calculate the middle row index
Umean_middleRowIndex = ceil(rows / 2);

% Extract the middle row
Umean_middleRow = Umean(Umean_middleRowIndex, :);
% Convert the middleRow into a single-row matrix
Umean_singleRowMatrix = Umean_middleRow;
Umean_singleRowMatrix = Umean_singleRowMatrix(:,1:end - columnsToRemove);

figure
plot(x_dist,Umean_singleRowMatrix,'r')
xticks([0:25:200])

```

```

yticks([0:10:50])

%% _____ Axial EXTRACTIONS _____
%%

%% _____ Turbulence Intensity _____ %%

%determine size of the matrix in columns
colnum = size(TI,2);
axialdist = 200;

%determine the axial position in mm of each column
axialposition = linspace(0,axialdist, colnum);

% Define the target axial positions
targetAxialPositions = [25:25:200];

% Find the column indices closest to the target axial positions
closestIndices = zeros(size(targetAxialPositions));
for i = 1:length(targetAxialPositions)
    [~, closestIndices(i)] = min(abs(axialposition -
targetAxialPositions(i)));
end

% Extract data from the closest columns
closestDataTI = cell(length(targetAxialPositions), 1);
for i = 1:length(targetAxialPositions)
    columnIndex = closestIndices(i);
    closestDataTI{i} = TI(:, columnIndex);
end

numMatrices = numel(closestDataTI);
%extract each matrix from the cell to be a standalone variable
for i=1:numMatrices
    eval(['TIaxialposn25x' num2str(i) ' = closestDataTI{' num2str(i)
'};']);
end

% Radial distance from 0 to 25mm
numRow = size(TIaxialposn25x1,1);
rad_dist_inc = 25/numRow;
radialDistance = [-12.5:rad_dist_inc:(12.5-rad_dist_inc)];

%plot the figures for TI radial profile at axial distances
figure;
for i= 1:numMatrices
    subplot(3,3,i);
    plot(closestDataTI{i},radialDistance)
    p = 25*i;
    title(['Axial Position ' num2str(p) ' [mm]']);
    xlabel('Turbulence Intensity (%)')
    ylabel('Radial Position [mm]');
    grid on
end

%% _____ Radial Velocity Profiles _____ %%

% Extract data from the closest columns

```



```

closestDataU = cell(length(targetAxialPositions), 1);
for i = 1:length(targetAxialPositions)
    columnIndex = closestIndices(i);
    closestDataU{i} = Umean(:, columnIndex);
end

numMatrices = numel(closestDataU);
%extract each matrix from the cell to be a standalone variable

figure;
for i=1:numMatrices
    eval(['Uaxialposn25x' num2str(i) ' = closestDataU{' num2str(i) '};']);
end

for i= 1:numMatrices
    subplot(3,3,i);
    plot(closestDataU{i},radialDistance)
    p = 25*i;
    title(['Axial Position ' num2str(p) ' [mm]']);
    xlabel('U Velocity [m/s]')
    ylabel('Radial Position [mm]');
    grid on
end

```

## B.5 Turbulent Lengthscale Calculator.

### B.5.1 Turbulent Lengthscale Calculator Description.

This MATLAB scripts calculates the integral and Kolmogorov lengthscales of turbulence. This is done by importing the velocity data into the script and further performing Fast Fourier Transfer (FFT) analysis upon both the  $u$  and  $v$  velocity fluctuations. A time averaged power spectra is performed by averaged across the time duration of the sample. The FFT highlights a dominant wavenumber which corresponds to a dominant wavelength of the turbulence. this is deduced by the following equation:

$$L = \frac{2\pi}{k}, \quad (\text{B.5})$$

where  $L$  is the integral lengthscale and  $k$  is the dominant wavenumber.

The Kolmogorov lengthscale of turbulence is then determined via the following equation:

$$\eta = \frac{L}{Re^{0.75}}, \quad (\text{B.6})$$

where  $\eta$  is the Kolmogorov lengthscale.

The values for both lengthscales are printed within the console.

### B.5.2 Turbulent Lengthscale Calculator Script.

Provided overleaf.

```

%% Lengthscale calculator
% this script operates by firstly taking the velocity data
% and performing FFT analysis on u and v velocity fluctuations.
% A averaged power spectra across the time steps is performed to obtain a
% time-averaged power spectra
% The FFT then identifies the dominant wavenumber which relates to the
% dominant wavelength of the turbulence:  $L = 2\pi/(k_{max})$ . The Kolmogorov
% lengthscale is then
% determined by  $\eta = L/[(Re)^{3/4}]$  where  $Re = UL/\nu$  - i.e. Kolmogorov
% scaling law.
% a gradient check is also included to see how close it is to the
Kolmogorov
% scaling power law of  $-(5/3) = -1.667$ 

%% Velocity Data
% this section operates by ascertaining the matrix size, denoting the
% number of RAW files (total - 1, where 1 is the mean data set), assigning
% the last data set to be the mean velocity data. The fluctuating
% velocities are calculated using a for loop and that data is assigned to
a
% new cell

% Organising matrix size through evaluating cells inputted

u_numMatrices = length(u_component); %determing total number of matrices
u_numfluc = u_numMatrices-1; %number of fluctuating matrices, last is the
Umean = u_component{u_numMatrices}; %mean velocity data from the last
% element of the velocity cell

% mean matrix
u_matrixSize = size(u_component{1}); % Assuming all matrices have the
% same size, this will provide detail on the matrix size for all matrices

% initialising a cell array to store the fluctuating velcoity matrices
u_RAW = cell(1,u_numfluc);

% loop through all matrices except for the last one, subtracting the mean
% velocity to ascertain the vel fluctations
for i=1:u_numfluc
    u_RAW{i} = u_component{i} - Umean;
end

% initialise a cell for the FFT analysis to be assigned to
U_fft = cell(1,numel(u_RAW));

for i = 1:numel(u_RAW)
    U_fft{i} = fft(u_RAW{i});
end

%initilaise an array to store power spectra for each time instance
power_spectra_cell = cell(1,numel(U_fft));

%loop through the FFt results to calculate power spectra
for i = 1:numel(U_fft)
    power_spectra_cell{i} = abs(U_fft{i}).^2;
end

%compute the time averaged power spectra

```

```

time_ave_power_spectra = zeros(size(power_spectra_cell{i})); %initialising
with zeros

for i = 1:numel(U_fft)
    time_ave_power_spectra = time_ave_power_spectra +
power_spectra_cell{i};
end

time_ave_power_spectra = time_ave_power_spectra/numel(U_fft);

% Calculating the total number of data points
N = length(time_ave_power_spectra);

prompt1 = 'What is the sample rate of this data set in ms? [0.035, 0.05,
0.07, 0.09] = ';
delta_t = input(prompt1)/1000;

%calculating the frequencies
freq = (0:(N-1))/(N*delta_t);

% calculating the wave number (spatial freq) 1D approach
k = 2*pi*freq;
%
% Find the peak wavenumber (dominant wavenumber) in the time-averaged
power spectra
%
[peak_power, peak_index] = max(time_ave_power_spectra);
dominant_wavenumber = k(peak_index);

% Estimate the integral length scale (L) using the dominant wavenumber
L = 2*pi./dominant_wavenumber;

fprintf('Dominant Wavenumber: %.4f rad/m\n', dominant_wavenumber);
fprintf('Integral Length Scale (L): %.4f m\n', L);

% Assuming you have 'freq' for temporal frequencies and 'k' for spatial
wavenumbers

% Plot the power spectra as a function of frequency
figure;
semilogx(freq, time_ave_power_spectra);
xlabel('Frequency (Hz)');
ylabel('Time-Averaged Power Spectra');
title('Time-Averaged Power Spectra vs. Temporal Frequency');
legend('Power Spectra');
% Plot the power spectra as a function of wavenumber
figure;
semilogx(k, time_ave_power_spectra);
xlabel('Wavenumber (rad/m)');
ylabel('Time-Averaged Power Spectra');
title('Time-Averaged Power Spectra vs. Wavenumber');
legend('Power Spectra');
% Define the range for calculating the gradient
k_positive = k(k > 0);
k_start = min(k_positive); % 10^3

% Initialize k_end to be greater than the maximum k value in the dataset
k_end = max(k) + 1;

```

```

% Find the indices corresponding to k values within the specified range
indices = find(k >= k_start & k <= k_end);

% Extract the k and time-averaged power spectra values within the range
k_range = k(indices);
power_range = time_ave_power_spectra(indices);

% Calculate the gradient (slope) using the first and last points in the
range
gradient = (log10(power_range(end)) - log10(power_range(1))) /
((log10(k_range(end)) - log10(k_range(1))));

% Check if the gradient is positive
while gradient <= 0 && k_end < max(k)
    k_end = k_end + 1; % Increase k_end
    indices = find(k >= k_start & k <= k_end);
    k_range = k(indices);
    power_range = time_ave_power_spectra(indices);
    gradient = (log10(power_range(end)) - log10(power_range(1))) /
(log10(k_range(end)) - log10(k_range(1)));
end

fprintf('k_end where gradient becomes positive: %.4f\n', k_end);

fprintf('Gradient between k_min and k_max (for negative gradient): \n\n
%.4f \n\n', gradient);
percentage_diff_grad = abs(((gradient-(-5/3))/(-5/3))*100);
fprintf('Percentage difference of calculated gradient and Kolmogorov
Scaling Law: \n\n %.4f \n\n',percentage_diff_grad)

nu = 1.48E-5; %[m^2/s]
% Find finite values of L (i.e., exclude Inf and NaN)
finite_L_values = L(isfinite(L));

% Check if any finite values were found
if ~isempty(finite_L_values)
    % Take the first finite value as an example; you can use other
criteria to choose L
    selected_L = max(finite_L_values)*1E3;
    fprintf('Selected Finite Value of L: \n\n%.4f [mm] \n\n', selected_L);
else
    fprintf('No finite values of L found.\n\n');
end

L = selected_L;

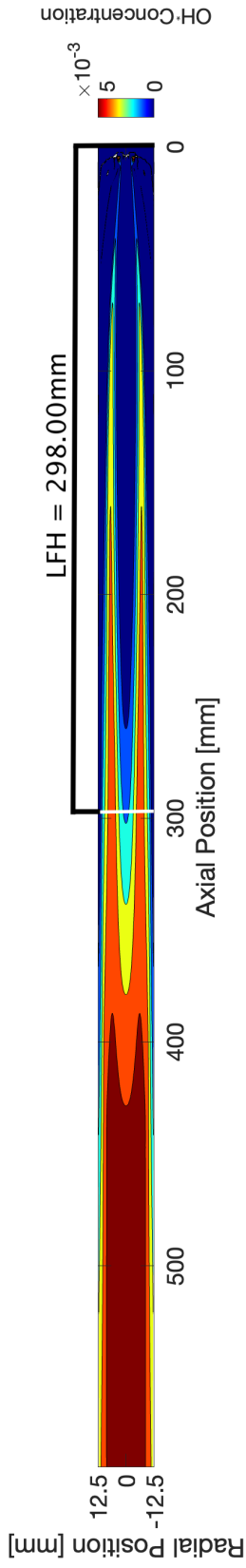
U = mean(Umean);
U = mean(U);
Re = U*L/nu;
eta = 1E3*(L/(Re^(3/4)));

fprintf('Kolmogorov Lengthscale:\n\n %.4f [mm] \n', eta);

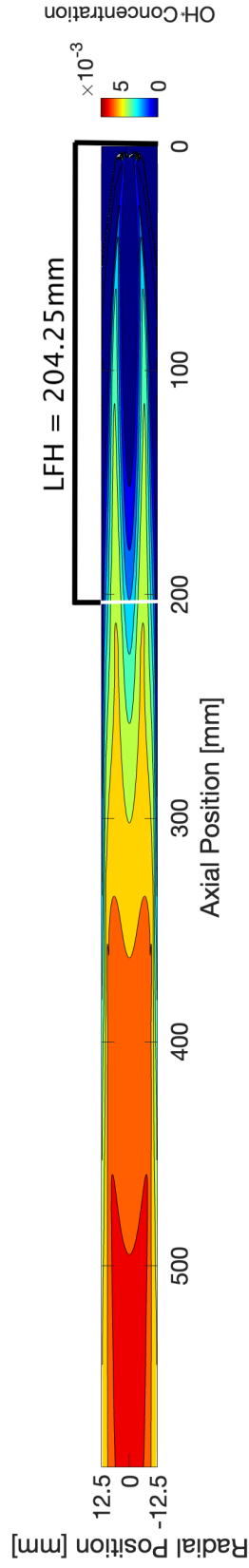
```

# Appendix C

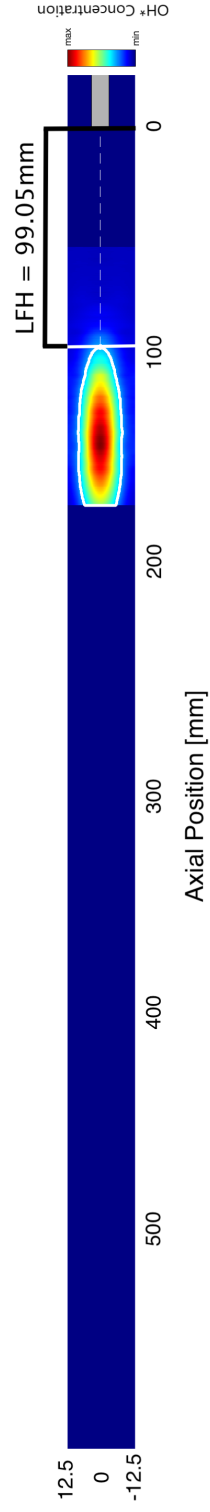
## APPENDIX C: CFD Contours



(a) CFD: Pressure based and effects  $CH_4/H_2$  80%/20% [%vol] OH concentration contour for the TDV case.



(b) CFD: Pressure based, radiation and compressibility effects  $CH_4/H_2$  80%/20% [%vol] OH concentration contour for the TDV case.



(c) Experimental derived  $CH_4/H_2$  80%/20% [%vol] chemiluminescence processed image for the TDV3 case.

**Figure C.0.1:** LFH analysis from both the CFD and experimental analysis for the  $CH_4/H_2$  80%/20% [%vol] TDV3 case. Gas flow is from right to left.

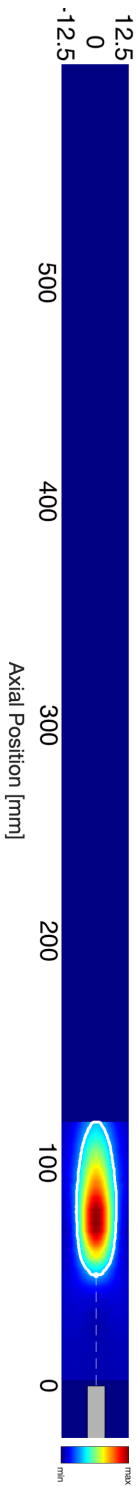
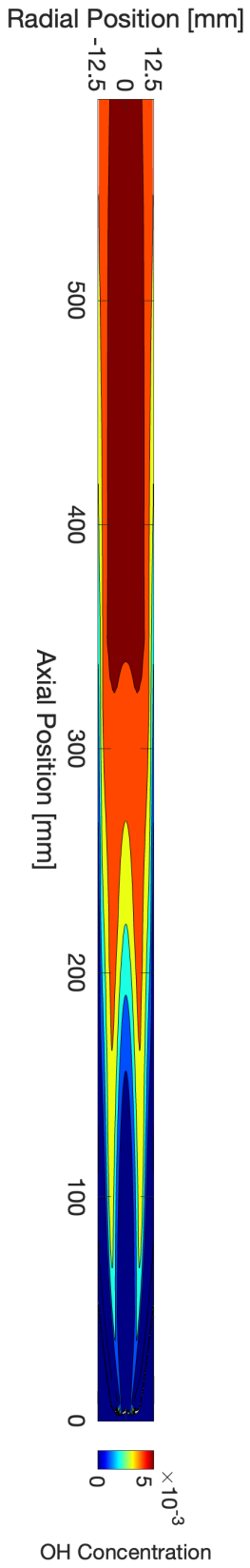
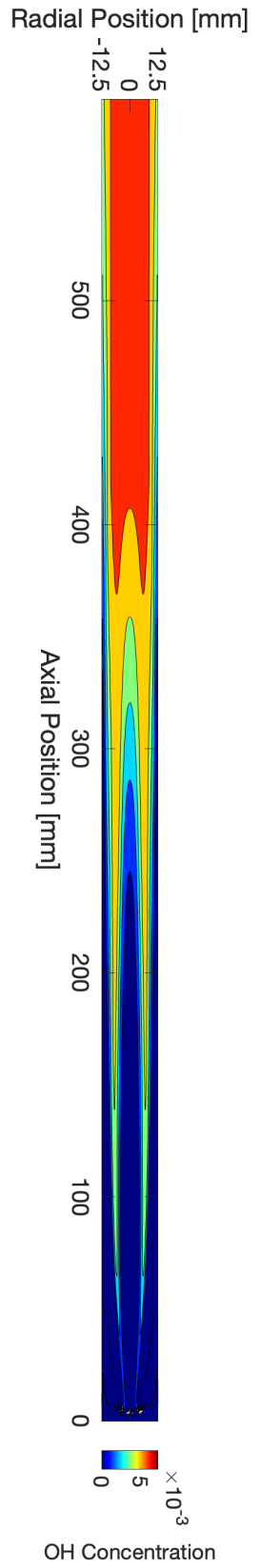
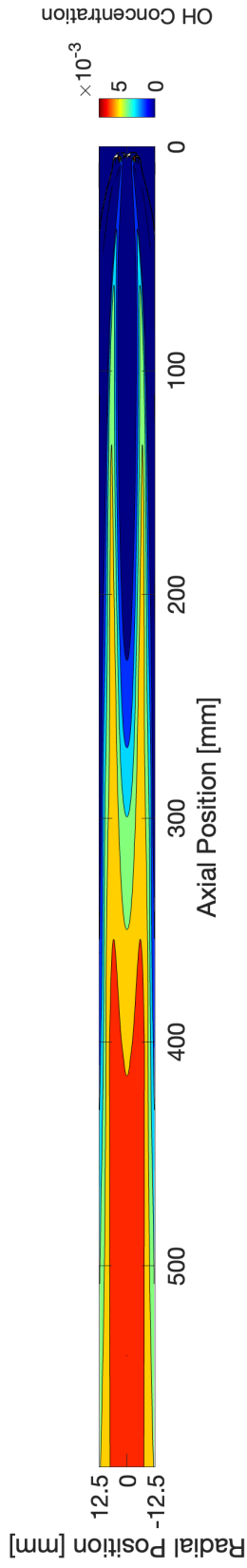
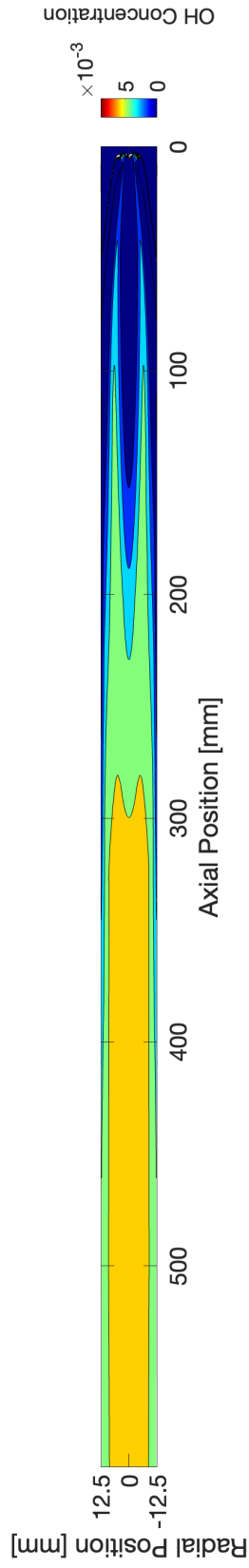


Figure C.0.2: LFH analysis from both the CFD and experimental analysis for the  $CH_4/H_2$  70%/30% [%vol] TDV3 case. Gas flow is from right to left.

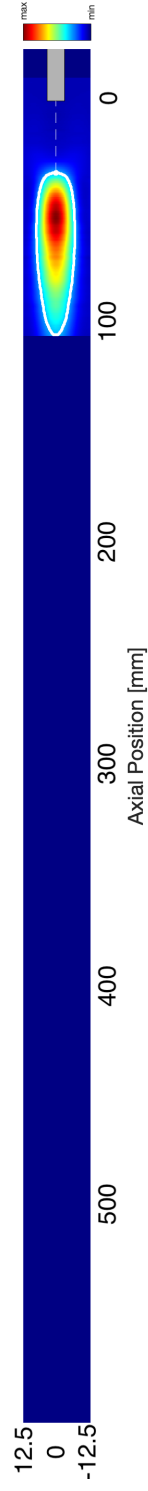




(a) CFD: Pressure based and effects  $CH_4/H_2$  60%/40% [%vol] OH concentration contour for the TDV case.



(b) CFD: Pressure based, radiation and compressibility effects  $CH_4/H_2$  60%/40% [%vol] OH concentration contour for the TDV case.



(c) Experimental derived  $CH_4/H_2$  60%/40% [%vol] chemiluminescence processed image for the TDV3 case.

**Figure C.0.3:** LFH analysis from both the CFD and experimental analysis for the  $CH_4/H_2$  60%/40% [%vol] TDV3 case. Gas flow is from right to left.

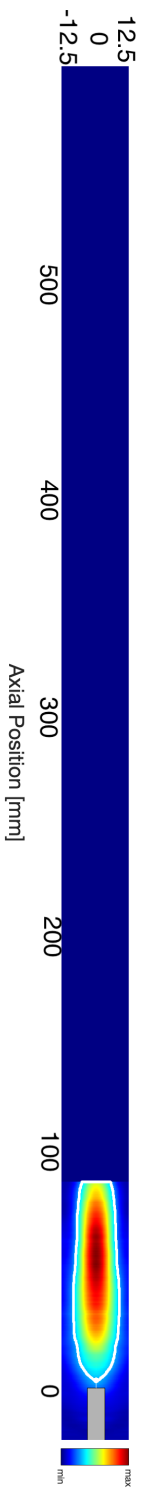
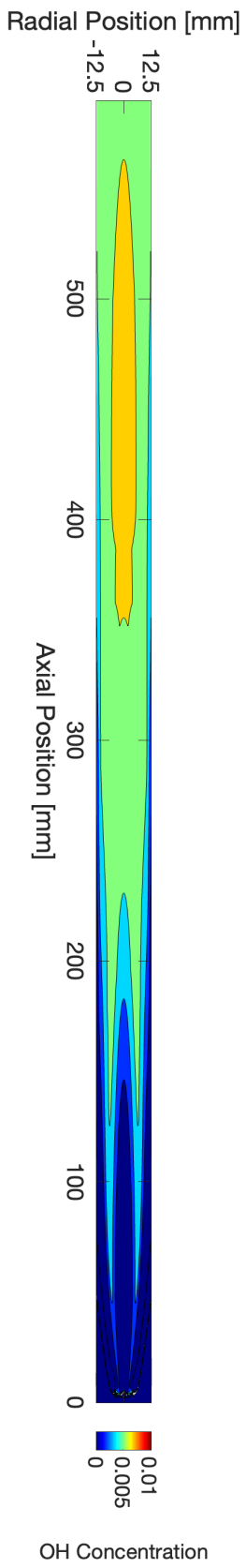
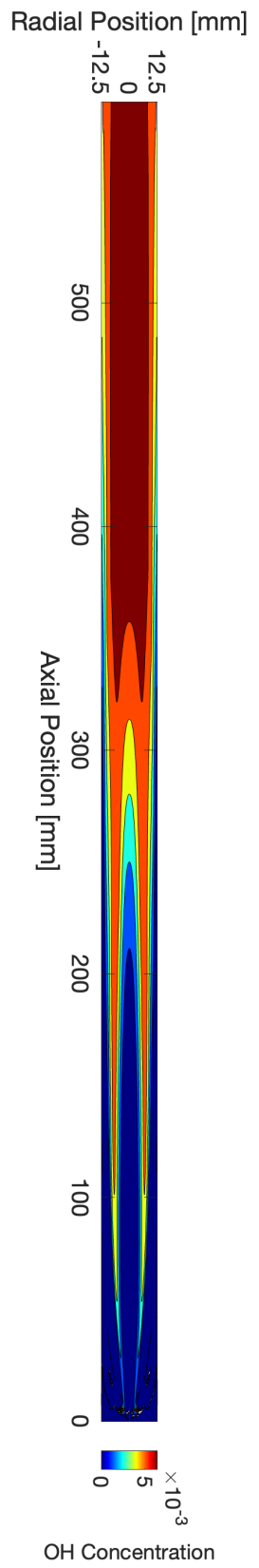
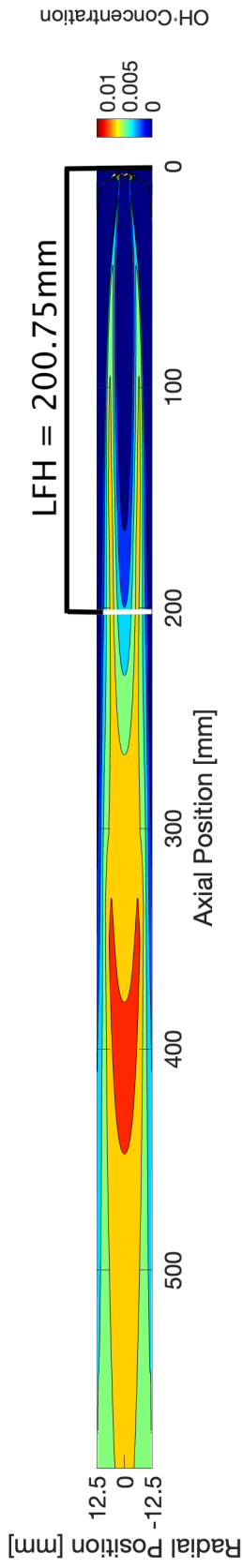
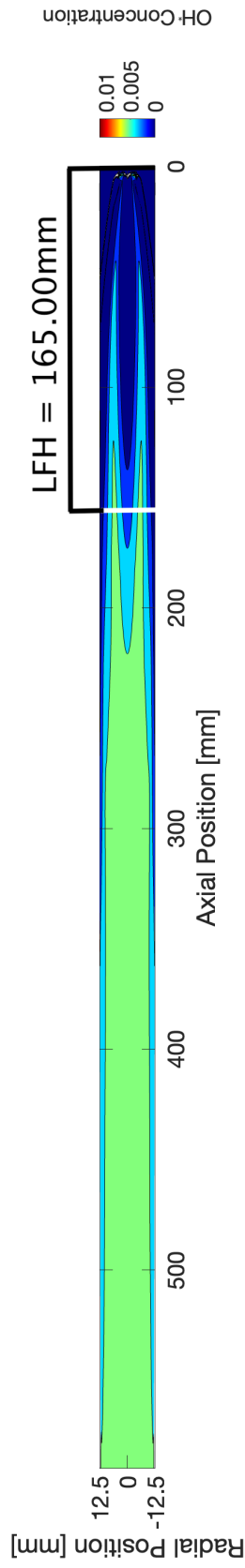


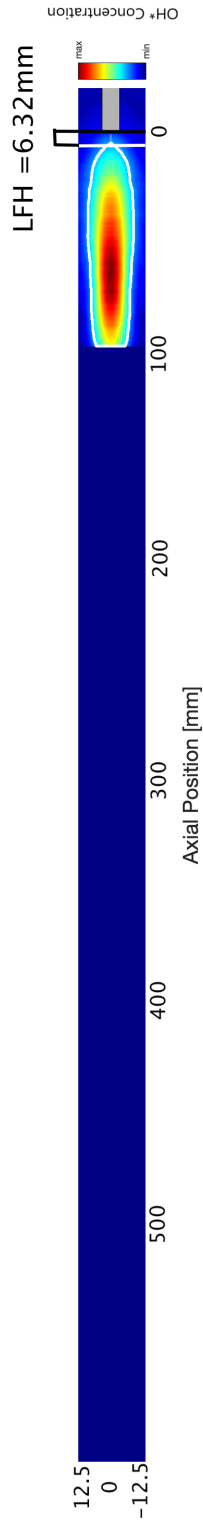
Figure C.0.4: LFH analysis from both the CFD and experimental analysis for the  $CH_4/H_2$  50%/50% [%vol] TDV3 case. Gas flow is from right to left.



(a) CFD: Pressure based and effects  $CH_4/H_2$  40%/60% [%vol] OH concentration contour for the TDV case.



(b) CFD: Pressure based, radiation and compressibility effects  $CH_4/H_2$  40%/60% [%vol] OH concentration contour for the TDV case.



(c) Experimental derived  $CH_4/H_2$  40%/60% [%vol] chemiluminescence processed image for the TDV3 case.

**Figure C.0.5:** LFH analysis from both the CFD and experimental analysis for the  $CH_4/H_2$  40%/60% [%vol] TDV3 case. Gas flow is from right to left.

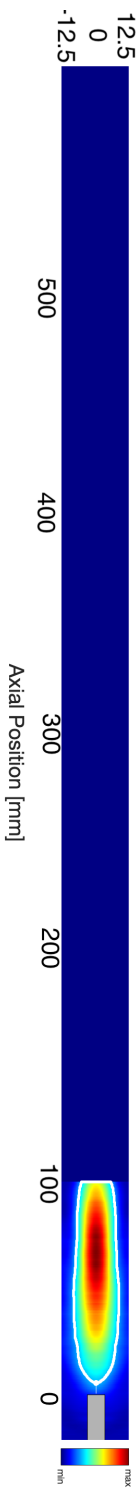
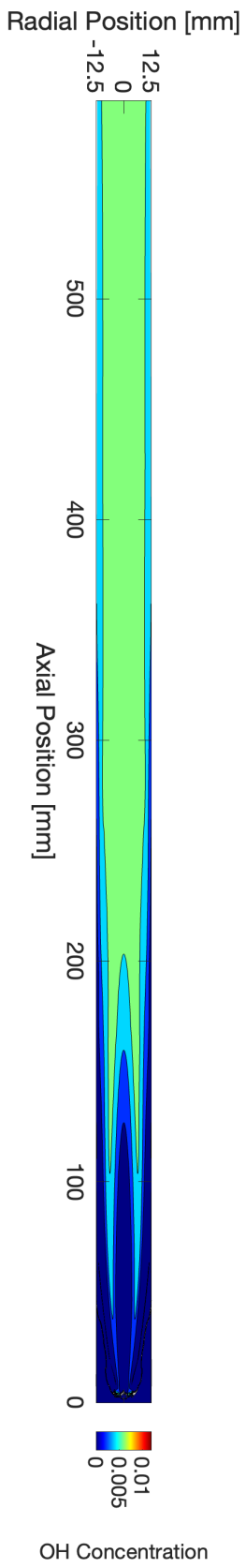
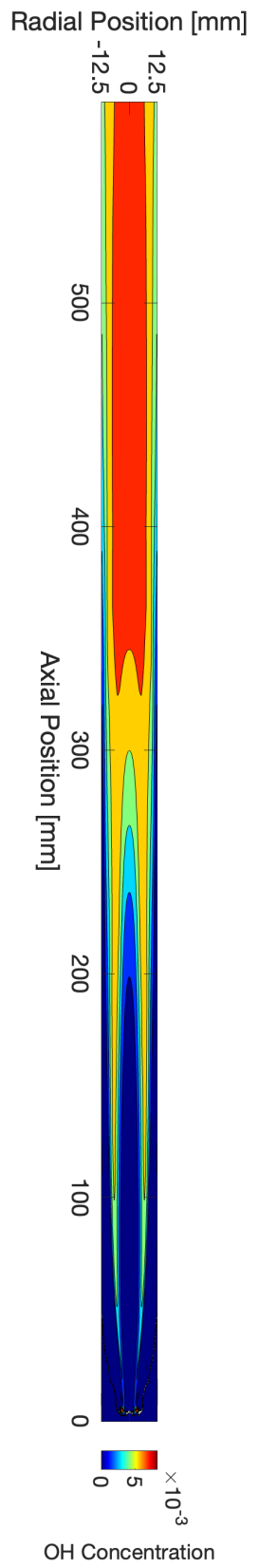
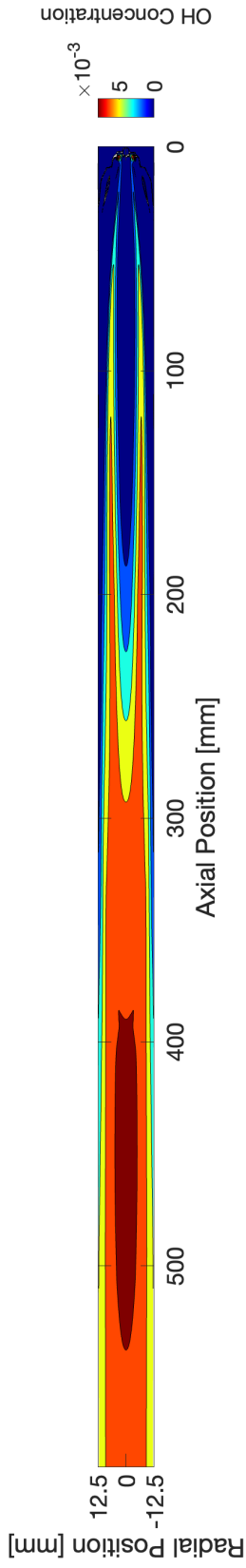
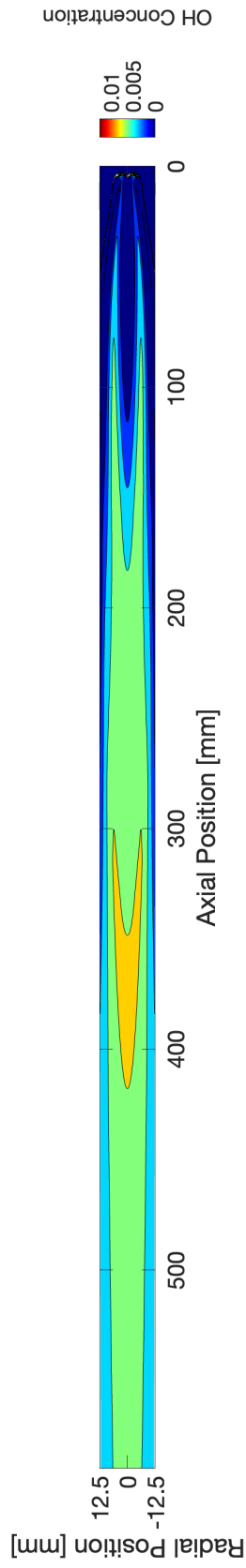


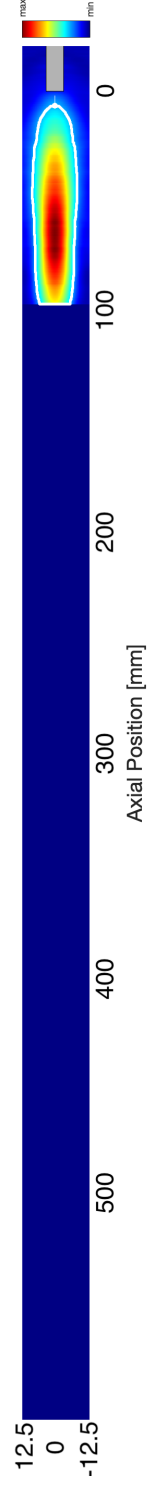
**Figure C.0.6:** LFH analysis from both the CFD and experimental analysis for the  $\text{CH}_4/\text{H}_2$  30%/70% [%vol] TDV3 case. Gas flow is from right to left.



(a) CFD: Pressure based and effects  $CH_4/H_2$  20%/80% [%vol] OH concentration contour for the TDV case.



(b) CFD: Pressure based, radiation and compressibility effects  $CH_4/H_2$  20%/80% [%vol] OH concentration contour for the TDV case.



(c) Experimental derived  $CH_4/H_2$  20%/80% [%vol] chemiluminescence processed image for the TDV3 case.

Figure C.0.7: LFH analysis from both the CFD and experimental analysis for the  $CH_4/H_2$  20%/80% [%vol] TDV3 case. Gas flow is from right to left.

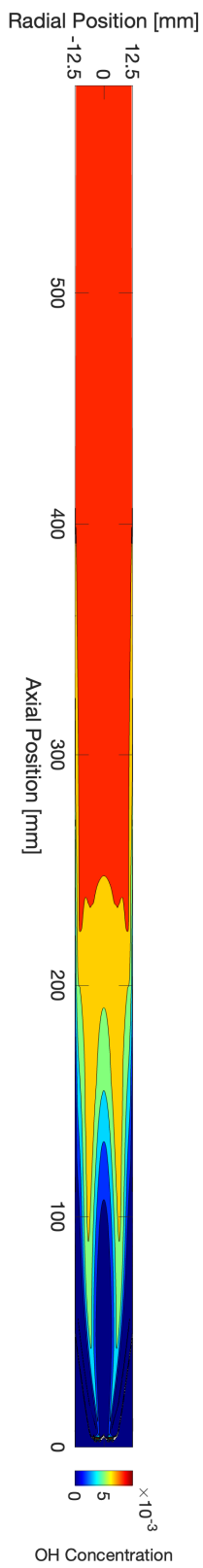
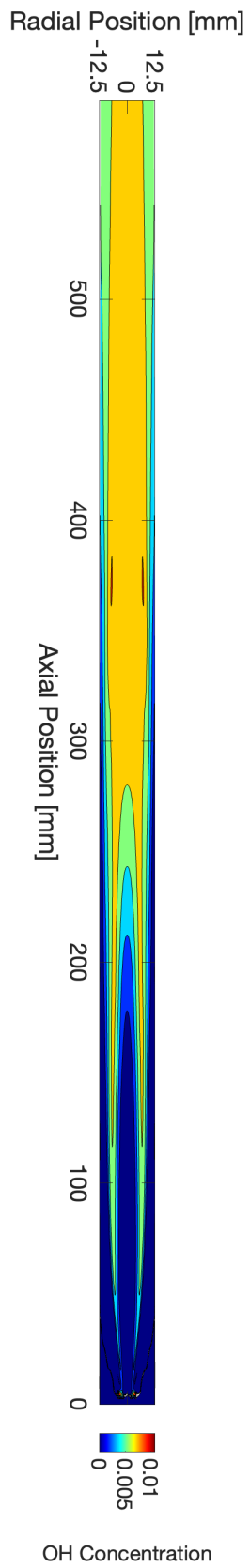
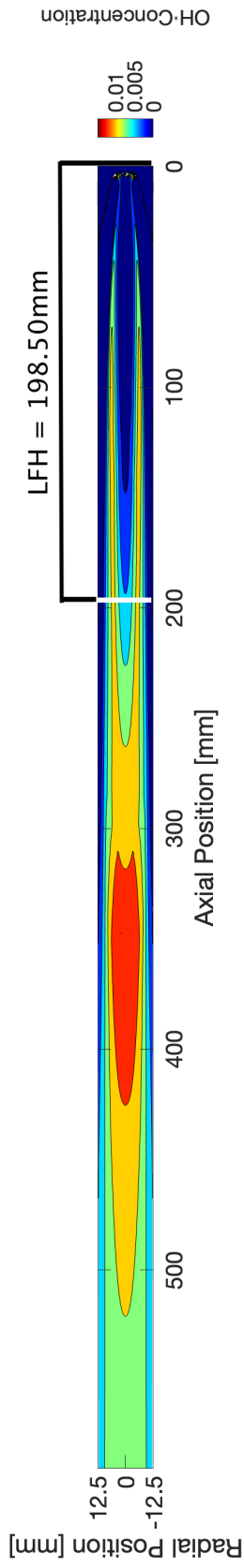
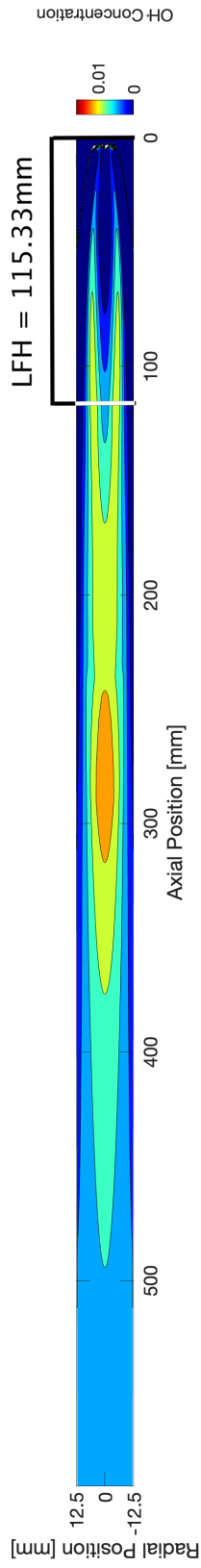


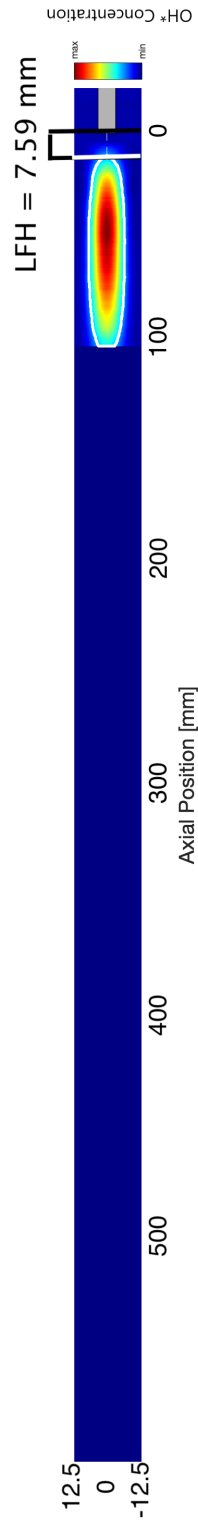
**Figure C.0.8:** LFH analysis from both the CFD and experimental analysis for the  $\text{CH}_4/\text{H}_2$  10%/90% [%vol] TDV3 case. Gas flow is from right to left.



(a) CFD: Pressure based and effects  $CH_4/H_2$  0%/100% [%vol] OH concentration contour for the TDV case.



(b) CFD: Pressure based, radiation and compressibility effects  $CH_4/H_2$  0%/100% [%vol] OH concentration contour for the TDV case.



(c) Experimental derived  $CH_4/H_2$  00%/100% [%vol] chemiluminescence processed image for the TDV3 case.

**Figure C.0.9:** LFH analysis from both the CFD and experimental analysis for the  $CH_4/H_2$  0%/100% [%vol] TDV3 case. Gas flow is from right to left.

# Appendix D

## APPENDIX D: Health and Safety Documentation

### D.1 Risk Assessment

Provided overleaf.



# Risk Assessment Form

**IMPORTANT:** Before carrying out the assessment, please read the Guidance Notes

## 1. General Information

<b>Department</b>	Engineering	<b>Building</b>	Gas Turbine Research Centre (GTRC)	<b>Room No</b>	GTRC – “Rig room”
<b>Name of Assessor</b>	James Bain	<b>Date of Original Assessment</b>	17/01/23	<b>Assessment No</b>	GTRC RA61

Status of Assessor: Supervisor  , Postgraduate  , Undergraduate  , Technician  , Other: \_\_\_\_\_  
(Specify)

## 2. Brief Description of Procedure/Activity including its Location and Duration

Set up and use of novel Turbulent Inhomogeneous Mixture Autoignition Rig (TIMAR) experimental facility at the GTRC for research purposes. The facility is comprised of a high-power, 30kW, electric air heater, to heat either air or a synthesised gas mixture to temperatures up to 1000degC in which various blends of methane and hydrogen (from 0-100% H2) will be injected into the hot flow and will autoignite within the optical chamber of the rig. TIMAR is located in the left-hand extraction bay and mounted on a purpose-built trolley, as shown by image below.



As aforementioned, blends of methane and hydrogen, including their pure forms will be supplied for operation during the test campaign. A suite of oxidants that include a differing compositions of N2, O2, CO2 and H2O are to be utilised to achieve certain test points. The desired temperature of the oxidants will be 900, 925, 950degC and will likely require heating past this temperature to achieve the target temperature due to heat loss. Fuel is to be delivered at atmospheric temperature

via dedicated mass flow controllers. Fuel is stored outside in the fuel skid and delivered by pressurised fuel delivery system.

Throughout the campaign a suite of diagnostic tools are to be used, including; Chemiluminescence, Particle Image Velocimetry, Laser Doppler Anemometry and the use of a high speed HD camera.

**3. Persons at Risk** Are they... Notes - Consider new and expectant mothers, and women of child bearing age when carrying out this risk assessment.

Staff <input checked="" type="checkbox"/>	Trained <input checked="" type="checkbox"/>	The rig will typically be setup by the competent GTRC technician and/or research associate. The rig will be operated by the PhD student under the supervision of either the GTRC technician and/or research associate.
Students <input checked="" type="checkbox"/>	Competent <input checked="" type="checkbox"/>	
Visitor <input checked="" type="checkbox"/>	Inexperienced <input checked="" type="checkbox"/>	
Contractor <input type="checkbox"/>	Disabled <input type="checkbox"/>	

<b>4. Level of Supervision</b>	Notes
None <input type="checkbox"/> Constant <input type="checkbox"/> Periodic <input checked="" type="checkbox"/> Training Required <input type="checkbox"/>	Supervision levels suitable for the activity/person. Periodic supervision suitable. However, during operation of the facility constant supervision will be required. Use of remote CCTV will be used to supervise the rig during operation and any persons who enter the rig room to change operational conditions on the control unit of the heater - permission from test controller required.

<b>5. Will Protective Equipment Be Used?</b> Please give <i>specific</i> details of PPE	
Head <input type="checkbox"/> Eye <input checked="" type="checkbox"/> Ear <input type="checkbox"/> Body <input checked="" type="checkbox"/> Hand <input checked="" type="checkbox"/> Foot <input checked="" type="checkbox"/>	Eye protection is to be used at all times. Gloves are to be used when using tools and manual handling. Steel toe cap boots when manual handling heavy components. Anti-static and flameproof overalls required when setting up fuel delivery and rig operation. Gas monitors to be used at any time that gas lines are pressurised (i.e. setting up and operation of rig) for protection of low O2 environments, LEL, HEL and CO2 level. Hearing protection to be used when air/oxidant is flowing through rig.

<b>6. Is the Environment at Risk?</b>	Notes
Yes <input type="checkbox"/> No <input checked="" type="checkbox"/>	Small amounts of waste combustion gases are emitted up the exhaust stack and diluted by the duct fan to safe levels

<b>7. Will Waste be generated?</b>	If 'yes' please give details of disposal
Yes <input checked="" type="checkbox"/> No <input type="checkbox"/>	Small amounts of waste combustion gases are emitted up the exhaust stack and diluted by the duct fan to safe levels

## 8. Hazards involved

Work Activity / Item of Equipment / Procedure / Physical Location	Hazard	Control Measures and Consequence of Failure	Likelihood (1 to 5) ×	Severity (1 to 5) =	Level of Risk
TIMAR setup and operation	Slips, trips and falls	<p><u>Consequence:</u> Personal injury, either minor or sever.</p> <p><u>Control:</u> Induction, housekeeping workplace inspections, appropriate footwear, use of handrails, ensuring that the rig room is clear and tidy. Cover loose cables to prevent tripping.</p>	2	2	4
	Fire and explosion	<p><u>Consequence:</u> Potential for serious injury and damage to property.</p> <p><u>Control:</u></p> <p>Competent personnel setup and operate the test rig.</p> <p>Staff trained in compressed gas safety, fire awareness and fire prevention.</p> <p>4 eyed (two person) check on fuel line setup prior to use.</p> <p>Fuel lines leak checked prior to use and nitrogen purged at the end of the test day.</p> <p>Fixed and personal gas detection with audible and visual alarms.</p> <p>Forced ventilation in the extraction bay.</p> <p>Specific DSEAR risk assessment for extraction bays, DSEAR 3.</p> <p>Rig operated remotely from the control room.</p> <p>30min facility check and walk around by test controller during testing.</p> <p>Anti-static flame-retardant overalls, antistatic safety shoes and protective glasses must be worn.</p> <p>ATEX rated equipment used within applicable zones (reference DSEAR assessment) or suitable zoning and controls applied to non-ATEX rated equipment.</p>	1	5	5
	Hazardous substances, carbon monoxide, oxides of nitrogen.	<p><u>Consequence:</u> Asphyxiation, inflammation of airways and increased susceptibility to respiratory infections and allergens.</p> <p><u>Control:</u> Appropriate use of forced extraction by extraction</p>	1	5	5

	<p>fan within the extraction bay and the channelling of exhaust gases directing them to the extraction bay.</p> <p>Competent person setup and operation of rig.</p> <p>Personal gas monitors (calibrated and bump tested) with low O2.</p> <p>Fixed low O2 alarms in the control room and rig room.</p>			
Asphyxiation; nitrogen, CO2	<p><u>Consequence:</u> Asphyxiation.</p> <p><u>Control:</u> Competent personnel setup and operate the test rig.</p> <p>Staff trained in compressed gas safety</p> <p>Forced ventilation in the extraction bay and rig room.</p> <p>External bottle stores well ventilated.</p> <p>Personal gas monitors worn with low O2 (calibrated and bump-tested)</p> <p>Fixed low O2 alarms in the control room and rig room</p>	1	5	5
Noise	<p><u>Consequence:</u> Damage to hearing.</p> <p><u>Control:</u> Hearing protection in noise hazard areas, signs, restricted access.</p> <p>Hearing defenders ton if in the rig rom during operation.</p> <p>Rig room entry policy GTRC 35</p> <p>General Noise Risk Assessment GTRC 17</p>	1	3	3
High temperature surfaces and gases	<p><u>Consequence:</u> severe burns to persons.</p> <p><u>Control:</u> Guarding (Perspex sheet covering extraction bay), lagging, signs.</p> <p>GTRC 35 – Rig room entry policy</p> <p>Test rig temperature monitoring with alarm levels</p>	1	4	4
High Voltage Electrical Supply.	<p><u>Consequence:</u> Potential for severe injury, electrocution and electrical fire.</p> <p><u>Control:</u> Combined inspection and testing regime for electrical items implemented. PAT and 5 year fixed wiring.</p>	1	5	5

		<p>RCD protection on all rig mains, internal and external sockets.</p> <p>Competent personnel and independent checking of electrical tasks.</p> <p>Operator trained in how to operate CO2 fire extinguisher and to isolate fire safely.</p> <p>Use of isolator switches when rig is not in operation.</p> <p>Appropriate earthing of rig and trolley.</p>			
	Working at height	<p><u>Consequence:</u> Falling from height.</p> <p><u>Control:</u> Suitable equipment provided and inspected, trained users of access ladders. Edge protection provided.</p> <p>Working at height risk assessment GTRC RA 13</p>	1	4	4
	Manual Handling	<p><u>Consequence:</u> Injury due to muscle strain and dropping of items on handler(s)</p> <p><u>Control:</u> Induction, lifting aids provided, workforce trained in manual handling techniques.</p> <p>Use of protective footwear and gloves.</p> <p>Use of suitable hardware for lifting heavy objects.</p> <p>Manual handling risk assessment GTRC RA 12</p>	1	3	3
	Violence, illness, injury	<p>Communication with buddy, building security measures, School of Engineering lone working authorisation procedure.</p>	1	3	3
Compressed Bottle and Pipework.	Flammable Gas leak.	<p><u>Consequence:</u> Gas Leak may cause an explosive environment, leading to fire or explosion. Gas leak may also cause of low O2 environment causing asphyxiation.</p> <p><u>Control:</u></p> <p>Calibrated and bump-tested gas monitor to be worn in close proximity to nose and mouth.</p> <p>Works to be undertaken by trained and competent persons.</p> <p>ATEX rated equipment used within applicable zones</p>	1	5	5

		<p>(reference assessment). DESEAR</p> <p>Appropriate ventilation applied.</p> <p>Four-eyed (two-person) checks to be undertaken.</p> <p>Cylinders are to be stored externally and fed into the rig room into the extraction bay where the extraction fan will minimise the build-up of an explosive atmosphere.</p> <p>Leak test of cylinder to be performed prior to testing.</p> <p>Leak test and line purge performed with Nitrogen prior to testing.</p> <p>Gas bottle regulator to be in-date and correctly specified.</p>			
	Gas Cylinder Falling.	<p><u>Consequence:</u> Falling cylinder may result in damage and/or rupture of cylinder bottle.</p> <p><u>Control:</u> Competent persons to handle gas bottles.</p> <p>Valve protectors are to be used.</p> <p>Move by use of dedicated trolley.</p> <p>When stationary, gas bottle must be stored upright a strapped to fixed location.</p> <p>Cylinders are stored externally.</p>	1	3	3
	Air Gas Leak	<p><u>Consequence:</u> Reduction in rig controllability during operation.</p> <p><u>Control:</u> Fitted by competent staff.</p> <p>Leak check to performed prior to operation.</p> <p>Staff trained in compressed gas safety.</p>	1	3	3

**9. Chemical Safety (COSHH Assessment)**

January 17<sup>th</sup>

Hazard	Control Measures	Likelihood (1 to 5) ×	Severity (1 to 5) =	Level of Risk
CO, NOx, CH4, H2, CO2	COSHH 22	1	5	5

**Scoring Criteria for Likelihood (chance of the hazard causing a problem)**

1 – Very Unlikely, 2 – Unlikely, 3 – Likely, 4 – Very Likely, 5 – Almost certain to happen

**Scoring Criteria for Severity of injury (or illness) resulting from the hazard**

1 – First Aid is adequate, 2 – Minor injury, 3 – "Three day" injury, 4 – Major injury, 5 – Fatality or disabling injury

**10. Source(s) of information used to complete the above**

GTRC Centre Manager  
 GTRC 01-Emergency incident response policy and procedure  
 GTRC 02-Safety method statement for gaseous fuel leak testing  
 GTRC 03-Fire response flow chart  
 GTRC 04-Gas release response flow chart  
 GTRC 06-Management of change policy and procedure  
 GTRC 08-Role of fire warden  
 GTRC 35-Rig room entry policy  
 GTRC 46-GTRC Delivery procedure  
 GTRC DSEAR 03  
 COSHH 22  
 BCGA guidance CP4  
 DSEAR 2002  
 PER 1999  
 PSSR 2002

**11. Further Action**

Highest Level of Risk Score	Action to be taken
1 to 5 <input checked="" type="checkbox"/>	No further action needed
6 to 11 <input type="checkbox"/>	Appropriate additional control measures should be implemented
12 to 25 <input type="checkbox"/>	Additional control measures <b>MUST</b> be implemented. Work <b>MUST NOT</b> commence until such measures are in place. If work has already started it must <b>STOP</b> until adequate control measures are in place.

**12. Additional Control Measures – Likelihood and Severity are the values with the additional controls in place**

Work Activity / Item of Equipment / Procedure / Physical Location	Hazard and Existing Control Measures	Additional Controls needed to Reduce Risk	Likelihood (1 to 5) ×	Severity (1 to 5) =	Level of Risk

After the implementation of new control measures the procedure/activity should be re-assessed to ensure that the level of risk has been reduced as required.

**13. Action in the Event of an Accident or Emergency**

Report to supervisor / centre manager as per induction briefing

**14. Arrangements for Monitoring the Effectiveness of Control**

Regular visual checks, technician, and centre manager safety

**15. Review:** This assessment must be reviewed by (date): 17/01/24  
 January 17<sup>th</sup>

Name of Reviewer:	Steve Morris	Date of Review:	14.02.23
Have the Control measures been effective in controlling the risk?			
Have there been any changes in the procedure or in information available which affect the estimated level of risk?			
What changes to the Control Measures are required?			

**16. Signatures for printed copies:**

Assessor: James Bain	Signature:	Date: 17/01/23
Approved by: Steve Morris	Signature:	Date: 14/02/23
This copy issued to:	Signature:	Date:
This copy issued to:	Signature:	Date:
This copy issued to:	Signature:	Date:
This copy issued to:	Signature:	Date:



## **D.2 DSEAR Assessment**

### **D.2.1 DSEAR Specific Case Document**

Provided overleaf.

# TIMAR - DSEAR Assessment Considerations and Controls Document

**IMPORTANT:** Before carrying out the assessment, please read the Guidance Notes

## 1. General Information

<b>Department</b>	Engineering	<b>Building</b>	Gas Turbine Research Centre (GTRC)	<b>Room No</b>	GTRC – “Rig room”
<b>Name of Assessor</b>	James Bain	<b>Date of Original Assessment</b>	17/01/23	<b>Assessment No</b>	

Status of Assessor: Supervisor  , Postgraduate  , Undergraduate  , Technician  , Other: .....  
(Specify)

## 2. Outline and Reasoning

The activities required to undertaken to fulfil this PhD research project requires the use of dangerous substances and has the potential risk to the safety of GTRC personnel resulting from a fire, explosion of similar energetic events, hence, a DSEAR (Dangerous Substances and Explosive Atmosphere Regulations) assessment of works is necessary. This document is intended to be accompanied by the GTRC’s DSEAR 3 assessment associated with the lefthand experimental bay (LHEB), following its procedure and guidelines leading to engineering decisions to reduce risk as low as reasonably practicable when operating TIMAR.

Since work activities are to be undertaken at extremely high temperatures circa. 1000degC, the rig itself will be considered as an ignition source due to the high temperature materials (assumed to be greater than the autoignition of the fuels used in this test campaign). Hence, location and size of potential fuel leaks are to be identified and calculated, leading to zone classification in accordance with DSEAR.

Referenced Documents:

- [1] DSEAR – Available at: <https://www.legislation.gov.uk/ukxi/2002/2776/contents/made>
- [2] DSEAR 3 – Extraction Bay, below.
- [3] TIMAR\_dP\_FDS001, below.

## 3. Sites of Potential Risk

The potential sites of fuel leakages in the extraction bay are associated with the fuel delivery system and are to be considered as secondary releases. As the fuels are supplied by cylinder, the delivery pressure is expected to be 10bar max. Within the LHEB, a joint between the cylinder and the mass flow controllers (MFCs) is considered a potential leak source (see image in Figure 1) with a maximum pressure of 10bar. Further, an additional leak source may be between the MFCs and the joint to the fuel injection of TIMAR (see image in Figure 1), at present to be considered no greater than 1.2bar as determined by calculations shown in supporting document “TIMAR\_dP\_FDS001.” Note also that the MFCs used for the fuel delivery to TIMAR are housed in a cabinet with forced ventilation that extracts any potential leaks from the MFCs out of the LHEB and exhausts it to stack, this also must be done to circumvent the fact that the MCFs are not ATEX compliant. All other potential locations of a leak are outside of the minimum radius required as detailed by following analysis on critical gas cloud size.



#### 4. Critical Gas Cloud Calculations and Zoning

Two release pressures are to be considered: i) 10bar H<sub>2</sub> release and ii) 1.2bar H<sub>2</sub> release. Whilst a range of fuel blends of methane and hydrogen are to be used during the operation of TIMAR under LHEB, analysis has been limited to hydrogen to provide protection of the worst case scenario.

##### 10bar H<sub>2</sub> Release:

Using the “V<sub>z</sub>\_calc\_Part4\_WS1” spreadsheet developed by the management team at the GTRC and following the guidelines stated in “DSEAR 3 – Extraction Bay” for the 10bar release a critical V<sub>z</sub> **was calculated to be 0.44m<sup>3</sup>**, and a ventilation classification of “medium”. Thus, meaning that an ignition source must be outside of a spherical radius of 0.47m.

As a ratio of the explosive gas cloud occupied to the total volume of the extraction bay is:

$$\frac{V_z}{V_0} = \frac{0.44}{6.75} = 0.065 = 6.5\%$$

Since  $\frac{V_z}{V_0} > 1\%$  and the gas cloud  $> 0.1\text{m}^3$  the ventilation is classified as medium.

By following the guidance given by the DSEAR standard, shown in Table 1 below, the zone attributed to this risk is **Zone 2**.

##### 1.2bar H<sub>2</sub> Release:

Using the same methodology stated above, the V<sub>z</sub> **was calculated to be 0.10m<sup>3</sup>** with a spherical radius of 0.29m.

As a ratio of the explosive gas cloud occupied to the total volume of the extraction bay is:

$$\frac{V_z}{V_0} = \frac{0.1}{6.75} = 0.0148 = 1.5\%$$

Since the absolute value of V<sub>z</sub> is  $< 0.1\text{m}^3$  (0.09764 4 sig fig), the ventilation is classified as high.

By following the guidance given by the DSEAR standard, shown in Table 1 below, the zone attributed to this risk is **Zone 2NE**.

**Table 1 – DSEAR zoning in relation to release type and ventilation degree.**

Grade of release	Ventilation						
	Degree						
	High			Medium			Low
	Availability						
	Good	Fair	Poor	Good	Fair	Poor	Good, fair or poor
Continuous	(Zone 0 NE) Non-hazardous <sup>a</sup>	(Zone 0 NE) Zone 2 <sup>a</sup>	(Zone 0 NE) Zone 1 <sup>a</sup>	Zone 0	Zone 0 + Zone 2	Zone 0 + Zone 1	Zone 0
Primary	(Zone 1 NE) Non-hazardous <sup>a</sup>	(Zone 1 NE) Zone 2 <sup>a</sup>	(Zone 1 NE) Zone 2 <sup>a</sup>	Zone 1	Zone 1 + Zone 2	Zone 1 + Zone 2	Zone 1 or zone 0 <sup>c</sup>
Secondary <sup>b</sup>	(Zone 2 NE) Non-hazardous <sup>a</sup>	(Zone 2 NE) Non-hazardous <sup>a</sup>	Zone 2	Zone 2	Zone 2	Zone 2	Zone 1 and even zone 0 <sup>c</sup>

## 5. TNT Equivalent

The methodology of this work is described in detail in the “DSEAR 3 – Experimental Bays” document [2].

Equivalent mass of TNT ( $W_{TNT}$ ) is equal to:

$$W_{TNT} = \frac{\eta * W_f * H_f}{H_{TNT}}$$

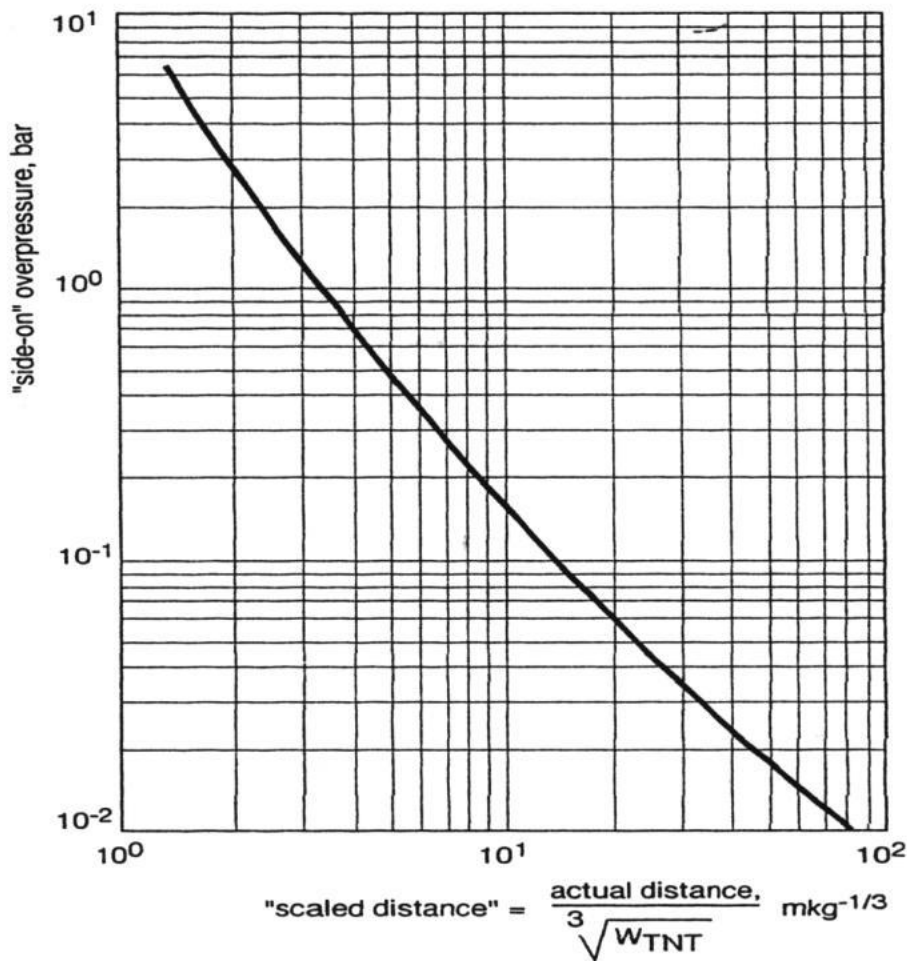
Where,  $\eta$  = TNT efficiency factor,  $W_f$  = mass of fuel,  $H_f$  = heat of combustion of the fuel (HHV) and  $H_{TNT}$  the heat of combustion of TNT (4.68MJ/kg)

Therefore, for consideration with hydrogen (10 second release of 0.3g/s – worst case scenario),

$$W_{TNT} = \frac{0.03 * 0.03 * 141}{4.68} = 0.0271 \text{ kg TNT equivalent.}$$

Now an equivalent mass of TNT has been determined, a theoretical peak overpressure can now also be ascertained through empirical data. Using the below figure and the determination of an equivalent scaled distance  $\bar{R}$ , which is obtained from the following expression:

$$\bar{R} = \frac{R}{W_{TNT}^{\frac{1}{3}}}$$



Returning the following estimations of overpressure in bar.

**Table 2** – Equivalent scaled distance and overpressure.

R (m)	$\bar{R}$ (m)	Approx OP, from chart (bar)
0.05	0.166	
0.1	0.333	
0.15	0.499	
0.2	0.666	
0.25	0.832	
0.3	0.999	
0.35	1.165	
0.4	1.332	
0.45	1.498	6.5
0.5	1.665	
0.55	1.831	
0.6	1.998	1.8
0.65	2.164	
0.7	2.330	
0.75	2.497	1
0.8	2.663	
0.85	2.830	
0.9	2.996	1.2
0.95	3.163	
1	3.329	

	1.05	3.496	
	1.1	3.662	
	1.15	3.829	
	1.2	3.995	0.7
	1.25	4.162	
	1.3	4.328	
	1.35	4.494	
	1.4	4.661	
	1.45	4.827	
	1.5	4.994	0.5

**5. Review:** This assessment must be reviewed by (date):

Name of Reviewer:	James Bain	Date of Review:	17/01/23
Have the Control measures been effective in controlling the risk?			
Have there been any changes in the procedure or in information available which affect the estimated level of risk?			
What changes to the Control Measures are required?			

**16. Signatures for printed copies:**

Assessor: James Bain	Signature:	Date: 17/01/23
Approved by: Steve Morris	Signature:	Date: 18/02/23
This copy issued to:	Signature:	Date:
This copy issued to:	Signature:	Date:
This copy issued to:	Signature:	Date:
This copy issued to:	Signature:	Date:

## **D.2.2 DSEAR Supporting Standard Document**

DSEAR 3 - Experimental Bays document is only available by request due to its sensitive nature and limited access to authorised personnel.

## **D.2.3 Supporting Calculations**

Provided overleaf.







## D.3 COSSH Assessment

Provided overleaf.

## School of Engineering COSHH Assessment

Date	20/03/23	Location	GTRC Control Room	Assessment No.	COSHH
What is the process or activity?	General setup and use of the GTRC TIMAR facility (maximum span gas concentrations quoted, exhaust gas could comprise larger fractions). This forms one of four inter-related safety documents for using this equipment, the other two being the Risk/DSEAR Assessments, and the Safe Operating Procedure.				

What is being used/produced/handled/stored?											Is the substance:																
											Dangerous for the Environment (N)	Irritant (Xi)	Harmful (Xn)	Corrosive (C)	Toxic (T)	Very Toxic (T+)	Oxidising (O)	Explosive (E)	Highly Flammable (F+)	Extremely Flammable (F++)							
Substance / Product / Hazard	Used or Produced	Substance/Product Form						WEL		Amount/Quantity																	
		Solid	Liquid	Gas	Vapour	Mist	Fume	Dust/Powder	LTEL		STEL																
Carbon Monoxide	Produced			X					25	50	ppm			X			X										
Carbon Dioxide	Used			X					5000	15000	ppm	Only harmful as an asphyxiant															
NO <sub>x</sub>	Produced			X					100		ppm						X										
NO	Produced			X					25		ppm						X										
Hydrogen (pure H2 or blended with methane)	Used			X					-	-	ppm															X	
Helium (use as surrogate fuel)	Used			X					-	-	ppm	Only harmful as an asphyxiant															
Ozone (Potentially produced in as combustion product)	Produced			X					0.1	0.3	ppm						X			X							
Methane (used as pure fuel or blended with hydrogen)	Used			X					-	-	Ppm															X	
Nitrogen	Used			X					-	-	ppm	Only harmful as an asphyxiant															

Who is at risk?	X	How is exposure likely to occur?	X	Frequency of Process or Activity	↓
Staff	x	Absorption		Intermittent use of TIMAR.	

Students	x	Inhalation	x	Process or Activity Duration (mins) ↓
Cleaners / Contractors		Ingestion		Experimental gases only added to air for short duration (Approx 10 seconds per test point). Combustion products produced during this time.
High Risk Groups Identify -				Any substance/group that substance(s) must not come into contact with ↓
Others (Identify)-		Carcinogenic, Mutagenic	n/a	n/a

### Controls to Reduce Risks –

Personal Protective Equipment Required & Type	X	Engineering Controls Required	X	Storage Requirements	X	Other Controls Required ↓
Hand Protection	ⓘ	Open Bench OK / None		Locked Cupboard		Local/personal O <sub>2</sub> monitor Local/personal CO monitor Local/personal LEL monitor Personal NO monitor Natural ventilation maintained with fire escape open, control room doors open and forced ventilation in operation. Leak checks performed before use.
Eye / Face Protection	ⓘ	Fume Cupboard	x	Cool/Dry/Dark conditions		
Respiratory Protection	ⓘ	Total Enclosure / Glove Box		Fireproof cabinet		
Protective Clothing	ⓘ	Local Ventilation	x	Other (Identify)	x	
Other (Identify)	ⓘ	Other (Identify)		Cylinder storage compound		
<b>Actions Required</b>	<b>X</b>	<b>Instruction, Training and Supervision</b>		<b>X</b>	<b>First Aid: What Action should be taken if substance (Meth spirits):</b>	
Monitoring of Exposure		Work is not to be carried out without direct personal supervision			Is Ingested: Ingestion not considered a route of exposure.	
Workplace Air Monitoring	x	Work can be carried out without direct personal supervision		x	Is Inhaled: Remove victim to fresh air and keep comfortable.	
Health Surveillance		Details of Special Instructions or Training Required:			Comes into contact with eyes:	
Other					Comes into contact with skin:	

### Emergency Procedures

V1.0 Author BainJT

**Fire Precautions: What actions will be taken in the event of a fire involving these substances? (Hydrogen and methane)**

If safe, jet fire will be allowed to burn, and isolated at source to prevent explosive build up.

Because of proximity to electrical equipment, electrical equipment will be isolated, and any flames will be extinguished with CO<sub>2</sub>. Refer to emergency response procedure GTRC 03

**How should an accidental release / spillage be dealt with?**

Supply isolated in lines and on cylinder, evacuate and ensure adequate ventilation is maintained. Refer to emergency response procedure GTRC 4 and GTRC 05

ENGIN – 23/01/23

**Assessment of Risk to Health**

<b>Scoring Criteria for Likelihood of Harm</b> 1-Very Unlikely, 2-Unlikely, 3-Likely, 4-Very Likely, 5-Extremely Likely  <b>Scoring Criteria for Severity of Injury or Illness</b> 1-First Aid is adequate, 2-Minor Injury, 3-Three Day Injury, 4-Major Injury, 5-Fatal or Disabling Injury	Likelihood (1 - 5)	X  Severity (1 - 5)	=  Level of Risk (1 - 25)	<b>Justification Notes</b>
Carbon Monoxide	1	4	4	Local exhaust ventilation in the Left Hand Extraction Bay (LHEB) employed to reduce concentrations, with atmospheric monitoring. All fittings leak checked with N <sub>2</sub> prior to use. Spreadsheet COSHH_GA_CO_1 model cloud size above a hazardous threshold (420ppm), from a fitting leak. This is shown to be 0.18m <sup>3</sup> , with an equivalent spherical radius of 0.35m. Fixed (local) and personal gas monitors are in place to continuously monitor atmospheric concentration.
Carbon Dioxide (9.008% span max)	1	2	2	Local exhaust ventilation in the Left Hand Extraction Bay (LHEB) employed to reduce concentrations, with atmospheric monitoring. All fittings leak checked with N <sub>2</sub> prior to use. Fixed (local) and personal gas monitors are in place to continuously monitor atmospheric O <sub>2</sub> concentration.
NO <sub>x</sub> (39ppm span max)	1	2	4	Local exhaust ventilation in the Left Hand Extraction Bay (LHEB) employed to reduce concentrations, with atmospheric monitoring. All fittings leak checked with N <sub>2</sub> prior to use.
NO	1	4	4	Local exhaust ventilation in the Left Hand Extraction Bay (LHEB) employed to reduce concentrations, with atmospheric monitoring. All fittings leak checked with N <sub>2</sub> prior to use. Personal gas monitors are in place to continuously monitor atmospheric concentration.
NH <sub>3</sub>	1	4	4	Local exhaust ventilation in the Left Hand Extraction Bay (LHEB) employed to reduce concentrations, with atmospheric monitoring. All fittings leak checked with N <sub>2</sub> prior to use. Personal gas monitors are in place to continuously monitor atmospheric concentration.
Hydrogen (40% FID fuel)	1	3	3	Local exhaust ventilation in the Left Hand Extraction Bay (LHEB) employed to reduce concentrations, with atmospheric monitoring. All fittings leak checked with N <sub>2</sub> prior to use. Fixed (local) and personal gas monitors are in place to continuously monitor atmospheric LEL. Explosive risk analysed in DSEAR assessment.
Helium (60% FID fuel)	1	1	1	Local exhaust ventilation in the Left Hand Extraction Bay (LHEB) employed to reduce concentrations, with atmospheric monitoring. All fittings leak checked with N <sub>2</sub> prior to use.
Ozone (Produced in NO <sub>x</sub> analyser)	1	3	3	Local exhaust ventilation in the Left Hand Extraction Bay (LHEB) employed to reduce concentrations, with atmospheric monitoring. All fittings leak checked with N <sub>2</sub> prior to use.
Nitrogen	1	2	2	Leak poses Asphyxiant risk, with local monitoring used to identify when Oxygen concentration drops below 19%. Local extract ventilation used, in addition to remote

			isolation valves. All fittings leak checked with N <sub>2</sub> prior to use.
1 – 5 Low	No further action required		
6 – 11 Medium	Appropriate additional control measures should be implemented		
12 – 25 High	Additional control measures <b>must</b> be implemented. Work <b>must not</b> commence until such measures are in place.		

**Additional Control Measures to Reduce Risks**

<b>Additional Control Measures to Reduce Risks</b>
-
-

**Assessment of Risk to Health after Additional Control Measures**

<b>Scoring Criteria for Likelihood of Harm</b> 1-Very Unlikely, 2-Unlikely, 3-Likely, 4-Very Likely, 5-Extremely Likely	Likelihood (1 - 5)	X	Severity (1 - 5)	Level of Risk = (1 - 25)	Justification Notes
<b>Scoring Criteria for Severity of Injury or Illness</b> 1-First Aid is adequate, 2-Minor Injury, 3-Three Day Injury, 4-Major Injury, 5-Fatal or Disabling Injury					
1 – 5 Low	No further action required				
6 – 11 Medium	Appropriate additional control measures should be implemented				
12 – 25 High	Additional control measures <b>must</b> be implemented. Work <b>must not</b> commence until such measures are in place.				

DECLARATION				
	Name:	Signature:	Date:	
Assessment completed by:	James Bain		20/03/23	
Supervisor/Line Manager:	Steve Morris		22/03/2023	Review By:

REVIEW				
Reviewed By:	Steve Morris			Review By:
Reviewed By:				Review By:
Reviewed By:				Review By:

## D.4 Safe Operating Procedure

Provided overleaf.





# SAFE OPERATING PROCEDURE

## Turbulent Inhomogeneous Mixture Autoignition Rig

### Abstract

This document is a safe operating procedure for the use of the novel TIMAR facility at Cardiff Universities Gas Turbine Research Centre. This document is required to be read and signed by all involved parties in the operation or spectating of TIMAR.

James Bain  
BainJT@cardiff.ac.uk

# I. Contents

1. Introduction .....	2
2. Experiment Location .....	2
2.1. Nearest Escape Route.....	2
2.2. Nearest Telephones .....	2
2.3. Operator Details .....	2
3. Experiment Equipment Overview.....	3
3.1. Diagnostics Employed.....	3
3.2. Material.....	3
3.3. Fuel Delivery. ....	3
3.4. Instrumentation.....	4
3.5. Ignition.....	4
3.6. Ancillary Equipment.....	4
4. Operational Procedure. ....	4
5. Priorities.....	7
6. Safety Requirement .....	7
7. Signature Sheet.....	7
II. Appendices. ....	8
A. Appendix A – General Assembly of TIMAR.....	8

## 1. Introduction

This document details the method statement for operating the Turbulent Inhomogeneous Mixture Autoignition Rig (TIMAR) develop at Cardiff University School of Engineering for the operation at the Gas turbine Research Centre (GTRC). This document is one of four inter-related safety documents that details the safe operation and further safety considerations. The other three documents being, COSHH, DSEAR (plus remediations) and a specific Risk Assessment.

## 2. Experiment Location

TIMAR has been designed to operate at Cardiff University's GTRC in Port Talbot. It has been located in the Lefthand Extraction Bay (LHEB) located in the Rig Room at the GTRC, to use the extraction fan to minimise the occurrence of an explosive atmosphere. TIMAR has been fitted to a mobile bench that can has been designed to house TIMAR in the right orientation and house most all additional components. The control unit for TIMAR is located outside of the LHEB to distance it from a potentially explosive atmosphere.

See Figure 1 for schematic of locations of egress points, test bays, extraction bays and telephones.

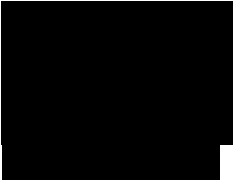
### 2.1. Nearest Escape Route

There are two means of egress in an event requiring an escape. Directly from the LHEB there is a fire exit located to the right of the extraction bay. There is also a means of egress through to the work shop also. The fire assembly point, or muster point, for the GTRC is the car park.

### 2.2. Nearest Telephones

In the case of an emergency use your mobile phone

### 2.3. Operator Details

<b>Name</b>	<b>Number</b>
James Bain	
Steve Morris	
Jack Thomas	
Tony Giles	
Burak Goktepe	

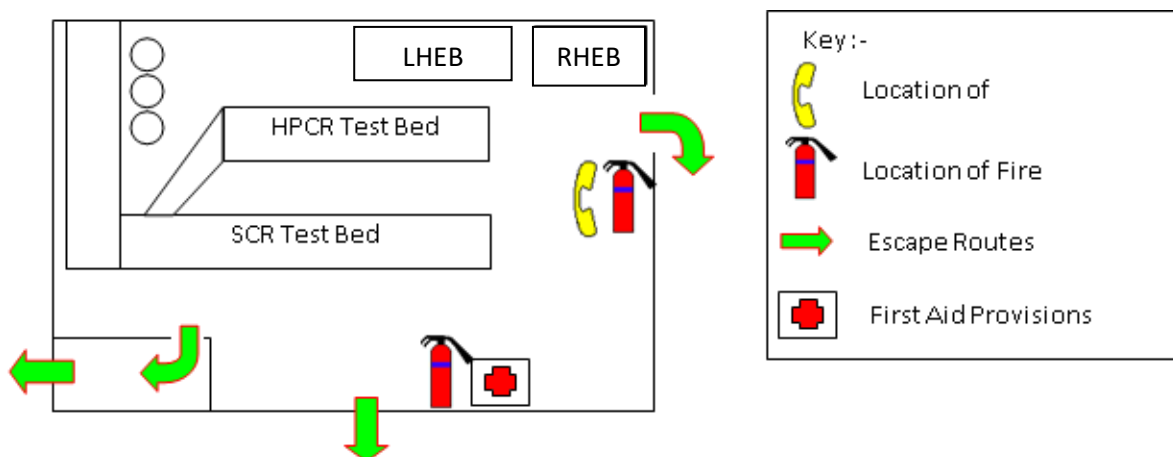


Figure 1 - Plan View of Rig Room, egress and telephone locations noted.

### 3. Experiment Equipment Overview.

TIMAR has been designed to investigate the effect of turbulence and temperature on high temperature reheat autoignition of methane hydrogen fuel blends. TIMAR operates by using an electric air heater to heat either air or a synthesised oxidant to temperatures circa 1000degC. Fuel is injected into the hot flow within the 'Mixing Duct' (MD). The MD is comprised of a square quartz tube to enable viewing of the combustion event.

#### 3.1. Diagnostics Employed.

Testing will comprise of two main bodies of testing: i) characterisation and ii) combustion. The characterisation work will require the use of Particle Image Velocimetry (PIV) and Laser Doppler Anemometry (LDA). Combustion work will use OH\* and CH\* (when applicable) chemiluminescence to determine the location of the ignition event.

#### 3.2. Material.

TIMAR has been manufactured with a combination of, 310, 314 stainless steels and Inconel 600. All materials are rated for high temperature operation and where applicable dissimilar metals face to minimise chances of metals fusing. As mentioned above, an optical chamber known as the MD is located on the downstream end of the rig to enable optical diagnostics to be performed. It is comprised of either Quartz glass or Borosilicate – again, both chosen for their suitability in high temperature conditions. The respective tubes are held into place by a "finger plate" (shown in Appendix A – General Assembly of TIMAR.) that is fixed by fasteners on A4 stud bar. Since TIMAR has only been designed to operate at atmospheric pressure, ability to operate resiliently at high temperature was prioritised. This was reflected in design considerations and calculations during the design phase.

#### 3.3. Fuel Delivery.

Fuels are introduced to TIMAR via the fuel delivery system employed at the GTRC. A pressurised gas delivery system consisting of 5 lines (of which two are used for fuel delivery) is used. Fuel is then controlled by mass flow controllers (MFCs) where a pressure drop of no more than 1.2bar is observed, hence, fuel delivery is near atmospheric conditions (see TIMAR\_dP\_FDS001 for detail). All of which

are to be purged with N<sub>2</sub> before and after operation to mitigate the formation of any flammable fuel/oxidant concentrations settling in TIMAR.

### 3.4. Instrumentation.

11 thermocouples (7 gas flow and 4 surface) are used to measure temperature across the length of TIMAR. 2 pressure transducers are also employed to measure pressure drop across TIMAR.

IMAGE.

### 3.5. Ignition.

The purpose of TIMAR is to evaluate changes in parameters that influence the autoignition delay time of the tested fuels. Hence, there will be no direct ignition source other than the hot oxidant supplied to the rig.

### 3.6. Ancillary Equipment.

Overall, TIMAR has the following ancillary equipment associated with it:

- i) Thermal insulation.
- ii) MFCs for oxidant and fuel delivery.
- iii) Fuel cylinders and relevant regulators.
- iv) N<sub>2</sub> cylinders and relevant regulators.
- v) CO<sub>2</sub> cylinders and relevant regulators.
- vi) Electric Air Heater Control Unit – mains operated.
- vii) 11x Type-K thermocouples.
- viii) 2x Druck -1bar to 1.6bar Pressure Transducers.
- ix) Water tank, pump and MFC for water injection.
- x) Air supply from compressor.
- xi) HD camera.
- xii) Dantek Traverse.
- xiii) High speed camera.
- xiv) OH\* or CH\* chemiluminescence lens.
- xv) Visual image intensifier.
- xvi) 2x National Instrument cards for Pressure Transducers and Thermocouples.
- xvii) Mains power supplies to various ancillary equipment.

## 4. Operational Procedure.

The general procedure is broken down into several parts, each part is then subdivided into specific actions.

Part A Preparation required before the test day.

Part B Preparation required to configure rig for test.

Part C Preparation required for setting gas delivery system.

Part D Procedure to run tests on the test day.

Part E Procedure to render the apparatus and test site safe at the end of the test day.

**Part A: Preparation required prior to any testing.**

- i) Ensure all personnel involved with the tests have read the Risk Assessment, DSEAR assessment, COSHH assessment and Safe Operating Procedure, and signed a record as having done so.
- ii) Ensure adequate supplies of fuel and other consumable gases.
- iii) Ensure TIMAR is fitted in its desired configuration for test runs intended.

**Part B: Preparation required to configure TIMAR for test.**

- Ensure all personnel working in the vicinity know the risks involved, and at least three competent persons present on site.
- Undertake visual inspection to ensure that the chamber is configured as required, is intact, is in good mechanical order and is free from dust and debris. Also ensure that the MD (whether Quartz or Borosilicate) is clean, clear of dust and has no surface damage e.g. cracks.
- Remove any flammable material from around the rig.
- Performing each listed check, sign inspection test sheet.
- Ensure extract valve is open in the operational bay (LHEB) and closed in the other (RHEB).
- Turn on extract ventilation and personal gas monitors – one monitor for the test controller and another located near the fuel delivery system in the extract bay.
- Switch on mains power to all instruments.
- Switch on compressor to deliver air to TIMAR ready for heating.
- Check software communications to cameras, ensuring filming and shutter speeds are correctly set.
- Erect warning signs and turn on external test flashing light.
- Open external evacuation gates.

**Part C: Procedure for setting gas delivery system.**

Fuel delivery set up in accordance with GTRC setup procedures (GTRC 0210, ensuring:

- Valves in cabinet 2 are correctly configured to introduce:
  - CO2 on line 1, controlled by M14 MFC.
  - Air on line 2, controlled by M14 MFC.
  - Hydrogen on line 3, controlled by M14 MFC.
  - Additional Nitrogen on line 4, controlled by Coriolis MFC.
  - Methane on line 5, controlled by M14 MFC.
  - Perform nitrogen drop test on the fuel lines then bleed pressure externally.
  - Perform CO2 drop test on CO2 line then bleed pressure externally.
  - Set air flow to 20g/s .
  - Turn on MFC cabinet ventilation fan.
  - Setup up desired gas pressures for the experiment.
  - Ensure rig room is vacated.
  - Flow each fuel through the rig at 0.1g/s until all the nitrogen has been removed. This is achieved by a density check with the MFCs.
  - Ensure at least double isolation on all fuel lines until they are ready to use.
  - The air preheater can be started and driven to desired experimental temperature.e

**Part D: Procedure to run test.**

- Ensure only required personnel are present.
- Ensure all ancillary equipment is ready as outlined in Part B of procedure.
- Ensure desired air flow into rig.

- When undertaking experimental test conditions (i.e. synthesised oxidant, CO<sub>2</sub>, N<sub>2</sub>), introduce necessary mass flows of constituents as outlined by test co-ordinator.
- Turn on electric air heater and control to desired test point at an interval of 50degC at a time, increasing only when control unit controls.
- Again, when undertaking experimental test conditions (i.e. synthesised oxidant), introduce the water for steam dilution at the required mass flow. To be done when rig temperature is at operation to allow water to fully vaporise.
- Adjust controller set point to re-attain the test temperature.
- Once temperature attained, run nitrogen fuel purge for 3 seconds and then introduce gaseous fuel through mass flow controller for a period of 10 seconds – set camera trigger to in tandem with fuel delivery.
- Combustion event expected in the rig.
- Close valve for gaseous fuel after 10 seconds.
- Perform nitrogen rig purge for 5 seconds.

Procedure for emergency or misfire.

- Stop fuel supply to TIMAR using automated valves or E-Stop in the control room.
- Feed nitrogen purge into fuel lines.
- Maintain air running in TIMAR.
- Maintain extraction fan running.
- If Rig Room deemed safe by test controller, reduce the operating temperature of electric air heater.
  - If below 1000degC, heater can be switched off immediately.
  - If above 1000degC, heater must be turned down 30degC/min, until 1000degC reached.
  - Air must remain running until
- Switch off power supply to heater.
- Allow air to run for an additional 10 mins to allow for sufficient cooling until switching off air supply.

**Part E: Procedure to render the apparatus and test site safe at the end of the test day.**

- Ensure no further gaseous fuel is supplied to the rig.
- Turn off fuel gas bottle
- Set air flow 20 20g/s
- If Rig Room deemed safe by test controller, reduce the operating temperature of electric air heater via control unit.
  - If below 1000degC, heater can be switched off immediately.
  - If above 1000degC, heater must be turned down 30degC/min, until 1000degC reached.
  - Air must remain running.
- Switch off power supply to heater.
- Bleed each fuel individually through the rig at 0.1g/s until the lines are depressurised.
- Perform 3x nitrogen purges (At 5bar) of the fuel lines externally leaving 5bar nitrogen in the line to be bled through the rig at 0.1g/s until depressurised
- Maintain air running in TIMAR.
- Maintain extraction fan running.
- Allow air to run for an additional 10 mins or until the rig temperatures are below 250C Before switching off the air supply.
- Turn off air compressor
- Turn off all electrical equipment
- Turn off extract fans

## 5. Priorities

- Ensure all personnel are familiar and accept the terms of the safety documentation. Discussion is encouraged to adapt and improve the document.
- All works should be in line with the suite of safety documentation. Any changes to operation method will require a re-assessment of the safety documentation.
- To ensure the safety of personnel within the vicinity of the tests. Authorised personnel only are allowed access to the Rig Room during testing, at the discretion of the designated test controller – once the experiment is known to be under control. Whilst TIMAR is running, all personnel must wear ear and eye protection if access granted.
- During experimental set up for running and during operation, the Rig Room must be clear of personnel, all warning signs erect and the GTRC facility closed for all other personnel not involved in testing.

## 6. Safety Requirement

Any activities performed in the set-up and operation of TIMAR must adhere to all the safety documentation that satisfies the necessary safety regulations. The purpose is to keep all personnel safe by being aware of any risk of a hazardous event and employing suitable safety controls to minimise them as low as reasonably practicable.

All works must be performed with the correct PPE being used at all times. Such as:

- Where the possibility of gas leaks occurs i.e. when opening any of the compressed gas cylinders EYE PROTECTION AND GLOVES MUST BE WORN.
- Where the possibility of toxic gas leak occurs (use of CO), an apt GAS DETECTOR ALARM MUST BE WORN.
- When moving cylinders – PROTECTIVE FOOTWEAR MUST BE WORN.
- When observing TIMAR in operation – ANTI-STATIC OVERALLS AND PROTECTIVE FOOTWEAR.

Carbon Dioxide fire extinguishers shall be in the reach of the designated controller in case that fire breaks out in the laboratory.

If there are any doubts, questions or further comments please know that an open discussion around the safe undertaking of any works regarding TIMAR is encouraged.

## 7. Signature Sheet.

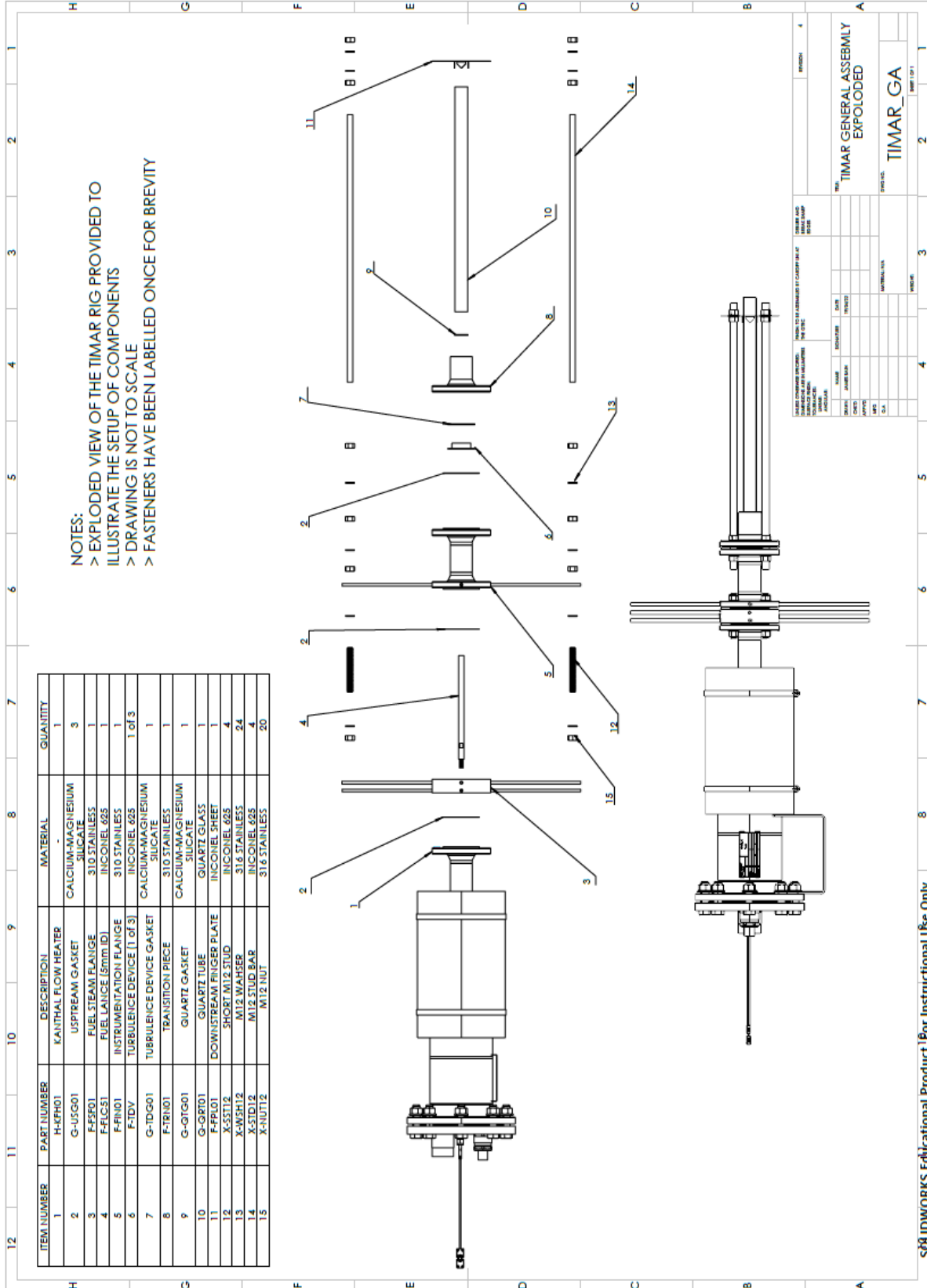
All personnel who are involved in work on the apparatus whilst conducting experimentation are required to read this document prior to starting work. Everyone must then sign below to record having done so.

Name	Signature	Date.
James Bain		03/04/23
Steve Morris		03/04/23
Burak Goktepe		03/04/23
Jack Thomas		03/04/23
Tony Giles		06/04/23



## II. Appendices.

### A. Appendix A – General Assembly of TIMAR.



## D.5 SEV Oxidant Inlet Composition Investigation

### D.5.1 Introduction

This document provides detail on the attainment of flue gas compositions that would approximate the flue gas composition of the flue gas entering the SEV burner of the GT26.

### D.5.2 Test Matrix Development

The test matrix was developed with two forms of testing in mind. The first being a fundamental study of the effect of varying oxidant composition on turbulent ignition. The second required a hypothetical inlet composition to the SEV be estimated for each fuel blend to achieve an “applied” condition that is specific to that fuel blend.

### D.5.3 Fundamental Study of Each Constituent in the Oxidant.

In essence, the idealised oxidants to be synthesised would be varying combinations of N<sub>2</sub>/O<sub>2</sub>/CO<sub>2</sub>/H<sub>2</sub>O and an initial test campaign would be launched to evaluate the effect of each one. The initial oxidant compositions to be tested were of nitrogen and oxygen, where their proportion in relation to one another is described by:

$$\beta = \frac{n_{O_2}}{\sum_n^i n_i} \quad (D.1)$$

The  $\beta$  values proposed for testing were: 0.1, 0.12, 0.15, 0.18 and 0.21.

It was then further proposed to build upon this testing whilst also introducing CO<sub>2</sub> into the oxidant mixture. The range of  $\beta$  values was the same, however, it would be tested at 4 CO<sub>2</sub> levels of 2.5%, 5.0%, 7.5% and 10.0% by volume. This range was chosen specifically as it captured the range of the predicted CO<sub>2</sub> concen-

trations in the exhaust of the first stage combustor. The purpose of being to test the extinguishing effect of CO<sub>2</sub> on the autoignition of the fuels in question.

Similarly, the percentage volume of H<sub>2</sub>O was also considered in isolation with a N<sub>2</sub>/O<sub>2</sub> of the  $\beta$  values described. The percentage volumes of water proposed were 5%, 10%, 15% and 20%. Again, values at equal interval from one another and within the range of percentage volumes expected in the flue gas from a first stage combustion of the fuel blends under evaluation.

#### **D.5.4 Applied Conditions Relevant to the Fuel Blend Under Evaluation.**

It was expected that following on from the fundamental study of varying each oxidant composition independently will have provided a foundation of knowledge to how these oxidant constituents affect the ignition of the fuel. The proceeding method aimed to build from that initial foundation.

To select appropriate test conditions, that have some semblance to the conditions in the GT26, an approach of determining an adiabatic flame temperature (AFT) for methane in the GT26 burner was undertaken. Note that there are shortcomings in this approach due to the limited data made available through publicly available literature and shared data by the authors industrial sponsors. There is also a scarcity of the detail regarding the cooling air, both in terms of volumes, temperatures and cooling air paths due to its confidential nature. Where possible a generalised description is provided.

By determining an AFT for CH<sub>4</sub> in the EV, it provides a bench-marking temperature for the other fuels blends to match. From there determination of this temperature, the ER or the subsequent fuel blends can be determined. Using the determined ER will then provide detail on the flue gas composition from the first stage burner. These flue gas compositions along with dilution and cooling air, will then comprise the oxidant conditions for TIMAR testing.

## D.5.5 Adiabatic Flame Temperature

Initial means of calculating the AFT were performed considering the heat of combustion and the enthalpy of formation of the products was undertaken. This proved to be a limited endeavour as it only considered stoichiometric combustion.

Therefore, a parametric study was undertaken using the equilibrium tool within CHEMKIN (2020 R1) using GrimMech3.0 for all CH<sub>4</sub> containing fuel blends and H<sub>2</sub>-Conaire [202] for the pure H<sub>2</sub> case. With the data ascertained by the author from their sponsors, the combustion air temperature and fuel preheat temperatures are known alongside accompanying flow rates for air and fuel. This enabled the determination of a ‘mixture’ temperature that is required by the equilibrium tool. note the mixture temperature is an average of the fuel preheat and the combustion air temperature. Therefore the mixture temperature was calculated by the following equation:

$$T_i = T_{\text{fuel}} \left( \frac{1}{\left(\frac{A}{F}\right)_{\text{op}}} \right) + T_{\text{oxi}} \left( \left(\frac{A}{F}\right)_{\text{op}} - \frac{1}{\left(\frac{A}{F}\right)_{\text{op}}} \right) \quad (\text{D.2})$$

Hence, an average initial temperature of the fuel and air mixture is considered to be 800K. A study was performed in determining the AFT for a pure methane case varying the ER of combustion. The results of which are displayed in Figure D.5.1.

To determine what the bench-marking AFT should be from a pure methane case, three methods were investigated. The first of which relied on knowing the turbine inlet temperature to the high pressure turbine (TIT1) of the GT26 and the amount, and temperature of, dilution air delivered to the EV plenum. the turbine inlet temperature was calculated by the following equation, which enabled the identification of the AFT that would return that given TIT1.

$$TIT1 = \frac{(\dot{m}_{\text{combustion,air}} + \dot{m}_{\text{fuel}})(AFT) + (\dot{m}_{\text{diltuion}} T_{\text{dilution}})}{\dot{m}_{\text{combustion,air}} + \dot{m}_{\text{fuel}} + \dot{m}_{\text{diltuion}}} \quad (\text{D.3})$$

The value of the TIT1 is displayed versus the equivalence ratio as detailed in Figure ?? below. note that the richer the combusting, the more available air there is for

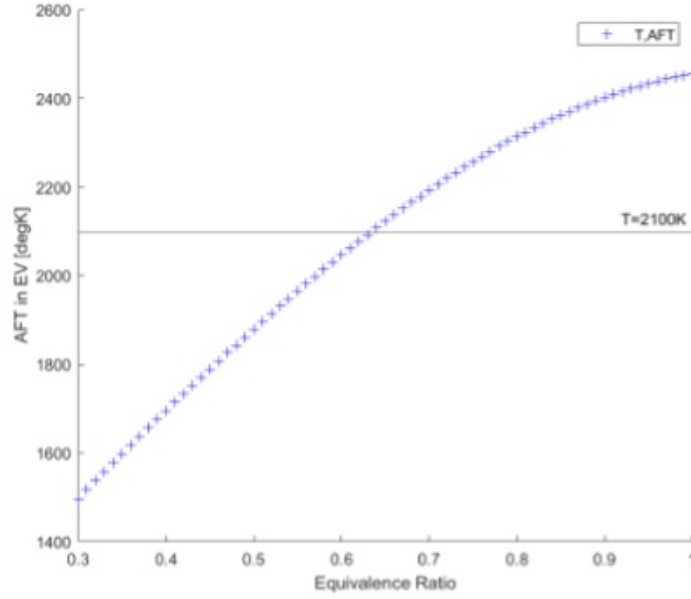


**Figure D.5.1:** Adiabatic Flame temperatures of methane performed in CHEMKIN for ER 0.3 – 1.0.

dilution and since the dilution air is cooler than that of the flame, it will have a cooling effect on the flue gas prior to the HPT. Therefore, an ER of 0.74 is returned as the optimal balance between a sufficiently high AFT and accounting for the requisite dilution air to achieve an operational TIT1.

### D.5.6 O<sub>2</sub> Level into the HPT.

The second method relies upon a detail found with the paper published by Guthe F. et al previously discussed in the literature review of this thesis [129] in which the following is quoted: *“the reheat concept also makes very efficient use of the O<sub>2</sub> from the air by operating the second stage ca. 15% O<sub>2</sub> at the inlet.*

Hence, a target of 15% O<sub>2</sub> at a position relating to TIT1 is the second decision criterion. The following equation was employed across the range of ERs to determine O<sub>2</sub> content as a percentage volume considering both the O<sub>2</sub> consumed in the combustion and the addition resulting from the excess air.

$$O_2\%vol = \frac{n_{O_2\ produced} + n_{O_2\ dilution}}{n_{combustion\ prod} + n_{air\ dilution}} \quad (D.4)$$

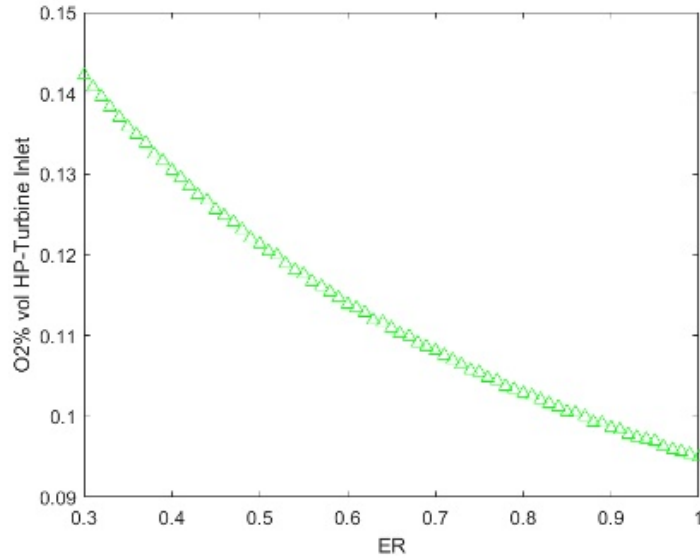


**Figure D.5.2:**  $O_2$  percentage volume entering the HPT.

Where  $n$  denotes the number of moles of the oxygen derived from a specific part of the process, as indicated by the subscripts. When this analysis is conducted across an equivalence ratio (ER) range spanning from 0.3 to 1.0, Figure D.5.2 illustrates the observed trend in the oxygen content that enters the High-Pressure Turbine (HPT) turbine. This oxygen content is derived from the first-stage lean combustion of the EV and the air dilution prior to the HPT. Rather notably, not at any of the conditions considered above does the  $O_2$  level reach the threshold of 15%. The author believes that since the 15%  $O_2$  stated by Guthe, F. et al [129] is relating to the SEV entry environment specifically (i.e. downstream of HPT), and therefore additional air will be added to the flow as a result of cooling air through the HPT blades and also through the “shielding-air” associated with the SEV fuel injection. The next step aims to quantify the air addition downstream of the turbine inlet of the HPT.

### D.5.7 $O_2$ Level Entering the SEV Combustor

Therefore, the approach developed once again through deriving the known amount of air that is used in the fuel shielding in the SEV fuel injection regime. The principle of this approach is from knowing the amount of air used in the fuel delivery in the

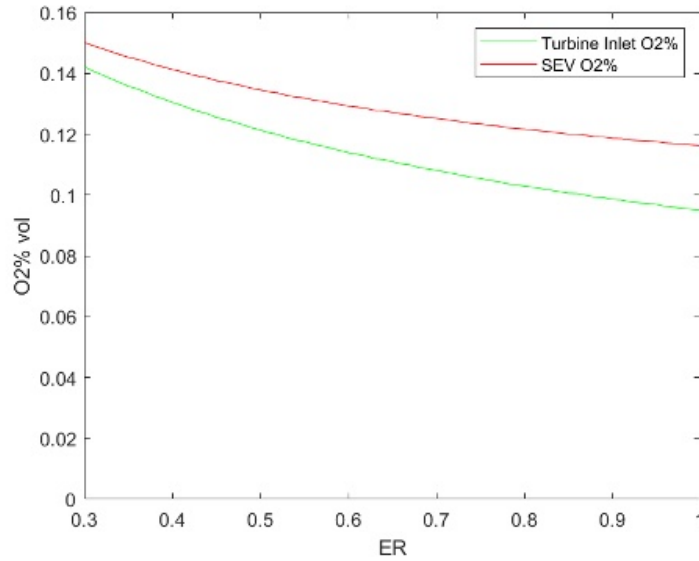


**Figure D.5.3:** *O<sub>2</sub> percentage volume of the gas flow entering HPT and an estimated O<sub>2</sub> level for SEV inlet.*

SEV, this value can be subtracted from the amount of dilution air required to reach 15% O<sub>2</sub>.

Again, the O<sub>2</sub> %vol, considering all flows of cooling air known to the author, was evaluated across the ER of the first stage combustor. This is detailed in Figure D.5.3, where the comparison between the O<sub>2</sub> level on the HPT intake and the SEV is illustrated, showing the improvement in the method. Figure D.5.3 illustrates that the only condition that achieves a 15% O<sub>2</sub> level in the SEV combustor is the case of the EV combustor operating at an equivalence ratio of 0.3. However, the author has considered the following:

- Calculations have been performed using a combination of operational data from one of the units at Pembroke Power station and approximated data that was derived from a confidential OEM document. Therefore, degrees of error can occur due to the data readings and instrumentation from operational data and of course, the inherent error in approximated data in OEMs document.
- OEM document also stated values for a GT26 operating circa. 2002/2003. Since, Pembroke have been operating with a MXL2 upgrade, therefore an unknown error may be introduced here also.

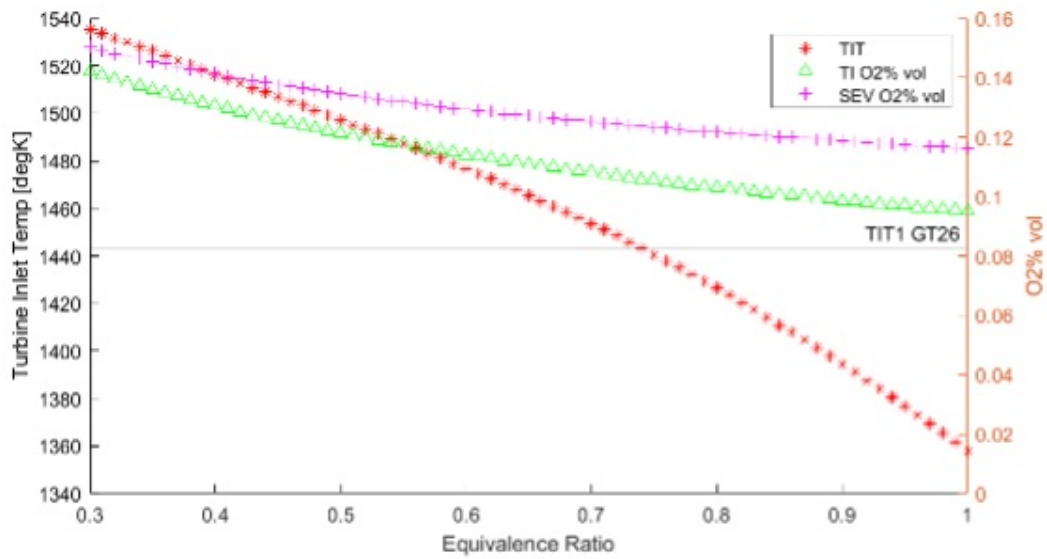


**Figure D.5.4:** Turbine Inlet Temperature, O<sub>2</sub> Level at HPT Inlet and SEV, and the estimation of turbine inlet temperature across ER range of 0.3-1.0.

- Guthe, F. et al state that the SEV environment is “*circa* 15%” and since the ER range of 0.5-0.7 provides an O<sub>2</sub> vol% in the SEV range of 13.4%-12.5% respectively, this error is accepted by the author.
- O<sub>2</sub> levels in the SEV may also change for varying power loads of the GT26 also.

### D.5.8 Determining ER for CH<sub>4</sub> combustion in GT26.

Drawing this section to a close, Figure D.5.4 below depicts the relationship between ER and the calculated AFT in the EV of the GT26; and the O<sub>2</sub>% volume estimated at both the HPT turbine inlet and then in the SEV inlet (downstream of the HPT), accounting for all the relevant cooling air. From this analysis, and due to the compounding effect of estimations of data, there is no clear solution for a value of the EV burners ER. The EV would have to run at an ER=0.3 to achieve a 15% O<sub>2</sub> level in the SEV. In addition to achieve a TIT1 of 1443K the EV would have to operate at an ER=0.74.

Important to note however, is that AFT is a theoretical property of the fuel. In real applications it is never achieved as there will always be heat lost to its



surrounding environment.

Taking all of the above information from the investigation described, the author proposes that the ER for the EV is approximated to 0.6, as the author believes that an ER=0.74 would be an overestimate due to the errors carried in the calculations, and it has an acceptable O<sub>2</sub> level of 12.9%. Hence, the associated AFT for a ER=0.6 flame in the EV, considering the combustion air and fuel preheat temperatures, is given as 2046K. This is the bench-marking temperature that will be used to determine the ER of other fuel blends.

The reason for matching AFTs across the fuel blends is analogous to GT operators and designers desire to attain a given turbine inlet temperature.

### **D.5.9 Confidential 0D Model.**

During this investigation of ER's and AFT's, the author was granted access to a confidential 0D model, developed by Cranfield University for RWE's use. Without divulging any further information, another instance of the EV's ER = 0.3 was found.

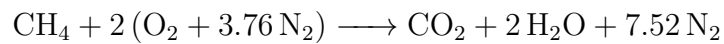
This is unprecedentedly lean for natural gas combustion in a lean premixed configuration, and the other passed them off as being too lean. It is regarded by the author that the Er of circa. 0.3 is for the global ER of the EV combustor, thus including downstream dilution of the flame and addition of air to the plenum, not the local ER in direct relation to the EV as a standalone component.

Hence, the author considers that the assumption of an EV=0.6 is reasonable and considered.

### **D.5.10 Flue Compositions From EV**

Now that an AFT had been attained, the necessary equivalent ratios from the EV for the various fuels to achieve said AFT was derived. Furthermore, oxidant compositions from the EV combustor from the fuel blends are derived by two methods i) rudimentary balanced chemical equations and ii) CHEMKIN Plug Flow Reactor (PFR) model

**Balanced Chemical Equations:** Whilst rudimentary in nature, the determination of the flue gas compositions from balanced chemical equations was involved. The process necessitated the determination of the chemical equation for complete stoichiometric combustion. Again, at this phase of the project, fuel blends in increments of 25% were in contention. An example of the complete combustion equation for stoichiometric combustion of methane is given by:



The air fuel ratio required on a volumetric and mass basis is further determined. Taking into account the ER attributed to the given fuel blend, the amount of excess air is determined. The percentage of excess air is included in the product side of the balanced chemical equation and is further used to determine the proportions of reactants from the reaction.

For the ER=0.6 methane case considered already, an ER of 0.6 means an addition of 67% of excess air. Therefore 167% of stoichiometric air is required (note  $2(1.67) = 3.34$ ). This is included in the balanced chemical equation of combustion, as shown below.



Each constituent in turn can be presented as a vol% by determining the total number of moles in the mixture and dividing to attain its fraction within the mixture. The composition by volume for this methane case considered is: CO<sub>2</sub> 9.29%, H<sub>2</sub>O 7.60%, O<sub>2</sub> 9.01% and N<sub>2</sub> 74.10%.

Note that when the compositions are presented again, they shall also include consideration for the dilution that the EV flue gas will receive.

**CHEMKIN Chemical Reactor Network:** In an attempt to improve upon the results of the balanced chemical equations, a Chemical Reactor Network (CRN) was

developed in CHEMKIN to derive the same results. The CRN is based upon a reactor network for a single stage GT combustor, which was exemplified in [203]. It is comprised of three major sections i) flame/ignition region, ii) recirculation zone and iii) a post-flame zone.

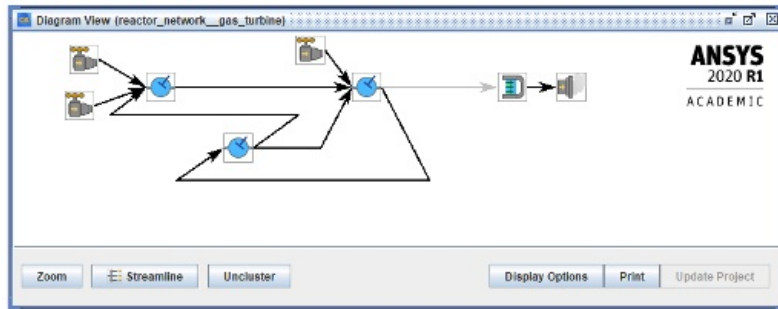
Whilst the GT26's EV precise combustion characteristics are unknown to the author due to the protection of proprietary information, this generic model is utilised. This CRN employs two reactor network clusters wherein the first reactor network cluster aims to represent the flame (air/fuel mixing, flame zone, recirculation zone) by a series of perfectly stirred reactors (PSR), and the second reactor network cluster is comprised of a plug flow reactor (PFR) as the post-flame region prior to the turbine inlet [203]. It is within this post-flame region that the dilution air is introduced. The CRN and its principles are depicted by Figure D.5.5a and D.5.5b, respectively.

Note, the PSR is defined as an ideal reactor that perfectly mixes the reactants in the control volume and assumes total homogeneity. By solving conservation equations, mixture fractions and temperature of products is attainable from the given inlet conditions of the system [204]. The PFR is defined as a series of thin reaction elements, known as plugs. These plugs travel in the axial direction of the reactor, and a reaction is modelled across each element, along the length of the reactor. It enables the description of idealised chemical reactions in a continuous flowing system [205].

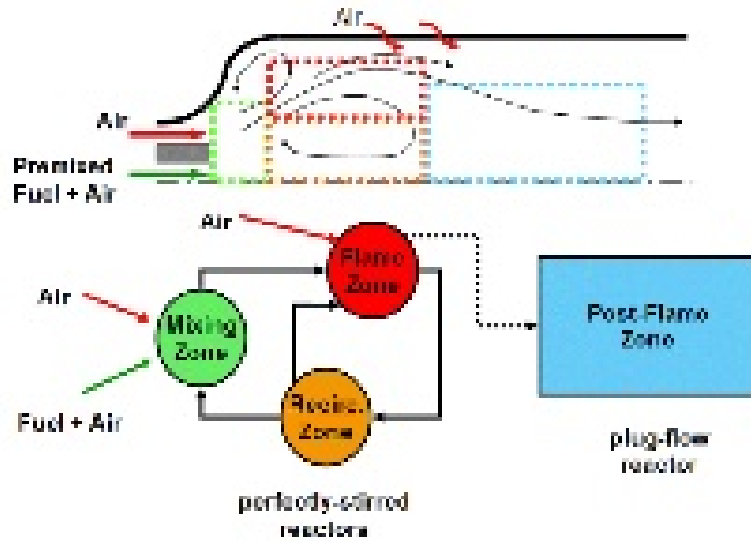
The results of the chemical balanced equation (denoted as CBE) and the CHEMKIN CRN model, coupled with their dilution, are detailed in Table 4.2 below.

### **D.5.11 Conclusion**

This document has outlined the investigative work undertaken to determine the oxidant conditions entering the SEV of the GT26 when operating on natural gas. This work was further built upon to predict the likely oxidant conditions at the inlet to the SEV for hydrogen and methane fuel blends.



(a) CRN used in the determination of the EV exhaust compositions.



(b) Principles of CRN schematically described.

**Figure D.5.5:** Illustrations depicting both the CRN's principles and the CRN itself.

This involved determining the adiabatic flame temperature (AFT) for methane and subsequently matching this temperature for other fuel blends. Despite the limitations posed by scarce and approximated data, a reasonable equivalence ratio (ER) for the EV burner was determined to be 0.6. This value balanced the need for an operational turbine inlet temperature (TIT1) and an acceptable oxygen level at the SEV inlet.

The study's methodical approach ensured the determination of flue gas compositions through both rudimentary balanced chemical equations and a detailed Chemical Reactor Network (CRN) model in CHEMKIN. The comparison between these methods highlighted the variations and potential errors inherent in each approach but ultimately provided a reliable foundation for understanding the flue gas compositions for different fuel blends, as is shared in Table D.1. The author intends

**Table D.1:** *Composition of natural gas used in commissioning.*

	<b>CH4</b>	<b>H2</b>	<b>ER</b>	<b>CO2</b>	<b>H2O</b>	<b>O2</b>	<b>N2</b>
	[%vol]	[%vol]	[-]	[%vol]	[%vol]	[%vol]	[%vol]
<b>CBE</b>	100%	0%	0.6	3.10%	6.20%	14.07%	76.64%
<b>CBE</b>	75%	25%	5.889	2.80%	6.55%	14.15%	76.50%
<b>CBE</b>	50%	50%	0.575	2.37%	7.11%	14.24%	76.27%
<b>CBE</b>	25%	75%	0.551	1.62%	8.09%	14.40%	75.88%
<b>CBE</b>	0%	100%	0.4925	0.00%	10.07%	14.82%	75.11%
<b>CRN</b>	100%	0%	0.6	2.58%	6.00%	14.40%	76.31%
<b>CRN</b>	75%	25%	5.889	1.94%	5.56%	15.32%	76.47%
<b>CRN</b>	50%	50%	0.575	1.49%	5.57%	15.81%	76.49%
<b>CRN</b>	25%	75%	0.551	1.07%	6.34%	15.85%	76.24%
<b>CRN</b>	0%	100%	0.4925	0.00%	9.72%	14.87%	74.89%

this document to be of value to future investigations of this topic.

# Bibliography

- [1] Prof. Svante Arrhenius. Xxxi. on the influence of carbonic acid in the air upon the temperature of the ground. *The London, Edinburgh, and Dublin Philosophical Magazine and Journal of Science*, 41(251):237–276, 1896.
- [2] D. Carrington. World close to 'irreversible' climate breakdown, warn major studies, 2022. Available at: <https://www.theguardian.com/environment/2022/oct/27/world-close-to-irreversible-climate-breakdown-warn-major-studies>, Date Accessed: 19th of September, 2023.
- [3] Eugene F. Stoermer and Paul J. Crutzen. The 'anthropocene'. IGBP Newsletter, 2000. Published in the International Geosphere-Biosphere Programme (IGBP) newsletter.
- [4] NASA. Giss surface temperature analysis, 2020. Available at: <https://earthobservatory.nasa.gov/world-of-change/decadaltemp.php>, Date Accessed: 28th of July, 2020.
- [5] United Nations. Paris agreement, 2015. Available at: [https://unfccc.int/files/essential\\_background/convention/application/pdf/english\\_paris\\_agreement.pdf](https://unfccc.int/files/essential_background/convention/application/pdf/english_paris_agreement.pdf), Date Accessed: 28th of Jul, 2020.
- [6] International Energy Agency (IEA). Net zero by 2050 - a roadmap for the global energy sector, 2021. Available at: <https://www.iea.org/reports/net-zero-by-2050>, Date Accessed: 22nd of April, 2022.
- [7] Stéphanie Bouckaert, Araceli Fernandez Pales, Christophe McGlade, Uwe

- Remme, Brent Wanner, Laszlo Varro, Davide D'Ambrosio, and Thomas Spencer. Net zero by 2050: A roadmap for the global energy sector, 2021.
- [8] Department for Energy Security and Net Zero. Hundreds of new north sea oil and gas licences to boost british energy independence and grow the economy, 2023. Available at: <https://www.gov.uk/government/news/hundreds-of-new-north-sea-oil-and-gas-licences-to-boost-british-energy-independence-and-grow-the-economy-31-july-2023>, Date Accessed: 3rd of Aug, 2023.
- [9] BP. Bp statistical review, 2019. Available at: <https://www.bp.com/content/dam/bp/business-sites/en/global/corporate/pdfs/energy-economics/statistical-review/bp-stats-review-2019-full-report.pdf>, Date Accessed: 30th of March, 2020.
- [10] World Energy Council. Energy security key according to 2015 world energy council energy trilemma index, 2015. Available at: <https://www.worldenergy.org/news-views/entry/energy-security-key-according-to-2015-world-energy-council-energy-trilemma-index>, Date Accessed: 13th of November, 2023.
- [11] Natalie Grover & Ahmed Ghaddar (Reuters). What israel-hamas war means for global oil market, 2023. Available at: <https://www.reuters.com/markets/commodities/what-impact-will-israelhamas-war-have-oil-2023-10-13/>, Date Accessed: 13th of November, 2023.
- [12] Jilian Ambrose. Why oil prices are rising amid israel-hamas war, 2023. Available at: <https://www.theguardian.com/business/2023/oct/20/oil-prices-israel-hamas-war>, Date Accessed: 13th of November, 2023.
- [13] Yuval Noah Harari. *Sapiens: A brief history of humankind*. Random House, 2014.

- [14] International Energy Agency IEA. Key world energy statistics, 2021. Available at: <https://www.iea.org/reports/key-world-energy-statistics-2021>  
Date Accessed: 3rd of August, 2023.
- [15] Nancy Stauffer. Moving away from fossil fuel energy? not without aggressive policy action, Oct 2017.
- [16] The Federal Ministry for Economics and Climate Protection Germany. List of LNG terminals in Germany, 2022. Available at: [https://www.bmwi.de/Redaktion/DE/Downloads/F/faq-liste-lng-terminal-in-deutschland.pdf?\\_\\_blob=publicationFile&v=8](https://www.bmwi.de/Redaktion/DE/Downloads/F/faq-liste-lng-terminal-in-deutschland.pdf?__blob=publicationFile&v=8),  
Date Accessed: 6th of Jul, 2022.
- [17] World Energy Council. Policies for the future: 2011 assessment of country energy and climate policies - executive summary, 2011. Available at: [https://www.worldenergy.org/assets/downloads/PUB\\_wec\\_2011\\_assessment\\_of\\_energy\\_and\\_climate\\_policies\\_executive\\_summary\\_2011\\_WEC.pdf](https://www.worldenergy.org/assets/downloads/PUB_wec_2011_assessment_of_energy_and_climate_policies_executive_summary_2011_WEC.pdf),  
Date Accessed: 16th of Aug, 2023.
- [18] IEA. World energy outlook 2022, 2022.
- [19] United Nations. Revision of world population prospects. Technical report, United Nations, 2022.
- [20] Mai Bui, Claire S Adjiman, André Bardow, Edward J Anthony, Andy Boston, Solomon Brown, Paul S Fennell, Sabine Fuss, Amparo Galindo, Leigh A Hackett, et al. Carbon capture and storage (ccs): the way forward. *Energy & Environmental Science*, 11(5):1062–1176, 2018.
- [21] European Commission. Paris agreement. Available at: [https://ec.europa.eu/clima/policies/international/negotiations/paris\\_en](https://ec.europa.eu/clima/policies/international/negotiations/paris_en), date Accessed: 14th of July 2021.
- [22] European Commission. EU renewable energy directive. Available at: <https://energy.ec.europa.eu/topics/renewable-energy/renewable-energy->



directive-targets-and-rules/renewable-energy-directive\_en, Datae  
Accessed: 3rd of Aug, 2023.

- [23] European Commission. A hydrogen strategy for a climate-neutral europe, 2020. Available at: <https://eur-lex.europa.eu/legal-content/EN/TXT/?uri=CELEX:52020DC0301>, Date Accessed: 3rd of August, 2023.
- [24] European Comission. Hydrogen. Available at: [https://energy.ec.europa.eu/topics/energy-systems-integration/hydrogen\\_en](https://energy.ec.europa.eu/topics/energy-systems-integration/hydrogen_en), Date Accessed: 3rd of Aug, 2023.
- [25] EMR Settlement. Contracts for difference. Available at: <https://www.emrsettlement.co.uk/about-emr/contracts-for-difference/>, Date Accessed: 3rd of Aug, 2023.
- [26] HM Government. The ten point plan for a green industrial revolution, 2020. Available at: [https://assets.publishing.service.gov.uk/government/uploads/system/uploads/attachment\\_data/file/936567/10\\_POINT\\_PLAN\\_BOOKLET.pdf](https://assets.publishing.service.gov.uk/government/uploads/system/uploads/attachment_data/file/936567/10_POINT_PLAN_BOOKLET.pdf), Date Accessed: 15th of July, 2021.
- [27] Statistica. Electric vehicles market data analysis & forecast, 2022. Available at: <https://www.statista.com/study/103895/electric-vehicles-report/>, Date Accessed: 3rd of Aug, 2023.
- [28] Rolls Royce. Small modular reactors. Available at: <https://www.rolls-royce.com/innovation/small-modular-reactors.aspx#/>, Date Accessed: 3rd of Aug, 2023.
- [29] SSE. Construction begins on the world's largset offshroe wind farm, 2022. Available at: <https://www.sse.com/news-and-views/2022/04/construction-begins-on-the-world-s-largest-offshore-wind-farm/>, Date Accessed: 3rd of Aug, 2023.
- [30] energy Business and Industrial Strategy Committee. Decarbonisation of the power sector. Technical report, HM UK Government, 2021.

- [31] UK HM Government. Dispatchable power agreement, 2022. Available at: <https://assets.publishing.service.gov.uk/media/6373993e8fa8f559604a0b8b/ccus-dispatchable-power-agreement-business-model-summary.pdf>, Date Accessed: 20th of December, 2023.
- [32] UK Government. Uk hydrogen strategy, 2021. Available at: [https://assets.publishing.service.gov.uk/government/uploads/system/uploads/attachment\\_data/file/1175494/UK-Hydrogen-Strategy\\_web.pdf](https://assets.publishing.service.gov.uk/government/uploads/system/uploads/attachment_data/file/1175494/UK-Hydrogen-Strategy_web.pdf), date Accessed: 3rd of Aug, 2023.
- [33] IPCC. Ar5 climate change 2014: Mitigation of climate change: Annex iii, 2014. Available at: [https://www.ipcc.ch/site/assets/uploads/2018/02/ipcc\\_wg3\\_ar5\\_annex-iii.pdf](https://www.ipcc.ch/site/assets/uploads/2018/02/ipcc_wg3_ar5_annex-iii.pdf), Date Accessed: 16th of aug, 2023.
- [34] John D Podesta and Timothy E Wirth. Natural gas: a bridge fuel for the 21st century. *Center for American Progress*, 2009.
- [35] BEIS Toby McGarry. Uk electricity capacity and generation by fuel between 1920 and 2020. *Special Article - energy Trends collection 29 June 2023.*, 2023.
- [36] Mathilde Fajardy and Niall Mac Dowell. Can beccs deliver sustainable and resource efficient negative emissions? *Energy & Environmental Science*, 10(6):1389–1426, 2017.
- [37] Naomi E Vaughan and Clair Gough. Expert assessment concludes negative emissions scenarios may not deliver. *Environmental research letters*, 11(9):095003, 2016.
- [38] BP. Statistical review of world energy, 2022. Available at: <https://www.bp.com/content/dam/bp/business-sites/en/global/corporate/pdfs/energy-economics/statistical-review/bp-stats-review-2022-full-report.pdf>, Date Accessed: 7th of Aug, 2023.
- [39] European Turbine Network - ETN. Hydrogen gas turbines, 2020. Available

- at: <https://etn.global/wp-content/uploads/2020/01/ETN-Hydrogen-Gas-Turbines-report.pdf>, Date Accessed: 1st of April, 2020.
- [40] Meysam Qadrdan. *Modelling of an integrated gas and electricity network with significant wind capacity*. PhD thesis, Cardiff University, 2012.
- [41] David Appleyard. What every generation executive should know about the impact of ancillary services on plant economics, 2019. Available at: <https://www.ge.com/power/transform/article.transform.articles.2019.aug.ancillary-services-gas-power-plants#> Date Accessed: 29th of July 2020.
- [42] S. Priestley. Net zero in the uk, 2019. Available at: <https://commonslibrary.parliament.uk/research-briefings/cbp-8590/>, Date Accessed: 7th of July, 2020.
- [43] Mitsubishi Heavy Industries. State-of-the-art m701jac gas turbine exceeds 8,000 actual operating hours – air-cooled jac series establishes industry benchmark of reliability for 50hz power generation, 2022. Available at: <https://www.mhi.com/news/220905.html>, date Accessed: 30th of April, 2024.
- [44] Sonal Patel. A brief history of ge gas turbines, 2019. Available at: <https://www.powermag.com/a-brief-history-of-ge-gas-turbines-2/>, Date Accessed: 30th of April, 2024.
- [45] Shailendra Naik. *Basic Aspects of Gas Turbine Heat Transfer*. 04 2017.
- [46] L.S. Langston. Gas-turbine compressors: Understanding stall, surge,, not available. Available at: <https://www.ccj-online.com/combined-cycle-journal-number-50/gas-turbine-compressors-understanding-stall-surge/#:~:text=To%20illustrate%3A%20In%20the%20early,pressure%20ratio%20of%2018.4%3A1.>, Date Accessed: 30th of April, 2024.
- [47] K Ishizaka, K Saitoh, E Ito, M Yuri, and J Masada. Mitsubishi heavy industries technical review, 2017.

- [48] Atsushi Maekawa. Evolution and future trend of large frame gas turbine for power generation. *Journal of Power and Energy Systems*, 5:161–170, 2011.
- [49] IEA. The future of hydrogen, 2019. Available at: <https://www.iea.org/reports/the-future-of-hydrogen>, Date Accessed: 27th of July, 2020.
- [50] Jenny Larfeldt, Mats Andersson, Anders Larsson, and Daniel Moëll. Hydrogen co-firing in siemens low nox industrial gas turbines. *POWER-GEN Europe, Cologne, Germany, June*, pages 27–29, 2017.
- [51] Ibrahim Dincer. Green methods for hydrogen production. *International Journal of Hydrogen Energy*, 37(2):1954–1971, 2012. 10th International Conference on Clean Energy 2010.
- [52] National Grid. The hydrogen colour spectrum, 2023. Available at: <https://www.nationalgrid.com/stories/energy-explained/hydrogen-colour-spectrum>, Date Accessed: 1st of May, 2024.
- [53] International Renewable Energy Agency. Hydrogen, 2023. Available at: <https://www.irena.org/Energy-Transition/Technology/Hydrogen#:~:text=As%20at%20the%20end%20of,around%204%25%20comes%20from%20electrolysis.>, Date Accessed: 1st of May, 2024.
- [54] IEA. Ammonia – the co2-free fuel of the future? Available at: <https://www.iea.org/articles/ammonia-the-co2-free-fuel-of-the-future>, Date Accessed: 5th of July, 2022.
- [55] Asbjørn Klerke, Claus Hviid Christensen, Jens K Nørskov, and Tejs Vegge. Ammonia for hydrogen storage: challenges and opportunities. *Journal of Materials Chemistry*, 18(20):2304–2310, 2008.
- [56] A Valera-Medina, H Xiao, M Owen-Jones, W.I.F. David, and P.J. Bowen. Ammonia for power. *Progress in Energy and Combustion Science*, 69:63–102, 2018.

- [57] S. Mashruk, M.O. Viguera-Zuniga, M.E. Tejada del Cueto, H. Xiao, C. Yu, U. Maas, and A. Valera-Medina. Combustion features of  $\text{CH}_4/\text{NH}_3/\text{H}_2$  ternary blends. *International Journal of Hydrogen Energy*, 47(70):30315–30327, 2022. XXI International Meeting of the Mexican Hydrogen Society.
- [58] K.K. Gupta, A. Rehman, and R.M. Sarviya. Bio-fuels for the gas turbine: A review. *Renewable and Sustainable Energy Reviews*, 14(9):2946–2955, 2010.
- [59] Mark Lynas. *Nuclear 2.0: Why a green future needs nuclear power*. Bloomsbury Publishing, 2014.
- [60] P.K. Vijayan, V. Shivakumar, S. Basu, and R.K. Sinha. Role of thorium in the indian nuclear power programme. *Progress in Nuclear Energy*, 101:43–52, 2017. Development of Advanced Nuclear Technologies.
- [61] Uguru Edwin Humphrey and Mayeen Uddin Khandaker. Viability of thorium-based nuclear fuel cycle for the next generation nuclear reactor: Issues and prospects. *Renewable and Sustainable Energy Reviews*, 97:259–275, 2018.
- [62] Richard Martin. *Superfuel: thorium, the green energy source for the future*. St. Martin’s Press, 2012.
- [63] *World Thorium Occurrences, Deposits and Resources*. Number 1877 in TECDOC Series. INTERNATIONAL ATOMIC ENERGY AGENCY, Vienna, 2019.
- [64] Albert Juhasz, Richard Rarick, and Rajmohan Rangarajan. High efficiency nuclear power plants using liquid fluoride thorium reactor technology. In *7th International Energy Conversion Engineering Conference*, page 4565, 2009.
- [65] Ralph W Moir and Edward Teller. Thorium-fueled underground power plant based on molten salt technology. *Nuclear technology*, 151(3):334–340, 2005.
- [66] RWE Generation. Pembroke net zero centre, 2023. Available at: <https://>

- [//uk-ireland.rwe.com/innovation/pembroke-net-zero-centre-pnzc/](https://uk-ireland.rwe.com/innovation/pembroke-net-zero-centre-pnzc/),  
Date Accessed: 8th of Aug, 2023.
- [67] RWE AG. The new rwe: carbon neutral by 2040 and one of the world's leading renewable energy companies. Available at : <https://www.rwe.com/en/press/rwe-ag/2019-09-30-the-new-rwe>, Date Accessed: 14th of July, 2021.
- [68] RWE. Sustainable strategy report 2022, 2023. Available at: <https://www.rwe.com/-/media/RWE/documents/09-verantwortung-nachhaltigkeit/cr-berichte/sustainability-strategy-report-2022.pdf>, Date Accessed: 4th of Aug, 2023.
- [69] Ben Willis. Decarbonising the uk power sector, 2023. Available at: <https://uk.rwe.com/press-and-news/uk-statements-and-opinion/decarbonising-the-uk-power-sector/>, Date Accessed: 1st of May, 2024.
- [70] RWE. Hydrogen, 2020. Available at: <https://www.rwe.com/en/our-portfolio/innovation-and-technology/hydrogen>, Date Accessed: 15th of July, 2021.
- [71] RWE. Get h2 nukleus. Available at: <https://www.rwe.com/en/research-and-development/hydrogen-projects/hydrogen-project-get-h2/>, Date Accessed: 8th of Aug, 2023.
- [72] RWE. Pilot project H<sub>2</sub>@hydro. Available at: <https://www.rwe.com/en/research-and-development/hydrogen-projects/h2-at-hydro/>, date Accessed: 8th of Aug, 2023.
- [73] Serena Romano, Matteo Cerutti, Giovanni Riccio, Antonio Andreini, and Christian Romano. Effect of Natural Gas Composition on Low Nox Burners Operation in Heavy Duty Gas Turbine. *Journal of Engineering for Gas Turbines and Power*, 141(11), 10 2019. 114501.

- [74] Seif-Eddine Zitouni. *Combustion characteristics of lean premixed methane/higher hydrocarbon/hydrogen flames*. PhD thesis, Cardiff University, 2020.
- [75] The Engineering Toolbox. Fuel gases - flame temperatures, 2003. Available at: [https://www.engineeringtoolbox.com/flame-temperatures-gases-d\\_422.html](https://www.engineeringtoolbox.com/flame-temperatures-gases-d_422.html), Date Accessed: 7th of May, 2024.
- [76] Anupam Ghosh, Natalia M. Munoz-Munoz, Karl P. Chatelain, and Deanna A. Lacoste. Laminar burning velocity of hydrogen, methane, ethane, ethylene, and propane flames at near-cryogenic temperatures. *Applications in Energy and Combustion Science*, 12:100094, 2022.
- [77] The Engineering Toolbox. Fuels - higher and lower calorific values, 2003. Available at: [https://www.engineeringtoolbox.com/fuels-higher-calorific-values-d\\_169.html](https://www.engineeringtoolbox.com/fuels-higher-calorific-values-d_169.html), Date Accessed: 410th of May, 2024.
- [78] The Engineering Toolbox. Gases - explosion and flammability concentration limits, 2003. Available at: , date Accessed: 10th of May, 2024.
- [79] Ryo Ono, Masaharu Nifuku, Shuzo Fujiwara, Sadashige Horiguchi, and Tetsuji Oda. Minimum ignition energy of hydrogen–air mixture: Effects of humidity and spark duration. *Journal of Electrostatics*, 65(2):87–93, 2007.
- [80] Thorne and Derrick International. Mie minimum ignition energy, Not Available. Available at: <https://www.heatingandprocess.com/product/hazardous-area-zones/mie-minimum-ignition-energy/>, Date Accessed: 10th of May, 2024.
- [81] The Engineering Toolbox. Adiabtic flame temperatures, 2005. Available at: [https://www.engineeringtoolbox.com/adiabatic-flame-temperature-d\\_996.html](https://www.engineeringtoolbox.com/adiabatic-flame-temperature-d_996.html), Date Accessed: 10tyh of May, 2024.
- [82] James Bain. Hydrogen gas turbine technology assessment, 2020. EngD Report.

- [83] Helen Lou, Daniel Chen, Christopher Martin, Xianchang Li, Kuyen Li, Hitesh Vaid, Kanwar Devesh Singh, and Preeti Gangadharan. Optimal reduction of the c1 c3 combustion mechanism for the simulation of flaring. *Industrial & Engineering Chemistry Research*, 51, 10 2012.
- [84] Chung K Law. *Combustion physics*. Cambridge university press, 2010.
- [85] Peter Glarborg, James A Miller, Branko Ruscic, and Stephen J Klippenstein. Modeling nitrogen chemistry in combustion. *Progress in Energy and Combustion Science*, 67:31–68, 2018.
- [86] J Zeldovich. The oxidation of nitrogen in combustion and explosions: Acta. *In Physiochem*, 1946.
- [87] James P Downs and Kenneth K Landis. Turbine cooling systems design: Past, present and future. In *ASME Turbo Expo 2009: Power for Land, Sea, and Air*, pages 819–828. American Society of Mechanical Engineers Digital Collection, 2009.
- [88] Christos Nicolaos Markides. *Autoignition in turbulent flows*. PhD thesis, University of Cambridge, 2006.
- [89] Irvin Glassman and Richard A. Yetter. Chapter 7 - ignition. In Irvin Glassman and Richard A. Yetter, editors, *Combustion (Fourth Edition)*, pages 379–408. Academic Press, Burlington, fourth edition edition, 2008.
- [90] Naeim Abdou Henein and Jay A Bolt. Kinetic considerations in autoignition and combustion of fuel sprays in swirling air. In *MECHANICAL ENGINEERING*, volume 94, page 55. ASME-AMER SOC MECHANICAL ENG 345 E 47TH ST, NEW YORK, NY 10017, 1972.
- [91] Peter Sunn Pedersen and Bjørn Qvale. A model for the physical part of the ignition delay in a diesel engine. *SAE Transactions*, pages 2625–2638, 1974.



- [92] R.T.E. Hermanns. *Laminar burning velocities of methane-hydrogen-air mixtures*. PhD thesis, Mathematics and Computer Science, 2007.
- [93] JL Gauducheau, B Denet, and G Searby. A numerical study of lean  $\text{CH}_4/\text{H}_2/\text{air}$  premixed flames at high pressure. *Combustion Science and Technology*, 137(1-6):81–99, 1998.
- [94] Zheng Chen. Effects of hydrogen addition on the propagation of spherical methane/air flames: a computational study. *International journal of hydrogen energy*, 34(15):6558–6567, 2009.
- [95] M Fairweather, MP Ormsby, CGW Sheppard, and R Woolley. Turbulent burning rates of methane and methane–hydrogen mixtures. *Combustion and Flame*, 156(4):780–790, 2009.
- [96] M. Ilbas, A.P. Crayford, İ. Yilmaz, P.J. Bowen, and N. Syred. Laminar-burning velocities of hydrogen–air and hydrogen–methane–air mixtures: An experimental study. *International Journal of Hydrogen Energy*, 31(12):1768–1779, 2006.
- [97] Eroglu A Larfeldt J. et al. Hydrogen capabilities of siemens energy gas turbines, an oem perspective. *10th International Gas turbine Conference*, "2021".
- [98] S Gersen, NB Anikin, AV Mokhov, and HB Levinsky. Ignition properties of methane/hydrogen mixtures in a rapid compression machine. *International Journal of Hydrogen Energy*, 33(7):1957–1964, 2008.
- [99] Changpeng Liu, Heping Song, Peng Zhang, Zhi Wang, Margaret S Wooldridge, Xin He, and Guotao Suo. A rapid compression machine study of autoignition, spark-ignition and flame propagation characteristics of  $\text{H}_2/\text{CH}_4/\text{CO}/\text{air}$  mixtures. *Combustion and Flame*, 188:150–161, 2018.
- [100] Yingjia Zhang, Xue Jiang, Liangjie Wei, Jiaxiang Zhang, Chenglong Tang, and Zuohua Huang. Experimental and modeling study on auto-ignition char-

- acteristics of methane/hydrogen blends under engine relevant pressure. *International Journal of Hydrogen Energy*, 37(24):19168–19176, 2012. 2011 International Workshop on Molten Carbonates & Related Topics.
- [101] Yingjia Zhang, Zuohua Huang, Liangjie Wei, Jiaxiang Zhang, and Chung K. Law. Experimental and modeling study on ignition delays of lean mixtures of methane, hydrogen, oxygen, and argon at elevated pressures. *Combustion and Flame*, 159(3):918–931, 2012.
- [102] Madhavan Poyyapakkam, John Wood, Steven Mayers, Andrea Ciani, Felix Guethe, and Khawar Syed. Hydrogen combustion within a gas turbine reheat combustor. In *Turbo Expo: Power for Land, Sea, and Air*, volume 44687, pages 847–854. American Society of Mechanical Engineers, 2012.
- [103] Yuyin Zhang, Jianghong Wu, and Satoru Ishizuka. Hydrogen addition effect on laminar burning velocity, flame temperature and flame stability of a planar and a curved  $\text{CH}_4\text{-H}_2\text{-air}$  premixed flame. *International Journal of Hydrogen Energy*, 34(1):519–527, 2009.
- [104] E Yunusova, V Larionov, A Malakhov, S Nazarychev, E Saifullin, and N Konstantinov. The influence of hydrogen concentration on the flame temperature of a mixture of methane-hydrogen fuel with air. *Journal of Physics: conference Series 2019 vol. 1328 N1*, 2019.
- [105] Anna Hasche, Ali Navid, Hartmut Krause, and Sven Eckart. Experimental and numerical assessment of the effects of hydrogen admixtures on premixed methane-oxygen flames. *Fuel*, 352:128964, 2023.
- [106] J.-Y Ren, W Qin, F.N Egolfopoulos, and T.T Tsotsis. Strain-rate effects on hydrogen-enhanced lean premixed combustion. *Combustion and Flame*, 124(4):717–720, 2001.
- [107] Erjiang Hu, Zuohua Huang, Jiajia He, Chun Jin, and Jianjun Zheng. Experimental and numerical study on laminar burning characteristics of pre-

- mixed methane–hydrogen–air flames. *international journal of hydrogen energy*, 34(11):4876–4888, 2009.
- [108] Ekenechukwu C. Okafor, Akihiro Hayakawa, Yukihide Nagano, and Toshiaki Kitagawa. Effects of hydrogen concentration on premixed laminar flames of hydrogen–methane–air. *International Journal of Hydrogen Energy*, 39(5):2409–2417, 2014.
- [109] Nicolas Bouvet, Fabien Halter, Christian Chauveau, and Youngbin Yoon. On the effective lewis number formulations for lean hydrogen/hydrocarbon/air mixtures. *International Journal of Hydrogen Energy*, 38(14):5949–5960, 2013.
- [110] J.P. Frenillot, G. Cabot, M. Cazalens, B. Renou, and M.A. Boukhalfa. Impact of h<sub>2</sub> addition on flame stability and pollutant emissions for an atmospheric kerosene/air swirled flame of laboratory scaled gas turbine. *International Journal of Hydrogen Energy*, 34(9):3930–3944, 2009.
- [111] Stuart R Bell and Manishi Gupta. Extension of the lean operating limit for natural gas fueling of a spark ignited engine using hydrogen blending. *Combustion Science and Technology*, 123(1-6):23–48, 1997.
- [112] GE Energy. Specification for fuel gases for combustion in heavy-duty gas turbines, 2016.
- [113] JON Runyon. *Gas turbine fuel flexibility: pressurized swirl flame stability, thermoacoustics, and emissions*. PhD thesis, Cardiff University, 2017.
- [114] United Kingdom Health and Safety Executive. Gas safety (management) regulations 1996 - gs(m)r, 1996. Available at: <http://www.legislation.gov.uk/uksi/1996/551/contents/made>, Date Accessed: 7th of July, 2020.
- [115] BSEN ISO. Measurement of properties—calorific value and wobble index.
- [116] C. George Segler. Gas engineers handbook, 1965.

- [117] Ted A Williams. Aga staff paper: technical background and issues of gas interchangeability. In *Building Energy Codes and Standards Committee*. American Gas Association, 2006.
- [118] General Electric. 6b.03 gas turbine. Available at: <https://www.ge.com/gas-power/products/gas-turbines/6b>, Date Accessed: 9th of Aug, 2023.
- [119] David Noble, David Wu, Benjamin Emerson, Scott Sheppard, Tim Lieuwen, and Leonard Angello. Assessment of Current Capabilities and Near-Term Availability of Hydrogen-Fired Gas Turbines Considering a Low-Carbon Future. *Journal of Engineering for Gas Turbines and Power*, 143(4):041002, 02 2021.
- [120] AG Siemens. Hydrogen combustion in siemens gas turbines: Sales information v 3.0. *Orlando, FL*, 2019.
- [121] Andrés Colorado, Vincent McDonell, and Scott Samuelsen. Direct emissions of nitrous oxide from combustion of gaseous fuels. *International Journal of Hydrogen Energy*, 42(1):711–719, 2017.
- [122] Jeff Goldmear GE. Power to gas - hydrogen powered gas turbines. Available at: [https://www.ge.com/content/dam/gepower/global/en\\_US/documents/fuel-flexibility/GEA33861%20Power%20to%20Gas%20-%20Hydrogen%20for%20Power%20Generation.pdf](https://www.ge.com/content/dam/gepower/global/en_US/documents/fuel-flexibility/GEA33861%20Power%20to%20Gas%20-%20Hydrogen%20for%20Power%20Generation.pdf), Date Accessed: 24th of November, 2023.
- [123] Department of Energy NETL (US). a literature review of hydrogen and natural gas turbines: current state of the art with regard to performance and nox control. Technical report, National Energy Technology Laboratory, 2022. Available at: <https://netl.doe.gov/sites/default/files/publication/A-Literature-Review-of-Hydrogen-and-Natural-Gas-Turbines-081222.pdf>, Date Accessed: 24th of November 2023.

- [124] Siemens Energy. Hydrogen power and heat with siemens energy gas turbines: reliable and flexible carbon free energy. Technical report, 2022. Available at: <https://www.siemens-energy.com/global/en/home/publications/whitepaper/download-hydrogen-gas-turbine-readiness-white-paper.html>, date Accessed: 24th of November, 2023.
- [125] Harald H-W Funke, Nils Beckmann, Jan Keinz, and Atsushi Horikawa. 30 years of dry-low-nox micromix combustor research for hydrogen-rich fuels—an overview of past and present activities. *Journal of Engineering for Gas Turbines and Power*, 143(7):071002, 2021.
- [126] *Combustor Development and Engine Demonstration of Micro-Mix Hydrogen Combustion Applied to M1A-17 Gas Turbine*, volume Volume 3B: Combustion, Fuels, and Emissions of *Turbo Expo: Power for Land, Sea, and Air*, 06 2021.
- [127] *Combined Heat and Power Supply Demonstration of Micro-Mix Hydrogen Combustion Applied to M1A-17 Gas Turbine*, volume Volume 3A: Combustion, Fuels, and Emissions of *Turbo Expo: Power for Land, Sea, and Air*, 06 2022.
- [128] *Development and Testing of a FuelFlex Dry-Low-NO<sub>x</sub> Micromix Combustor for Industrial Gas Turbine Applications With Variable Hydrogen Methane Mixtures*, volume Volume 4A: Combustion, Fuels, and Emissions of *Turbo Expo: Power for Land, Sea, and Air*, 06 2019.
- [129] Felix Güthe, Jaan Hellat, and Peter Flohr. The reheat concept: the proven pathway to ultralow emissions and high efficiency and flexibility. *Journal of Engineering for Gas Turbines and Power*, 131(2), 2009.
- [130] Ansaldo Energia. Gt26: The best value. Available at: <https://www.ansaldoenergia.com/Pages/GT26.aspx>, Date Accessed: 12th of August, 2020.

- [131] K Michael Düsing, Andrea Ciani, Urs Benz, Adnan Eroglu, and Klaus Knapp. Development of gt24 and gt26 (upgrades 2011) reheat combustors, achieving reduced emissions and increased fuel flexibility. In *Turbo Expo: Power for Land, Sea, and Air*, volume 55119, page V01BT04A034. American Society of Mechanical Engineers, 2013.
- [132] Fernando Biagioli and Felix Güthe. Effect of pressure and fuel–air unmixedness on nox emissions from industrial gas turbine burners. *Combustion and Flame*, 151(1-2):274–288, 2007.
- [133] K Michael Düsing, Andrea Ciani, and Adnan Eroglu. Effect of mixing quality on nox emissions in reheat combustion of gt24 and gt26 engines. In *Turbo Expo: Power for Land, Sea, and Air*, volume 54624, pages 633–642, 2011.
- [134] Klaus Döbbeling, Jaan Hellat, and Hans Koch. 25 years of bbc/abb/alstom lean premix combustion technologies, 2007.
- [135] Martin Zajadatz, Rudolf Lachner, Stefano Bernero, Christian Motz, and Peter Flohr. Development and design of alstom’s staged fuel gas injection ev burner for nox reduction. In *Turbo Expo: Power for Land, Sea, and Air*, volume 47918, pages 559–567, 2007.
- [136] A Ciani, A Eroglu, F Güthe, and B Paikert. Full-scale atmospheric tests of sequential combustion. In *Turbo Expo: Power for Land, Sea, and Air*, volume 43970, pages 759–768, 2010.
- [137] Adnan Eroglu, Peter Flohr, Philipp Brunner, and Jaan Hellat. Combustor design for low emissions and long lifetime requirements. In *Turbo Expo: Power for Land, Sea, and Air*, volume 48838, pages 435–444, 2009.
- [138] *Development of the Sequential Combustion System for the ABB GT24/GT26 Gas Turbine Family*, volume Volume 4: Heat Transfer; Electric Power; In-

- dustrial and Cogeneration of *Turbo Expo: Power for Land, Sea, and Air*, 06 1996.
- [139] Adnan Eroglu, Klaus Do"bbeling, Franz Joos, and Philipp Brunner. Vortex generators in lean-premix combustion. *J. Eng. Gas Turbines Power*, 123(1):41–49, 2001.
- [140] A. Eroglu, K. Do"bbeling, F. Joos, and P. Brunner. Vortex Generators in Lean-Premix Combustion . *Journal of Engineering for Gas Turbines and Power*, 123(1):41–49, 10 1999.
- [141] Oliver Riccius, Richard Smith, Felix G"uthe, and Peter Flohr. The gt24/26 combustion technology and high hydrocarbon ("c2+") fuels, 01 2005.
- [142] Torsten Wind, Felix G"uthe, and Khawar Syed. Co-firing of hydrogen and natural gases in lean premixed conventional and reheat burners (alstom gt26), 06 2015.
- [143] Torsten Wind, Felix G"uthe, and Khawar Syed. Co-firing of hydrogen and natural gases in lean premixed conventional and reheat burners (alstom gt26). In *Turbo Expo: Power for Land, Sea, and Air*, volume 45684, page V04AT04A053. American Society of Mechanical Engineers, 2014.
- [144] Ansaldo Energia. Ansaldo energia: Gty26 performance and flexibility upgrades. Available at:[https://www.ansaldoenergia.com/fileadmin/Brochure/Interactive\\_GT26\\_Brochure.pdf](https://www.ansaldoenergia.com/fileadmin/Brochure/Interactive_GT26_Brochure.pdf), Date Accessed: 14th of Sept, 2023.
- [145] Mirko R Bothien, Andrea Ciani, John P Wood, and Gerhard Fruechtel. Sequential combustion in gas turbines: The key technology for burning high hydrogen contents with low emissions. In *Turbo Expo: Power for Land, Sea, and Air*, volume 58615, page V04AT04A046. American Society of Mechanical Engineers, 2019.

- [146] Julia Fleck, Peter Griebel, Rajesh Sadanandan, Adam M Steinberg, Michael Stöhr, and Manfred Aigner. Characterization of a generic, fuel flexible reheat combustor. In *Proceedings*, 2010.
- [147] Rainer Lückerrath, Wolfgang Meier, and Manfred Aigner. Flox® combustion at high pressure with different fuel compositions, 2008.
- [148] Julia M Fleck, Peter Griebel, Adam M Steinberg, Michael Stöhr, Manfred Aigner, and Andrea Ciani. Experimental investigation of a generic, fuel flexible reheat combustor at gas turbine relevant operating conditions. In *Turbo Expo: Power for Land, Sea, and Air*, volume 43970, pages 583–592, 2010.
- [149] Julia Fleck, Peter Griebel, Adam M Steinberg, Michael Stöhr, Manfred Aigner, and Andrea Ciani. Autoignition limits of hydrogen at relevant reheat combustor operating conditions, 2012.
- [150] Julia Fleck, Peter Griebel, Manfred Aigner, and Adam M Steinberg. Autoignition of hydrogen/natural gas/nitrogen fuel mixtures at reheat combustor operating conditions, 2012.
- [151] *Experimental Investigation of a Generic, Fuel Flexible Reheat Combustor at Gas Turbine Relevant Operating Conditions*, volume Volume 2: Combustion, Fuels and Emissions, Parts A and B of *Turbo Expo: Power for Land, Sea, and Air*, 06 2010.
- [152] GE. Gt26 high efficiency gas turbine upgrade, N/A. Available at: <https://www.ge.com/gas-power/services/gas-turbines/gt26-service-solutions/high-efficiency>, Date Accessed: 15th of September, 2023.
- [153] C.N. Markides, G. De Paola, and E. Mastorakos. Measurements and simulations of mixing and autoignition of an n-heptane plume in a turbulent flow of heated air. *Experimental Thermal and Fluid Science*, 31(5):393–401, 2007. Fourth Mediterranean Combustion Symposium.



- [154] CN Markides and E Mastorakos. An experimental study of hydrogen autoignition in a turbulent co-flow of heated air. *Proceedings of the Combustion Institute*, 30(1):883–891, 2005.
- [155] CN Markides, G De Paola, and E Mastorakos. Measurements and simulations of mixing and autoignition of an n-heptane plume in a turbulent flow of heated air. *Experimental thermal and fluid science*, 31(5):393–401, 2007.
- [156] Hendrik Tennekes and John Leask Lumley. *A first course in turbulence*. MIT press, 1972.
- [157] Epaminondas Mastorakos. Ignition of turbulent non-premixed flames. *Progress in energy and combustion science*, 35(1):57–97, 2009.
- [158] R Cabra, T Myhrvold, JY Chen, RW Dibble, AN Karpetis, and RS Barlow. Simultaneous laser raman-rayleigh-lif measurements and numerical modeling results of a lifted turbulent  $\text{H}_2/\text{N}_2$  jet flame in a vitiated coflow. *Proceedings of the Combustion Institute*, 29(2):1881–1888, 2002.
- [159] R Cabra, J-Y Chen, RW Dibble, AN Karpetis, and RS Barlow. Lifted methane–air jet flames in a vitiated coflow. *Combustion and Flame*, 143(4):491–506, 2005.
- [160] E Oldenhof, MJ Tummers, EH Van Veen, and DJEM Roekaerts. Role of entrainment in the stabilisation of jet-in-hot-coflow flames. *Combustion and Flame*, 158(8):1553–1563, 2011.
- [161] E. Oldenhof, M.J. Tummers, E.H. van Veen, and D.J.E.M. Roekaerts. Ignition kernel formation and lift-off behaviour of jet-in-hot-coflow flames. *Combustion and Flame*, 157(6):1167–1178, 2010.
- [162] Suhui Li, Wenkai Qian, Haoyang Liu, Guijun Liu, and Min Zhu. Autoignition and flame lift-off behavior of a fuel jet mixing with turbulent hot air coflow. *Proceedings of the Combustion Institute*, 38(4):6385–6392, 2021.

- [163] Guijun Liu and Yuxin Wu. Lift-off height model of hydrogen autoignited flame in turbulent hot air coflow. *International Journal of Hydrogen Energy*, 2023.
- [164] Kyuho Van, Ki Sung Jung, Chun Sang Yoo, Soohyun Oh, Byeong Jun Lee, and Min Suk. Decreasing liftoff height behavior in diluted laminar lifted methane jet flames. *Proceedings of the Combustion Institute*, 37(2):2005–2012, 2019.
- [165] O. Schulz, U. Doll, D. Ebi, J. Droujko, C. Bourquard, and N. Noiray. Thermoacoustic instability in a sequential combustor: Large eddy simulation and experiments. *Proceedings of the Combustion Institute*, 37(4):5325–5332, 2019.
- [166] Oliver Schulz and Nicolas Noiray. Autoignition flame dynamics in sequential combustors. *Combustion and Flame*, 192:86–100, 2018.
- [167] *Morphology and Dynamics of a Premixed Hydrogen-Methane-Air Jet Flame in Hot Vitiated Turbulent Crossflow*, volume Volume 4B: Combustion, Fuels, and Emissions of *Turbo Expo: Power for Land, Sea, and Air*, 09 2020.
- [168] Roberto Solana-Perez, SA Shcherbanev, Andrea Ciani, and Nicolas Noiray. Effect of mixing on the anchoring and combustion regimes of pure hydrogen flames in sequential combustors. *Journal of Engineering for Gas Turbines and Power*, 145(3):031026, 2023.
- [169] Roberto Solana-Pérez, Sergey A. Shcherbanev, Bayu Dharmaputra, Andrea Ciani, and Nicolas Noiray. Combustion regime transition of h2 flames during steady and transient operation of a sequential combustor. *Proceedings of the Combustion Institute*, 39(4):4335–4344, 2023.
- [170] Jon Runyon, Richard Marsh, Yura Alexander Sevcenco, Daniel Pugh, and Steven Morris. Development and commissioning of a chemiluminescence imaging system for an optically-accessible high-pressure generic swirl burner. *EMC 2015: 7th European Combustion Meeting*, 2015.
- [171] Jon Runyon, Richard Marsh, Philip Bowen, Daniel Pugh, Anthony Giles, and Steven Morris. Lean methane flame stability in a premixed generic swirl

- burner: Isothermal flow and atmospheric combustion characterization. *Experimental Thermal and Fluid Science*, 92:125–140, 2018.
- [172] *Experimental Analysis of Confinement and Swirl Effects on Premixed CH<sub>4</sub>-H<sub>2</sub> Flame Behavior in a Pressurized Generic Swirl Burner*, volume Volume 4B: Combustion, Fuels and Emissions of *Turbo Expo: Power for Land, Sea, and Air*, 06 2017.
- [173] Kanthal. Flow heater control system, N/A. Available at: <https://www.kanthal.com/en/products/air-heaters/flow-heaters/flow-heater-control-system/>, Date accessed: 30th of August, 2023.
- [174] Momentive Tech. Quartz properties, N/A. Available at: <https://www.momentivetech.com/quartz-properties/>, Date Accessed: 22nd of September, 2023.
- [175] Grimech3.0. Available at: <http://combustion.berkeley.edu/gri-mech/version30/text30.html>, Date Accessed: 6th of December, 2023.
- [176] Crane Co. Flow of fluids through valves, fittings, and pipe, 1988.
- [177] H Schmick. Über den einfluß der molekularen anziehungskräfte auf die innere reibung und wärmeleitfähigkeit von gasmischungen (concerning the influence of molecular attraction on the viscosity and thermal conductivity of gas mixtures). *phys. Phys. Z*, 29:633–640, 1928.
- [178] S. Jiménez. Relevance of heat conduction in the correction and interpretation of high temperature, fine wire thermocouple measurements. *Combustion and Flame*, 240:112022, 2022.
- [179] S. W. Churchill and M. Bernstein. A Correlating Equation for Forced Convection From Gases and Liquids to a Circular Cylinder in Crossflow. *Journal of Heat Transfer*, 99(2):300–306, 05 1977.

- [180] Fuyuan Yang, Tianze Wang, Xintao Deng, Jian Dang, Zhaoyuan Huang, Song Hu, Yangyang Li, and Minggao Ouyang. Review on hydrogen safety issues: Incident statistics, hydrogen diffusion, and detonation process. *International journal of hydrogen energy*, 46(61):31467–31488, 2021.
- [181] R.W. Schefer, W.D. Kulatilaka, B.D. Patterson, and T.B. Settersten. Visible emission of hydrogen flames. *Combustion and Flame*, 156(6):1234–1241, 2009.
- [182] Muyi Pana, Xiao Wanga, Ahmed Albadia, YP Hanb, and Yang Zhanga. Further investigation of hydrogen flame colour. *Institute Dynamics of Explosion and Reactive Systems*, 2019.
- [183] Alfred Gordon Gaydon and Alfred Egerton. Spectroscopy and combustion theory. (*No Title*), 1948.
- [184] Mohammed El-Adawy, M.R. Heikal, A.A.R. Aziz, and Rasheed Opatola. Stereoscopic particle image velocimetry for engine flow measurements: Principles and applications. *AEJ - Alexandria Engineering Journal*, 60, 02 2021.
- [185] William Thielicke and René Sonntag. Particle image velocimetry for matlab: Accuracy and enhanced algorithms in pivlab. *Journal of Open Research Software*, 9(1), 2021.
- [186] William Thielicke. Pulse-length induced motion blur in piv particle images: To be avoided at any cost? 2022.
- [187] W. Thielicke. *The flapping flight of birds*. PhD thesis, University of Groningen, 2014.
- [188] Irvin Glassman, Richard A Yetter, and Nick G Glumac. *Combustion*. Academic press, 2014.
- [189] Abelm inversion algorithm, 2023. Available at: <https://www.mathworks.com/matlabcentral/fileexchange/43639-abel-inversion-algorithm>, Date Accessed: 23rd of August, 2023.

- [190] Image reproduced from Hamatsu Website [https://www.hamamatsu.com/eu/en/product/optical-sensors/pmt/pmt-module/for-special-applications\\_peripheral-equipments/C7169.html](https://www.hamamatsu.com/eu/en/product/optical-sensors/pmt/pmt-module/for-special-applications_peripheral-equipments/C7169.html), Date Accessed: 17th of Aug, 2023.
- [191] FA Williams. Combustion theory, 2<sup>nd</sup> edition, 1985.
- [192] Erjiang Hu, Zuohua Huang, Jiajia He, Chun Jin, and Jianjun Zheng. Experimental and numerical study on laminar burning characteristics of premixed methane–hydrogen–air flames. *International Journal of Hydrogen Energy*, 34(11):4876–4888, 2009. 2nd International Workshop on Hydrogen.
- [193] ANSYS INC. Ansys meshing user’s guide, 2021. Available at: [https://dl.cfdexperts.net/cfd\\_resources/Ansys\\_Documentation/Ansys\\_Meshing/Ansys\\_Meshing\\_Users\\_Guide.pdf](https://dl.cfdexperts.net/cfd_resources/Ansys_Documentation/Ansys_Meshing/Ansys_Meshing_Users_Guide.pdf), Date Accessed: 15th of December, 2023.
- [194] ANSYS Inc. Ansys theory guide, 2021. Available at: [https://dl.cfdexperts.net/cfd\\_resources/Ansys\\_Documentation/Fluent/Ansys\\_Fluent\\_Theory\\_Guide.pdf](https://dl.cfdexperts.net/cfd_resources/Ansys_Documentation/Fluent/Ansys_Fluent_Theory_Guide.pdf), Date Accessed: 16th of December, 2023.
- [195] A. Wimshurst. [cfd] the discrete oxidants (doo) radiation model., 2020. Available at: <https://youtu.be/yMj-Tjkxc8g?si=3zGoXkPw5Q9WgjEq>, Date Accessed: 16th of December, 2023.
- [196] John D Anderson. McGraw-hill series in aeronautical and aerospace engineering. *Fundamentals of Aerodynamics*, by, pages 54–56, 2003.
- [197] Ueber die Gesetze der Flüssigkeitsbewegung in engen Röhren *On the laws of fluid movement in narrow tubes.*, 1839.
- [198] E N Sieder and G E Tate. Heat transfer and pressure drop of liquids in tubes. *Industrial & Engineering Chemistry*, 28(12):1429–1435, 1936.

- [199] Volker Gnielinski. New equations for heat and mass transfer in turbulent pipe and channel flow. *International chemical engineering*, 16(2):359–367, 1976.
- [200] Frederick William Dittus. Heat transfer in automobile radiators of the tubular type. *Univ. of California Pub., Eng.*, 2(13):443–461, 1930.
- [201] Yunus A Cengel and Afshin J Ghajar. Introduction and basic concepts. In *Heat and Mass Transfer Fundamental and Applications*, pages 7–10. McGraw-Hill Education, 2015.
- [202] Marcus Ó Conaire, Henry J Curran, John M Simmie, William J Pitz, and Charles K Westbrook. A comprehensive modeling study of hydrogen oxidation. *International journal of chemical kinetics*, 36(11):603–622, 2004.
- [203] CHEMKIN-PRO 15112. Chemkin tutorials manual, 2011.
- [204] KAUST. Perfectly stirred reactor, N/A. Available at : , Date Accessed: 27th of September, 2023.
- [205] Vapour Tec. Plug flow reactor, N/A. Available at: <https://www.vapourtec.com/flow-chemistry/plug-flow-reactor/>, Date Accessed: 27th of September, 2023.